

**EVALUATING RADIATION INDICATORS IN THE VHTR POWER
PLANT USING MAVRIC**

A Thesis
Presented to
The Academic Faculty

by

Timothy M. Flaspoebler

In Partial Fulfillment
of the Requirements for the Degree
Master of Science in Nuclear and Radiological Engineering in the
School of Mechanical Engineering

Georgia Institute of Technology
December 2012

EVALUATING RADIATION INDICATORS IN THE VHTR POWER PLANT USING MAVRIC

Approved by:

Dr. Bojan Petrovic, Advisor
School of Nuclear and Radiological Engineering
Georgia Institute of Technology

Dr. Chaitanya Deo
School of Nuclear and Radiological Engineering
Georgia Institute of Technology

Dr. Nolan Hertel
School of Nuclear and Radiological Engineering
Georgia Institute of Technology

Dr. Douglas Peplow
Oak Ridge National Laboratory

Date Approved: June 14, 2012

ACKNOWLEDGEMENTS

First and foremost, I want to thank my advisor, Dr. Bojan Petrovic, for his guidance to myself starting as an oblivious undergraduate. Without his tireless help and supervision this thesis would not have been possible. In the process, I have learned a great deal. Furthermore, I would like to thank Dr. Nolan Hertel and Dr. Chaitanya Deo for taking time out of their busy schedule to provide their professional feedback as members of my thesis committee.

I wish to extend a special thanks to Dr. Douglas Peplow for his willingness to give advice when needed, his mentorship provided during two summers, and his development of the software used in this thesis. Additionally, his division at Oak Ridge National Laboratory has been a huge asset by not only providing data, but by providing useful incite and direction along the way.

I would also like to thank my family and those closest to me for their unwavering support over my entire life. Undoubtedly, without the significant amount of time and money that my parents have invested into developing myself I would be nowhere.

Finally, I recognize that this research would not have been possible without the financial support of the National Academy of Nuclear Training (NANT) and the Woodruff School of Mechanical Engineering. Additionally, research was partly funded by UT-Battelle, LLC, acting under contract DE-AC05-00OR22725 with the U.S. Department of Energy.

TABLE OF CONTENTS

ACKNOWLEDGEMENTS	iii
LIST OF TABLES	viii
LIST OF FIGURES	x
SUMMARY	xvii
1 Introduction.....	1
2 HTGR Background	5
Attractive Features	5
Past HTGR Experience in the United States.....	5
International HTGR Development.....	6
3 Methodology for Efficient Shielding Analysis	11
Shielding Analysis	11
Monaco	12
Issues with MC and Variance Reduction Methods.....	14
CADIS.....	15
FW-CADIS	17
MAVRIC.....	17
4 Validation of MAVRIC using LWR Benchmarks.....	18
Poolside Critical Facility at ORNL.....	19
Geometry and Materials Definition	19
Source Definition	20
Reaction Rates	22

	Deterministic Denovo Model and Biasing Parameters	25
	Results.....	27
	VENUS-3 Experiment	32
	Geometry and Materials Definition	32
	Source Definition	37
	Deterministic Denovo Model and Biasing Parameters.....	39
	Results.....	40
5	VHTR Model for Shielding Analysis	44
	Model Basis	44
	Fuel Type	45
	Prismatic Fuel Blocks	46
	Control Rods.....	48
	Core Barrel.....	51
	Reactor Pressure Vessel (RPV)	53
	Power Conversion System	56
	Plant Layout	57
	Preliminary Studies.....	60
	Impact of Core Homogenization on MAVRIC Results.....	60
	Using Parallel Denovo for Speedups and Better Variance Reduction.....	70
6	Fast Fluence and Vessel Dosimetry.....	76
	Source Definition using KENO-VI.....	77
	Reactions of Interest	77

	Deterministic Denovo Model and Biasing Parameters	79
	Results.....	81
7	Personel Dosimetry in the VHTR plant	84
	Preliminary Analyses with a Uniform Mesh	86
	Finer Mesh and Condensed Geometry.....	88
	Increased Quadrature Set and Mesh Refinement.....	95
8	Tritium Production from Core Components	104
	Core and Source Description	109
	Deterministic DENOVO Model	112
	Ternary Fission	114
	Burnable Absorbers	116
	Control Rods	121
	Graphite Impurities	125
	⁶ Li Impurities	127
	¹⁰ B (n, α) ⁷ Li.....	130
	¹⁰ B (n, t2α)	132
	⁷ Li Impurities	133
	Helium Coolant.....	135
	Sectional Method	138
	Standard MC	144
	Total Tritium Source.....	149
	Permeation to Hydrogen Product.....	153

9	Conclusions and Future Work	154
10	APPENDIX A: Results from the VENUS-3 Simulation	157

LIST OF TABLES

Table 1. Material Compositions (w%).....	20
Table 2. Reaction cross sections, averaged over 235U Spectrum	23
Table 3. Denovo parameters.	26
Table 4. MAVRIC performance.	26
Table 5. PCA Reaction Rates compared to measured data.....	31
Table 6. Material Descriptions for MAVRIC	35
Table 7. Denovo Parameters.....	40
Table 8. MAVRIC Performance.....	40
Table 9. C/E ratios $[(C/E \pm uC/E) \pm s]$ obtained from MAVRIC.....	43
Table 10. TRISO Particle Specification.....	46
Table 11. Fuel Compact Homogenization	46
Table 12. Material Compositions (wt%).....	53
Table 13. The location (cm) of each control rod relative to the bundle as shown in Figure 28. .	55
Table 14. The bundle locations (cm) relative to the upper head as shown in Figure 28.	55
Table 15. Run Times.....	65
Table 16. Error in total flux due to homogenization, at a radius of 335 cm	68
Table 17. A comparison of MAVRIC and Denovo times when using parallel.	71
Table 18. MAVRIC performance and Denovo parameters.	80
Table 19. Results obtained from MAVRIC for detectors shown in Figure 46.	82
Table 20. MAVRIC performance and Denovo parameters.	86
Table 21. MAVRIC performance and Denovo parameters.	89
Table 22. MAVRIC performance and Denovo parameters.	96
Table 23. Important pathways of tritium production.	105
Table 24. Material descriptions adapted from Triton depletion calculation (a/b•cm).	110
Table 25. Denovo parameters.	112

Table 26. Important overall tritium-producing reaction cross sections averaged over the flux spectrum.....	120
Table 27. The MAVRIC Performance.....	126
Table 28. Sources of tritium production in VHTRS (Oh & Kim, 2011).	149
Table 29. A comparison of the tritium sources.....	150
Table 30. The tritium sources assuming worst-case scenario for impurities.....	151
Table 31. The tritium sources assuming best-case scenario for impurities.	152

LIST OF FIGURES

Figure 1. The PCA layout (top view) showing mockup components. The numbers in the core indicate homogenized core regions given in Table 1. The red dots indicate detector locations. (All units are in cm).....	19
Figure 2. The source distribution used in MAVRIC extracted from the SINBAD package.	21
Figure 3. The source distribution in the x, y and z directions centered around (x, y, z) = (20.85, 7.35, 0.00) cm.	22
Figure 4. Different views of the source used by MAVRIC. The black lines indicate the plane location of each other view centered around (x, y, z) = (20.85, 7.35, 0.00) cm.	22
Figure 5. A comparison of the foil cross sections. The ²³⁷ Np reaction provides some coverage of the entire spectrum.	24
Figure 6. A CDF of each reaction rate. Notice that the ²³⁷ Np(n,f) reaction is the only reaction with a significant contribution occurring below 0.1 MeV.	25
Figure 7. The grid used for the Denovo (XY). The red indicates the region set as the adjoint source.	26
Figure 8. (Top) Denovo total neutron, forward flux. (Bottom) Stochastic MC total neutron flux.	27
Figure 9. Relative uncertainties for the reaction used to bias particles towards.	29
Figure 10. C/M ratios grouped by detector location.	30
Figure 11. C/M ratios grouped by response.	30
Figure 12. The VENUS-3 core layout is shown for one-quarter of the core with detector locations. The geometry is symmetric about each axis with only the neutron pad and detectors occurring in the quadrant shown.	33
Figure 13. Geometry and material specification for different fuel elements.	34
Figure 14. VENUS-3 LWR-PVS Benchmark Experiment. The red represents the active fuel region.	35

Figure 15. Neutron source distribution provided in SINBAD benchmark (left), and Fission rate calculated by KENO-VI (right).	38
Figure 16. Ratio of fission source distributions (KENO-VI to that specified in SINBAD) along x-direction at several y-positions, all at the axial core centerline.....	38
Figure 17. The total forward neutron flux together with the black dots representing foils positions. The box represents the adjoint source region.	39
Figure 18. C/E Ratios for the $^{58}\text{In}(n, p)^{58}\text{Co}$ reaction.	41
Figure 19. C/E Ratios for the $^{115}\text{In}(n, n')^{115}\text{mIn}$ reaction.	42
Figure 20. C/E Ratios for the $^{27}\text{Al}(n, \alpha)^{24}\text{Na}$ reaction.	42
Figure 21. Cutout view of the core.	45
Figure 22. Standard fuel block layout with dimensions.	47
Figure 23. Fuel block with hole for control rod insertion.	48
Figure 24. Control Rods inserted through the entire core.	50
Figure 25. Helium outlet and inlet geometries showing the reconfigured design.	51
Figure 26. The helium circulation within the core barrel. Also the dimensions for the graphite, core barrel and RPV.	52
Figure 27. Dimensions for the RPV showing the three separate sections. (all units are given in cm)	54
Figure 28. The positions of control rod assemblies in the upper head.	55
Figure 29. Assumed dimensions (cm) defining the Power Conversion System.	56
Figure 30. VHTR facility used to extrapolate dimensions (Baccaglini, 2003) (left). Final VHTR Model implemented in MAVRIC (right).	57
Figure 31. Front view of the VHTR power plant with dimensions axial (cm).	58
Figure 32. Top view of the VHTR power plant at different axial levels with dimensions (cm).	59
Figure 33. Media cards demonstrating the first level of homogenization.	61
Figure 34. Each graphite block is homogenized leaving only control rod channels as unhomogenized regions.	62

Figure 35. Notice the areas where the lines of the fuel blocks intersect with those of the simplified core new core.	63
Figure 36. All of the different levels of helium coolant homogenization. Not included is the coolant flow through the bottom reflector, directly above the outlet plenum.	64
Figure 37. Lethargy plot at a radius of 253 cm.	66
Figure 38. Lethargy plot at a radius of 300 cm.	66
Figure 39. Lethargy plot at a radius of 335 cm.	67
Figure 40. The neutron flux in the z-direction for the reference case and with all levels of homogenization.	68
Figure 41. The speedup of each meshing based on the number of CPUs.	72
Figure 42. The efficiency of each meshing based on the number of CPUs.	72
Figure 43. The speedup of the total Denovo CPU time for each meshing based on the number of processors used in the simulation.	74
Figure 44. The efficiency of the total Denovo CPU time for each meshing based on the number of processors.	74
Figure 45. KENO-VI based fission source distribution.	77
Figure 46. Side and top views of the problem space. The detector locations are indicated by the black dots and the dashed box represents the adjoint source region used for each simulation. Additionally, the red region indicates the active core.	78
Figure 47. From left to right: Top view of the mesh importance map for the $^{237}\text{Np}(n,f)$, fast neutron flux ($>0.1\text{MeV}$), and $^{27}\text{Al}(n,\alpha)$ simulations.	79
Figure 48. From left to right: Side view of the mesh importance map for the $^{237}\text{Np}(n,f)$, fast neutron flux ($>0.1\text{MeV}$), and $^{27}\text{Al}(n,\alpha)$ simulations.	80
Figure 49. From left to right: Top view of the relative uncertainty for each reaction rate used to define the adjoint source for FW-CADIS.	81
Figure 50. Different views of the problem space.	85
Figure 51. Neutron dose rate for a 6 day MC simulation.	87

Figure 52. Photon dose rate for a 6 day MC simulation.	88
Figure 53. Total dose rate for a 1 week MC simulation (left) with the relative uncertainty (right).	90
Figure 54. (Left) Neutron dose rate for a 1 week Monaco simulation. (Right) Photon dose rate.	91
Figure 55. (Left) The relative uncertainty in the neutron and gamma dose rates for a 1 week Monaco simulation.....	91
Figure 56. The total neutron and gamma dose for seven one-day simulations. The figure below each image represents the number of tracked particles. Notice that the majority of statistics in the access room come from the first run.	92
Figure 57. The total dose relative uncertainty for seven one-day Monaco simulations.	92
Figure 58. The gamma dose for seven one-day Monaco simulations. The figure below each image represents the number of tracked particles. Notice that the majority of statistics in the access room come from one run.	93
Figure 59. The gamma dose relative uncertainty for seven one-day Monaco simulations.....	93
Figure 60. The neutron dose for seven one-day simulations.	94
Figure 61. The neutron dose relative uncertainty for seven one-day Monaco simulations.	94
Figure 62. The mesh refinement scheme used for the Denovo.....	95
Figure 63. Total dose rate for a 7 week MC simulation (left) with the relative uncertainty (right).	98
Figure 64. The total n+ γ dose rate on the x-axis in the accessible room at different elevations on the centerline of the model.....	99
Figure 65. (Left) Neutron dose rate for a 7 week Monaco simulation. (Right) Photon dose rate.	100
Figure 66. (Left) The relative uncertainty in the neutron and gamma dose rates for a 7 week Monaco simulation. (Right) The photon uncertainty.....	100

Figure 67. The total gamma and neutron dose for each week-long simulation. Note that the rightmost result on the bottom row is the combined results from each 7 day simulation.	101
Figure 68. The total gamma and neutron dose uncertainty for each week-long simulation.	101
Figure 69. The total gamma dose for each week-long simulation.	102
Figure 70. The total gamma dose uncertainty for each week-long simulation.	102
Figure 71. The total neutron dose for each week-long simulation.	103
Figure 72. The total neutron dose uncertainty for each week-long simulation.	103
Figure 73. 1/6 core reflective core geometry from Dan Ilas.	110
Figure 74. Neutron source comparison as simulated by KENO-VI.	111
Figure 75. The total forward neutron flux with both a fast and thermal group shown.	113
Figure 76 - (Top) Top view of the mesh-based ternary fission tritium production. (Bottom) Front view.	115
Figure 77. Important cross sections for tritium production via ^{10}B and ^7Li	116
Figure 78. Cumulative Distribution Function of the reaction rates relative to tritium production from ^{10}B	117
Figure 79. Views of the spatial tritium production rate in burnable absorbing rods by the $^{10}\text{B}(n,t)$ reaction as calculated by a standard MC simulation for 1 day.	118
Figure 80. Views of the spatial tritium production rate in the graphite reflector by the $^{10}\text{B}(n,t)$ reaction as calculated by a standard MC simulation for 1 day.	119
Figure 81. The neutron flux energy distribution within the burnable absorbers.	120
Figure 82. The time-dependent, total tritium production rate in the burnable absorbers.	121
Figure 83. Top view of the spatial tritium production rate in inserted control rods as via by the $^{10}\text{B}(n,t)$ reaction as calculated by a standard MC simulation for 1 day.	122
Figure 84. The FW-CADIS weighted MC flux (Left) with relative uncertainty (center). The total adjoint flux showing the source region where the specific control rod was located (right).	123

Figure 85. Reaction rate distribution around an inserted control rod.	124
Figure 86. (Left) The $^{10}\text{B}(n, \alpha) ^7\text{Li}$ reaction rate distribution in a typical annular operating rod. (Right) The total track-length estimated neutron fluence spectrum for an operating rod, demonstrating the attenuation of the thermal neutron flux.	124
Figure 87. The time-dependent, tritium production rate in the operating control rods assuming an 11% insertion factor.	125
Figure 88. Important tritium-producing reaction cross sections, highlighting the $^6\text{Li}(n, t) ^4\text{He}$ reaction.	127
Figure 89. The total adjoint neutron flux with both a fast and thermal group displayed.	128
Figure 90. The $^6\text{Li}(n, t) ^4\text{He}$ reaction rate spatial distribution in graphite. For each location the response is given on the left while the relative uncertainty is on the right.	129
Figure 91. A comparison of microscopic cross sections in ^{10}B and the lithium isotopes.	130
Figure 92. The $^{10}\text{B}(n,\alpha)^7\text{Li}$ reaction rate distribution as calculated by MAVRIC.	131
Figure 93. The $^{10}\text{B}(n,t2\alpha)$ reaction rate distribution as calculated by MAVRIC.	132
Figure 94. The distribution of tritium production strictly from ^7Li impurities in the core graphite.	134
Figure 95. The $^3\text{He}(n, p) ^3\text{H}$ reaction distribution when using FW-CADIS with an adjoint source set to the helium in the entire model and the $^3\text{He}(n, p) ^3\text{H}$ reaction.	136
Figure 96. The $^3\text{He}(n, p) ^3\text{H}$ reaction distribution when using FW-CADIS with an adjoint source set to the entire model and the $^3\text{He}(n, p) ^3\text{H}$ reaction.	137
Figure 97. The three sections used for biasing particles in separate simulations.	139
Figure 98. Combined results demonstrated by the $^7\text{Li}(n,t)^*$ reaction.	140
Figure 99. The $^6\text{Li}(n,t)$ reaction.	141
Figure 100. The reaction rate distribution for the $^{10}\text{B}(n,t2\alpha)$ reaction is shown.	142
Figure 101. The reaction rate distribution for the $^3\text{He}(n,p)t$ reaction is shown.	143
Figure 102. The relative uncertainty distribution in each impurity, tritium-producing reactions in graphite.	144

Figure 103. "Sectional Method" results for the ${}^6\text{Li}$ tritium-production rate in graphite..... 145

Figure 104. "Sectional Method" results for the ${}^{10}\text{B}$ lithium-production rate in graphite..... 146

Figure 105. "Sectional Method" results for the ${}^{10}\text{B}$ tritium-production rate in graphite. 147

Figure 106. "Sectional Method" results for the ${}^3\text{He}$ tritium-production rate in graphite..... 148

Figure 107. The tritium distribution from core to hydrogen product. (Oh & Kim, 2011)..... 153

SUMMARY

In this work, the MAVRIC sequence of the Scale6.1 code package was tested for its accuracy and efficacy in calculating a wide range of shielding parameters with respect to HTGRs. One of the NGNP designs that has gained large support internationally is the VHTR. The development of the Scale6.1 code package at ORNL has been primarily directed towards supporting the current United States' reactor fleet of LWR technology. Since plans have been considered to build a prototype VHTR, it is important to verify that the MAVRIC sequence can adequately meet the simulation needs of a different reactor technology. This was accomplished by creating a detailed model of the VHTR power plant; identifying important, relevant radiation indicators; and implementing methods using MAVRIC to simulate those indicators in the VHTR model.

The proposed plant is a graphite-moderated, helium-cooled reactor with a rated power of 600MWth. Fuel temperatures are expected to reach over 1,000°C, while the helium coolant outlet and inlet temperatures are 950°C and 590°C respectively. The high temperatures allow for an increased thermal efficiency in power conversion. Additionally, the very high temperatures were designed to provide not just power generation but to supply heat for other industrial purposes. One such application is hydrogen production. Since tritium, a heavier radioactive isotope of hydrogen is produced in nuclear reactors it is important to know the distribution of tritium production and the subsequent diffusion from the core to secondary systems in order to ensure an uncontaminated hydrogen product can be effectively produced.

The graphite moderator used in the design results in a different flux spectrum than water-moderated reactors. The different flux spectrum could lead to new considerations when quantifying shielding characteristics and possibly a different gamma-ray spectrum escaping the core and surrounding components. One key portion of this study was obtaining personnel dose rates in accessible areas within the power plant from both neutron and gamma sources.

Additionally, building from professional and regulatory standards a reactor pressure vessel dosimetry program was analyzed using surveillance capsule monitoring.

Accurately modeling of radiation indicators using MAVRIC is the main goal. However, it is almost equally as important for simulations to be carried out in a timely manner. Deterministic methods provide solutions to the transport equation using a discretized geometry. The discretization leads to inaccuracies in final solutions that are self-propagating in shielding problems. Stochastic methods allow for the exact geometry to be modeled, giving accuracy to solutions. The time required to converge the precision on these stochastic solutions becomes very large in deep-penetration problems. The MAVRIC sequence applies a hybrid deterministic/stochastic method to mitigate these issues.

MAVRIC implements automated variance reduction methods to drastically reduce the uncertainty obtained by Monte Carlo simulations of neutral particles. It uses the discrete ordinates method to solve the fixed-source transport equation for both neutron and gamma rays on a crude geometric representation of the detailed model. This deterministic forward solution is used to define an adjoint problem with the adjoint source specified by the user. The adjoint solution is then used to create an importance map and a biased source that can be used in the Monte Carlo simulation. The goal of using this hybrid methodology is to provide accuracy with high precision while decreasing overall simulation times by orders of magnitude.

The MAVRIC sequence provides a platform to quickly alter inputs so that vastly different shielding studies can be simulated using a single model with minimal effort by the user. Each separate shielding study required unique strategies while looking at different regions in the VHTR plant. MAVRIC proved to be effective for each case.

CHAPTER 1

INTRODUCTION

As the world's developing nations' demand for energy increases, it is impossible to visualize a realistic scenario of supplying that energy demand without an expansion of the nuclear power industry. Appeals for decreasing mankind's carbon footprint cannot be met by alternative energy sources alone. Coupling nuclear power with technological improvements in other energy industries makes a cleaner future seem attainable. Nuclear power carries a stigma in the eyes of the general public that has been further tainted by the accidents surrounding the Fukushima Daiichi disaster. Therefore, the main priorities of innovative nuclear power plant designs must be the continued dedication to safety and reliability that has been demonstrated globally for over half a century. The Very High Temperature Reactor (VHTR) design has gained more traction than other Generation IV (Gen IV) reactor concepts towards actual construction. With proper simulation abilities, safety can be demonstrated and improved upon. The purpose of this work is to analyze the efficacy of the MAVRIC sequence of the Scale6.1 code package developed at ORNL in calculating different radiation shielding indicators throughout a model of the VHTR power plant (Peplow, 2009a).

The Scale6.1 code package offers a collection of radiation simulating software focused on two main areas: "safety analysis and design." It provides 89 computational modules covering the majority of nuclear industrial applications including reactor physics, depletion, criticality safety, radiation shielding, radiation source characterization, and sensitivity and uncertainty analysis. One goal is for user-friendliness in both ease of modeling and interpretation of results. Currently, it receives funding from both the U.S. Nuclear Regulatory Commission (NRC) and the Department of Energy (DOE). The original sponsor for the package was the NRC, meaning that its development was targeted primarily toward the assortment of Light Water Reactor (LWR) technology used in the United States. The research presented here aims to explore the

ability of the MAVRIC sequence of the Scale6.1 package to model radiation shielding in High Temperature Gas-Cooled Reactor (HTGR) technology. The MAVRIC sequence implements the CADIS and FW-CADIS methodologies developed by J.C. Wagner, A. Haghghat and D. Peplow (SCALE, 2009; Wagner & Haghghat, 1998; Wagner, Blakeman, & Peplow, 2007).

Recently, international research has been directed toward one specific HTGR, the Very High Temperature Reactor (VHTR). The Generation IV International Forum (GIF) selected the VHTR to be one of six designs to be developed towards a set of goals defining the next generation of nuclear power plants. Subsequently, in 2005 the United States created the Next Generation Nuclear Plant project to implement such a design before 2030 in partnership with the private sector. The core used in the VHTR design has recently been chosen to be the design basis for the construction of a plant at Idaho National Laboratory (INL) slated to demonstrate hydrogen production coupled with gains in efficient energy conversion. Since the Scale6.1 package is used for regulation by the NRC, it is important that methods are established that can be implemented within the MAVRIC sequence to accurately and efficiently simulate important shielding parameters (Energy, 2005).

The region in the power plant receiving the most immediate neutron and photon fluence is the core and reactor support structures. The graphite moderated core is expected to be able to withstand high operating temperatures while receiving radiation damage from high neutron fluence. The majority of fuel is removed after a few loadings, reducing total neutron exposure and damage within the core. However, external reflector components and support structures are permanent. While receiving a lower fluence rate, the total time-integrated fluence is expected to be a significant contribution towards material property change and activation. Steel components are chosen to be able to withstand the specific radiation and thermal environments. Therefore, it is important to be able to simulate the actual environment and exposure. In practice, surveillance capsule monitoring programs are used to verify that calculations of reaction rates match those

physically measured. Verifying these reaction rates gives validity to calculations of Displacements per Atom (DPA) in supporting components. DPA can then be extrapolated to important property changes in materials. A mock-up surveillance capsule monitoring program was established to demonstrate the practice applied to the VHTR design within the MAVRIC sequence while also calculating DPA to structural components (ASTM E693, 2007; ASTM E1035, 2008).

Lastly, neutron and photon dose to personnel in areas accessible during operation were calculated. Achieving accurate and precise dose rates for large volumes through deep-shielding problems in a full nuclear power plant is computationally a very memory and time intensive problem. It is desired to preserve an accurate representation of the physical model and radiation sources when simulating dose rates. The MAVRIC sequence was able to obtain acceptable dose rates in the accessible area directly above core within the nuclear island, while keeping a high fidelity description of the model.

Furthermore, the NNGP project seeks to provide high temperature process heat for other applications without contaminating those applications with the radioactive by-products of nuclear technology. The reactor was optimized to provide process heat for chemical, fuel and hydrogen production in an attempt to bring process industry facilities back to the United States while not increasing the use of fossil fuel resources. Hydrogen production has been the main focus of design along with electricity generation. Tritium is a radioactive isotope of hydrogen and is produced in nuclear reactors. Being an isotope of the lightest element, tritium particles may diffuse from core components to secondary systems more easily than heavier fission products. Therefore, to support the analysis of tritium permeation from the VHTR, tritium production was extensively modeled within components surrounding the core. Since tritium is produced both in fuel and shielding regions, unique methods were implemented within the

MAVRIC sequence to ensure accurate calculations were obtained from the simulations (Kupitx, 2011).

CHAPTER 2

HTGR BACKGROUND

Attractive Features

High Temperature Gas-Cooled Reactors (HTGRs) have been in development since the 1940s. Two main designs have been developed: the prismatic block and pebble bed reactors. The latter uses graphite pebbles that are embedded with tristructural-isotropic (TRISO) particles and fed through a hopper-like system. Helium gas is used as a coolant. The other prismatic block design stacks graphite elements containing fuel rods consisting of TRISO particles compacted into a graphite matrix. From a thermodynamics standpoint, the higher outlet temperatures allow for higher efficiencies in power conversion, which has been proven for both designs. The helium coolant experiences no phase change and therefore introduces no reactivity effects into the core. The graphite moderator has a very high heat capacity, and even during emergency shutdown the core requires minimal passive heating. Additionally, the fuel form can retain fission products while undergoing a higher burn-up than typical LWRs (Design, 2005).

Past HTGR Experience in the United States

In the past, two HTGR facilities were operated in the United States. The Peach Bottom Unit 1 Demonstration Plant was the first prototype design and started commercial operation on June 1, 1967. It operated at 115 MWth with a 37% thermal efficiency. Through two core life cycles between 1967 and 1974, it demonstrated that the concept of a helium-cooled, graphite-moderated power reactor was feasible. The initial core loading contained both thorium and uranium carbides pyrolytically coated in dense carbon and dispersed in a graphite matrix. The initial loading experienced a large amount of fuel failure, but attained 450 full-power days before shutdown. The second core loading used Buffer-Isotropic (BISO) particles, which used two layers of coating to better prevent fuel failure and retain fission products. The new fuel

showed great improvement from the previous core loading, giving more credibility to the design. The plant successfully demonstrated a new fuel form, core concept and fission product trapping system. Decommissioning was completed in 1978 (Everett & Kohler, 1978).

The second operating reactor, the Fort Saint Vrain (FSV) Generating Station, produced nuclear power between 1977 and 1992. The reactor produced 842 MWth and 330MWe obtaining an efficiency of 39%. Current HTGR designs use prismatic blocks of the same dimensions of the FSV core. The helium coolant supplied heat to a steam generating system. The plant boasted higher efficiencies and as a proof-of-point for commercial HTGR technology was a success. However due to potentially hazardous operating conditions, it was converted to a natural gas power plant and is currently producing power (Copinger & Moses, 2004).

ORNL released monthly reports for FSV between 1981 and 1989 to the Office for Analysis and Evaluation of Operational Data (AEOD) of the NRC. In the 7 year period, 279 events were reported. The only ones considered to hold consequential weight involved the coupling of the very hot, pressurized outlet gas to a secondary steam cycle. A low but constant moisture intrusion into the core degraded control rod drives and reserve shutdown systems. During a scram event in 1984, six of the control rod mechanisms failed due to the moisture leakage into the primary gas-cooled system. Failures of safety system are considered extremely hazardous to the safety of the plant and the general public. Other expected, reported incidents considered to be inconsequential, such as cracking of core components. On one hand, FSV demonstrated the success of HTGR technology in terms of being inherently safe but also highlighted design issues to be resolved in the future. The recent HTGR concepts have been greatly simplified, solving the major operating flaws facing early technology (Copinger, 2004).

International HTGR Development

The Dragon Project in the United Kingdom started as early as the late 1940s, but officially began following discussion on a possible thorium-based cycle with gas-cooled reactors

in the 1950s. The prototype operated at 20 MWth and began operation from 1965 to 1976. The core featured graphite and fuel tubes arrayed in a hexagonal lattice. Based on preliminary studies a single layer of carbon was not significant enough to retain fission products, so the idea of adding extra layers of silicon carbide was used in the fuel. The fission product release from fuel regions was over-predicted, leading to helium-coolant purification systems being over-engineered. Similar to the Peach Bottom reactor in the United States, the Dragon Project concurrently demonstrated the viability of the HTGR design and the establishment of a new ceramic coated particle fuel (Price, 2012).

The AVR (Arbeitsgemeinschaft Versuchsreaktor) reactor was a small pebble-bed prototype that began operation in 1967 at 46 MWth and was able to reach an outlet temperature of 950°C in 1974. The pebbles were loaded with thorium and highly enriched uranium. In 1983 Germany began operating the THTR-300 and continued until 1987. The reactor was based on the same pebble-bed design of the AVR. Commercially, the reactor was a failure and had an early shutdown do to the rising cost of the plant and safety issues (Kuptix & Dee, 2011).

Currently, China has the most active HTGR program in the world, with one operating test facility and two new units under construction. The Chinese have operated the HTR-10, a 10MWth pebble-bed reactor. Building from the success of the prototype, two scaled-up 250 MWth reactors began construction in 2011. Each unit uses TRISO particles enriched to 8.9% and helium coolant with an outlet temperature of 750°C and a pressure of 7 MPa. Besides demonstrating the many safety and design features of HTGR technology, other main goals of the plant are to prove economic competitiveness and pave the way for the small modular reactor concept (Petti, 2010).

In 1999, the Japanese High Temperature Test Reactor reached full-power criticality operating at 30 MWth. The core is helium-cooled and graphite-moderated with an outlet coolant between 850 and 950 C°. The helium flows downward through the core's prismatic

blocks at 4 Mpa. The VHTR design used in the study is similar to this design, but much larger (20x the power output) (Saito et al., 1991).

The Generation IV International Forum (GIF) formed in 2000 and established research and development needs in developing the evolutionary next generation of nuclear power plant designs for the world. By 2006, twelve countries along with Euratom comprised the forum: Argentina, Brazil, Canada, France, Japan, the People's Republic of China, the Republic of Korea, the Republic of South Africa, the Russian Federation, Switzerland, the United Kingdom, and the United States. In the end, six systems were chosen to encompass both fast and thermal neutron spectra; a range of power outputs; open and closed fuel-cycles, and different industrial applications. New designs also were desired to have added safety, proliferation resistance, and economic incentives. The end goal was to work with government and regulatory agencies to develop the designs and to make them implementable for commercial introduction between 2015 and 2030. The United States and other countries have invested much research and development resources into one specific HTGR design: the VHTR. Note that as time passes, policies change and interest varies. Therefore, for all countries involved funding for research and development can be quickly halted through elections, regime change, public opinion, etc. (Petti, 2010).

The Energy Policy Act of 2005 created the Next Generation Nuclear Plant (NGNP) project in the United States operated by the DOE. The act projects to have an operational HTGR by 2021 and assumes shared costs with the private sector to have the plant constructed. In 2009, reactor vendors and other nuclear companies developed the NGNP Industry Alliance to promote the development of the HTGR in conjunction with the DOE's NGNP project. Three companies' designs were chosen to compete for ultimate construction: the Gas Turbine Modular Helium Reactor (GT-MHR) by General Atomics, the ANTARES-based design by AREVA, and the Pebble Bed Modular Reactor (PBMR) by Westinghouse. The latter pebble-bed reactor utilizes a

hopper filled with TRISO particles. Helium gas is pumped through the core to remove heat and generate power (Energy, 2005).

The GT-MHR and ANTARES designs possess almost identical prismatic-block cores. The design uses TRISO particles compacted into graphite fuel elements that are then placed into a hexagonal graphite block. The block has alternating regions of fuel compacts and helium coolant channels with regions demarcated for fuel handling, burnable absorbers and emergency shutdown. Active fuel blocks are arranged in an annular structure and stacked to form a ten-layered core. The graphite elements are used as moderators and heat transfer surfaces capable of operating at over 1000°C. Helium coolant again removes the heat from the core which drives turbines to produce power. One important aspect of the design is the coolant outlet temperature of 850°C. Using higher outlet temperatures, power conversion cycles can achieve higher thermal efficiencies (~50%) compared to current LWR technology (~33%).

The GT-MHR design being led by GA was chosen for this study and has been extensively modeled using the Scale General Geometry Package (SGGP). The main difference between the AREVA and GA designs is the heat-exchange mechanism. The core layout and support structures are essentially identical, meaning that shielding studies are equally valid between the two concepts. In February of 2012, the NGNP Industry Alliance chose AREVA's Steam Cycle HTGR (SC-HTGR) as the reactor design concept to be used for industrial application and electricity production. The plant layout and secondary systems are not the same as the model used for in this study.

Key design features of the proposed VHTR improve upon Gen-III technology. Multiple barriers are placed between fission events and leakage of radioactive fission products to the public. TRISO particles are designed with multiple layers to hold fission products. TRISO particle failure may allow leakage from fuel compacts. Fission products are then preserved by the reactor vessel, purification systems, and the reactor building. Furthermore, no action by plant

operators or external power is required to ensure safe shutdown of the reactor since gravity is allowed to control shutdown systems. After shutdown, heat is removed naturally from the core so that no external power or cooling fluid is required. TRISO particles are proliferation resistant since they require much effort and means to extract fissile material once burnt. The spent fuel elements can be stored in dry containment and cooled by natural circulation.

CHAPTER 3

METHODOLOGY FOR EFFICIENT SHIELDING ANALYSIS

Shielding Analysis

The general form of the Boltzmann transport equation defines the angular flux distribution of neutral particles (neutrons and photons) for all space, angle, energy and time in essentially the entire universe. Therefore, there are seven variables defining the distribution of particles. In Cartesian coordinates these are: $\vec{r} = x, y, z$; $\Omega = \theta, \phi$; E ; and t . In shielding problems, the equation is assumed to be steady state eliminating the time-dependence. Additionally, a fixed source is assumed which eliminates the neutron multiplication term leaving a simplified equation as given in Eq. [1].

$$\begin{aligned} \hat{\Omega} \cdot \nabla \varphi(\vec{r}, \Omega, E) + \sigma(\vec{r}, E, t) \varphi(\vec{r}, \Omega, E) \\ = \int \int \sigma_s(\vec{r}; \Omega', E' \rightarrow \Omega, E) \varphi(\vec{r}, \Omega', E') d\Omega' dE' + S(\vec{r}, \Omega, E). \end{aligned} \quad (1)$$

A solution to Eq. 1 is found using one of two computational methods: deterministic or stochastic. Deterministic solutions are found by discretizing both space and angle to solve for the angular neutral particle flux. Numerical solutions are found for the discretized problem, but the discretization degrades the accuracy in the representation to the real model. Stochastic solutions use the Monte Carlo method to simulate, preserving the exact geometry and physics of the problem. Each particle history is then combined with all other histories to obtain an average solution. The average carries with it a statistical standard deviation. Both methods are widely used and choosing between methods may be a trade-off between memory and CPU time. Deterministic methods are precise according to their model, but their accuracy falls with the level of discretization. In order to achieve better accuracy, larger computing resources and time must be used. Stochastic simulations have potential to be perfectly accurate, but their precision

can only be achieved by simulating a large number of histories. Once again in order to achieve better accuracy, larger computing resources and time must be used.

Monaco

The Monaco code uses the Monte Carlo method to track neutral particles through models using the Scale General Geometry Package (SGGP). Simulations are done in batches with each batch having a specific number of particle histories. Monaco uses a multi-group energy structure to randomly samples neutral particles defined by a fixed source. Additional particles may be created by secondary reactions in the geometry, but fission neutrons in the fuel are normally assumed to be accounted for by the fixed source and not resampled. In the physics defining neutron and gamma interaction with matter, the only loss of accuracy is associated with the collapsing of cross sections to multi-group shielding libraries. Two libraries are available for the sequence: one containing 200 neutron and 47 gamma energy groups; the other containing 27 and 19 groups, respectively (Peplow, 2009b).

The group-wise scalar flux ϕ_{gi} is calculated at the end of each batch i by averaging the history h_j from each J particles, by combining contribution c_j weighted w_j ,

$$\phi_{gi} \pm \sigma_{gi} = \frac{1}{J} \sum_j c_{ij} w_{ij} = \frac{1}{J} \sum_j h_{ij} \pm \sqrt{\frac{1}{J} \sum_j [\phi_{gi}^2 - h_{ij}^2]}. \quad (2)$$

The standard deviation σ_{gi} associated with the average scalar flux ϕ_{gi} is found by,

$$\sigma_{gi} = \sqrt{\frac{1}{J} \sum_j [\phi_{gi}^2 - h_{ij}^2]}. \quad (3)$$

The overall simulation-averaged group flux ϕ_g for I batches ($N=IJ$ histories) then would be:

$$\phi_g \pm \sigma_g = \frac{1}{I} \sum_i \phi_{gi} \pm \sqrt{\sum_i (\sigma_{gi})^2} = \frac{1}{N} \sum_i \sum_j h_{ij} \pm \sqrt{\frac{1}{N} \sum_i \sum_j [\phi_g^2 - h_{ij}^2]} \quad (4)$$

Tallies are obtained by folding the multi-group scalar flux with response functions. Response functions can be inputted by the user, pulled from reaction rate cross sections used in the model, or taken from a list of commonly used shielding functions contained in the package. Region tallies use a flux estimated by both a track-length estimate and a collision density. The track-length estimate or the group flux uses the length of each simulated particle's path through a given region to estimate the group-wise scalar flux. The collision density estimator uses collisions only that are simulated within the region and generally requires more particles to converge for each group. Mesh tallies use the track length estimator to obtain results within voxels in a user-defined mesh. Point detector tallies are a form of variance reduction, which after each collision tracks the probability of the collided particle reaching the specific point without any further collision. The contribution from each track is weighted by its squared distance from the point detector. For each type of tally, response R is the integrated scalar flux ϕ_g weighted by the response function f_g as seen in Eq. [5]

$$R \pm \sigma_R = \sum_g f_g(\phi_g \pm \sigma_g) \quad (5)$$

As mentioned earlier, a large issue with stochastic simulations can be the amount of computational time required to reduce the statistical uncertainties to a desired level. Equation 4 shows that the uncertainty in a solution is directly proportional to the square root of the number of histories. In order to reduce the uncertainty by an order of magnitude, for example from 10% to 1%, the simulation would require 100 times the number of particles which would require 100 times the CPU time. For large geometries, the simulation time required to converge deep-penetration results would require multiple years. Fortunately, variance reduction methods have been developed that when used correctly decrease the simulation time by orders of magnitude while converging solutions.

Issues with MC and Variance Reduction Methods

Building from decades of experience, multiple variance reduction techniques have been developed to bias MC simulations towards a desired calculation. Modified sampling methods alter the random walk cycle of the MC game in both the source and physics defining the problem. Normally this is implemented using a weight window methodology. Weights may be assigned to the source particle that is carried through the simulation. Source particles can be biased based on angle, space and energy towards a distribution more favorable of obtaining a solution. From the onset, the biased source particles carry a weight that ultimately is used to correct the final tallies for the difference in the biased source and the actual source. Another modified technique is implicit capture. Instead of allowing absorption to be sampled, at each collision the particle is forced to have a scattering event while at the same time lowering the weight of the particle by a factor of $(1 - \sigma_a/\sigma_t)$ (Wagner & Haghigat, 1998).

Another method used for variance reduction involves increasing the number of particles sampled as a single particle moves into a new geometric location. The problem space is subdivided into regions that each has a specific importance or weight. The weight of an incoming particle is evaluated when moving between regions based on a weight window defined in the input deck. Weight windows are used to apply Russian roulette and splitting techniques. If the weight of the particle is below that of the lower bound of the weight window in the new region, the particle is sampled as to whether it is killed (hence Russian roulette) or kept alive with a weight that is increased to be within the weight window. If the particle is above the upper bound of weight window for the new region, the particle is split into multiple particles. The new particles carry weights within the window of the new region. Particles incoming within the bounds of the weight windows are unaffected by the game.

Methods initially were developed where users had to manually input the importances of different regions within the problem space. The process was iterative. After each run, the

regions' importances were again manually edited in order to better sample particles towards the desired converged solution. Playing the game in this manner required a significant level of expertise, as well as, extra time from the practitioner iterating between solutions. Therefore, automated variance reduction methods are highly desirable.

CADIS

The CADIS (Consistent Adjoint Driven Importance Sampling) methodology was developed to automate variance reduction by automating the generation of weight windows which are then used to bias MC simulations. The method begins with the fixed-source, time-independent Boltzmann transport equation for a non-multiplying system given in Eq. 1. The equation can be rewritten using the following transport operator:

$$H = \hat{\Omega} \cdot \nabla + \sigma(\vec{r}, E, t) - \int \int \sigma_s(\vec{r}; \Omega' \rightarrow \Omega, E' \rightarrow E) \varphi(\vec{r}, \Omega', E') d\Omega' dE'. \quad (6)$$

Substituting this into Eq. 1 gives a rewritten transport equation:

$$H\varphi = q. \quad (7)$$

If both sides are multiplied by the adjoint flux and integrated over all independent variables (represented by Dirac brackets $\langle \cdot \rangle$), it can be shown that for vacuum boundary conditions the following adjoint property:

$$\langle \varphi^+, H\varphi \rangle = \langle \varphi, H^+ \varphi^+ \rangle, \quad (8)$$

holds true for the adjoint operator H^+ given by

$$H^+ = -\hat{\Omega} \cdot \nabla + \sigma(\vec{r}, E, t) - \int \int \sigma_s(\vec{r}; \Omega, E \rightarrow \Omega', E') d\Omega' dE'. \quad (9)$$

The adjoint function φ^+ can be solved in terms of a predefined adjoint source q^+ . MAVRIC uses the Denovo code to solve a deterministic form of Eq. 9 which is explained in the next section.

$$H^+ \varphi^+ = q^+ \quad (10)$$

Combining Eq. 7,8 and 10, the following relationship can be found:

$$\langle \varphi^+, H\varphi \rangle - \langle \varphi, H^+ \varphi^+ \rangle = \langle \varphi^+, q \rangle - \langle \varphi, q^+ \rangle \quad (11)$$

Since the right-hand side is equal to zero as shown in Eq. 8, it can be rewritten to obtain:

$$\langle \varphi^+, q \rangle = \langle \varphi, q^+ \rangle \quad (12)$$

If the adjoint source is set to the detector response $q^+ = \sigma_D$, then Eq. 12 can be rewritten to equal the detector response:

$$\langle \varphi^+, q \rangle = \langle \varphi, \sigma_D \rangle = R \quad (13)$$

Therefore, the adjoint-weighted, fixed source distribution is equal to the detector response.

Additionally, Wagner shows that the optimal weight window targets for Monte Carlo biasing are given by:

$$\bar{w}(\vec{r}, E) = \frac{R}{\varphi^+(\vec{r}, E)} \quad (14)$$

A biased source distribution can be derived from the same set of equations and is given in Eq 15.

$$\hat{q}(\vec{r}, E) = \frac{\varphi^+(\vec{r}, E)q(\vec{r}, E)}{R} \quad (15)$$

Biased source particles must start with a weighting that will preserve the final reaction rate and give optimal variance reduction. The weight can be found by setting the biased source times the weight equal to the original source strength:

$$\hat{w}(\vec{r}, E)\hat{q}(\vec{r}, E) = q(\vec{r}, E) \quad (16)$$

The biased source particles must then begin with a weight of:

$$\hat{w}(\vec{r}, E) = \frac{q(\vec{r}, E)}{\hat{q}(\vec{r}, E)} = \frac{R}{\varphi^+(\vec{r}, E)} \quad (17)$$

FW-CADIS

The CADIS methodology is further extended by Forward-Weighted CADIS (FW-CADIS) which was developed to obtain uniform uncertainties at multiple locations or on a global scale. Since multiple tallies are used the adjoint source must be weighted by the expected flux spectrum and magnitude at each location. The adjoint source can then be created by folding the expected flux with the reaction rates of interest in the regions of interest. Instead of only using the response function given in Eq. 11, the adjoint source is given for all positions as,

$$q^+(\vec{r}, E) = \frac{\sigma_D(\vec{r}, E)}{\int \varphi(\vec{r}, E) \sigma_D(\vec{r}, E) dE} \quad (18)$$

Therefore, if equal variance reduction is desired over the entire problem space, each mesh should be given an adjoint source described by Eq. 18 (Wagner, Blakemen, & Peplow, 2007).

MAVRIC

The MAVRIC sequence (Monaco with Automated Variance Reduction using Importance Calculations) of the Scale6.1 code applies the CADIS and FW-CADIS methodologies to bias particles in the Monaco code. MAVRIC is used for deep-shielding problems that are not feasible to calculate using standard MC. The FW-CADIS methodology is implemented by first solving a multi-group discrete ordinates model for the forward flux over a three-dimensional, discretized mesh representation of the model developed for Monaco. The forward flux is solved by the Denovo code, which is then placed into a multi-group form of Eq. 17 to define the adjoint source. The adjoint flux for the problem is then solved using again Denovo. The CADIS methodology is implemented by skipping the forward flux calculation and solving the adjoint flux by the user-defined adjoint source. Finally, MAVRIC uses the adjoint flux solved by Denovo to create an importance map and biased source distribution that is used in the final neutral particle transport.

CHAPTER 4

VALIDATION OF MAVRIC USING LWR BENCHMARKS

Understanding the methodology is very important for effectively and accurately using the MAVRIC sequence for shielding calculations. While the variance reduction is automated, improper use can lead to unintentionally misleading results that are normally the practitioner's ignorance of the method. Therefore, before discussing the experience of using the MAVRIC sequence within the VHTR design a number of benchmarks were performed. The goal of studying the benchmark cases was to understand the methodology and validity its implementation.

As the first generation of nuclear power plants has obtained the first lifetime extension (after 40 years) and is considering the second extension ('life after 60'), it is clear that enhanced guidelines and benchmarks are needed for measuring and regulating radiation-induced lifetime damage occurring in the support structures exposed to fast neutron irradiation. RPV dosimetry programs typically correlate surveillance capsules data around the reactor core to DPA, which may be related to changes in important material properties caused by a given radiation field. The Shielding Integral Benchmark Archive and Database (SINBAD) contains a set of models used to validate radiation transport methods specific to shielding applications. The Pool-side Critical Assembly (PCA) at ORNL was selected to validate the calculation of the attenuation in different reaction rates through a pressure vessel in a relatively simple geometry. The VENUS-3 Critical Facility was designed to validate calculating axial variations in transport codes. The two models provided validation for methodologies within MAVRIC of surveillance capsule monitoring programs, which were then extended to the HTGR design (Hunter et al., 1994).

Poolside Critical Assembly at ORNL

The PCA at Oak Ridge National Laboratory was designed to validate transport methods specifically looking at the attenuation of reaction rates within a relatively simple geometry. The experiments were performed from 1978-1981 (McElroy, 1981).

Geometry and Materials Definition

The PCA geometry is shown in Figure 1 together with dimensions. The material compositions of the regions used in analysis (structural materials and fuel) are given in Table 1. The core used aluminum, plate-type MTR fuel enriched to 93% ²³⁵U in a 5x5 assembly. Unfortunately the actual composition of the plates was not given, so only homogenized core regions were modeled in the Monaco simulation (Remec & Kam, 1997).

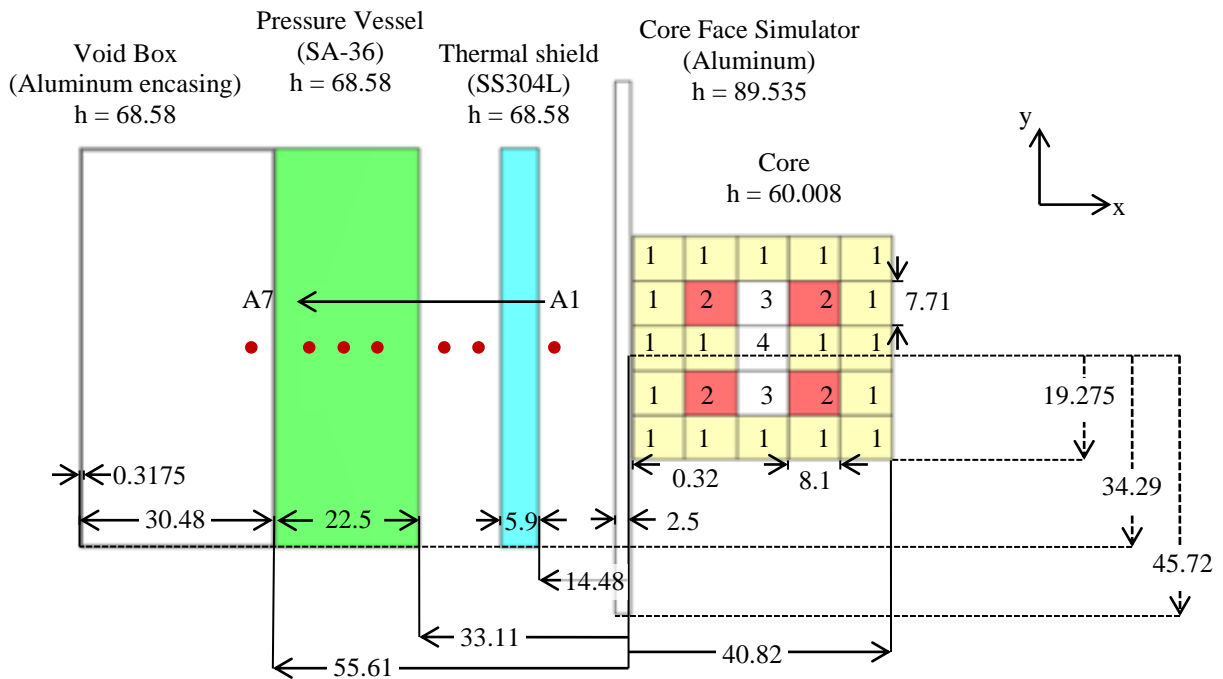


Figure 1. The PCA layout (top view) showing mockup components. The numbers in the core indicate homogenized core regions given in Table 1. The red dots indicate detector locations. (All units are in cm).

Table 1. Material Compositions (w%)

	Fuel Region Homogenizations				SS304L	SA-36	Al	Water
	1	2	3	4				
$\rho(g/cm^3)$	1.741	1.607	1.782	1.709	8.0	7.85	2.7	1
^{238}U	0.162	0.0875	0.167	0.155	-	-	-	-
^{235}U	2.14	1.63	2.2	2.07	-	-	-	-
^{27}Al	64.248	57.7825	66.253	62.675	-	-	100	-
^1H	3.75	4.5	3.48	3.9	-	-	-	-
^{16}O	29.7	36	27.9	31.2	-	-	-	-
C	-	-	-	-	0.03	0.25	-	-
Mn	-	-	-	-	2	-	-	-
Si	-	-	-	-	1	-	-	-
Cr	-	-	-	-	18	-	-	-
Ni	-	-	-	-	11	-	-	-
Fe	-	-	-	-	67.97	99.66	-	-
P	-	-	-	-	-	0.04	-	-
S	-	-	-	-	-	0.05	-	-
H ₂ O	-	-	-	-	-	-	-	100

Source Definition

The fission source distribution is derived from fission chamber measurements provided in the SINBAD package. Quarter-core symmetry is assumed except for measurements in the columns directly to the left and right of the centerline of the core as can be seen in Figure 2. All other values are mirrored exactly over each quarter. The z-distribution follows a chopped-cosine shape (30.004 to -30.004 cm) defined by:

$$p(z) = \cos(0.0442(z - 0.42)) \text{ (cm)} \quad (19)$$

Inputting 3D mesh-based sources into MAVRIC cannot be directly done. Instead a set of individual 2D sources must be used. For this problem individual sources are defined as 2D source distributions in the X-Z plane and these are stacked in the Y-direction. The X-Z plane

consists of a y-distribution represented by a histogram between points in Figure 2 and a z-distribution defined by the cosine shape given in Eq. 19. Each source strength is set to the sum of the column across all y-values from Figure 2 divided by the sum of the entire table in order to normalize the total neutron source strength to one neutron. Using this method, the source is distributed as a step function in the y-direction while being continuously interpolated in the X and Z as can be seen in Figure 3. Additionally, Figure 4 shows different views of the source as sampled. Much care needs to be placed on this practice to ensure that relative strengths between 2D sources are properly preserved.

(cm) y/x	1.15	4.3	7.45	9.25	12.4	15.55	17.35	20.5	23.65	25.27	28.42	31.57	33.37	36.52	39.67
19.275	0.2570	0.2902	0.3434	0.3877	0.4386	0.4386	0.4719	0.4630	0.4564	0.4386	0.4386	0.3877	0.3434	0.2902	0.2570
16.245	0.2503	0.2725	0.3168	0.3545	0.4032	0.4143	0.4409	0.4342	0.4431	0.4143	0.4032	0.3545	0.3168	0.2725	0.2503
14.595	0.2880	0.3013	0.3833	0.4386	0.4984	0.4829	0.4852	0.4852	0.4940	0.4829	0.4984	0.4386	0.3833	0.3013	0.2880
11.565	0.3168	0.3434	0.4320	0.5560	0	0.5383	0.7023	0.6823	0.7288	0.5383	0	0.5560	0.4320	0.3434	0.3168
8.535	0.3279	0.3611	0.4564	0.6026	0	0.5893	0.7466	0.6823	0.7599	0.5893	0	0.6026	0.4564	0.3611	0.3279
6.885	0.3545	0.3833	0.4940	0.6358	0	0.6247	0.7864	0.7599	0.8307	0.6247	0	0.6358	0.4940	0.3833	0.3545
3.855	0.3722	0.3988	0.4940	0.5627	0.6557	0.6380	0.6247	0.6181	0.6247	0.6380	0.6557	0.5627	0.4940	0.3988	0.3722
0.825	0.3589	0.3965	0.4719	0.5162	0.5915	0.6114	0.6358	0.6269	0.6159	0.6114	0.5915	0.5162	0.4719	0.3965	0.3589
-0.825	0.3722	0.3988	0.4940	0.5627	0.6557	0.6380	0.6247	0.6181	0.6247	0.6380	0.6557	0.5627	0.4940	0.3988	0.3722
-3.855	0.3545	0.3833	0.4940	0.6358	0	0.6247	0.7864	0.7599	0.8307	0.6247	0	0.6358	0.4940	0.3833	0.3545
-6.885	0.3279	0.3611	0.4564	0.6026	0	0.5893	0.7466	0.6823	0.7599	0.5893	0	0.6026	0.4564	0.3611	0.3279
-8.535	0.3168	0.3434	0.4320	0.5560	0	0.5383	0.7023	0.6823	0.7288	0.5383	0	0.5560	0.4320	0.3434	0.3168
-11.565	0.2880	0.3013	0.3833	0.4386	0.4984	0.4829	0.4852	0.4852	0.4940	0.4829	0.4984	0.4386	0.3833	0.3013	0.2880
-14.595	0.2503	0.2725	0.3168	0.3545	0.4032	0.4143	0.4409	0.4342	0.4431	0.4143	0.4032	0.3545	0.3168	0.2725	0.2503
-16.245	0.2570	0.2902	0.3434	0.3877	0.4386	0.4386	0.4719	0.4630	0.4564	0.4386	0.4386	0.3877	0.3434	0.2902	0.2570
-19.275	0.2570	0.2902	0.3434	0.3877	0.4386	0.4386	0.4719	0.4630	0.4564	0.4386	0.4386	0.3877	0.3434	0.2902	0.2570
Strength	0.0469	0.0510	0.0631	0.0759	0.0458	0.0806	0.0915	0.0888	0.0929	0.0806	0.0458	0.0759	0.0631	0.0510	0.0469

Figure 2. The source distribution used in MAVRIC extracted from the SINBAD package.

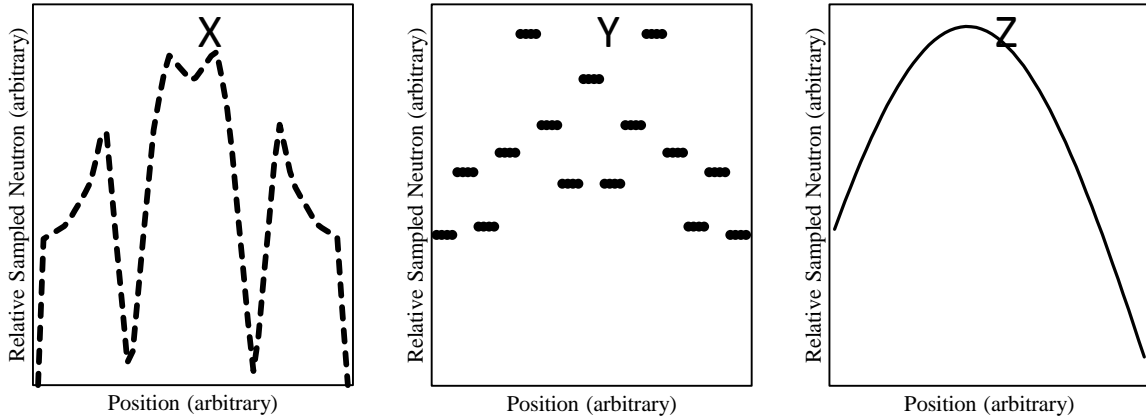


Figure 3. The source distribution in the x, y and z directions centered around $(x, y, z) = (20.85, 7.35, 0.00)$ cm.

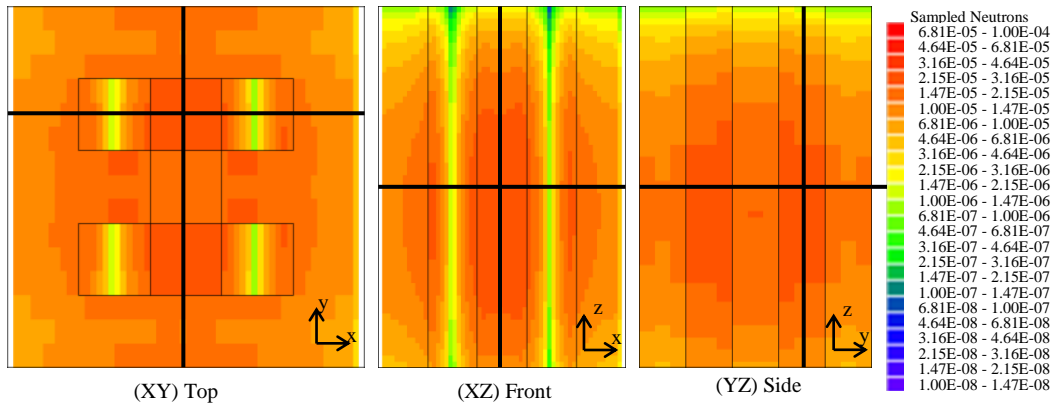


Figure 4. Different views of the source used by MAVRIC. The black lines indicate the plane location of each other view centered around $(x, y, z) = (20.85, 7.35, 0.00)$ cm.

Reaction Rates

In the PCA Benchmark, measurements being reported are fission-equivalent, reaction rates normalized to one fission neutron at the positions indicated in Figure 1 (Remec & Kam, 1997). Detectors were placed at the centerline of the core in the y and z directions and are respectively 12, 23.8, 29.7, 39.5, 44.7, 50.1, 59.1 cm from the right face of the aluminum Core-Face-Simulator. The final response for reaction i at point x in terms of fission-equivalent reaction rate is defined as:

$$R_{xi} = \frac{\int \phi_x(E) \sigma_{xi}(E) dE}{\int \chi(E) \sigma_{xi}(E) dE} = \frac{\sum_G \phi_{Gx} \sigma_{Gxi}}{\sum_G \chi_G \sigma_{Gxi}}. \quad (20)$$

The denominator of the equation is the cross section for the reaction of interest weighted by the uranium fission spectrum. These can be extracted from the benchmark, but for the sake of consistency the values should be based on the cross sections used while simulating. The first row in Table 2 shows these values with their relative uncertainty from the original benchmark, using the BUGLE-96 cross-section library evaluated from ENDFB-VI. The second row provides the values calculated using the multi-group fission spectrum and cross sections from the 200n47g shielding library contained in Scale6.1 based on the ENDFB-VII library, which did not provide relative uncertainties. If the uncertainty between in the ratios is assumed to be only from the BUGLE-96 cross-section library, then the uncertainty is higher than the error between the two calculations.

Table 2. Reaction cross sections, averaged over ²³⁵U Spectrum

	²³⁷ Np(n,f)	²³⁸ U(n,f)	¹⁰³ Rh(n,n')	¹¹⁵ In(n,n')	⁵⁸ Ni(n,p)	²⁷ Al(n,a)
1. BUGLE-96 / ENDFB-VI	1.312E+00 ± %3.81	3.050E-01 ± %2.95	7.330E-01 ± %5.18	1.890E-01 ± %4.23	1.090E-01 ± %5.50	7.050E-04 ± %5.67
2. 200n47g / ENDFB-VII	1.354E+00	3.093E-01	7.157E-01	1.884E-01	1.058E-01	7.290E-04
(1. / 2.)	0.969 ± 0.038	0.986 ± 0.030	1.024 ± 0.052	1.003 ± 0.042	1.031 ± 0.055	0.967 ± 0.057

Notice that the ²³⁷Np(n,f) and ²³⁸U(n,f) reactions have some response in the thermal spectrum while all other reactions are threshold reactions with a threshold at or above 0.1MeV. In principle, best results should be expected when generating variance reduction parameters for each reaction separately; this is facilitated in MAVRIC through automation. However, when many reactions are sought, one could consider combining several at a time. If one of the threshold reactions is chosen for biasing particles, then responses of the more thermal reactions will only contain tallies for the spectrum portion above that threshold. The results for the more thermal reaction may indicate good statistics, but will completely ignore the portion of the spectrum not being simulated and lead to erroneous results. Figure 6 shows on the y-axis, the

contribution of each reaction integrated up to the energy (independent variable on the x-axis) and normalized to the total reaction rate. The idea is to emulate a Cumulative Distribution Function (CDF) demonstrating the importance of each portion of the spectrum. For the six response functions, the thermal spectrum only significantly contributes to the $^{237}\text{Np}(n,f)$ reaction.

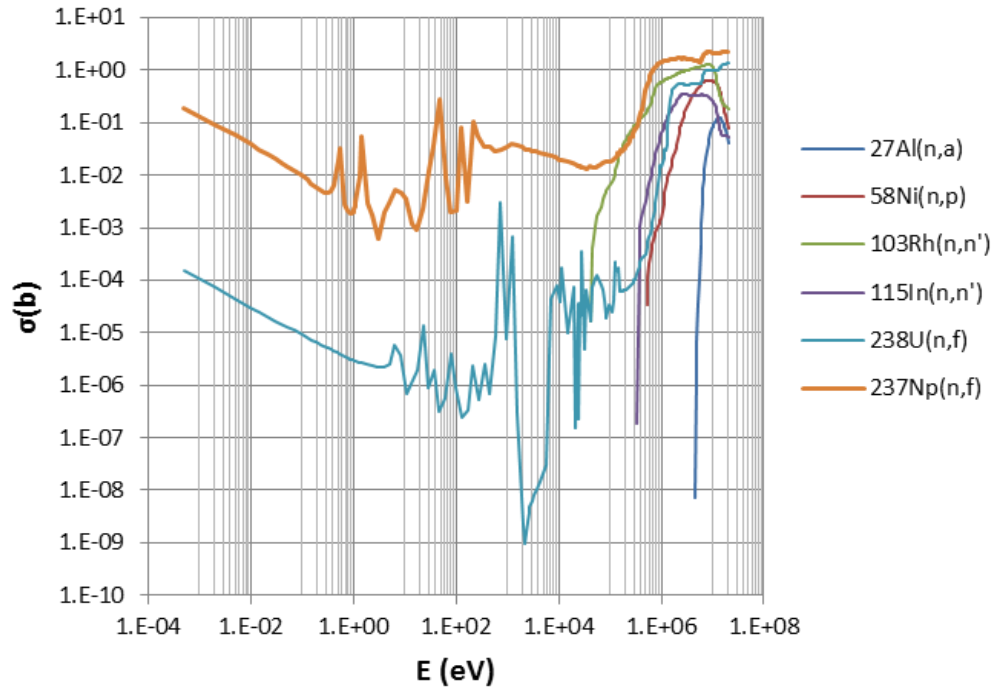


Figure 5. A comparison of the foil cross sections. The ^{237}Np reaction provides some coverage of the entire spectrum.

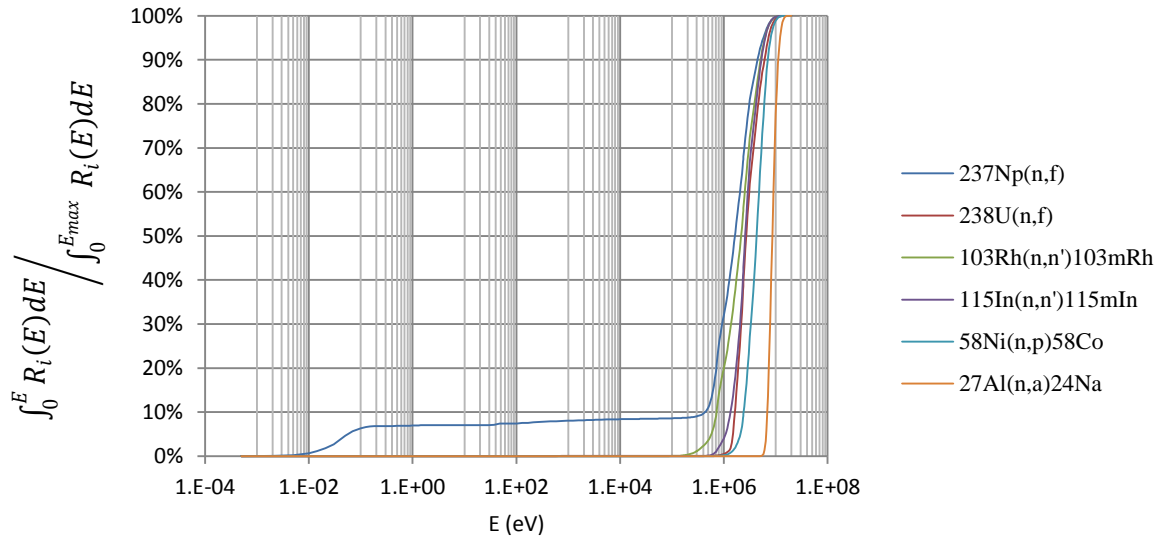


Figure 6. A CDF of each reaction rate. Notice that the $^{237}\text{Np}(n,f)$ reaction is the only reaction with a significant contribution occurring below 0.1 MeV.

Deterministic Denovo Model and Biasing Parameters

The forward and adjoint Denovo model encompasses PCA and used $43 \times 30 \times 72 = 92,880$ voxels as shown in Figure 7. An S_4 quadrature set together with P_1 Legendre expansion was used in all simulations. The adjoint source region is indicated by red box and was selected to include all detector positions. Further details are provided in Table 3.

Six separate MAVRIC simulations were performed, one for each reaction of interest used to generate variance reduction parameters (i.e., used as the adjoint source). The MC time was set to run for 3 hours in batches of 10,000 source particles. Table 4 summarizes the six simulations performed, including the forward and adjoint Denovo CPU time, as well as the total time.

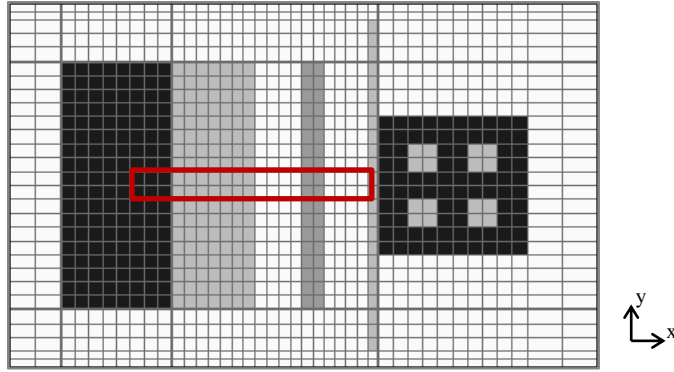


Figure 7. The grid used for the Denovo (XY). The red indicates the region set as the adjoint source.

Table 3. Denovo parameters.

<u>Denovo</u>	
<i>Global Dimensions</i>	
X (max, min, total)	(40.82, -100, 140.82) cm
Y (max, min, total)	(50, -50, 100) cm
Z (max, min, total)	(50, -50, 100) cm
Volume	1,408,200 cm ³
Meshing (X*Y*Z=total)	(43x30x72 = 92,880 voxels)
Average Voxel Size	15.2 cm ³
<i>Adjoint Source Region</i>	
X (max, min, total)	(-5, -61, 56) cm
Y (max, min, total)	(1, -1, 2) cm
Z (max, min, total)	(-1, -1, 2) cm
Volume	224 cm ³
<i>Parameters</i>	
Quadrature sets (S _N)	4
Legendre polynomials (P _L)	1
Krylov space size	10

Table 4. MAVRIC performance.

	Adjoint Source Response Function					
	237Np(n,f)	238U(n,f)	103Rh(n,n')	115In(n,n')	58Ni(n,p)	27Al(n,a)
<u>Time (min)</u>						
Forward	4.36	4.50	4.31	4.45	4.31	4.35
Adjoint	5.87	5.83	1.98	1.76	1.54	1.02
Total Denovo	10.23	10.33	6.29	6.21	5.85	5.37
Total MC	180.94	181.24	180.93	181.05	180.93	180.98
Total	191.17	191.57	187.22	187.26	186.78	186.35
<u>MC Performance</u>						
Batches	237	337	291	318	367	491
Particles (millions)	2.37	3.37	2.91	3.18	3.67	4.91
Time/Particle (ms)	4.6	3.2	3.7	3.4	3.0	2.2

Results

The preliminary analysis compared the total forward flux obtained by Denovo and Monaco. This FW-CADIS simulation used the adjoint source defined as the red region in Figure 7, thus it will not generate high-quality results over the whole region. The $^{237}\text{Np}(n,f)$ reaction was used as the adjoint source spectrum since it has some response over the whole spectrum, but is again not optimum for the integral flux. The total neutron flux distributions obtained from the MC calculation and the forward Denovo calculation are compared in Figure 8. The similarity between the two figures suggests consistency between the deterministic and stochastic simulations.

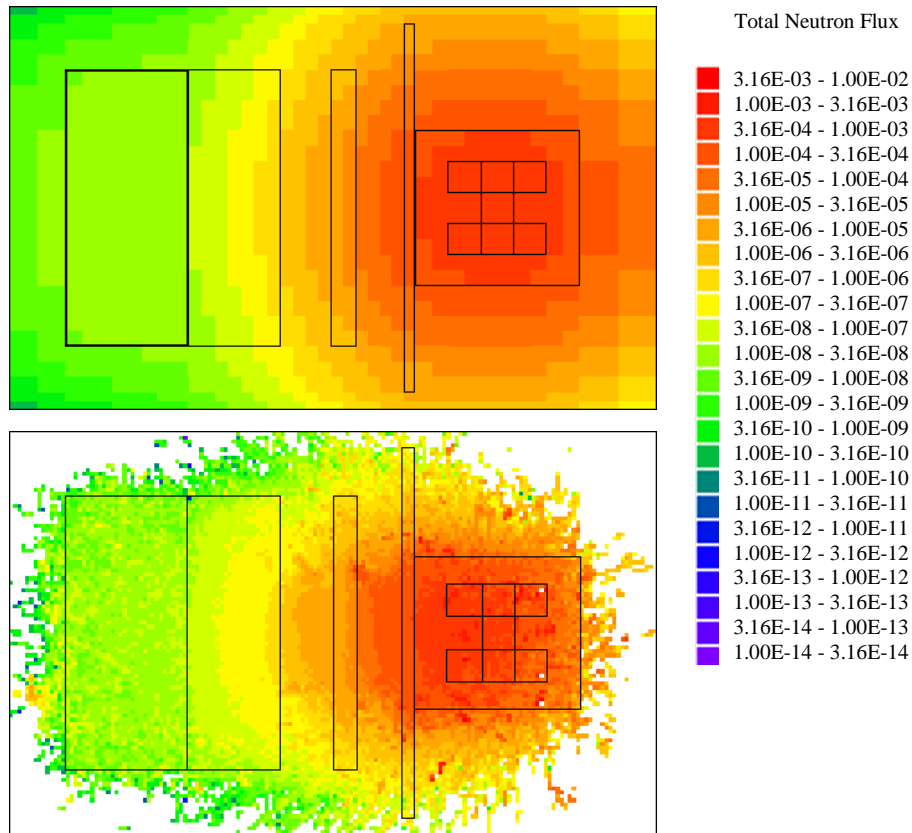


Figure 8. (Top) Denovo total neutron, forward flux. (Bottom) Stochastic MC total neutron flux.

For each type of foil a separate simulation was performed, setting the adjoint source spectrum equal to the cross section of the reaction rate of interest. Figure 9 shows a map of the relative uncertainty of each simulation for the corresponding response. It is apparent that statistics are within 10% uncertainty for each region of interest. The shape of the relative uncertainties provides an insight into how much scattering is taking place in each simulation and how important that is to the final results as determined by MAVRIC. For the very fast $^{27}\text{Al}(n,\alpha)^{24}\text{Na}$ reaction, the region of relative uncertainty less than 10% ($\sigma_{\text{Ri}} < 0.1$) is the narrowest. Scattered neutrons can almost be completely ignored for this reaction so the important region does not fan out from the region of interest as much as for other reactions. On the other end of the spectrum, levels of uncertainty spread farther from the adjoint source region in the $^{237}\text{Np}(n,f)$ reaction due to its dependence on scattering neutrons. The same logic, and even more the fact that the neutrons below few MeV are “killed”, explains why in Table 4, the time spent per simulated particle for the $^{27}\text{Al}(n,\alpha)^{24}\text{Na}$ reaction is less than half of that of the $^{237}\text{Np}(n,f)$ reaction.

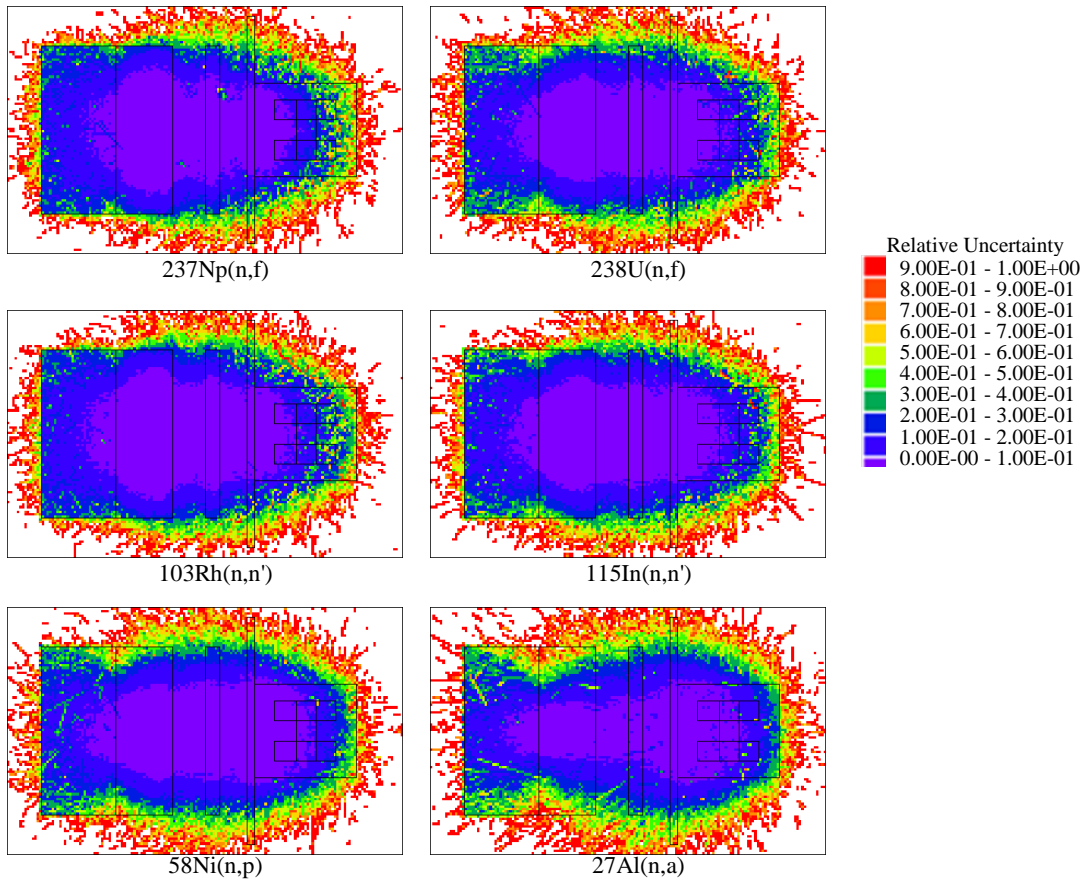


Figure 9. Relative uncertainties for the reaction used to bias particles towards.

The purpose of performing this analysis was to validate calculating reaction rates outside of a pressure vessel using the MAVRIC sequence. Benchmarked results in RPV dosimetry are reported in C/M ratios (calculated-to-measured). Figures 10 and 11 show two plots of the C/M ratios arranged according to detector location and reaction rate, respectively. The error bars represent a combined one sigma uncertainty of the PCA measurements and the MC results. In Figure 10 it seems there is an overall pattern of overestimating the foil activity with an average overestimation of 4%. When grouping by reaction rate as in Fig. 11, certain trends seem to be evident within groupings which may be reflective of slight biases introduced by the cross sections.

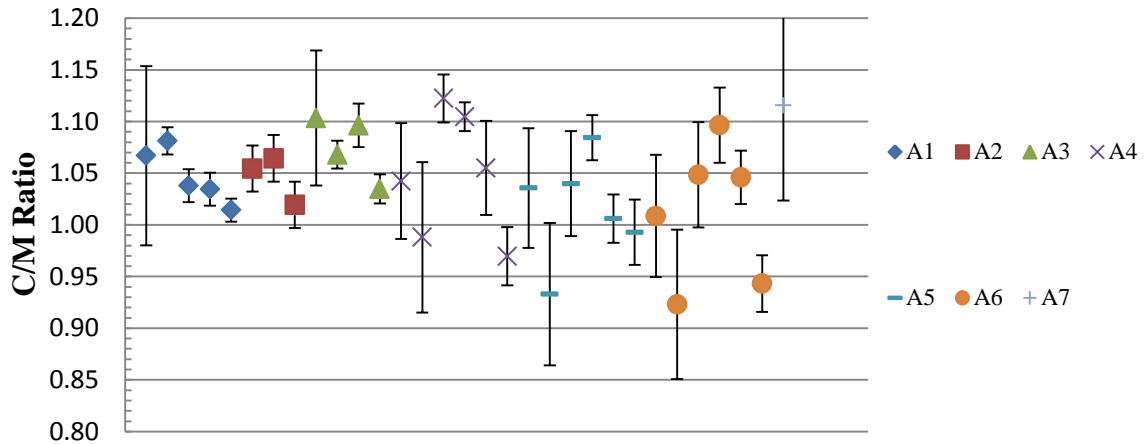


Figure 10. C/M ratios grouped by detector location.

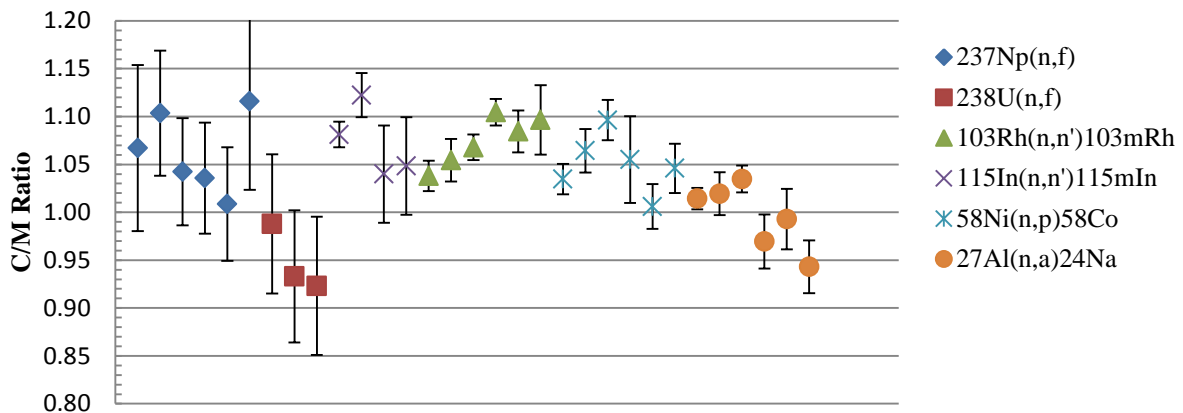


Figure 11. C/M ratios grouped by response.

Results obtained from the MAVRIC sequence are in better agreement to the PCA benchmark than results provided in SINBAD. Table 5 gives values for the calculated and measured data as well as the C/M ratio. On average the calculated reaction rates have an error of $\pm 5.6\%$ compared to the measured reaction rates. On average the measured values have an uncertainty of 3%, the results obtained from MAVRIC have an average uncertainty of 1%. The average combined one sigma uncertainty was 4% primarily introduced by the uncertainties in measured data from the experiment. Previous discrete ordinates calculations using older cross section libraries reported an arithmetic mean C/M ratio of 0.93 ± 0.03 , compared to 1.04 ± 0.04 obtained by MAVRIC. Therefore, a combination of the FW-CADIS methodology and newer

cross section libraries improve upon previous results. Moreover, while the previous difference seemed statistically significant (being over 2σ), it is now within $\pm 1\sigma$.

Table 5. PCA Reaction Rates compared to measured data.

	Measured Reaction Rate by position						
	A1	A2	A3	A4	A5	A6	A7
$^{237}\text{Np}(n,f)$	6.64E-06±%6.20	-	2.27E-07±%6.30	9.27E-08±%5.50	5.18E-08±%5.70	2.70E-08±%5.80	7.25E-09±%9.20
$^{238}\text{U}(n,f)$	-	-	-	6.11E-08±%6.90	2.74E-08±%6.80	1.12E-08±%7.10	-
$^{103}\text{Rh}(n,n')$	5.54E-06±%1.00	-	-	7.74E-08±%1.50	4.35E-08±%5.00	2.19E-08±%5.00	-
$^{115}\text{In}(n,n')$	5.61E-06±%1.00	6.06E-07±%2.00	1.99E-07±%1.00	5.87E-08±%0.70	2.76E-08±%1.50	1.17E-08±%3.00	-
$^{58}\text{Ni}(n,p)$	5.83E-06±%1.40	6.18E-07±%2.00	2.31E-07±%1.40	5.30E-08±%1.00	2.09E-08±%1.80	7.43E-09±%2.20	-
$^{27}\text{Al}(n,a)$	7.87E-06±%1.00	1.02E-06±%2.00	4.48E-07±%1.00	1.02E-07±%2.00	4.10E-08±%2.20	1.54E-08±%2.20	-

	Calculated Reaction Rate by position						
	A1	A2	A3	A4	A5	A6	A7
$^{237}\text{Np}(n,f)$	7.08E-06±6.07%	7.68E-07±1.70%	2.50E-07±1.73%	9.66E-08±1.10%	5.36E-08±1.05%	2.72E-08±1.23%	8.09E-09±0.58%
$^{238}\text{U}(n,f)$	5.73E-06±0.64%	6.44E-07±1.73%	2.20E-07±0.86%	6.04E-08±2.31%	2.56E-08±1.17%	1.03E-08±1.31%	2.73E-09±0.60%
$^{103}\text{Rh}(n,n')$	5.99E-06±0.87%	6.93E-07±1.07%	2.27E-07±1.56%	8.69E-08±1.77%	4.52E-08±0.86%	2.30E-08±0.97%	6.65E-09±0.52%
$^{115}\text{In}(n,n')$	5.82E-06±1.24%	6.39E-07±0.96%	2.13E-07±0.90%	6.48E-08±1.20%	2.99E-08±1.58%	1.28E-08±2.05%	3.40E-09±0.56%
$^{58}\text{Ni}(n,p)$	6.03E-06±0.75%	6.58E-07±1.08%	2.53E-07±1.58%	5.59E-08±4.43%	2.10E-08±1.49%	7.77E-09±1.35%	2.13E-09±0.70%
$^{27}\text{Al}(n,a)$	7.98E-06±0.49%	1.04E-06±1.02%	4.64E-07±0.98%	9.89E-08±2.00%	4.07E-08±2.28%	1.45E-08±1.65%	4.89E-09±1.12%

	Calculated to Experimental Ratios (C/E)						
	A1	A2	A3	A4	A5	A6	A7
$^{237}\text{Np}(n,f)$	1.07	-	1.10	1.04	1.04	1.01	1.12
$^{238}\text{U}(n,f)$	-	-	-	0.99	0.93	0.92	-
$^{103}\text{Rh}(n,n')$	1.08	-	-	1.12	1.04	1.05	-
$^{115}\text{In}(n,n')$	1.04	1.05	1.07	1.10	1.08	1.10	-
$^{58}\text{Ni}(n,p)$	1.03	1.06	1.10	1.06	1.01	1.05	-
$^{27}\text{Al}(n,a)$	1.01	1.02	1.03	0.97	0.99	0.94	-

	Abs(1-C/E)							Average
	A1	A2	A3	A4	A5	A6	A7	
$^{237}\text{Np}(n,f)$	0.07	-	0.10	0.04	0.04	0.01	0.12	0.06
$^{238}\text{U}(n,f)$	-	-	-	0.01	0.07	0.08	-	0.05
$^{103}\text{Rh}(n,n')$	0.08	-	-	0.12	0.04	0.05	-	0.07
$^{115}\text{In}(n,n')$	0.04	0.05	0.07	0.10	0.08	0.10	-	0.07
$^{58}\text{Ni}(n,p)$	0.03	0.06	0.10	0.06	0.01	0.05	-	0.05
$^{27}\text{Al}(n,a)$	0.01	0.02	0.03	0.03	0.01	0.06	-	0.03
Average	0.05	0.05	0.08	0.06	0.04	0.06	0.12	0.056

VENUS-3 Experiment

The VENUS-3 LWR-PVS Benchmark Experiment was performed at CEN/SCK (Studiecentrum voor Kernenergie) Mol, Belgium at the VENUS Critical Facility. The facility was loaded to represent typical power-producing LWRs in order to study methods for measuring radiation profiles throughout the pressure vessel. The “3” in the title stands for “3D” and the fact that the study was interested in assessing axial variations in measuring important quantities. The axial variation was shaped through loading periphery regions of the core with Partial Length Shielded Assemblies, replacing the bottom half of the rods’ fuel region with stainless steel (Maerker, 1989).

Geometry and Materials Definition

The VENUS-3 geometry is shown in Figure 12 through Figure 14. The core uses a standard pin-to-pin pitch (1.26cm) from typical 17x17 fuel assemblies while placing the rods in 16 15x15 fuel assemblies using 3.3-4% enriched UO₂ fuel pins depending on the region. The geometry of the problem is well-defined so that no homogenizations have been made in important regions. Some areas above and below the core are defined as mixtures of steel and water as indicated in Figure 12 through Figure 14. Each region in the Figures shows labels each mixture as defined in Table 6.

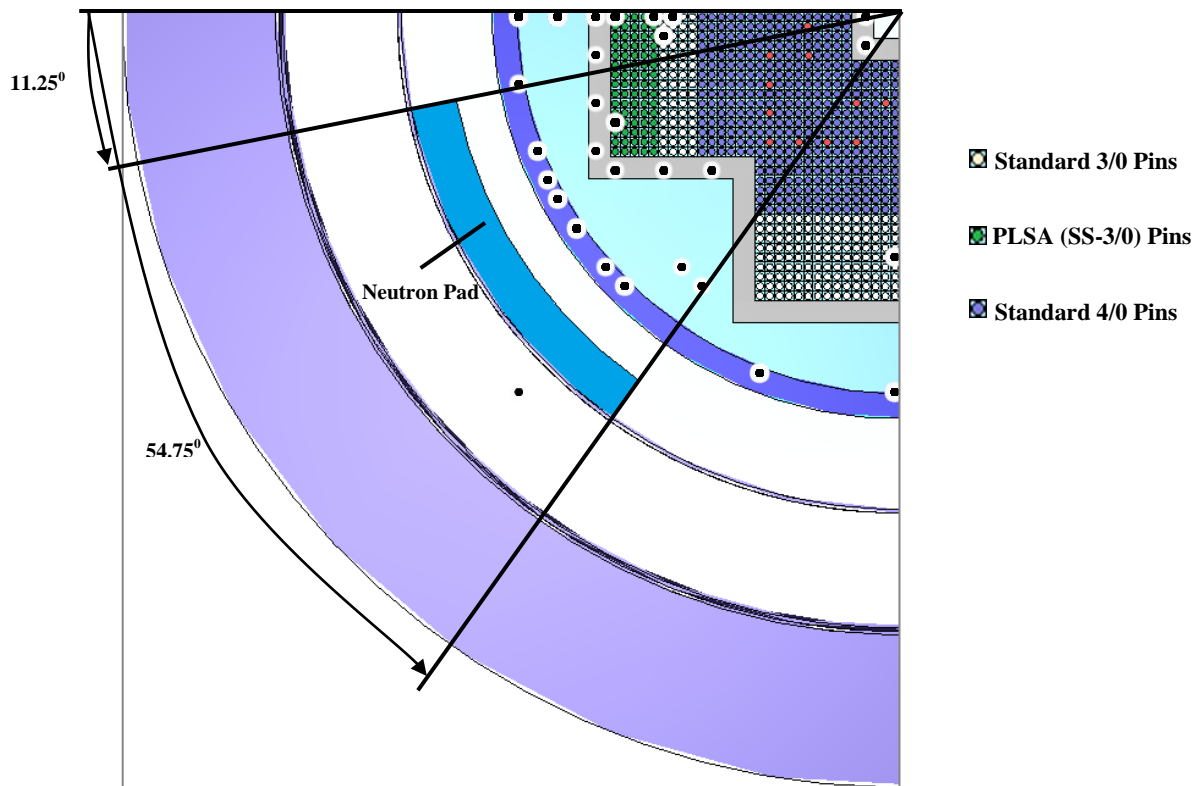


Figure 12. The VENUS-3 core layout is shown for one-quarter of the core with detector locations. The geometry is symmetric about each axis with only the neutron pad and detectors occurring in the quadrant shown.

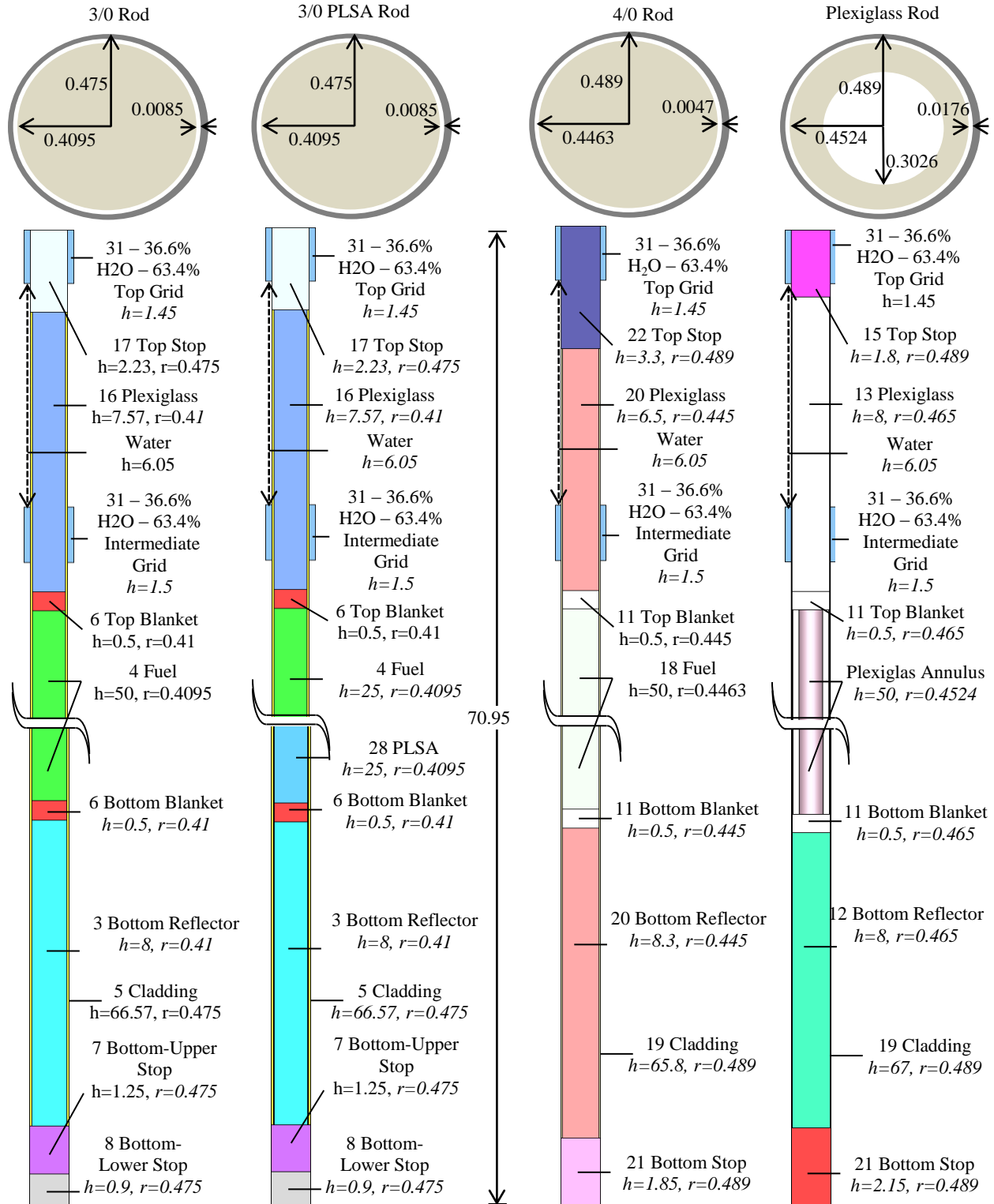


Figure 13. Geometry and material specification for different fuel elements.

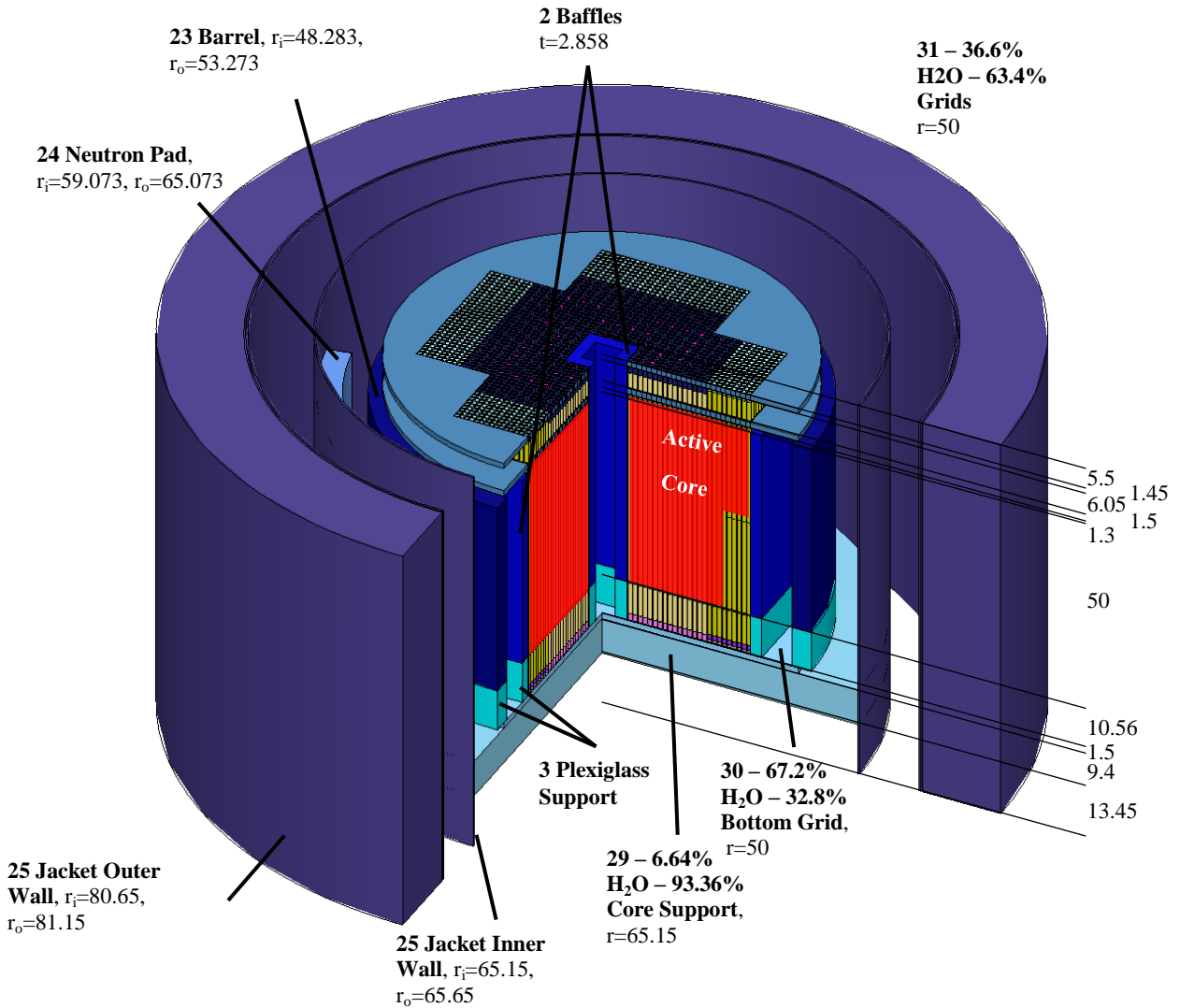


Figure 14. VENUS-3 LWR-PVS Benchmark Experiment. The red represents the active fuel region.

Table 6. Material Descriptions for MAVRIC

	4.3/0	18.4/0
$\rho(\text{g}/\text{cm}^3)$	10.25029	10.25029
^{238}U	96.649	95.924
^{236}U	0.016	0.023
^{235}U	3.306	4.022
^{234}U	0.029	0.031

(Table cont.)

	2.Inner Baffle	5.Cladding 3/0	6.Blanket	7.Upper	8.Lower	9.Pyrex	10.PyrexClad
$\rho(g/cm^3)$	7.902	6.645605	7.839399	4.923663	7.872218	2.223035	7.9
^{16}O	-	0.12	-	0.13	-	53.99554	-
C	0.059	-	0.042	-	0.042	-	0.03
^{55}Mn	1.651	-	1.58	-	1.58	-	0.87
^{31}P	0.03	-	0.025	-	0.025	-	-
S	0.013	-	0.028	-	0.028	-	-
Si	0.285	-	0.46	-	0.46	36.70766	0.29
Cr	16.37	0.1	18.2	0.12	18.2	-	18.4
Ni	8.72	-	8.6	-	8.6	-	9.5
Mo	0.454	-	-	-	-	-	0.07
^{59}Co	0.138	-	0.12	-	0.12	-	-
Fe	72.28	0.02	70.945	0.22	70.945	0.034971	70.84
Zr	-	98.35	-	98.02	-	-	-
^{23}Na	-	-	-	-	-	2.55199	-
Sn	-	-1.41	-	1.51	-	-	-
^{27}Al	-	-	-	-	-	1.221908	-
B	-	-	-	-	-	4.549862	-
K	-	-	-	-	-	0.938067	-
^{14}N	-	-	-	-	-	-	-
Cd	-	-	-	-	-	-	-

(Table 6 cont.)

	11.Al	14.Bottom Stop	15.Top Stop	17.BtTp Lower	19.Clad 4/0	21.Bottom Stop	22.Top Stop
$\rho(g/cm^3)$	2.693986	6.695768	7.947065	7.970973	7.890913	7.893818	8.46622
^{16}O	-	-	-	-	-	-	-
C	-	0.059	0.059	0.042	0.04	0.059	0.059
^{55}Mn	-	1.651	1.651	1.58	1.29	1.651	1.651
^{31}P	-	0.03	0.03	0.025	0.02	0.03	0.03
S	-	0.013	0.013	0.028	0.015	0.013	0.013
Si	-	0.285	0.285	0.46	0.135	0.285	0.285
Cr	-	16.37	16.37	18.2	18.3	16.37	16.37
Ni	-	8.72	8.72	8.6	10.03	8.72	8.72
Mo	-	0.454	0.454	-	0.132	0.454	0.454
^{59}Co	-	0.138	0.138	0.12	-	0.138	0.138
Fe	-	72.28	72.28	70.945	70.038	72.28	72.28
Zr	-	-	-	-	-	-	-
^{23}Na	-	-	-	-	-	-	-
Sn	-	-	-	-	-	-	-
^{27}Al	100	-	-	-	-	-	-
B	-	-	-	-	-	-	-
K	-	-	-	-	-	-	-
^{14}N	-	-	-	-	-	-	-

(Table 6 cont.)

	25/29/30.			
	23.Reflector	24.NeutronPad	JacketWall	28.Partial
$\rho(g/cm^3)$	7.9	7.9	7.9	7.9
¹⁶ O	-	-	-	-
C	0.015	0.016	0.024	0.024
⁵⁵ Mn	1.303	0.83	1.168	1.186
³¹ P	0.028	0.026	0.025	0.025
S	0.005	0.004	0.008	0.008
Si	0.513	0.395	0.374	0.374
Cr	18.464	18.022	17.619	18.71
Ni	10.199	10.588	9.836	9.832
Mo	0.474	0.425	0.452	0.183
⁵⁹ Co	0.097	0.196	0.113	0.105
Fe	68.822	69.498	70.354	69.543
Zr	-	-	-	-
²³ Na	-	-	-	-
Sn	-	-	-	-
²⁷ Al	-	-	-	-
B	-	-	-	0.005
K	-	-	-	-
¹⁴ N	0.08	-	0.027	-
Cd	-	-	-	0.005

(Table 6 cont.)

	Plexiglass					
	3	12	13	16	20	31
$\rho(g/cm^3)$	1.187271	1.186531	1.132063	1.111528	1.186278	1.186278

Source Definition

The VENUS-3 source is defined for one-quarter of the core with an axial profile applied to that distribution as provided in SINBAD (Hunter, 1994). The MAVRIC sequence only supports vacuum boundary conditions so a full model was developed and the source is mirrored in all other quadrants for the simulation. Additionally, a separate source was generated using the KENO-VI sequence which generates a mesh-based fission source distribution based off of an

MC criticality simulation. Figure 15 shows the two sources compared on similar meshes and relative scales (equal minimum to maximum ratios). Figure 16 shows a graph of the ratio of KENO-IV over SINBAD-specified fission source density along the x-axis at the axial centerline for different y-coordinates. Ideally, the KENOVI-based source will provide a more accurate source description and more accurate foil activation rates.

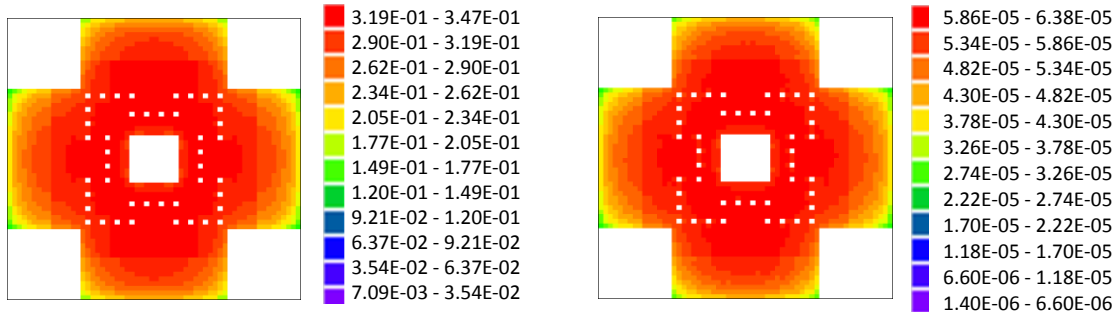


Figure 15. Neutron source distribution provided in SINBAD benchmark (left), and Fission rate calculated by KENO-VI (right).

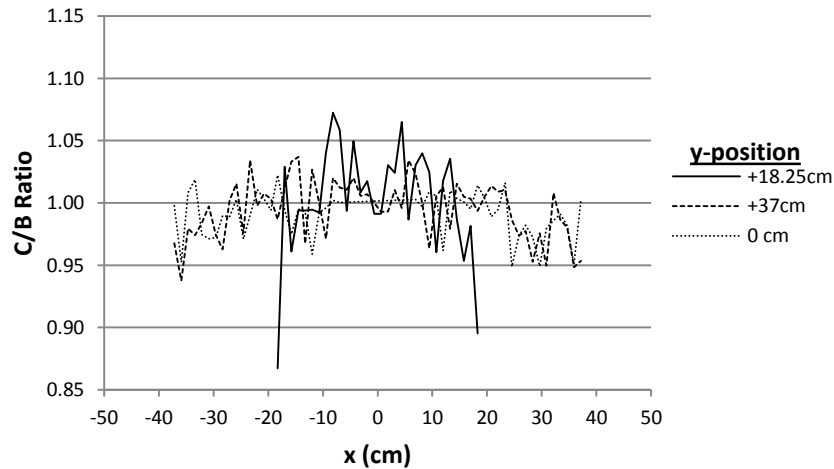


Figure 16. Ratio of fission source distributions (KENO-VI to that specified in SINBAD) along x-direction at several y-positions, all at the axial core centerline.

Reaction Rates

The benchmarked results include 387 tallies representing 3 different reactions rates: ^{58}Ni (n,p), ^{115}In (n,n'), and ^{27}Al (n, α). As in the PCA benchmark, reaction rates are described by the fission equivalent reaction rates given by Eq. 20. The foils are located in the inner baffle, outer baffle, core barrel, water gap, PLSA and the 3.3% Fuel Positions. The radial positions can be

seen in Figure 17 overlaying the adjoint source, and at each radial site there are multiple foils at different axial positions.

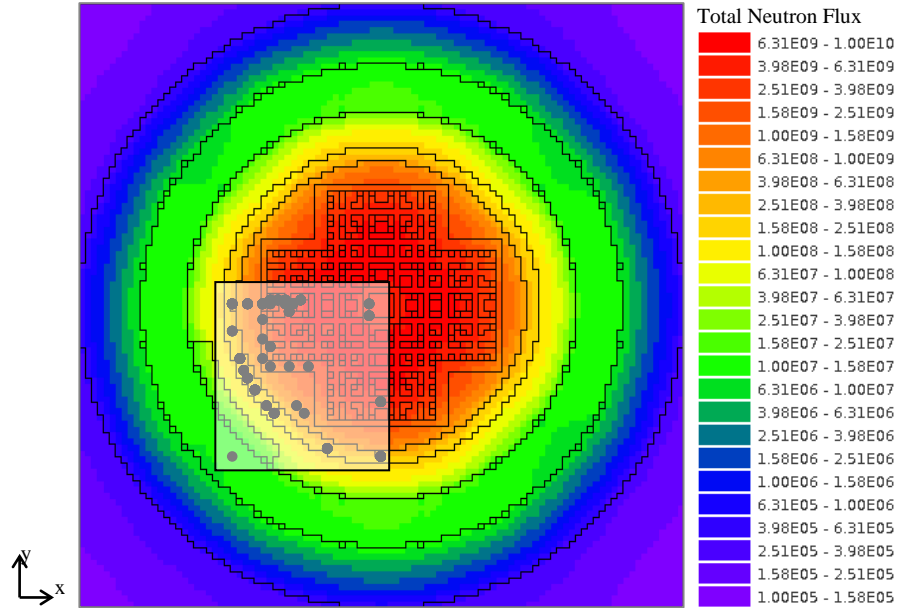


Figure 17. The total forward neutron flux together with the black dots representing foils positions. The box represents the adjoint source region.

Deterministic Denovo Model and Biasing Parameters

The forward and adjoint Denovo model use $100 \times 100 \times 50 = 500,000$ meshes. An S_8 quadrature set together with P_3 Legendre expansion was used in all simulations. The adjoint source region is indicated by red box and was selected to include all detector positions. Further details are provided in Table 7 and the run times are compiled in Table 8.

Table 7. Denovo Parameters.

Denovo	
<i>Global Dimensions</i>	
X (max, min, total)	(101.553, -101.553, 203.106) cm
Y (max, min, total)	(101.553, -101.553, 203.106) cm
Z (max, min, total)	(170.8, 70, 100.8) cm
Volume	4,158,206 cm ³
Meshing (X*Y*Z=total)	(100x100x50 = 500,000 voxels)
Average Voxel Size	8.3 cm ³
<i>Adjoint Source Region</i>	
X (max, min, total)	(10, -65, 75) cm
Y (max, min, total)	(10, -65, 75) cm
Z (max, min, total)	(165, 95, 70) cm
Volume	393,750 cm ³
<i>Parameters</i>	
Quadrature sets (S _N)	8
Legendre polynomials (P _L)	3
Krylov space size	10

Table 8. MAVRIC Performance.

	---- KENOVI Source ----			---- Benchmark Source ----		
	⁵⁸ Ni(n,p)	¹¹⁵ In(n,n')	²⁷ Al(n,α)	⁵⁸ Ni(n,p)	¹¹⁵ In(n,n')	²⁷ Al(n,α)
Time (hr)						
Forward	1.92	1.90	1.88	1.82	1.82	1.83
Adjoint	0.64	0.59	0.35	0.64	0.56	0.34
Total Denovo	2.57	2.49	2.23	2.46	2.38	2.16
Total MC	145.12	144.93	147.92	24.13	24.35	24.15
Total	150.25	149.91	152.38	26.59	26.72	26.32
MC Performance						
Batches	170	190	190	29	29	28
Particles (millions)	17	19	19	2.9	2.9	2.8
Time/Particle (ms)	30.73	27.46	28.03	29.95	30.23	33.84

Results

Three separate MAVRIC simulations were performed for each source, one for each reaction of interest used to generate variance reduction parameters (i.e., used as the adjoint source). For the benchmark source, the MC time was set to run for 24 hours in batches of 100,000 source particles. The simulation using the KENO-VI source was allowed to run for 6

days to better converge statistics, since preliminary results had a high error from the measured values. The C/E ratios for each reaction can be seen in Figure 18 through Figure 20. The ratios are sorted by axial location and a polynomial fitted line is overlaid. The line was introduced to demonstrate the error in the KENO-VI source distribution when compared with the one defined in the SINBAD benchmark. The KENO-VI source was found to have a larger buckling, which leads to higher reaction rates in the center of the core and lower reaction rates at the edges. Table 9 gives C/E ratios by reaction rate and location for each source distribution. The average C/E ratios ($\overline{C/E}$) are presented with an uncertainty ($u_{C/E}$) and a standard deviation (s). The uncertainty comes from averaging a group of MC tallies, each with its own uncertainty. The standard deviation demonstrates the spread within each group of individual tallies from the average C/E ratio. The results are presented as $(\overline{C/E} \pm u_{C/E}) \pm s$.

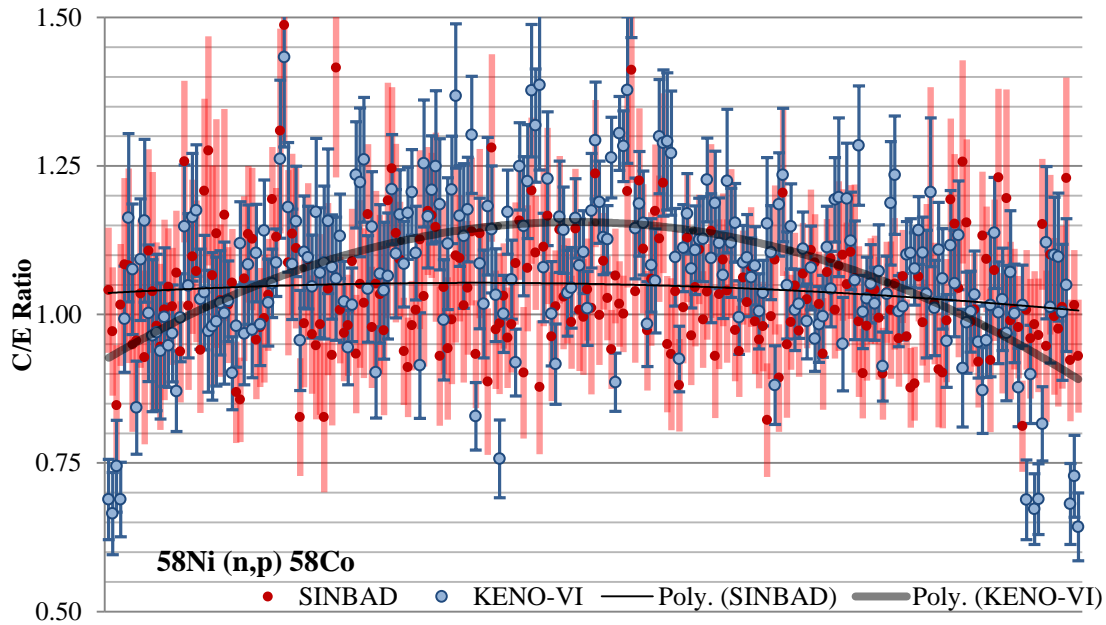


Figure 18. C/E Ratios for the $^{58}\text{In}(n, p)^{58}\text{Co}$ reaction.

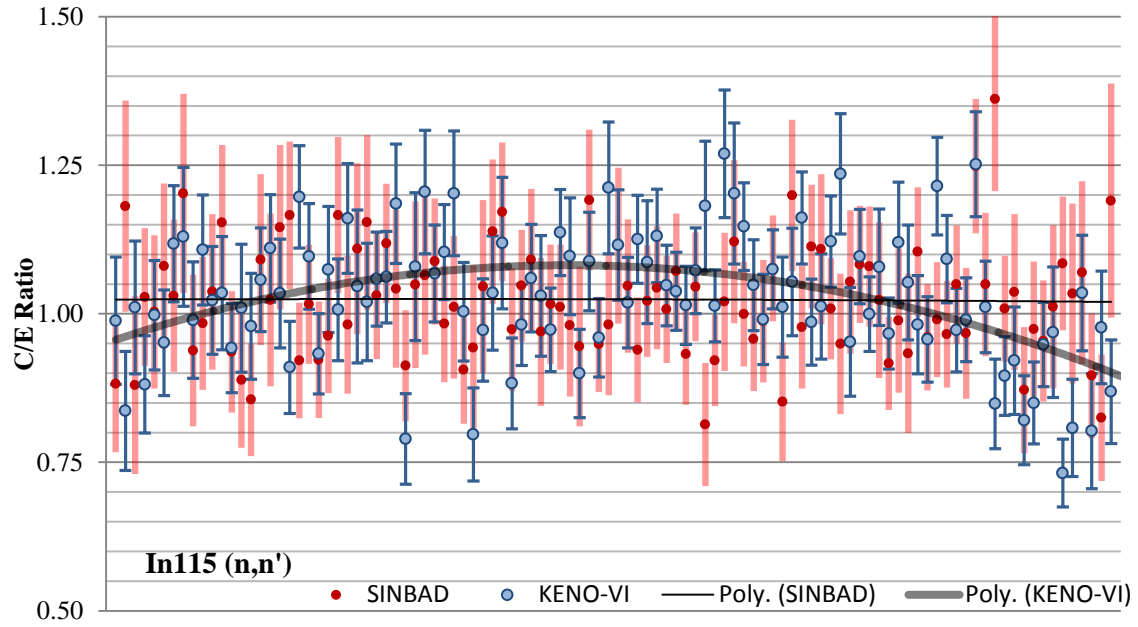


Figure 19. C/E Ratios for the $^{115}\text{In}(n,n')^{115\text{m}}\text{In}$ reaction.

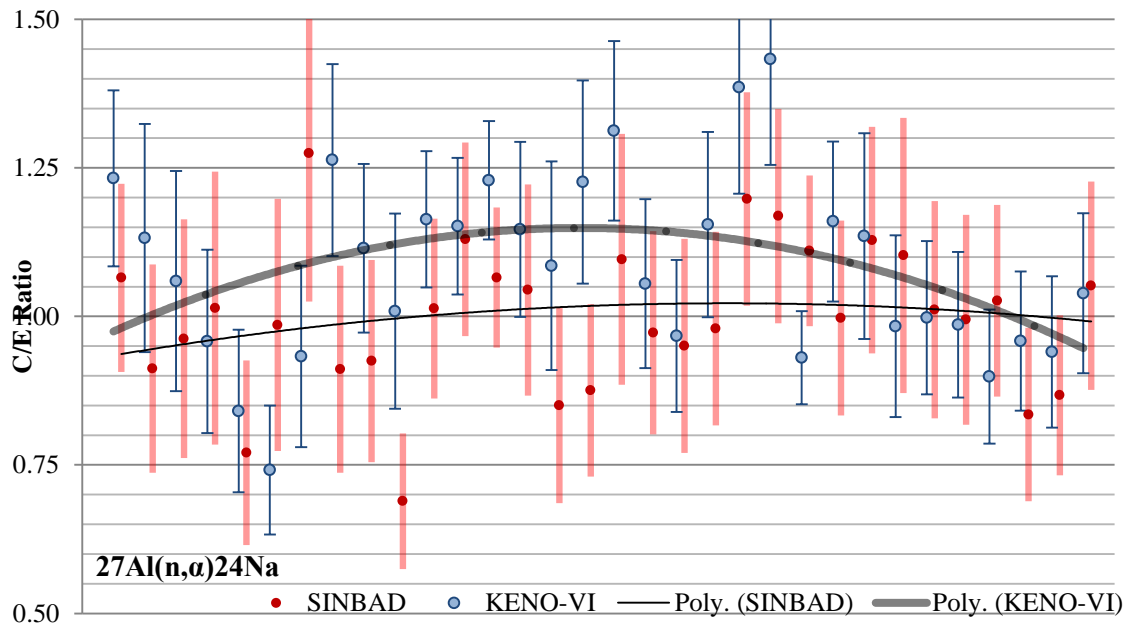


Figure 20. C/E Ratios for the $^{27}\text{Al}(n,\alpha)^{24}\text{Na}$ reaction.

Table 9. C/E ratios [$\overline{C/E} \pm u_{C/E} \pm s$] obtained from MAVRIC.

Region	^{58}Ni (n,p)		^{115}In (n,n')		^{27}Al (n, α)	
	KENO	BENCH	KENO	BENCH	KENO	BENCH
Inner Baffle	(1.16 \pm 0.08) \pm 0.11	(1.06 \pm 0.12) \pm 0.09	(0.99 \pm 0.08) \pm 0.13	(1.07 \pm 0.12) \pm 0.17	(1.05 \pm 0.09) \pm 0.12	(1.07 \pm 0.15) \pm 0.08
Outer Baffle	(1.10 \pm 0.06) \pm 0.11	(1.04 \pm 0.09) \pm 0.09	(0.98 \pm 0.08) \pm 0.12	(0.98 \pm 0.10) \pm 0.07	(1.13 \pm 0.10) \pm 0.17	(1.08 \pm 0.14) \pm 0.04
Core Barrel	(1.13 \pm 0.09) \pm 0.13	(1.07 \pm 0.12) \pm 0.12	(1.04 \pm 0.08) \pm 0.10	(1.03 \pm 0.11) \pm 0.10	(1.13 \pm 0.13) \pm 0.19	(0.98 \pm 0.18) \pm 0.14
Water Gap	(1.12 \pm 0.09) \pm 0.11	(1.06 \pm 0.13) \pm 0.11	(1.04 \pm 0.10) \pm 0.15	(1.02 \pm 0.13) \pm 0.10	(1.15 \pm 0.14) \pm 0.01	(0.98 \pm 0.18) \pm 0.07
PLSA	(1.03 \pm 0.09) \pm 0.13	(1.03 \pm 0.12) \pm 0.11	-	-	-	-
3.3% Fuel Positions	(0.99 \pm 0.07) \pm 0.14	(1.00 \pm 0.09) \pm 0.07	-	-	-	-
Average	(1.07 \pm 0.08) \pm 0.14	(1.04 \pm 0.11) \pm 0.10	(1.03 \pm 0.09) \pm 0.11	(1.02 \pm 0.11) \pm 0.10	(1.08 \pm 0.14) \pm 0.16	(0.98 \pm 0.18) \pm 0.14
Overall Average	KENO		(1.06 \pm 0.09) \pm 0.14	BENCH		(1.03 \pm 0.12) \pm 0.10

As summarized in Table 9, the average C/E ratios obtained using MAVRIC were (1.06 \pm 0.09) \pm 0.14 and (1.03 \pm 0.12) \pm 0.10 for the KENO-VI source and the benchmark source, respectively. The results obtained using the KENO-VI source have higher average C/E ratios, lower uncertainties, and higher standard deviations than those obtained using the source provided within the SINBAD benchmark. The majority of reaction rates being calculated were in the center of the core. Since the KENO-VI source had a higher buckling, those reaction rates were over-predicted leading to a higher average C/E ratio. The KENO-VI simulation was allowed to run longer, which is why the uncertainty is lower for the average value. Furthermore, the standard deviation is higher because again due to the different source distribution. Overall, each case validates the methodology for RPV dosimetry using the MAVRIC sequence.

CHAPTER 5

VHTR MODEL FOR SHIELDING ANALYSIS

Model Basis

Before discussing analyses of the different shielding studies with respect to the VHTR design, the model is presented for understanding of certain choices that were made. The model of the VHTR as implemented in the Scale6.1 package comes from the *NGNP and Hydrogen Production Preconceptual Design Studies Report* presented by General Atomics for the Battelle Energy Alliance, LLC, (Shenoy, 1997). Since it was in a pre-conceptual design phase there were aspects that are subject to change and others not yet developed. Therefore, some assumptions have been made that may not be valid for the final constructed model. Certain parts which were undecided upon are completely left out. The 600MWth, annular core is graphite-moderated and helium-cooled. The active region consists axially of 10 layers of prismatic blocks with the radial layout shown in Figure 21. Control rod positions can also be seen both inside and outside of the active region.

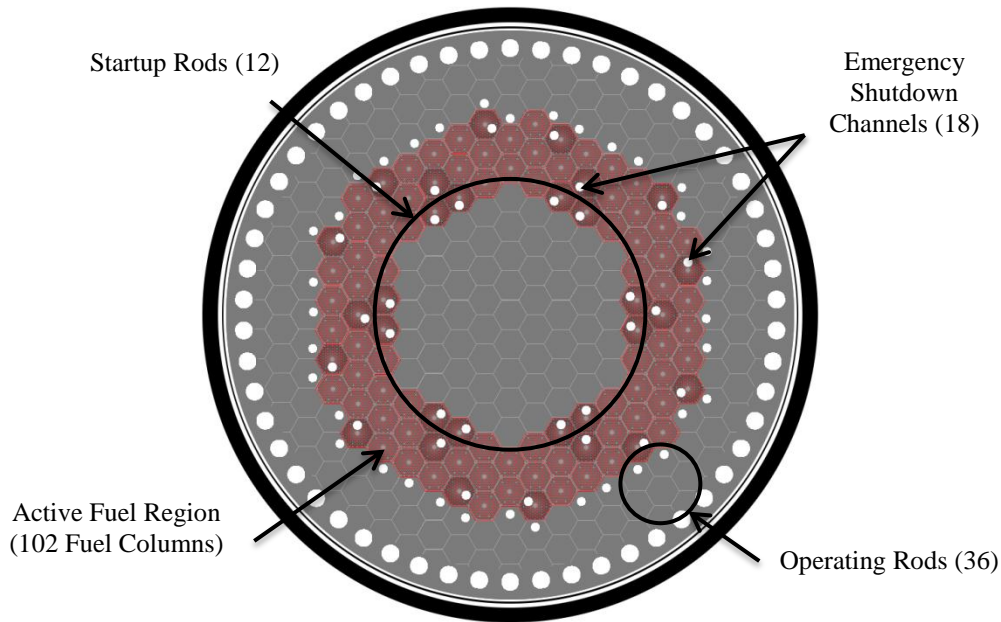


Figure 21. Cutout view of the core.

Fuel Type

The proposed fuel type was uranium oxycarbide microspheres which are coated with different layers of pyrolytic carbon and silicon carbide. The TRISO particles are then compacted into cylindrical fuel element and placed into a graphite matrix. Two types of particles would be mixed throughout the core and this distribution would change with each core reload, with one being a 19.8% enriched fissile particle and the other simply a natural uranium fertile particle. However, at the time of the design used the United States had no commercial TRISO pellet production capabilities. GA proposed acquiring TRISO pellets from Nuclear Fuel Industries in Japan, which has a limit of 10% enrichment and only produces pellets with UO_2 . The volume packing fraction is assumed to be 28.9% within a graphite matrix that has a density of 1.74 g/cm^3 . The fuel compacts have a radius of 0.6223 cm and a height of 4.93 cm (GT-MHR, 1996).

Since explicitly randomly defining hundreds of thousands of TRISO particles per fuel element is unrealistic in this model the fuel region was chosen to be homogenized. Doing so does not properly take into account the resonance self-shielding effects within the compacts due

to the layered particles (double-heterogeneity), so the cross sections within the fuel region do not provide a completely accurate representation of the fuel within the core. Since this is a shielding study, this in core-material cross sections are considered acceptable. Table 10 and Table 11 show the dimensions of the TRISO particles used and the final homogenized mixture used in the MAVRIC model.

Table 10. TRISO Particle Specification

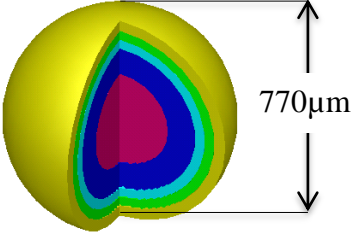
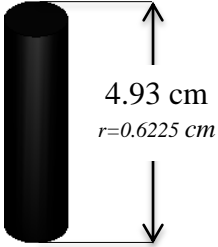
	<i>Radius (cm)</i>	<i>Density (g/cm³)</i>	
Fuel Kernel	0.0175	10.36	
Graphite Buffer	0.0275	1.0	
Inner Pyrocarbon	0.031	1.87	
Silicon Carbide	0.0345	3.2	
Outer Pyrocarbon	0.0385	1.83	

Table 11. Fuel Compact Homogenization

	<i>Weight Percent (%)</i>	
U-235	1.232	
U-238	11.084	
Oxygen	1.655	
Graphite	65.352	
Carbon	14.324	
Silicon	6.353	

Prismatic Fuel Blocks

As stated above the fuel blocks contain an array of compacts, coolant holes and burnable poisons distributed in graphite ($\rho_{\text{graphite}}=7.94 \text{ g/cm}^3$). The blocks are hexagonal prisms with a height of 79.4 cm and an apothem (the shortest distance from the center to the edge) of 18 cm. The coolant holes ($\rho_{\text{helium}}=0.00359 \text{ g/cm}^3$) are distributed so that there is 1 coolant channel for every 2 fuel compact channels. At each corner there is a hole for a Lumped Burnable Poison (LBP) and the center has a hole for handling the elements, which are filled with graphite plugs. The 6 coolant holes around the center fuel-handling hole have a radius of 0.635 cm. The normal

larger coolant holes have a radius of 0.794 cm. Also there are 4 positions on each block where a dowel socket is inserted at the top and bottom. The dowel ensures that the stacks of blocks remain aligned at all times for smoother helium flow. Under these positions are shorter cylinders for fuel compacts. Additionally there are different fuel blocks containing holes for the insertion of control rods with a radius of 10.16 cm. Figure 22 and Figure 23 show the dimensions for both fuel blocks (Shenoy, 1996).

From Figure 22 and Figure 23 it is easy to see that each block is an array of smaller units. Therefore, there are 6 units that make up the basis of every fuel block. Note that the burnable poisons were not included in this model since the design did not specify material or distribution within the core. The material for these will be mainly comprised of graphite with B_4C . The purpose of burnable absorbers in the design is to flatten the power peaking within the annular core. The power peaking is most severe in the center of the fuel annulus, which is where it would be expected to have the highest amount of boron absorber. Additionally, different core loads would be expected to have different distributions. In the model each LBP was filled with graphite.

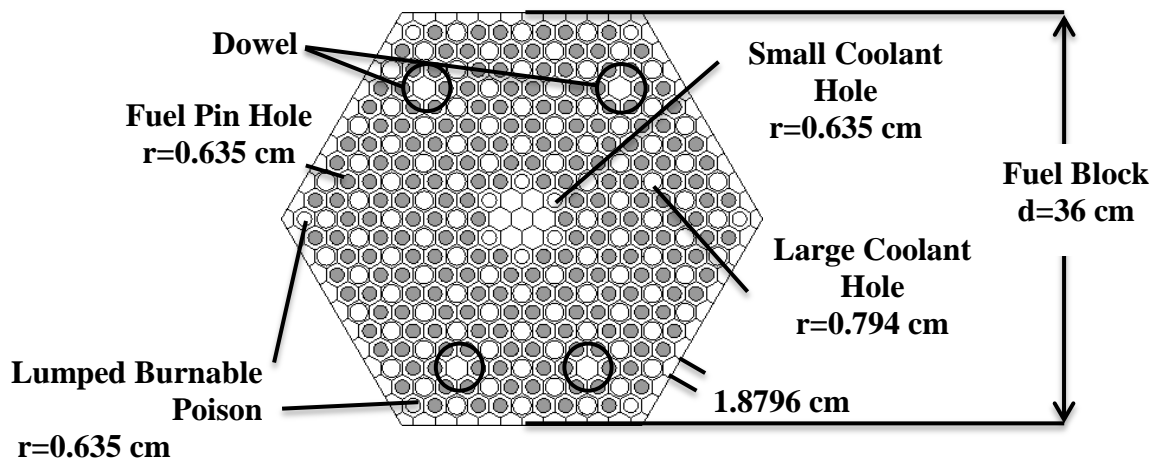


Figure 22. Standard fuel block layout with dimensions.

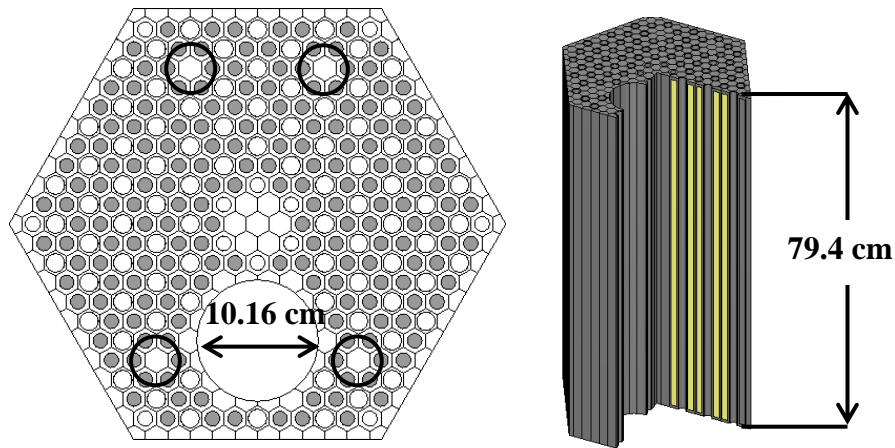


Figure 23. Fuel block with hole for control rod insertion.

Graphite elements surrounding the active region define the middle, outer and bottom reflector areas. Middle and outer components are solid graphite elements, with some containing insertions for operation rods as defined in Figure 21. The bottom reflector blocks extend the helium channel layouts of those blocks directly above. Elements in the bottom reflector directly below outer and central reflector regions will be solid graphite. Elements in the bottom reflector directly below active regions have the same geometric layout to match the helium channels, but fuel regions are filled with graphite. The blocks are separated by a 1mm helium gap that is included in the model and also allows for the units to be rotated within the SGGP without losing particles during simulations due to overlapping boundary issues.

Control Rods

The control rod distribution in the core can be seen in Figure 21. Note that the rods are generally bunched in groups of 3. Center bundles leave one hole available for dumping boron balls for emergency shutdown scenarios. The 2 remaining holes are for insertion of control rods. The control rods are annular for heat transfer reasons, and should be sheathed in thin layer of Inconel 880H which was not included in the model. The rods are made of B_4C granules in a graphite matrix formed into compacts, similar to the fuel pins. The compacts are 40% B_4C by weight, and the B_4C is enriched to 90% ^{10}B . The remaining 60% is graphite. The 12 rods of the

inner ring are shutdown rods that will be completely removed on startup. The outer 36 rods in the graphite reflector will be used during operation to control reactivity effects over the lifetime of each reload. The remaining control channels would be filled with boron balls in an emergency situation.

The model was designed to allow easy motion of the control rods with minimal change to the input of the file. Due to the complex assortment of arrays within units of the core, it proved to be complicated to allow for this motion without almost tripling the number of units for the core. In order to insert a rod all the way through the core to any position, the prismatic block units of the core array (shown in Figure 24) were stacked vertically in order to encompass from the upper core restraint through the bottom reflector. By doing this one unit could be rotated throughout the core allowing for a given level of operational rod insertion by only changing one number in the input file. By building these units axially through the entire core, within each unit a control rod can be inserted completely through all of the layers without having any particle tracking issues. Changing one unit causes all startup rods to be taken out or all operating rods can be adjusted to any given position. A height of 0 would mean that the rod was completely inserted through the active region. At a height of 794 cm, the rods are out of the core but still within inlet. A height of 963.1 would mean that the control rods are completely removed from the core barrel. Note that this change only works in the MAVRIC sequence and causes runtime issues in Keno-VI when developing the fixed-source, mesh-based fission distribution.

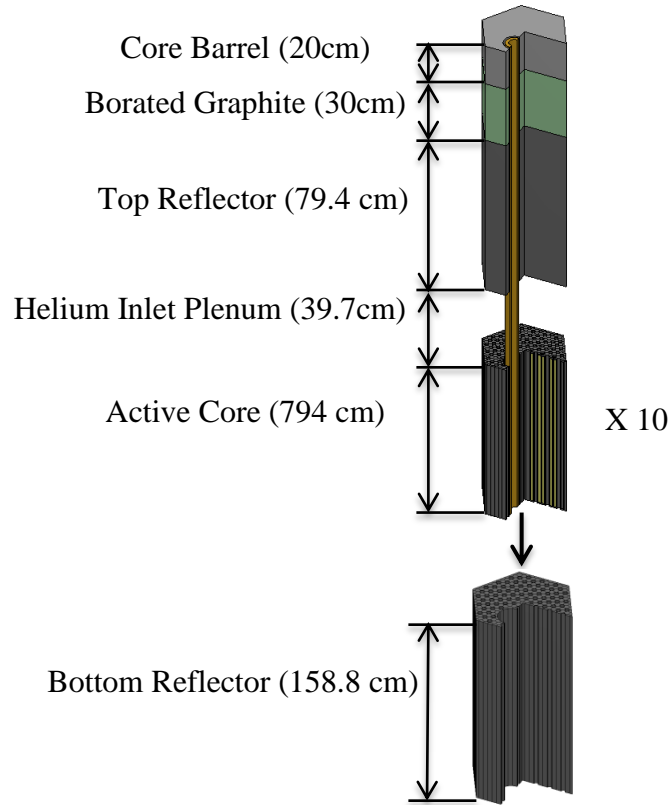


Figure 24. Control Rods inserted through the entire core.

The core is then inserted into a unit including the upper core restraint, a layer of borated graphite and the helium inlet plenum directly above the active core. The material description for the borated graphite layer was not specified and is not included in the model. Recently, the Generation IV International Forum increased the desired inlet temperature by 100K, and using the original helium inlet flow configuration more heat would be transferred to the core vessel than is desirable. By having the helium enter directly above the active fuel region steady-state pressure vessel temperatures returned to acceptable levels. The new design would require support columns inside the inlet plenum above the core, which are not included in the model. Figure 25 shows the new inlet plenum design with the outlet plenum configuration.

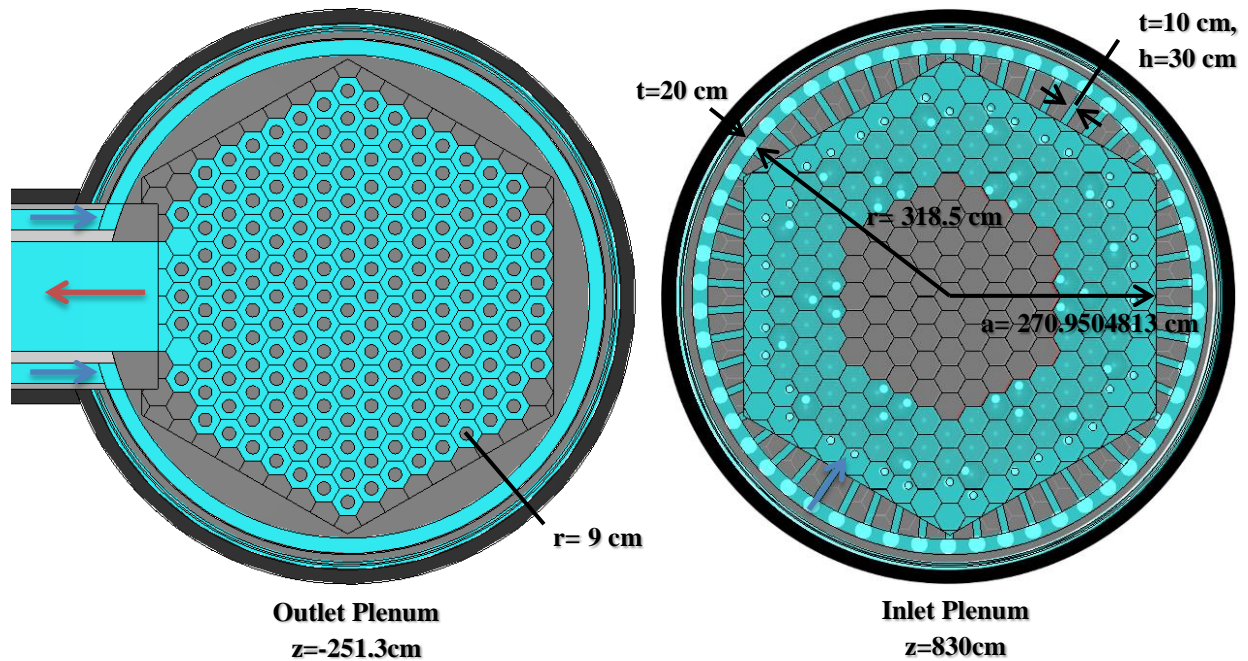


Figure 25. Helium outlet and inlet geometries showing the reconfigured design.

The cross vessel between the RPV and the Power Conversion System (PCS) is assumed to only be made of Incoloy 800H. In actuality there would be an extra layer of insulation between the two. This insulating material was not included in the design report and thus not in the model used for this study. The dimensions are displayed in Figure 25.

Core Barrel

With all the intricate details of the core modeled, it can be arrayed into an overall unit of the core, which is then placed into the global reactor barrel unit. The core is a very simple unit, but its outer hexagon is extended only to include the outer control rods, and the graphite outside the outer permanent reflector is then assumed to be solid graphite with no helium gaps in between blocks. Figure 26 more readily demonstrates the complication of the helium inlet and shows how everything is compiled. The steel used for the core barrel and inlet and outlet helium ducts was assumed to be Incoloy 800H. The material composition is shown in Table 12.

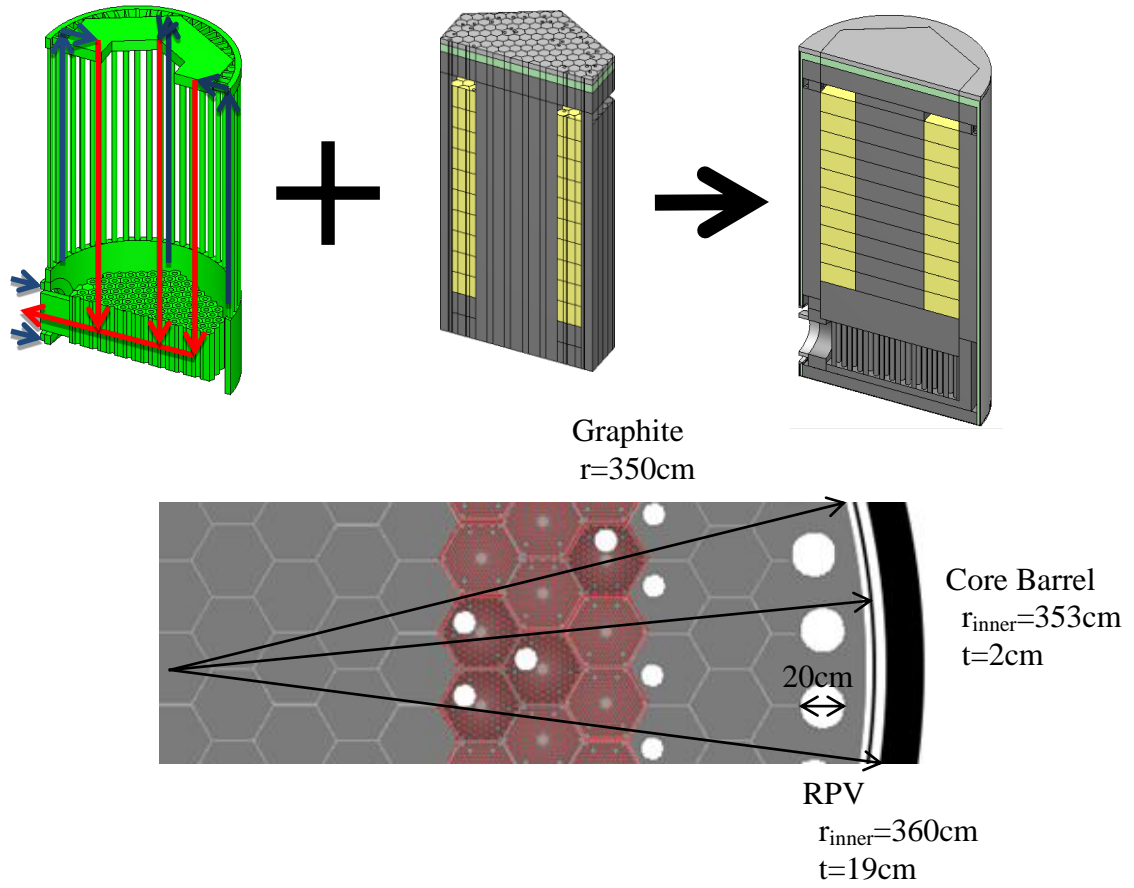


Figure 26. The helium circulation within the core barrel. Also the dimensions for the graphite, core barrel and RPV.

Table 12. Material Compositions (wt%)

	9Cr-1Mo-V	Incoloy 800H	ECS	EXC
$\rho(g/cm^3)$	8	7.95	1.98	0.501795
H	-	-	-	20
He	-	-	75	-
C	0.1	0.08	-	-
¹⁴ N	0.049	-	-	-
O	-	-	-	79.95
²⁷ Al	0.034	-	-	-
Si	0.38	0.35	-	-
³¹ P	0.02	0.02	-	-
Si	0.002	-	-	-
Ti	-	0.4	-	-
V	0.18	-	-	-
Cr	8.1	21	-	-
²⁵ Mn	0.46	1	-	-
Fe	89.352	44.85	25	0.05
Ni	0.33	32	-	-
Cu	-	0.3	-	-
⁹³ Nb	0.073	-	-	-
Mo	0.92	-	-	-

Reactor Pressure Vessel (RPV)

The RPV contains the reactor internals and support structures. It would be built in three distinct segments which provided a good separation for units within the model. The three components start with the main cylindrical section with an upper and lower hemispherical head mounted to each side. The lower head contains the Emergency Shutdown Cooling System and is sealed to the main cylindrical section surrounding the core barrel. The upper head contains penetrations for the control assemblies and is sealed to the main cylinder by a blind flange.

Figure 27 shows the dimensions used in simulated the model with Scale.

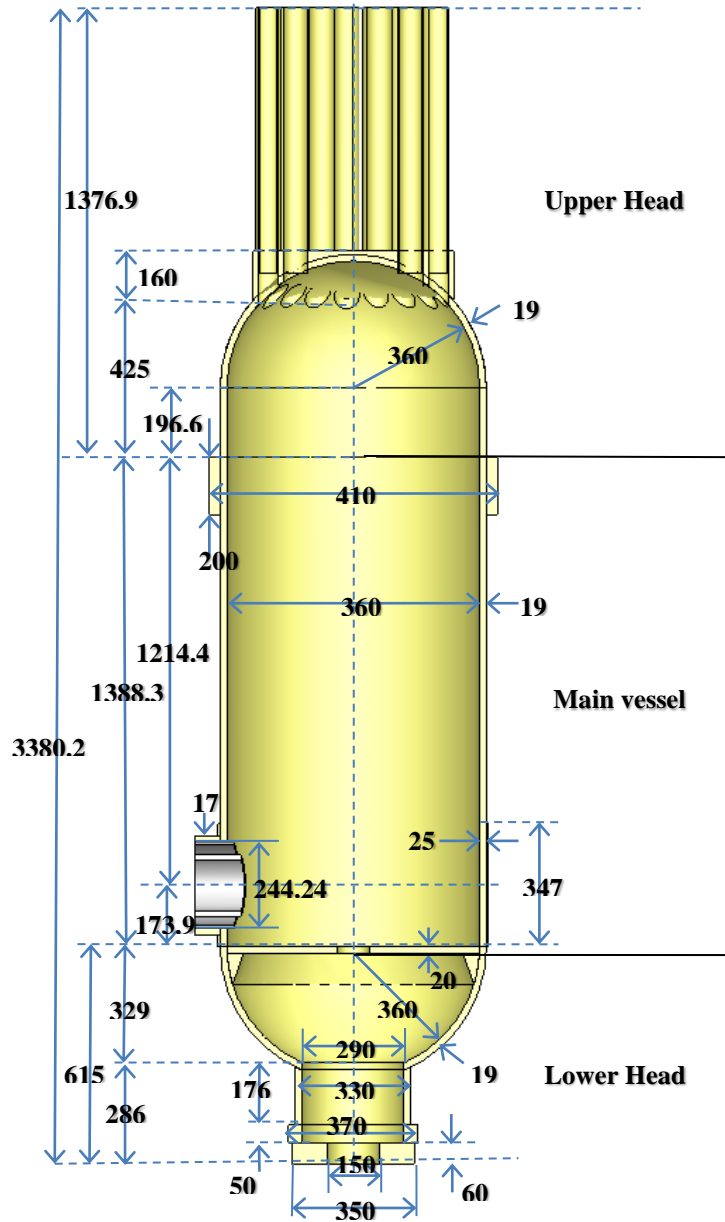


Figure 27. Dimensions for the RPV showing the three separate sections. (all units are given in cm)

Furthermore, the control rod assemblies located in the upper head must be aligned with control rod channels in the core. Assemblies were assumed to be organized into cylindrical bundles containing two or three assemblies. The bundle is centered on the average assembly position within the bundle. Four main control assembly bundles were modeled as separate units as shown on the right in Figure 28. Each unit is positioned within the RPV upper head

maintaining proper alignment with the core channels. A top view of the upper head is given in Figure 28 showing how each bundle is rotated for each of the six regions. Table 13 and Table 14 provide the data for positioning each control assembly and bundle within the different units.

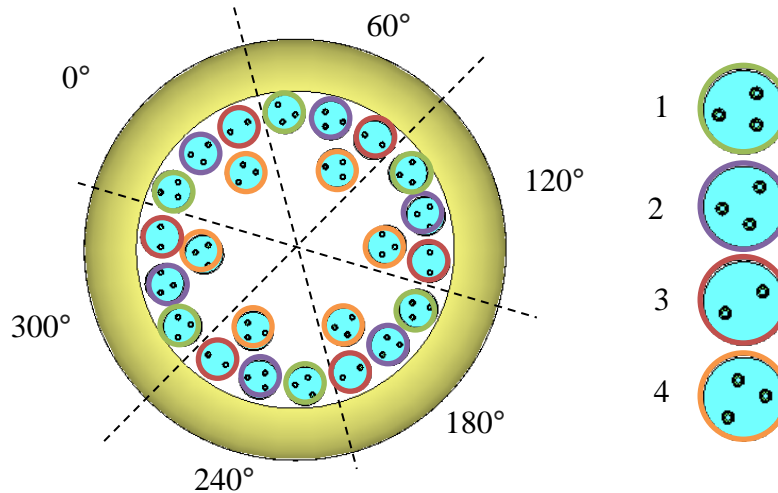


Figure 28. The positions of control rod assemblies in the upper head.

Table 13. The location (cm) of each control rod relative to the bundle as shown in Figure 28.

1		2		3		4	
x	y	x	y	x	y	x	y
13.23752739	16.42397667	15.63175854	9.025	4.788462304	-14.79795333	10.42117236	-11.54590667
4.788462304	14.79795333	15.63175854	9.025	13.23752739	16.42397667	10.42117236	14.79795333
18.02598969	1.626023333			-18.02598969	-1.626023333	-20.84234472	-3.252046667

Table 14. The bundle locations (cm) relative to the upper head as shown in Figure 28.

	1		2		3		4	
al	x	y	x	y	x	y	x	y
0°	-220.816727	106.673977	-169.555113	172.369883	-100.973245	220.74693	-89.0020889	137.895907
60°	-202.790737	-137.895907	-234.054254	-60.6540933	-241.659072	22.92807	-163.922403	-8.13011667
120°	18.0259897	-244.569883	-64.4991414	-233.023977	-140.685827	-197.81886	-74.9203138	-146.026023
180°	220.816727	-106.673977	169.555113	-172.369883	100.973245	-220.74693	89.0020889	-137.895907
240°	202.790737	137.895907	234.054254	60.6540933	241.659072	-22.92807	163.922403	8.13011667
300°	-18.0259897	244.569883	64.4991414	233.023977	140.685827	197.81886	74.9203138	146.026023

Power Conversion System

The power conversion vessel is located in the adjoining room of the reactor within the reactor island. Great detail is provided for the internal components including the turbomachine, recuperator, precooler, intercooler and shrouds. For shielding studies these internal components are not necessary to be accurately modeled, since this part will have effectively zero influence on quantities being simulated. The outer vessel containing the system is modeled. The internal is a homogenized mixture based of the overall weight of components assumed to be within the reactor. The material description was 25% iron and 75% helium outlet flow from the core with a density of $\rho=1.98\text{g/cm}^3$. The structure for the PCS Vessel is assumed to be Incoloy 800H.

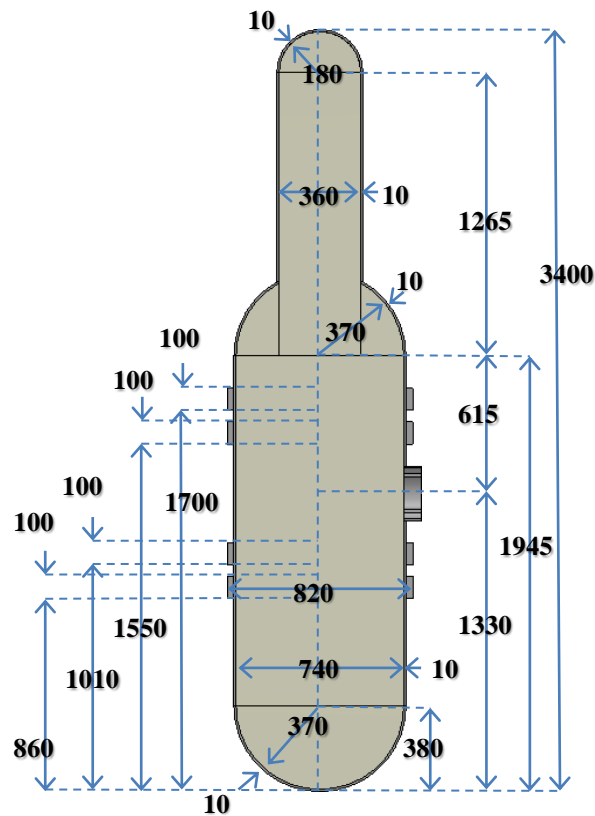


Figure 29. Assumed dimensions (cm) defining the Power Conversion System.

Plant Layout

The data providing the dimensions for the rest of the plant layout is not defined in the Preconceptual design report. Therefore, the rest of the model has been based off extrapolating dimensions and assuming wall materials to be concrete. Newer designs may have significant changes. However for the purpose of demonstrating MAVRIC with respect to an HTGR, the dimensions are not as important as the performance of the code and the subsequent lessons learned.

The remainder of the facility was taken from stock photographs representing the VHTR design, and scaling known dimensions to obtain unknown dimensions (Baccaglini, 2003). Figure 30 shows a comparison of the final model with the image used for extrapolating dimensions. Thicknesses of concrete were estimated as well as floor levels. Many of the secondary systems such as piping has not been included in the model, which should be a fine assumption, if not conservative. Figure 31 and Figure 32 show the assumed dimensions for the model of the VHTR power plant used in MAVRIC.

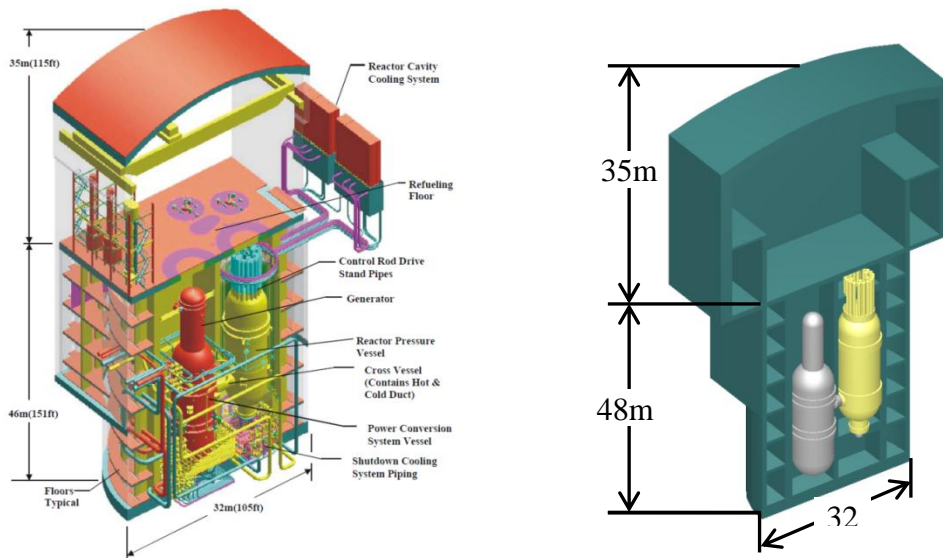


Figure 30. VHTR facility used to extrapolate dimensions (Baccaglini, 2003) (left). Final VHTR Model implemented in MAVRIC (right).

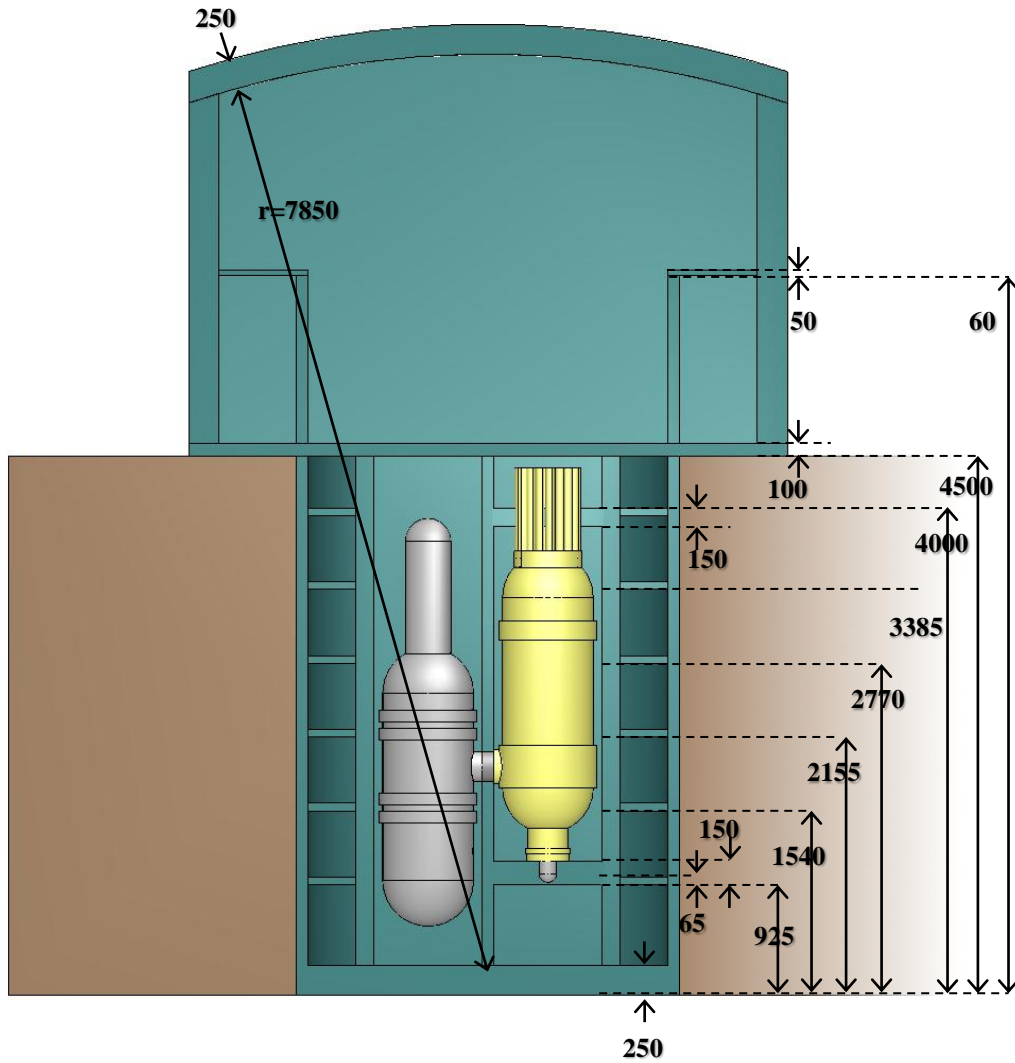


Figure 31. Front view of the VHTR power plant with dimensions axial (cm).

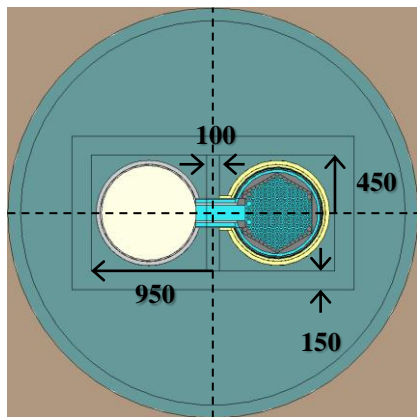
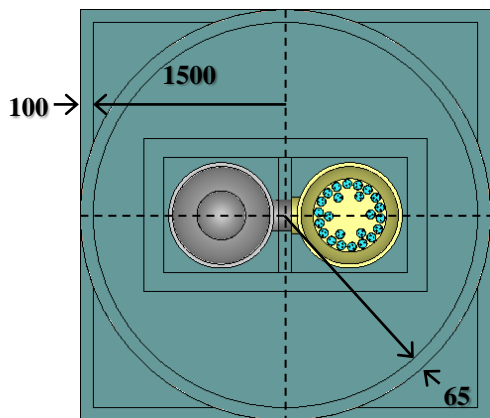
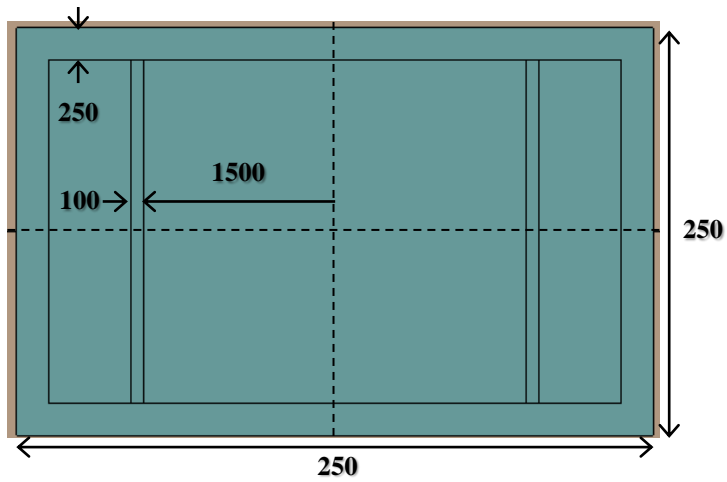


Figure 32. Top view of the VHTR power plant at different axial levels with dimensions (cm).

Preliminary Studies

Before beginning analyses of specific radiation indicators in the VHTR, a few preliminary studies were performed to verify the integrity of the model and to potentially optimize certain variance reduction. The first of the two studies dealt with how the flux spectrum leaving the core barrel would change with different levels of homogenization. Ideally, the change in the spectrum would be negligible and the simulation's CPU time would drastically decrease to obtain similar results. The second study analyzed the achievable improvements in MAVRIC performance that could be obtained while working within the workstation's memory limitations. Using a parallel version of Denovo would ideally improve the deterministic model used to bias particles.

Impact of Core Homogenization on MAVRIC Results

The majority of shielding calculations are concerned with the neutron or photon flux outside of the core barrel. Shielding studies may make large assumptions to simplify models so that methodologies can be more easily implemented. The general idea is that the larger the distance from the active source to the shielding parameter being calculated, the less important precise descriptions of core geometry and the fixed source become. Therefore, homogenizing the core description or source will have little effect on end results. Applying different levels of core homogenization within the VHTR model to achieve speedups when finding the neutron flux outside of the core barrel was analyzed in MAVRIC.

In the given model, different homogenization levels of the core can be easily achieved by manipulating a few units. Therefore, the majority of the content of each input is the same between models. Starting with the very basic units comprising the core, the homogenization was extended through all the helium coolant peripherals. At each level the speedup and deviation from the least homogenized version were calculated. The least homogenized version as described before does not take into account the TRISO particles and considers fuel elements to

be a homogenized mixture. It is important to note that neutrons are being sampled from the same source throughout each case, so they are born at roughly the same spatial distribution. The only slight deviations that occur are due to the way in which the mesh source overlays homogenized geometries.

Different Levels of Homogenization

A. Only Fuel Pins (02normal)

Technically the first level of homogenization is the fuel pins as stated previously. It would be too cumbersome and slow to model each individual TRISO pellet since they are less than a millimeter in diameter. Also as mentioned before the cross sections in doing this will not be completely accurate because they do not take into account resonance self-shielding effects, which primarily affects the fast spectrum.

B. Fuel Block Elements (03elements)

The second simplification is homogenizing individual elements that comprise the fuel blocks with the immediate surrounding graphite as shown in Figure 33. The fuel blocks still retain a relatively accurate geometry in terms of the materials within less than a 2cm accuracy. Where there was a coolant hole, for example, there will now be a solid graphite hexagon with a small amount of helium resulting in decline in density. Also, new materials are ascribed to each new unit. Only the blocks have changed so the global unit stays the same.

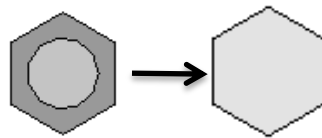


Figure 33. Media cards demonstrating the first level of homogenization.

C. Only Individual Fuel Blocks (04fuelType)

Next, entire prismatic fuel blocks are homogenized into one solid material as seen in Figure 34. There are still separate units for those with or without control rod insertions. These holes will simply result in a less dense material, but since the helium gas has such a low density

it is not a very dramatic effect. Also the model leaves insertions for control rods at this level. Therefore, it is not necessary to have separate units without and without control rods, because the rods will still be inserted in the geometry.

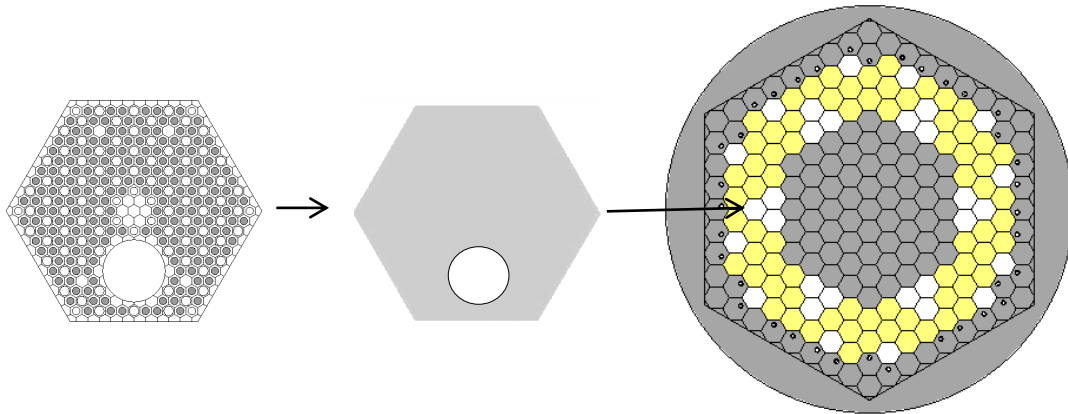


Figure 34. Each graphite block is homogenized leaving only control rod channels as unhomogenized regions.

D. Homogenized Core Blocks (05fuelTotal)

The next step is closer to an intermediate step between two levels. It has the exact geometry from above, except that each individual fuel block is homogenized with the rest so that there is a uniform material over the entire active region, instead of some blocks having different densities.

E. Homogenized Core (06volumeRing)

The last homogenization of the active core is making the entire region one solid annular hexagon. This level keeps the same volume and mass of the active region, which creates an issue with the source distribution being used. Since the fission density is meshed over the original geometry, the new active region does not encompass the entire source region. Consequently neutrons will no longer be born in these regions, but overall the same amount of neutrons will be sampled. This only occurs on the fringes, due to the original jagged nature of the line of the core's border formed by hexagons, which can be seen in Figure 35.

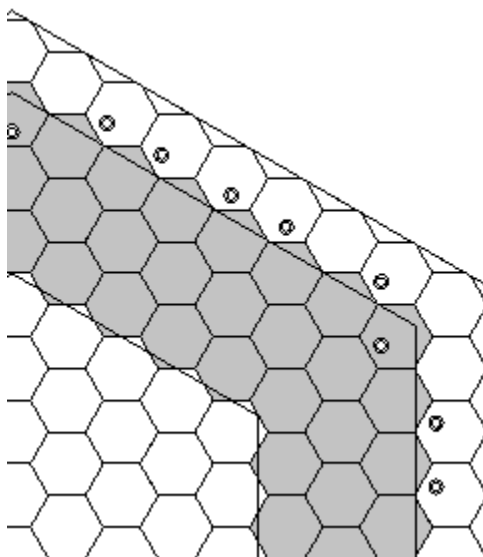


Figure 35. Notice the areas where the lines of the fuel blocks intersect with those of the simplified core new core.

F. Reflector Coolant Holes (07rodsRing)

Once again this step can almost be considered an intermediate step, but it is the first level that homogenizes a region outside of the active core. Now the operational rod channels are homogenized, which are immediately outside of the active region in the replaceable side reflector. This is the region in Figure 35 that is just outside of the active region, which is denoted by the grey area. Also, notice once again that some of the fuel region does intersect here, but is not included in the material description. The area is homogenized based on the volume of graphite, helium and control rod insertion within the region. Boron is spread over blocks containing control rods.

G. Helium Riser, Inlet and Outlet Plenum (08peripherals)

The last region to be homogenized mainly entails homogenizing the complex geometry that have to do with the helium coolant flow in both the inlet and outlet plenums as well as the bottom reflector.

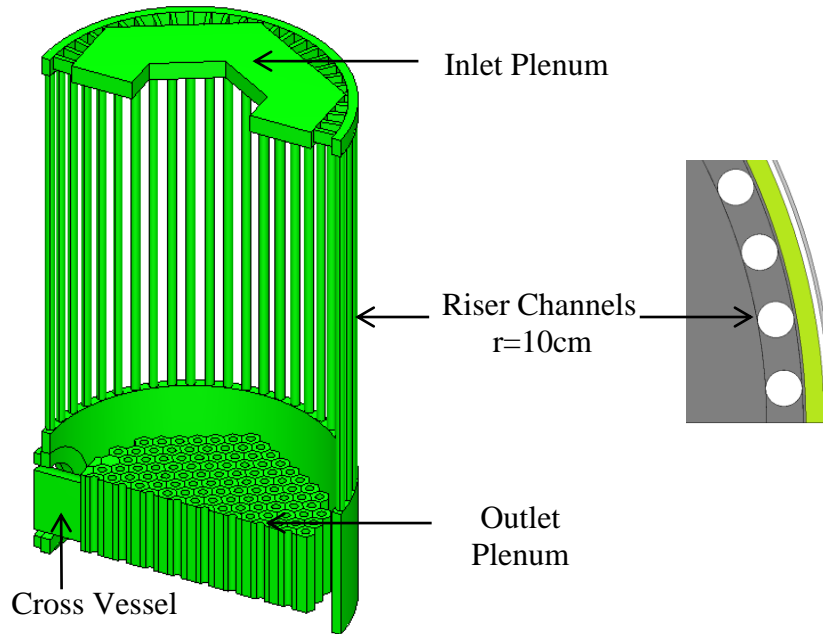


Figure 36. All of the different levels of helium coolant homogenization. Not included is the coolant flow through the bottom reflector, directly above the outlet plenum.

H. Core Barrel (09coreBarrel)

Finally, the last model simply combines all the peripherals and the core being homogenized. The previous level, used the original core so that the time and preservation of the flux could be determined relating to the outer parts independent of what was changed inside the core.

Results

As stated before, the goal was to determine what level of homogenization provides the best speedup with sufficiently accurate results. Therefore, each level must be compared for both accuracy and speed against the reference cases.

First and foremost the run time for each case was analyzed. Without any significant increase in speed, there is no reason to spend time homogenizing. If the fixed-source is calculated using the detailed model anyway, than homogenization requires added modeling time. Table shows the average time for a batch of 100,000 particles to run in Monaco. These are

biased runs using Forward Weighted-Consistent Adjoint Driven Importance Sampling (FW-CADIS).

Table 15. Run Times

Case	Folder Name	Avg. Time (minutes)	Speedup
A. Only Fuel Pins	02normal	3.188	0%
B. Fuel Block Elements	03elements	3.134	2%
C. Only Individual Fuel Blocks	04fuelType	3.034	5%
D. Homogenized Core Blocks	05fuelTotal	2.989	6%
E. Homogenized Core	06volumeRing	2.567	19%
F. Reflector Coolant Holes	07rodsRing	1.991	38%
G. Helium Riser, Inlet and Outlet Plenum	08peripherals	1.158	64%
H. Core Barrel	09coreBarrel	0.707	78%

From the Table 15 it is clear that the maximum speed up by homogenizing within only the core decreases the average run time by no more than 20%. On the other hand, by homogenizing everything else outside the core but within the core barrel, the time decreases by 64%, which is much more significant. Since the newly designed helium flow takes on a more complicated form with different channels instead of being an area of solid helium flow, Monaco has to track particles through many extra geometric bodies. When everything through the core barrel is homogenized, the speedup becomes 78%. Therefore, there is a significant potential for speedups, but still less than an order of magnitude.

The main goal of any simulation is to obtain accurate results (i.e., results of certain required accuracy). Doing it efficiently is the secondary goal, which cannot compromise the first. Thus, acceptable homogenizations should preserve the spectral shape and the magnitude of the flux leaving the core. In order to evaluate this, a flux map over the core barrel is attained for each level of homogenization, and the specific results are compared.

Using the new cylindrical mesh tally available in Monaco, it is possible to obtain the flux spectrum over the entire circumference of the core barrel. Since the borated graphite before the very edge of the core barrel had an unknown composition, the media for control rods is used. Surely the absorber will be significantly less enriched in B-10, so the flux was analyzed directly

before this point and at two other points closer radially to the center of the core. Figure 37 through Figure 39 present results from all levels of homogenization at these three radial positions.

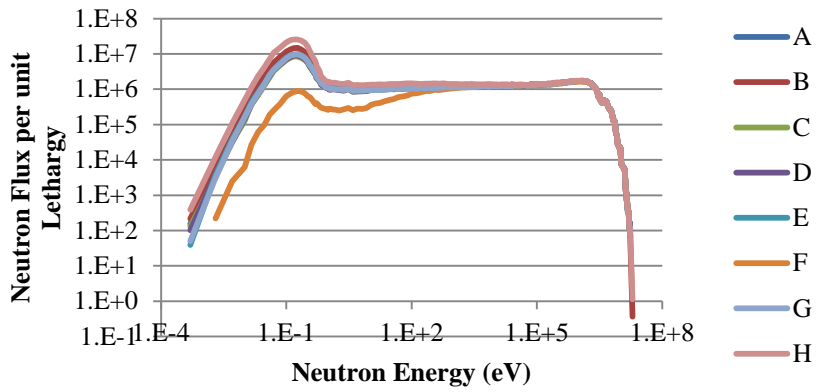


Figure 37. Lethargy plot at a radius of 253 cm.

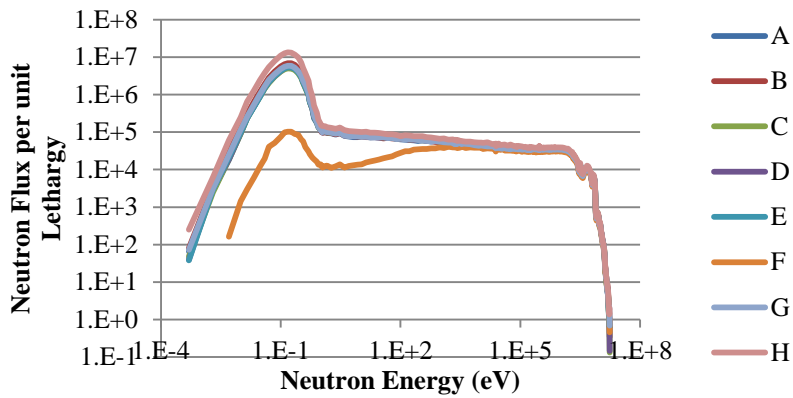


Figure 38. Lethargy plot at a radius of 300 cm.

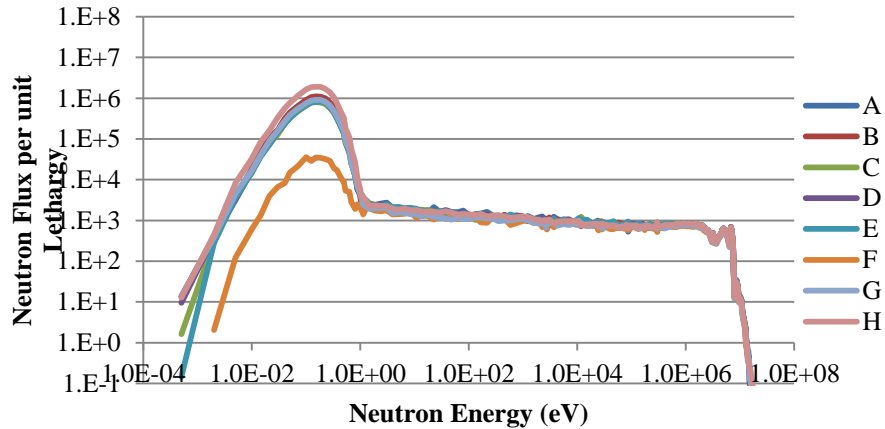


Figure 39. Lethargy plot at a radius of 335 cm.

The flux diminishes with distance from the core, which is more pronounced in the fast spectrum leading to a more thermal flux. From Figure 37 through Figure 39, different levels of homogenization, the spectrum is only minimally impacted for energies above $\sim 1\text{keV}$. With the exception of case F, there is also small change between the epithermal and thermal ranges. The most obvious deviation is in case F, which is the level where the control rods immediately outside the core in the outer reflector region are homogenized. The part of the spectrum with strong deviations is in the thermal and epithermal region below 1keV , where the fluxes are reduced by over one order of magnitude due to this homogenization. The reason for the drastic change comes from homogenizing the boron absorber in the control rods. When the absorber becomes distributed evenly around the entire region, self-shielding effects are significantly reduced and all boron from each rod is essentially seen by the entire flux leaving the core and not just the flux hitting the front surface of the annular rods. For this reason a greater amount of thermal neutrons are absorbed. By removing the dataset F, it can be noted that all thermal peaks are within a factor of 1.3 of the reference case. A quantitative comparison is given in Table 16 which lists the error in each case with respect to the reference.

Table 16. Error in total flux due to homogenization, at a radius of 335 cm

Case	Folder Name	Total Flux	Error
A. Only Fuel Pins	02normal	7.44e6	0 (reference)
B. Fuel Block Elements	03elements	7.66e6	+3.0%
C. Only Individual Fuel Blocks	04fuelType	7.10e6	-4.6%
D. Homogenized Core Blocks	05fuelTotal	7.75e6	+4.2%
E. Homogenized Core	06volumeRing	7.34e6	-1.3%
F. Reflector Coolant Holes	07rodsRing	4.49e5	-94%
G. Helium Riser, Inlet and Outlet Plenum	08peripherals	8.06e6	+8.3%
H. Core Barrel	09coreBarrel	8.40e6	+8.9%

The flux until now has been evaluated only at the center of the core axially. It is also important to consider variation that may arise in the flux in the z-direction. Figure 40 shows the flux in the z-direction for the reference case and that of the full core homogenization. Within the axial bounds of the active region (0-794 cm), the flux is preserved very well. The significant discrepancies in the fluxes above and below are due to homogenizing the bottom reflector coolant holes, and the inlet and outlet plenums. Depending on the area of interest, this may or may not be acceptable.

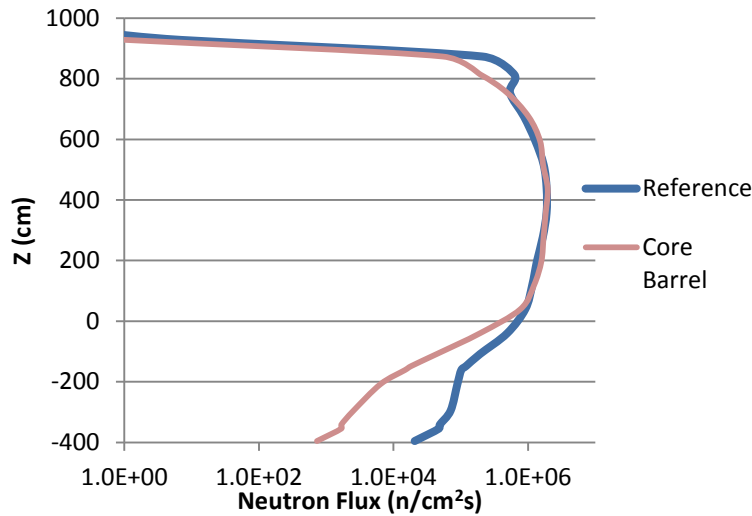


Figure 40. The neutron flux in the z-direction for the reference case and with all levels of homogenization.

Conclusion

From the spectrums and flux maps considered above, the only level of homogenization which really had a drastic effect on the spectrum was from homogenizing the control rods in the

reflector immediately outside of the active fuel region, case F. The main part of the spectrum with strong deviation is in the thermal and epithermal region below 1MeV, where the fluxes are more than one order of magnitude different (lower) over the spectrum. The reason for the drastic error for this level comes from homogenizing the boron absorber in the control rods. When the absorber becomes distributed evenly around the entire region, self-shielding effects are ignored and all boron from each rod is essentially seen by the entire flux leaving the core and not just the flux hitting the outer surface (shell) of the annular rods. For this reason a significantly greater amount of thermal neutrons are absorbed. This step provided some speed up (~20% compared to the previous level E), noticeable but hardly important, and certainly not acceptable from the accuracy standpoint.

The first homogenization level, A, is assumed necessary and taken as the reference. The next three homogenization levels, B-D, result in less than 5% loss of accuracy, for the total leakage flux integrated over the considered radius, but the speed up is negligible, below 6%, and local errors are possibly higher. Core homogenization, case E, provides a speedup of ~15% by itself, or ~19% when combined with all previous levels. The concern is that a miss-match between the core and fission source may cause higher local errors. Homogenization of the control rods holes in the reflector, Case F, drastically changes results, and is unacceptable. Homogenization of the complex helium flow geometry does speed up the simulations, almost by a factor of two. Its impact on the average core leakage flux is not large (within 10%), but since it removes detailed modeling of potential streaming paths, its impact on the detailed results radially farther out is expected to be non-negligible. Similar reasoning applies to Case H.

Overall, homogenization levels B and C may be acceptable since they preserve the individual position, shape, and average characteristics of each prismatic fuel block. The associated small speed up is probably not worth the small loss of accuracy, but it may be justified in preliminary analyses since it simplifies model development and the need for detailed

information, and potentially could reduce computer memory requirements, which may be significant in some cases. Level G seems to provide the largest individual gain in speed up, but further careful analysis is needed to establish the upper bound of the local error that it may cause. Use of other homogenization levels does not seem justified or acceptable.

Using Parallel Denovo for Speedups and Better Variance Reduction

The Denovo code is used in the MAVRIC sequence to complete the deterministic forward and adjoint portions of the simulation used for biasing particles. A version of the Denovo code was installed on the cluster allowing for the code to be ran in parallel. When running MAVRIC it can be told to only perform part of the simulation, leaving the Denovo inputs which can then be ran in parallel to eventually obtain the adjoint flux. MAVRIC will then take that flux and create the importance map for biasing particles in Monaco. Using the code in parallel requires the user to execute 5 commands at different points in the simulation as inputs are passed between codes. The goal of solving the deterministic portion of the equation is to reduce the wall-clock time of the overall simulation. Depending on the size of the problem, the speedup could be negligible compared to the total time for MAVRIC to execute and thus a serial version of the code could be sufficient. Therefore, speedups from parallel should be assessed to determine whether it is helpful in reducing simulation times.

Taking a problem space of the reactor room, the forward and adjoint fluxes were solved using Denovo on different meshings and number of CPUs. Using the same model, Denovo was solved using 1.8, 3.4, 6.3, 9.0, 12.3 and 24 million voxels. For each meshing, the adjoint and forward flux was solved using 1, 4, 16 and 64 CPUs. For the 12.3 and 24 cases, the simulation could not run in serial mode on 1 CPU due to memory limitations. The times for each case are given in Table 17 along with the meshing schemes. The total is given in terms of time required to create the input file for Denovo and then the actual solving time. On the largest meshing the

time required for Denovo only on 16 CPUs was equal to that of the smallest meshing on 1 CPU, while increasing the number of voxels by 13.6 times.

Table 17. A comparison of MAVRIC and Denovo times when using parallel.

Meshing	CPUs	Time (hours)					Total Den.
		for. input	Den. for.	adj. input	Den adj.	Total	
(96x96x192) = 1.77E+6 Voxels	1	0.27	1.16	0.03	1.16	2.63	2.33
	4	0.27	0.37	0.03	0.43	1.09	0.79
	16	0.27	0.17	0.03	0.17	0.64	0.34
	64	0.27	0.07	0.03	0.08	0.44	0.14
(104x104x312) = 3.37E+6 Voxels	1	0.92	1.96	0.03	2.23	5.15	4.19
	4	0.92	0.66	0.03	0.81	2.42	1.47
	16	0.92	0.27	0.03	0.34	1.57	0.61
	64	0.92	0.13	0.03	0.15	1.23	0.28
(128x128x384) = 6.29E+6 Voxels	1	2.13	3.14	0.06	3.14	8.47	6.29
	4	2.13	1.24	0.06	1.51	4.93	2.75
	16	2.13	0.52	0.06	0.62	3.32	1.14
	64	2.13	0.24	0.06	0.28	2.70	0.52
(144x144x432) = 8.96E+6 Voxels	1	6.64	4.70	0.08	5.69	17.11	10.40
	4	6.64	1.78	0.08	2.10	10.60	3.88
	16	6.64	0.75	0.08	0.86	8.33	1.61
	64	6.64	0.47	0.08	0.39	7.59	0.87
(160x160x480) = 1.23E+7 Voxels	4	28.18	2.35	0.11	2.77	33.40	5.12
	16	28.18	1.01	0.11	1.19	30.48	2.19
	64	28.18	0.47	0.11	0.55	29.31	1.03
(200x200x600) = 2.40E+7 Voxels	4						
	16	95.70	5.64	0.20	4.64	106.17	10.27
	64	95.70	2.40	0.20	1.99	100.29	4.39

For parallel computing the performance is normally measured in terms of speedup and efficiency. The speedup is given by the wall-clock time for a parallel calculation divided by the time for the serial version. The efficiency is the speedup divided by the number of processors. If the efficiency equals one, the speedup varies proportionally with the number of processors.

Doubling the number of processors would reduce by one half the time required for the calculation. Unfortunately, the speedup and efficiency for the two largest cases cannot be directly compared with the rest of the results since the problems could not be simulated on 1 CPU. Therefore, the performance of a single CPU was assumed by extrapolating from other runs to make results comparable. The speedups and efficiencies are shown in Figure 41 and Figure 42.

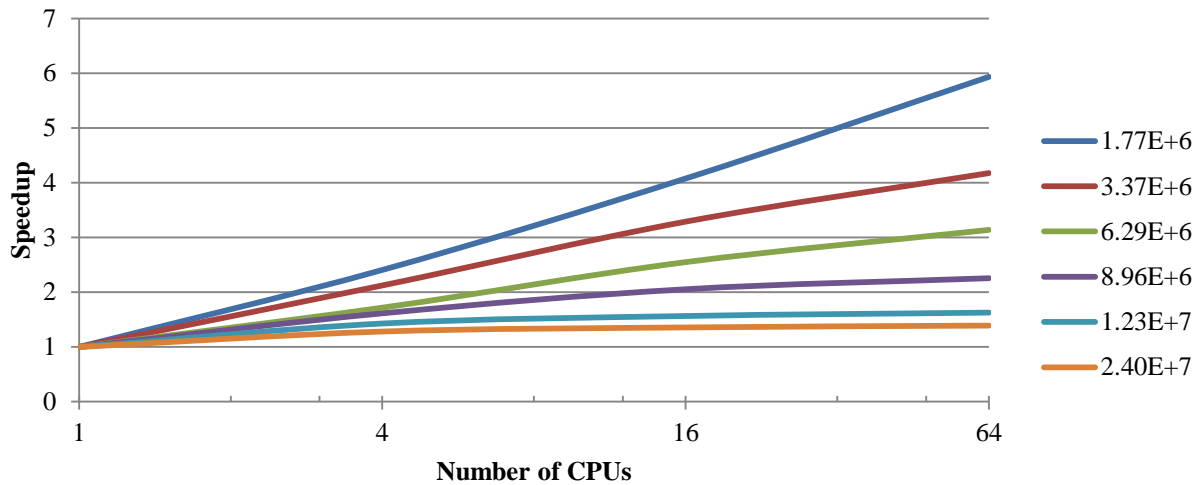


Figure 41. The speedup of each meshing based on the number of CPUs.

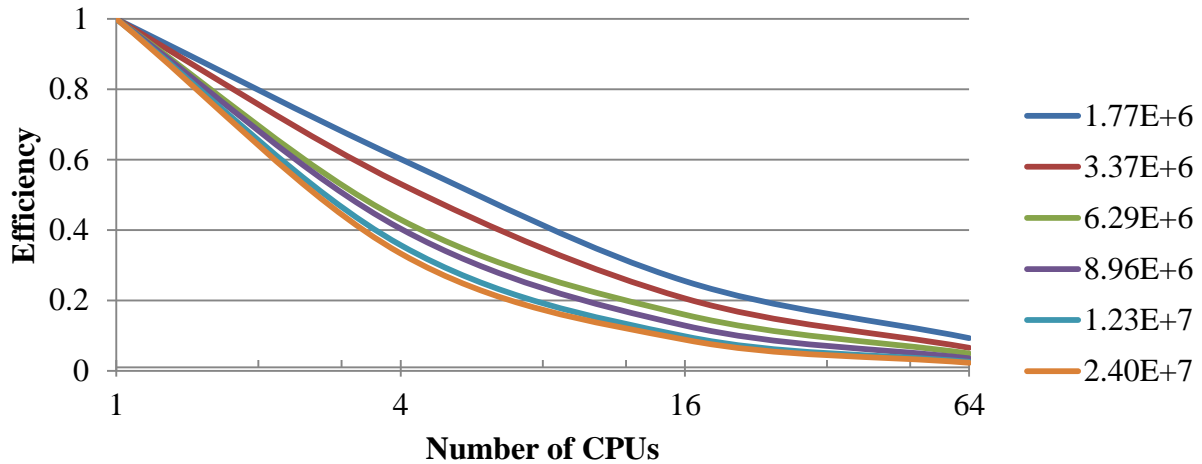


Figure 42. The efficiency of each meshing based on the number of CPUs.

The speedup for the case with the smallest meshing was found to be less than 6 for 64 CPUs. For the largest case it was estimated to be less than 2 times the speedup between the

parallel simulation using 64 processors and the serial version. For every case when using 64 CPUs, the efficiency was below 10%. The main time constraint for these simulations proved to be in generating the input files. For the largest case involving 24 million meshes, the total time required to generate Denovo input files for the forward and adjoint fluxes was over 90% of the total time required for the simulation. The time for input generation was found to scale proportionally with the square of the total number of voxels in the model.

The most recent version of the sequence from the Scale6.1 package, resolved the issue involved with the input generation. Compared with the earlier results, the time for the Denovo input to be generated for the forward flux was reduced by 540 times. Instead of being over 90% of the simulation time it became less than 2%. Therefore, the total simulation time using the MAVRIC sequence provided in Scale6.1 would be similar to comparing simulation times while ignoring the input file generation time. If it is assumed that the Denovo solving time is the only simulation time, then the results are much improved.

Figure 42 and Figure 43 show the speedup and efficiency for each meshing relative to the number of processors used for the simulation. The improved results show that even when solving the problem on the largest meshing, the speedup is still over an order of magnitude. The efficiencies never fall below 10%.

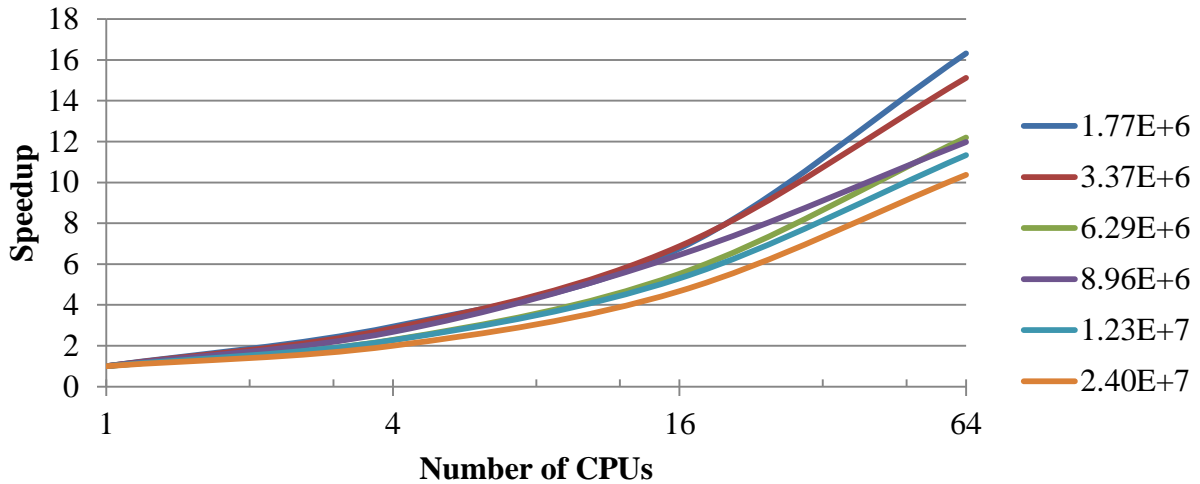


Figure 43. The speedup of the total Denovo CPU time for each meshing based on the number of processors used in the simulation.

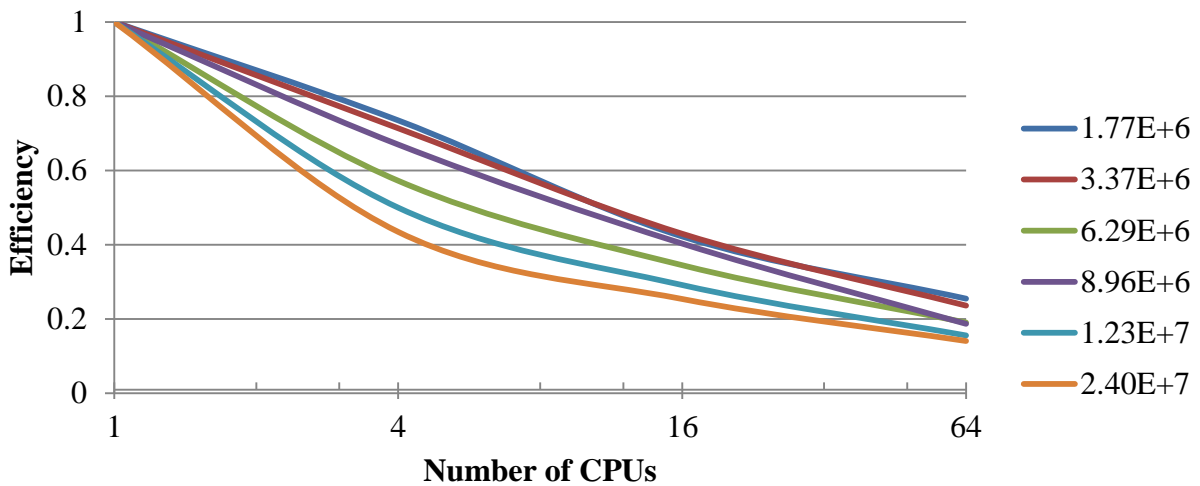


Figure 44. The efficiency of the total Denovo CPU time for each meshing based on the number of processors.

The end goal of Denovo is only to solve for an adjoint flux distribution, which MAVRIC uses to generate an importance map. The importance map is stored in the physical memory available to the Monaco simulation. If the amount of physical memory is exceeded by the amount required for the importance map than it is stored in virtual memory. When crossing between voxels and at collisions in the Monaco simulation, the importance of the particle

entering the new region is compared with the importance of that new region. Splitting methods are then applied to the particle. When the importance map is accessed in virtual memory it slows simulation times down by orders of magnitude. Losing the speedup of the larger meshing makes the methodology unusable. Therefore, there was found to be an upper limit on the number of voxels that could be stored in the importance map without required virtual memory. The upper limit was around 9 million voxels.

After testing methods and looking into potential speedups, different parameters were calculated using MAVRIC to investigate the performance of the code for each parameter. Each case focuses on different response functions and different areas in the model leading to a different experience.

CHAPTER 6

FAST FLUENCE AND VESSEL DOSIMETRY

The first parameters that will be discussed concerning the VHTR power plant is dosimetry to structural core components. Radiation damage to materials is caused by energetic neutrons. The simplest indicator for material damage is the fast neutron fluence, usually taken above 1 MeV, but sometimes 0.1 MeV. A theoretically more accurate measurement of damage is Displacements per Atom (DPA), which seeks to calculate when an atom is displaced from a lattice site. The motivation for using such a metric is having one variable that can account for the neutron spectrum in a way that can correlate a spectrum to property changes in a given material.

As a theoretical quantity there is no way to physically measure DPA, so it is normally validated against calculations of measurable reaction rates. Surveillance capsule monitoring programs seek to measure activation reaction rates in materials. Using the reaction rates, simulations can be validated and a calculated DPA value is assumed to be accurate. According to ASTM Standard E693 (ASTM E693, 2007), DPA calculations should always be coupled with fast neutron fluence.

In the VHTR design, the metals used in the core barrel, pressure vessel and cross duct were chosen based on being able to survive an assumed radiation environment at high temperatures for the a 60-year life of the plant. Therefore, it is important for MAVRIC to be able to simulate a surveillance program and accurately calculate different parameters within the VHTR model.

Source Definition using KENO-VI

The KENO-VI sequence of the Scale6.1 package was first used to simulate a mesh-based, fission source distribution (Figure 45) with respect to both position and energy using the same VHTR model. Both the MC and deterministic portions of the code used the same source. The total source strength was set to 4.565×10^{19} n/s based on the reactor power as given in Eq. 21. The Cartesian mesh used to describe the source does not align well with the fuel rods in the hexagonal graphite VHTR core, leading to apparent variations in the source distribution.

$$600MWt \cdot \frac{J/s}{MW} \cdot \frac{MeV}{1.6021(10^{-13})J} \cdot \frac{fission}{200MeV} \cdot \frac{2.4379n}{fission} = 4.565(10^{19}) \frac{{}^3H}{s} \quad (21)$$

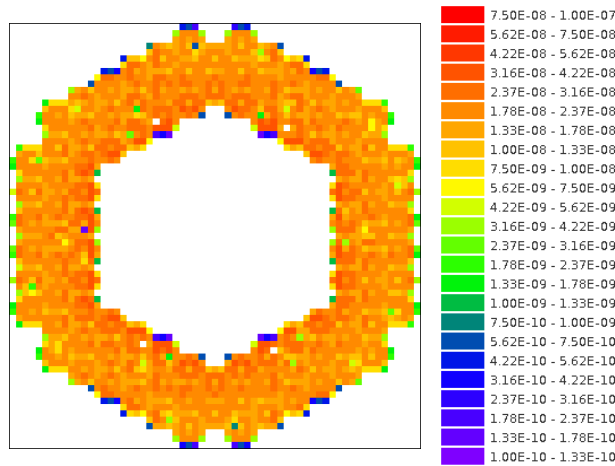


Figure 45. KENO-VI based fission source distribution.

Reactions of Interest

For RPV dosimetry, four reaction rates were chosen based off the LWR benchmarks discussed previously: ${}^{237}\text{Np}(n,f)$, ${}^{58}\text{Ni}(n,p)$, ${}^{27}\text{Al}(n,\alpha)$ and ${}^{115}\text{In}(n,n'){}^{115m}\text{In}$. The ${}^{237}\text{Np}(n,f)$ reaction was chosen since it has a thermal portion to the reaction cross section; however, this portion is expected to only make up 10% of the reaction rate. The ${}^{58}\text{Ni}(n,p)$ reaction can best

represent the total fast spectrum. The $^{27}\text{Al}(n,\alpha)$ reaction rate has a high energy threshold and should be simulated separately as noted in the VENUS-3 benchmark discussed previously. Finally, the $^{115}\text{In}(n,n')$ reaction rate was chosen since it has a reaction cross that cannot be found directly from ENDFB library and should be extracted from IRDF 2002 (International, 2006). The reaction rate from IRDF 2002 was processed into the 200n47g group structure to be used in MAVRIC (D. Wiarda, personal communication, 2011). Figure 46 shows the different foil locations. Two directions from the center of the core were chosen to account for the radial asymmetry introduced by the annular hexagonal core. One direction is directly above the core in the y-direction which is the closest position to source neutrons outside of the reflector. The other position is the farthest from source neutrons. In each direction some foils are placed within a helium riser channel and some immediately outside of the RPV. Additionally at each position three foils are placed axially, separated by roughly 50 cm.

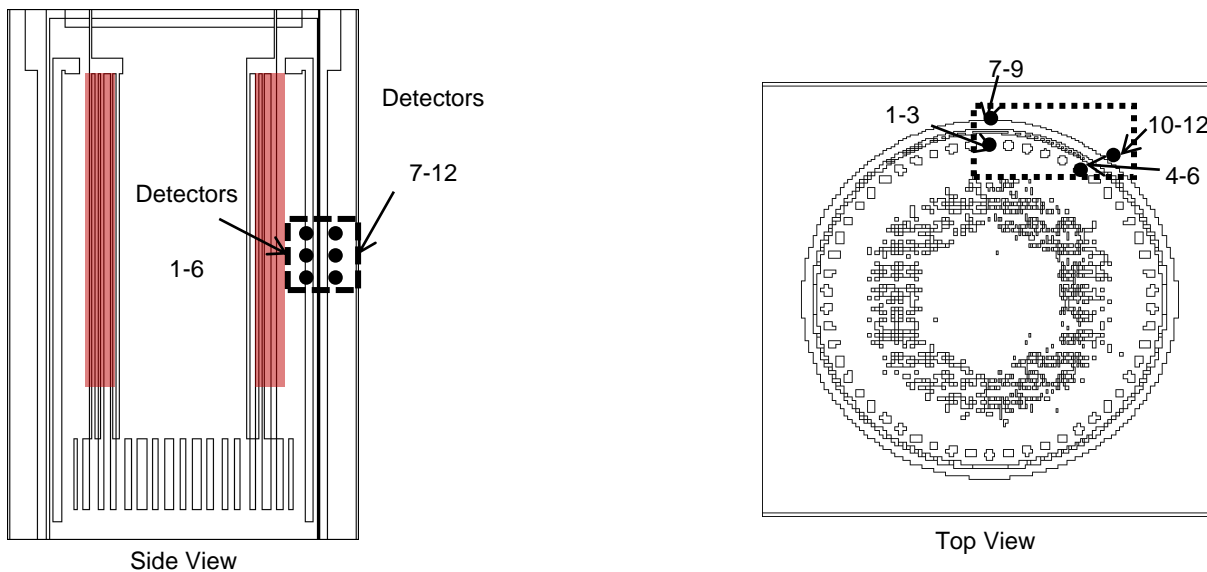


Figure 46. Side and top views of the problem space. The detector locations are indicated by the black dots and the dashed box represents the adjoint source region used for each simulation. Additionally, the red region indicates the active core.

Deterministic Denovo Model and Biasing Parameters

A mesh of $144 \times 130 \times 190 = 3,556,800$ voxels was used. Figure 46 shows the adjoint source region outlined by the dashed. Three separate cases were run to optimize results towards different quantities of interest. The first case was for the $^{237}\text{Np}(n,f)$ which as mentioned above has a contribution from thermal neutrons. The second case was for the fast neutron flux spectrum ($E > 0.1\text{MeV}$) attempting to simultaneously optimize the $^{58}\text{Ni}(n,p)$ and $^{115}\text{In}(n,n')$ $^{115\text{m}}\text{In}$ reactions. The final case took into account the $^{27}\text{Al}(n,\alpha)$ reaction, representing a faster spectrum. Figure 47 and Figure 48 show mesh-based importance map of Group 1 (20 MeV) for each case from different views. Further details are provided in Table 18.

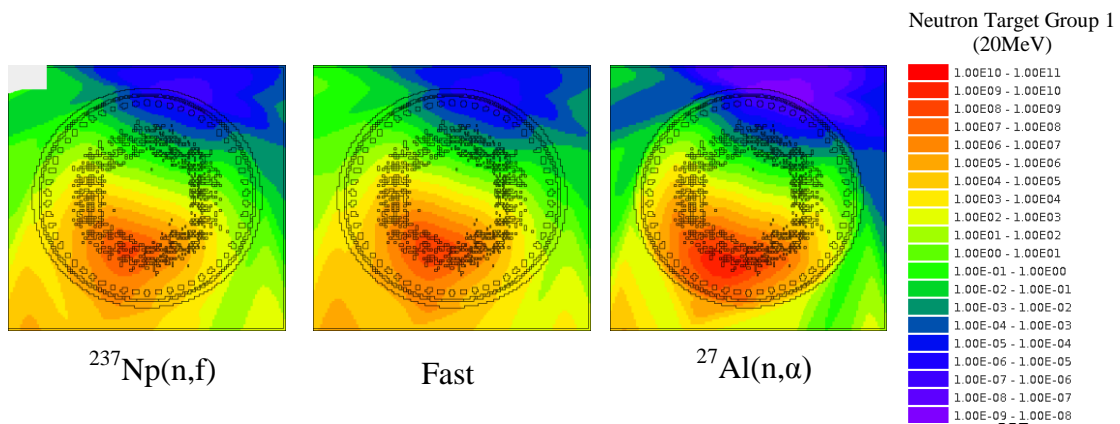


Figure 47. From left to right: Top view of the mesh importance map for the $^{237}\text{Np}(n,f)$, fast neutron flux ($>0.1\text{MeV}$), and $^{27}\text{Al}(n,\alpha)$ simulations.

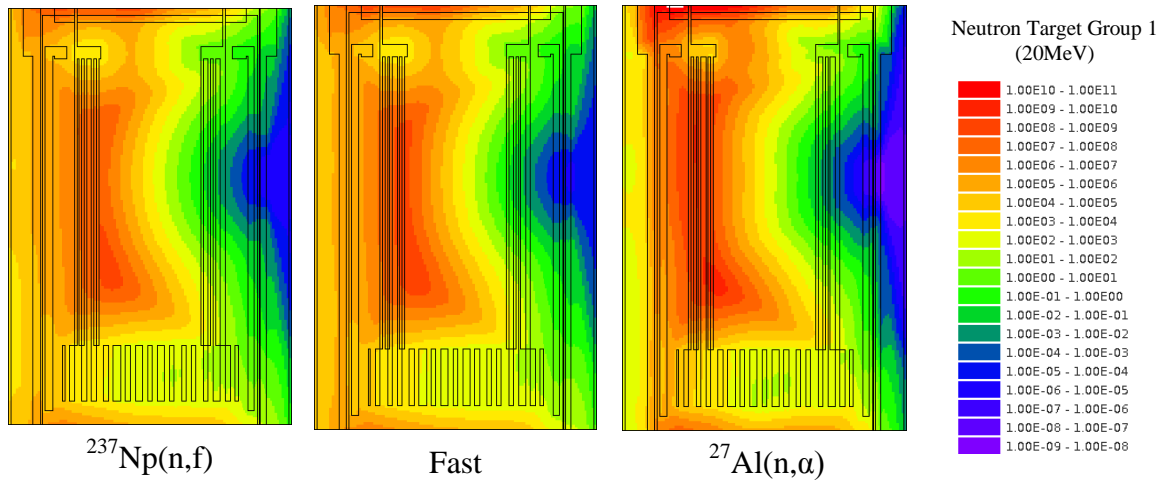


Figure 48. From left to right: Side view of the mesh importance map for the $^{237}\text{Np}(n,f)$, fast neutron flux ($>0.1\text{MeV}$), and $^{27}\text{Al}(n,\alpha)$ simulations.

Table 18. MAVRIC performance and Denovo parameters.

Denovo	
<i>Global Dimensions</i>	
X (max, min, total)	(460, -460, 920) cm
Y (max, min, total)	(460, -460, 920) cm
Z (max, min, total)	(963.1, -425.2, 1,388.3) cm
Volume	1,175 m ³
Meshing (X*Y*Z=total)	(144x130x190 = 3,556,800 voxels)
Average Voxel Size	330 cm ³
<i>Adjoint Source Region</i>	
X (max, min, total)	(220, -10, 230) cm
Y (max, min, total)	(390, 265, 125) cm
Z (max, min, total)	(480, 320, 160) cm
Volume	4,600,000 cm ³
Average Voxel Size (in adjoint region)	102 cm ³
<i>Parameters</i>	
Quadrature sets (S _N)	4
Legendre polynomials (P _L)	1
Krylov space size	10

	237Np(n,f)	Fast	27Al(n,a)
Time (hr)			
Forward	5.46	5.42	5.43
Adjoint	5.38	1.88	0.68
Total Denovo	10.84	7.29	6.11
Total MC	13.91	12.28	12.16
Total	24.75	19.57	18.27

(Table 18 cont.)

MC Performance			
Batches	5	54	153
Particles (thousands)	50	540	1,530
Time/Particle (ms)	16.70	1.36	0.48

Results

The final results for each detector location are given in Table 9 along with the exact positions. The DPA/s and fast neutron fluxes have been integrated over the 60-year life of the reactor assuming a 100% capacity factor. Figure 27 shows the relative uncertainties for the center of the core for each response used as the adjoint source distribution for FW-CADIS. Within the RPV statistics are as expected. However, the positions outside of the RPV have much higher uncertainties. Detectors 7-12 are outside the RPV and it seems that the variance reduction was not attained at these locations. The DPA is attenuated by more than 3 orders of magnitude between helium riser channels and the corresponding detectors outside of the RPV. The fast neutron fluence is only attenuated by 2 orders of magnitude. Between the two locations, the neutrons pass through a layer of graphite (~12cm depending on location), the core barrel (2cm) and the RPV (19cm). The majority of attenuation is assumed to be in the RPV, outside of which most reaction rates have high uncertainties.

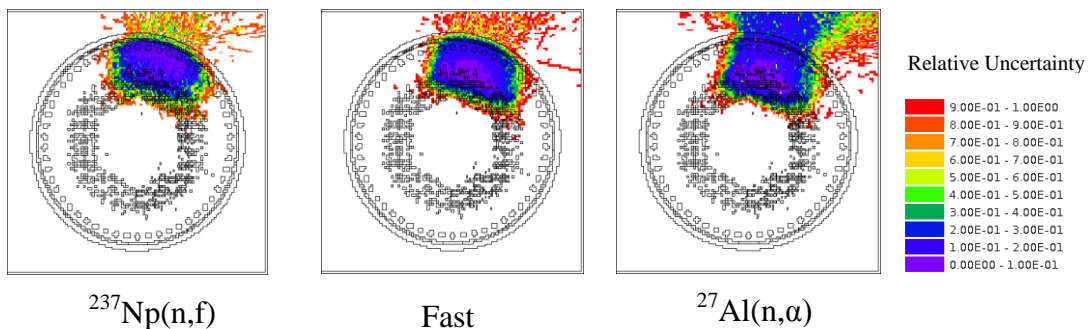


Figure 49. From left to right: Top view of the relative uncertainty for each reaction rate used to define the adjoint source for FW-CADIS.

Table 19. Results obtained from MAVRIC for detectors shown in Figure 46.

Detector	1	2	3
Position (x,y,z)	(0, 328.5, 397)	(0, 328.5, 450)	(0, 328.5, 350)
Total Flux	3.04E+13 ± 5.8%	2.57E+10 ± 8.8%	3.11E+13 ± 7.9%
²³⁷ Np(n,f)	1.43E+10 ± 3.8%	1.36E+10 ± 4.9%	1.37E+10 ± 4.6%
⁵⁸ Ni(n,p)	1.12E+09 ± 5.1%	1.09E+09 ± 7.2%	1.10E+09 ± 6.2%
²⁷ Al(n,α)	4.64E+05 ± 2.2%	4.47E+05 ± 3.1%	4.53E+05 ± 3.1%
¹¹⁵ In(n,n') ^{115m} In	8.80E+09 ± 4.3%	8.40E+09 ± 5.6%	8.63E+09 ± 5.2%
DPA (ASTM693)	0.22 ± 1.8%	0.21 ± 2.5%	0.23 ± 2.4%
Fast (>1MeV)	8.00E+18 ± 4.1%	7.64E+18 ± 5.3%	7.77E+18 ± 5.0%
Fast (>0.1MeV)	2.01E+19 ± 3.6%	1.93E+19 ± 4.5%	1.94E+19 ± 4.7%

(Table 19 cont.)

Detector	4	5	6
Position (x,y,z)	(147.43, 293.56, 397)	(147.43, 293.56, 450)	(147.43, 293.56, 350)
Total Flux	1.06E+10 ± 6.1%	8.68E+09 ± 6.4%	1.07E+10 ± 8.7%
²³⁷ Np(n,f)	6.56E+09 ± 3.7%	5.85E+09 ± 4.5%	6.40E+09 ± 4.5%
⁵⁸ Ni(n,p)	5.76E+08 ± 4.6%	5.29E+08 ± 6.0%	5.48E+08 ± 5.9%
²⁷ Al(n,α)	2.36E+05 ± 1.9%	2.28E+05 ± 2.4%	2.36E+05 ± 2.5%
¹¹⁵ In(n,n') ^{115m} In	4.28E+09 ± 4.0%	3.82E+09 ± 4.9%	4.08E+09 ± 5.1%
DPA (ASTM693)	0.23 ± 2.3%	0.22 ± 2.7%	0.25 ± 4.9%
Fast (>1MeV)	3.85E+18 ± 4.0%	3.43E+18 ± 4.7%	3.69E+18 ± 4.9%
Fast (>0.1MeV)	8.81E+18 ± 3.3%	7.88E+18 ± 4.2%	8.67E+18 ± 4.3%

Detector	7	8	9
Position (x,y,z)	(0, 380, 397)	(0, 380, 450)	(0, 380, 350)
Total Flux	4.92E+08 ± 26.6%	6.26E+08 ± 16.2%	5.61E+08 ± 15.4%
²³⁷ Np(n,f)	1.83E+08 ± 15.6%	2.32E+08 ± 22.5%	1.86E+08 ± 16.5%
⁵⁸ Ni(n,p)	2.88E+06 ± 29.2%	2.06E+06 ± 21.3%	4.55E+06 ± 54.1%
²⁷ Al(n,α)	2.10E+03 ± 13.4%	2.05E+03 ± 19.5%	1.69E+03 ± 15.9%
¹¹⁵ In(n,n') ^{115m} In	4.19E+07 ± 16.0%	1.10E+07 ± 33.0%	4.61E+07 ± 31.0%
DPA (ASTM693)	1.55E-04 ± 12.5%	1.51E-04 ± 17.4%	7.21E-05 ± 11.3%
Fast (>1MeV)	3.77E+16 ± 15.6%	8.56E+15 ± 32.0%	4.99E+16 ± 30.3%
Fast (>0.1MeV)	4.75E+17 ± 10.0%	6.21E+17 ± 16.9%	4.72E+17 ± 13.9%

Detector	10	11	12
Position (x,y,z)	(190, 329.09, 397)	(190, 329.09, 450)	(190, 329.09, 350)
Total Flux	4.03E+06 ± 23.5%	2.57E+08 ± 11.7%	3.04E+08 ± 17.7%
²³⁷ Np(n,f)	9.78E+07 ± 10.9%	7.99E+07 ± 15.1%	1.15E+08 ± 23.1%

$^{58}\text{Ni}(n,p)$	$1.08\text{E}+06 \pm 16.4\%$	$1.12\text{E}+06 \pm 20.8\%$	$1.24\text{E}+06 \pm 20.8\%$
$^{27}\text{Al}(n,\alpha)$	$8.59\text{E}+02 \pm 10.7\%$	$1.02\text{E}+03 \pm 21.2\%$	$1.17\text{E}+03 \pm 20.6\%$
$^{115}\text{In}(n,n')^{115\text{m}}\text{In}$	$2.25\text{E}+07 \pm 15.1\%$	$2.14\text{E}+07 \pm 25.1\%$	$5.41\text{E}+06 \pm 28.4\%$
DPA (ASTM693)	$7.04\text{E}-05 \pm 16.1\%$	$5.11\text{E}-05 \pm 17.4\%$	$2.08\text{E}-04 \pm 22.8\%$
Fast (>1MeV)	$2.79\text{E}+16 \pm 19.2\%$	$2.26\text{E}+16 \pm 24.8\%$	$4.18\text{E}+15 \pm 28.8\%$
Fast (>0.1MeV)	$2.91\text{E}+17 \pm 12.0\%$	$2.23\text{E}+17 \pm 12.0\%$	$2.63\text{E}+17 \pm 13.8\%$

CHAPTER 7

PERSONEL DOSIMETRY IN THE VHTR PLANT

MAVRIC's capabilities were further tested calculating dose to personnel in an accessible area during normal operating conditions. Most shielding indicators of interest around a reactor are relatively close to the fixed source and normally do not extend much past the pressure vessel. Finding dose rates in accessible areas covers a much larger volume and presents a deeper shielding problem. The quantity of interest is the neutron, photon and total dose rate in the accessible region in the dome directly above the reactor core. The neutron and photon flux-to-dose conversions are provided within the Scale6.1 code package and are taken from ANSI 1991. The units are rem/hour (ANSI, 1999).

Different views of the problem geometry can be seen in Figure 50 with the area marked by the red box being the adjoint source region. Neutrons and photons are tracked through a large domain and much attenuation further challenges MAVRIC's capabilities. The dose is attenuated between the core and the room by well over 15 orders of magnitude from roughly 10^{10} to 10^{-5} rem/hour. With properly biased particles, dose rates should be attained in a relatively reasonable amount of time. Extra layers of shielding are expected to require more simulation time, while still demonstrating the effectiveness of MAVRIC. Between the core and the air in the dome are two to three layers of concrete, the top graphite reflector region, the core barrel, the pressure vessel and control rods located within their assemblies. However, there are streaming paths through the control rod assemblies that bypass the top reflector, first layer of concrete and the core barrel. These regions have proven to be problematic with the methodology.

Three studies were performed with the goal of obtaining the dose in the area previously described. The preliminary run used a uniform mesh (3.4 million voxels) over the entire problem space. A second run used a more condensed model and more voxels (8.0 million

voxels). The third and final simulation built from previous results, but used a higher quadrature set and some mesh-refinement to attain better biasing.

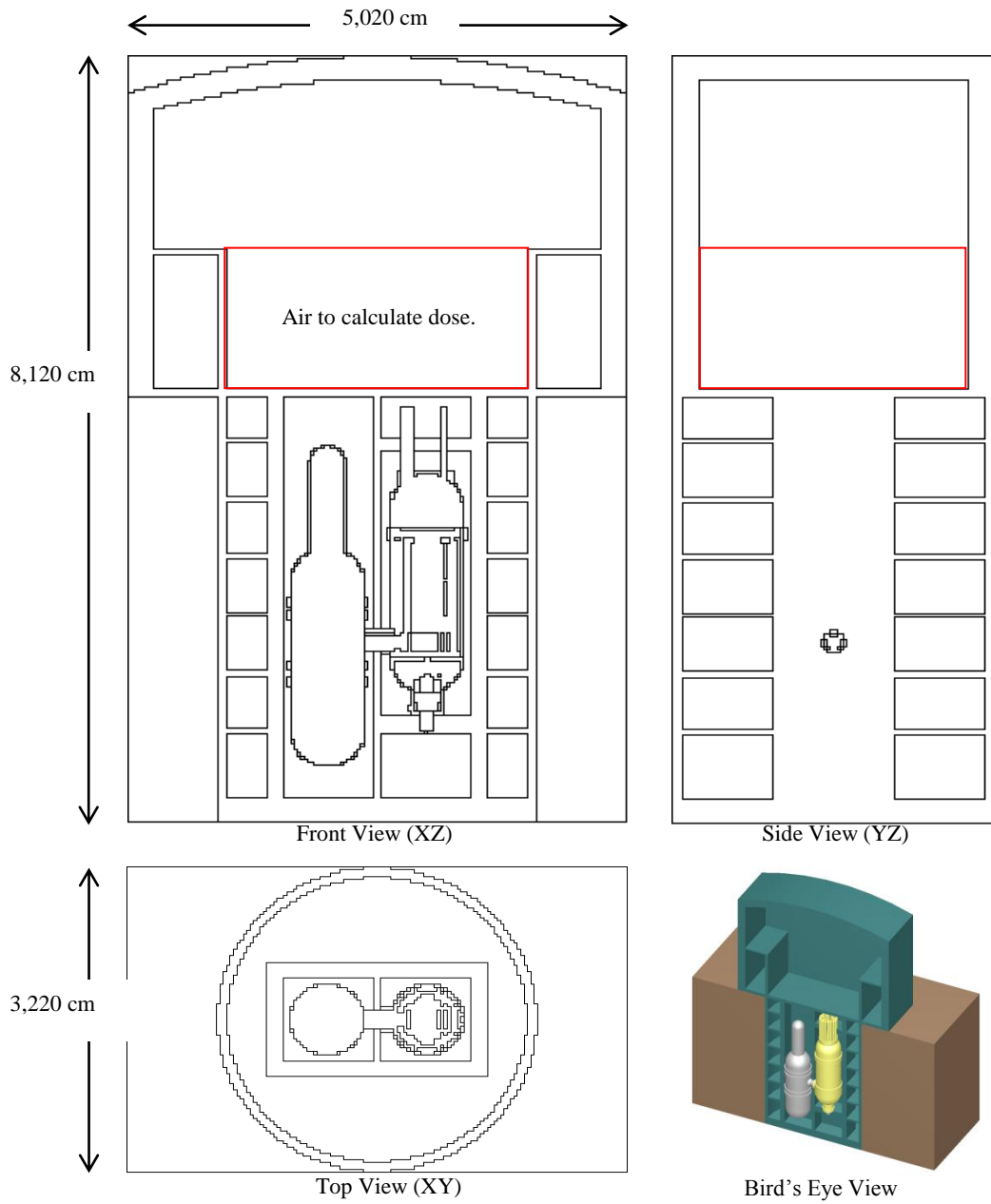


Figure 50. Different views of the problem space.

Preliminary Analyses with a Uniform Mesh

In order to get an idea of the issues with finding the dose in the dome above the reactor, an initial case was simulated using a mesh of 3,484,800 voxels. The lengths of each cubic voxel was roughly 34cm, which is very large. For accurate solutions using the discrete ordinates method, the voxel size should be close to the smallest mean free path of a neutron in all materials. The mean free path of a thermal neutron in graphite is 2.6cm. Therefore, the meshing is over an order of magnitude larger than would be desired. Basic parameters are summarized in Table 20. The Monaco portion of the simulation was allowed to run for 6 days. Figure 51 and Figure 52 show the neutron and photon dose rates with relative uncertainty. For both doses, the uncertainty does not seem to get below 50% in the adjoint source region. A drastic improvement in the importance map is needed, which is discussed in the next section.

Table 20. MAVRIC performance and Denovo parameters.

Denovo	
<i>Global Dimensions</i>	
X (max, min, total)	(2510, -2510, 5020) cm
Y (max, min, total)	(1610, -1610, 3220) cm
Z (max, min, total)	(8110, -10, -8120) cm
Volume	131,255 m ³
<i>Meshing</i>	
(X*Y*Z=total)	(150x96x242 = 3,484,800 voxels)
Average Voxel Size	37,665 cm ³
<i>Adjoint Source Region</i>	
X (max, min, total)	(1500, -1500, 3000) cm
Y (max, min, total)	(1350, -1350, 2700) cm
Z (max, min, total)	(6050, 4600, 1450) cm
Volume	11,745 m ³
<i>Parameters</i>	
Quadrature sets (S_N)	4
Legendre polynomials (P_N)	1
Krylov space size	10

(Table 20 cont.)

	1	2	3	4	5	6	7
Time (hr)							
Forward				7.3			
Adjoint				5.1			
Total Denovo				12.4			
Total MC				145.1			
Total				157.5			

MC Performance							
Batches				69			
Particles (millions)				69			
Time/Particle (ms)				0.13			

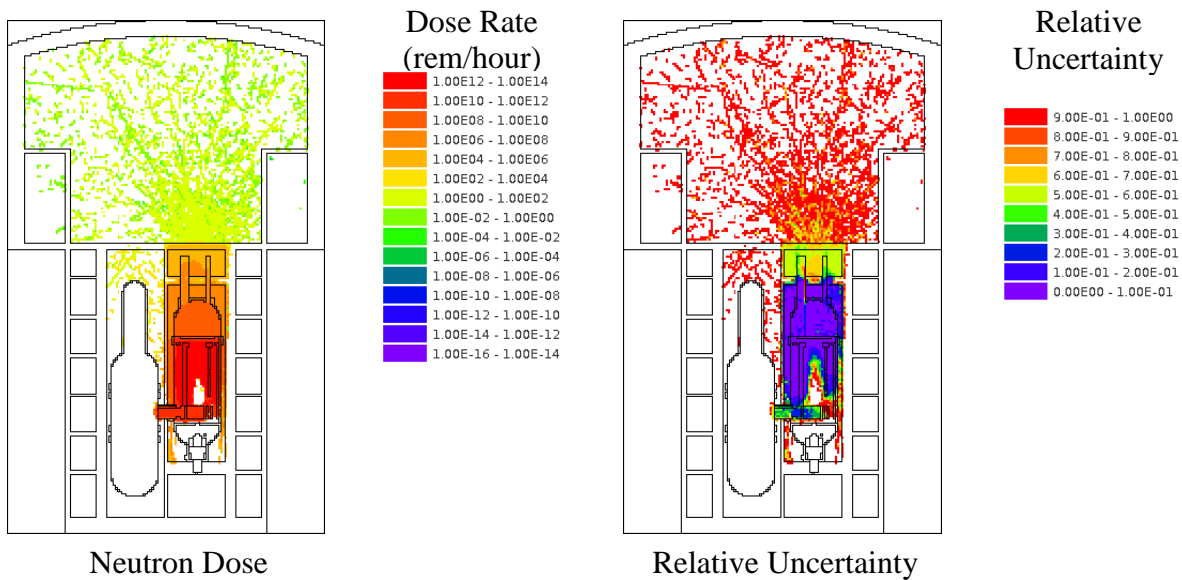


Figure 51. Neutron dose rate for a 6 day MC simulation.

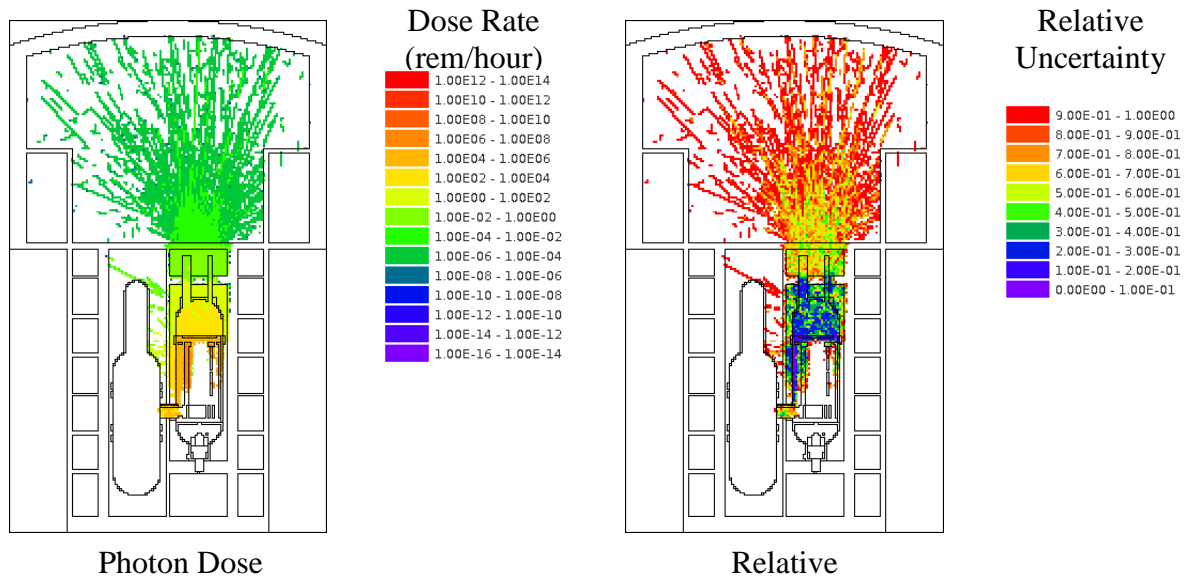


Figure 52. Photon dose rate for a 6 day MC simulation.

Finer Mesh and Condensed Geometry

Implementing a better importance map requires better results from the deterministic calculation. The previous study did not utilize the largest meshing possible within MAVRIC. Therefore, the first improvement in the discretized model was increasing the meshing from 3.5 million to 8 million voxels. Secondly, the portion of the plant model below the core barrel is excluded from the model. The combined result gives an average voxel size of $12,861 \text{ cm}^3$, with an average length of 23.4cm. That length is less than an order of magnitude greater than the mean free path of a thermal neutron in graphite. Basic parameters are summarized in Table . Seven Monaco runs were performed for 24 CPU hours each; the results are shown for each day separately as well as for each combined.

Table 21. MAVRIC performance and Denovo parameters.

Denovo	
<i>Global Dimensions</i>	
X (max, min, total)	(2510, -2510, 5020) cm
Y (max, min, total)	(1610, -1610, 3220) cm
Z (max, min, total)	(8110, 1734.8, 6375.2) cm
Volume	103,051 m ³
Meshing (X*Y*Z=total)	(198x134x302 = 8,012,664 voxels)
Average Voxel Size	12,861.05 cm ³
<i>Adjoint Source Region</i>	
X (max, min, total)	(1500, -1500, 3000) cm
Y (max, min, total)	(1350, -1350, 2700) cm
Z (max, min, total)	(6050, 4600, 1450) cm
Volume	11,745 m ³
Parameters	
Quadrature sets (S _N)	4
Legendre polynomials (P _N)	1
Krylov space size	10

	1	2	3	4	5	6	7	total
Time (hr)								
Forward				16.1				
Adjoint				11.8				
Total Denovo				27.9				
Total MC	25.6	24.7	12.5	13.2	25.3	24.4	25.3	151.0
Total	53.5	52.6	40.4	41.1	53.2	52.3	53.1	178.9

MC Performance								
Batches	5	6	3	3	6	6	6	35
Particles (millions)	5	6	3	3	6	6	6	35
Time/Particle (ms)	0.31	0.25	0.25	0.26	0.25	0.24	0.25	0.26

Figure 53 shows the combined neutron and photon dose with the relative uncertainty. The neutron and photon dose rate maps are given in Figure 54 and Figure 55, with their relative uncertainties. Note that each of the two horizontal layers of concrete between the core and the accessible area is roughly 100cm thick, and therefore the attenuation resulting from each is severe. From the dose map there is a clear, significant jump in the relative uncertainty of both neutrons and photons after each layer of concrete.

As mentioned above, the simulations were performed on a per day basis so that the final results could all be pulled into week long results. The results are less satisfactory than expected,

which is most likely due to the mesh being too coarse to properly discretize the geometry. Each voxel is approximately $33 \times 33 \times 33 \text{ cm}^3$ which certainly is much greater than the mean free path of most materials in the problem. Figure 56 through Figure 58 give the resultant coupled, neutron and photon dose maps respectively for 7 individual 24-hour simulations. It can be seen that the majority of statistics in the accessible area comes from the efforts of a single day's run and primarily from the photon dose. The relative uncertainties are given in Figure 57 and Figure 59.

The purpose of the methodology is to obtain a uniform relative uncertainty in the adjoint source region, which was not achieved. When compared to previous results, the entire region of interest did have some particles tracked. Unfortunately, the model has already been truncated and the meshing been pushed to the limits of a single-CPU Monaco simulation. Therefore, further refinement is required using a different approach as discussed in the next section.

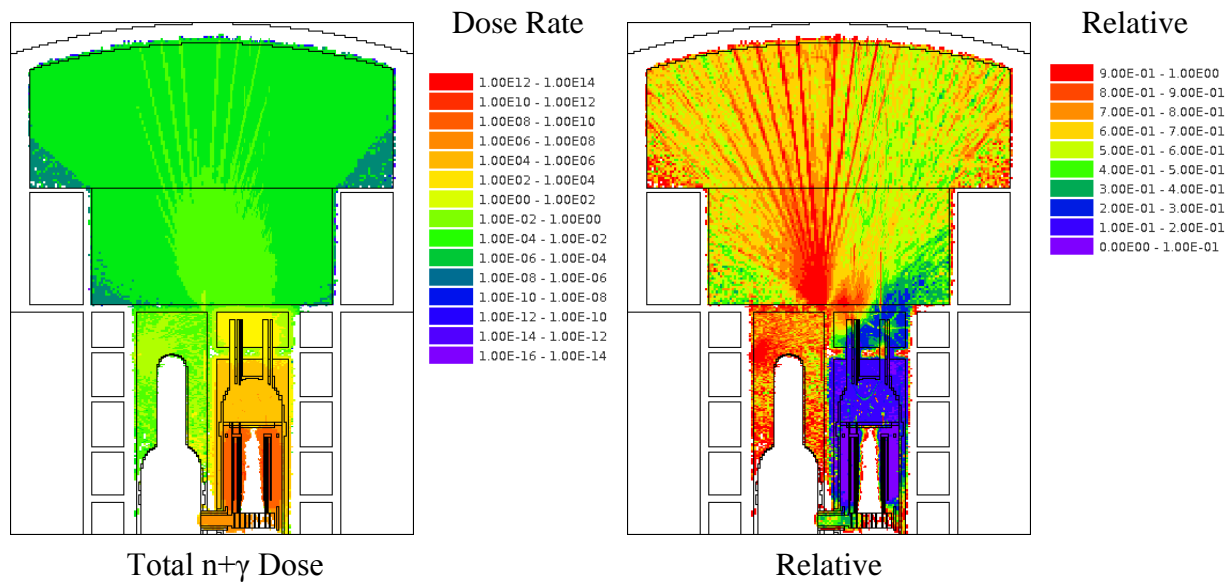


Figure 53. Total dose rate for a 1 week MC simulation (left) with the relative uncertainty (right).

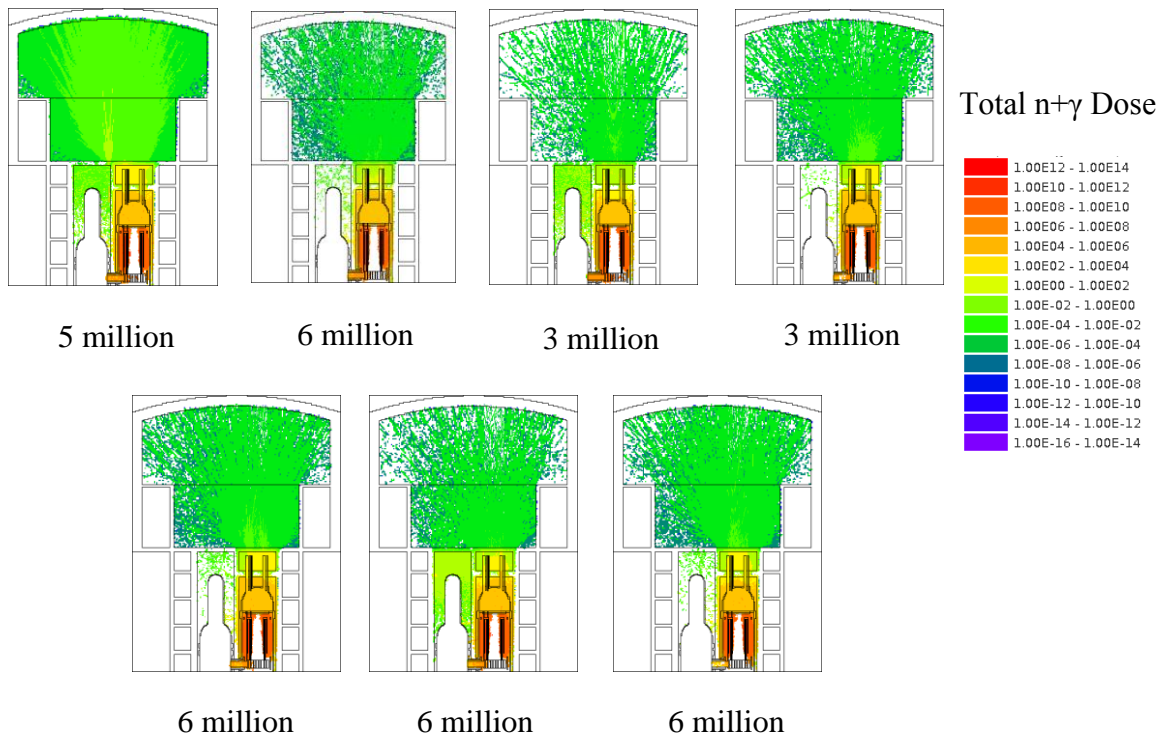


Figure 56. The total neutron and gamma dose for seven one-day simulations. The figure below each image represents the number of tracked particles. Notice that the majority of statistics in the access room come from the first run.

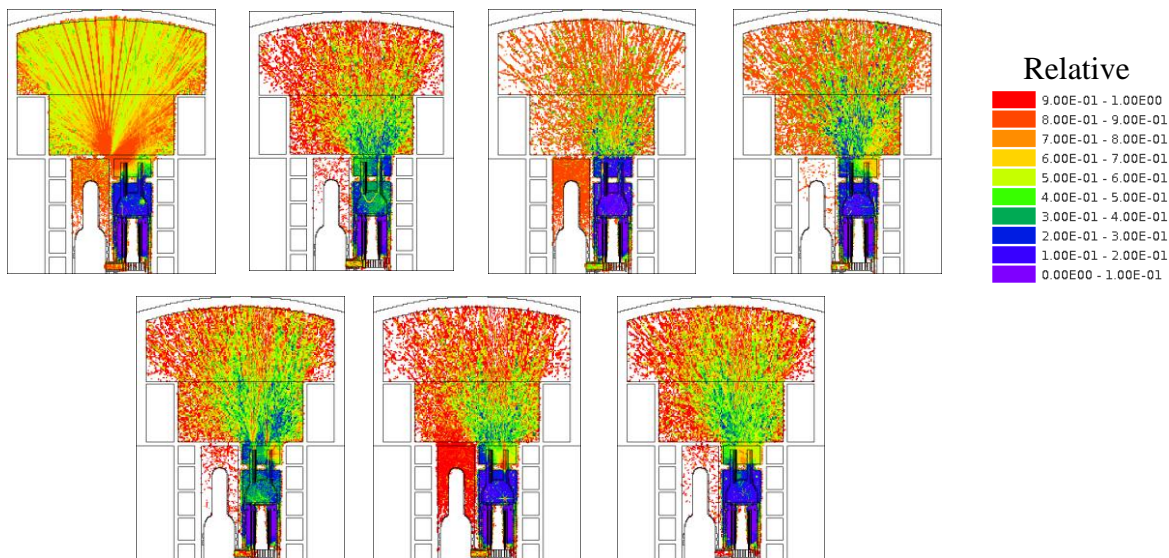


Figure 57. The total dose relative uncertainty for seven one-day Monaco simulations.

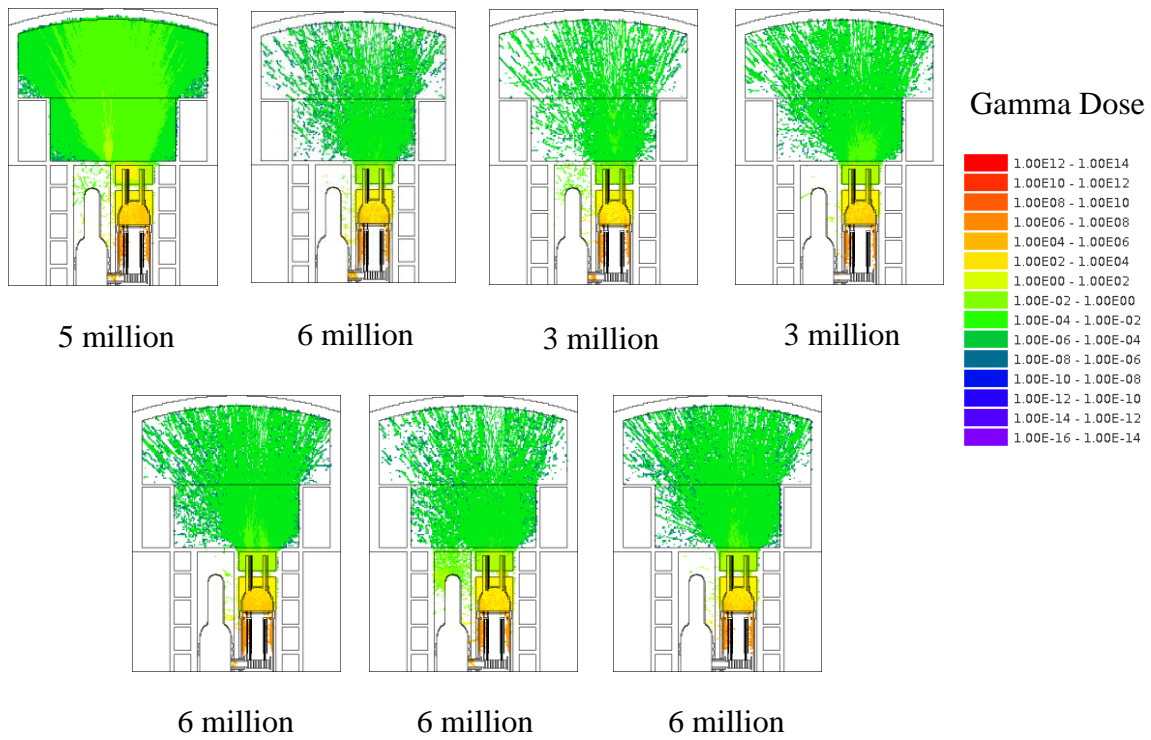


Figure 58. The gamma dose for seven one-day Monaco simulations. The figure below each image represents the number of tracked particles. Notice that the majority of statistics in the access room come from one run.

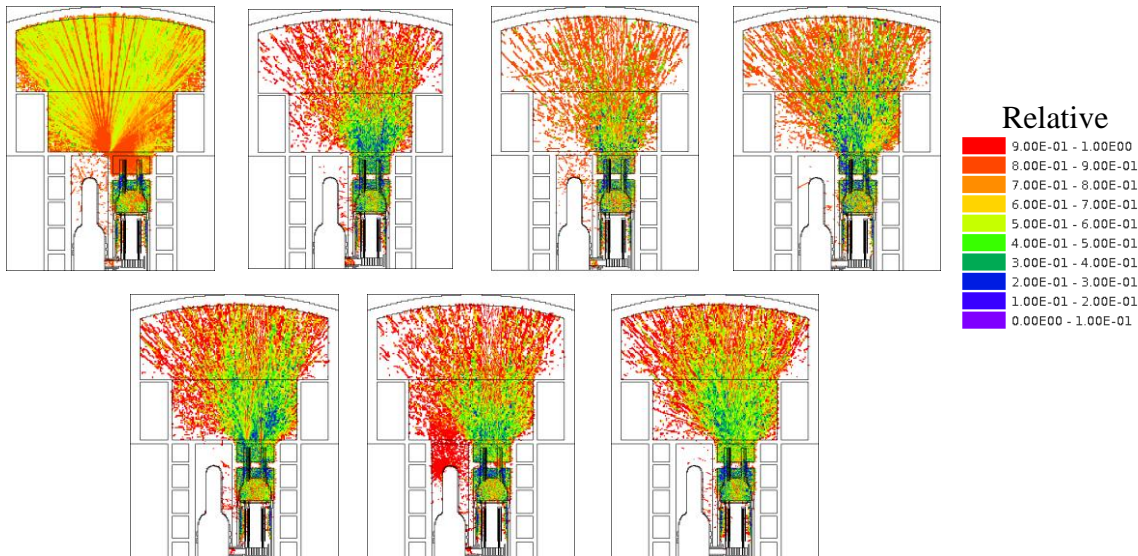


Figure 59. The gamma dose relative uncertainty for seven one-day Monaco simulations.

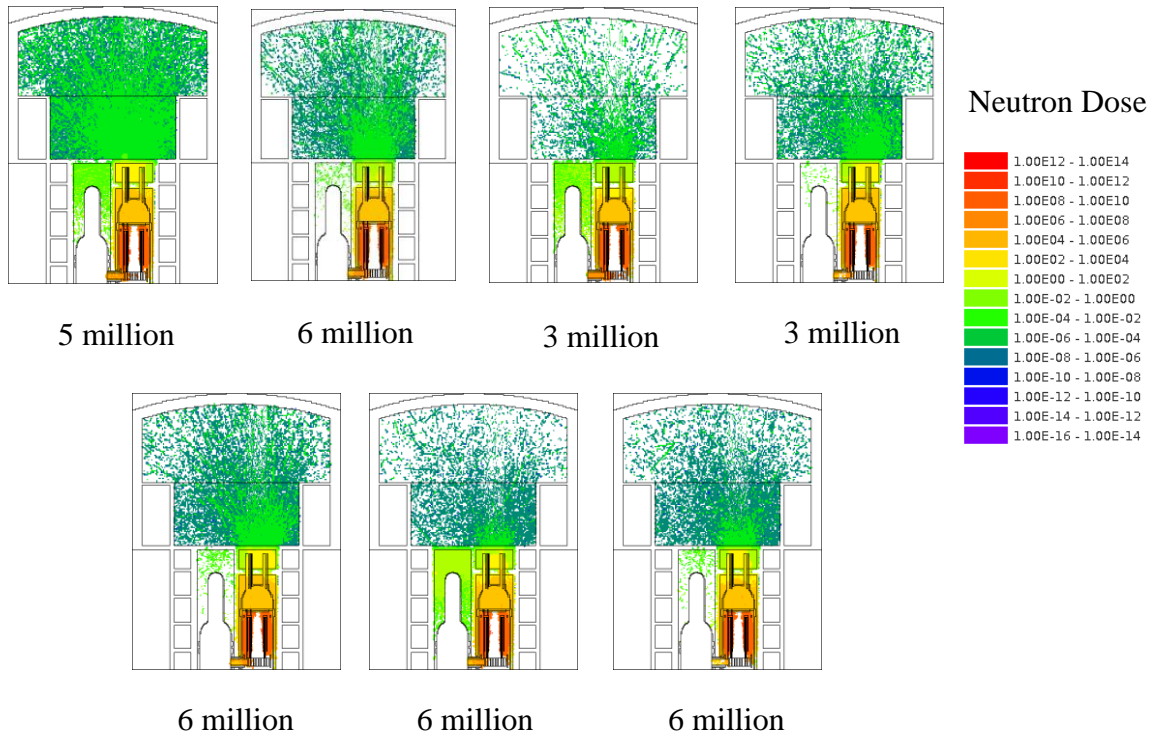


Figure 60. The neutron dose for seven one-day simulations.

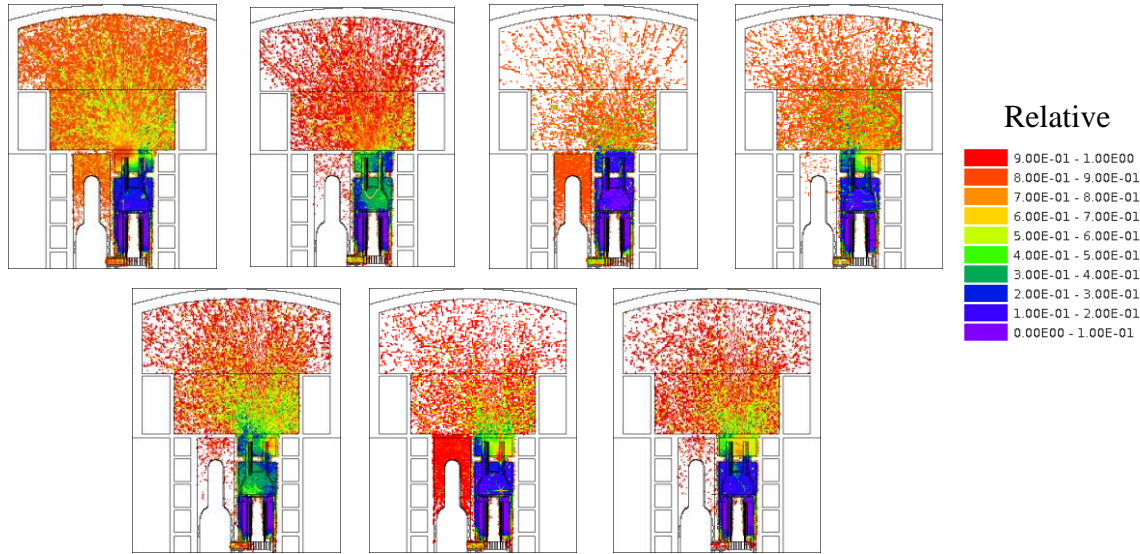


Figure 61. The neutron dose relative uncertainty for seven one-day Monaco simulations.

Increased Quadrature Set and Mesh Refinement

In order to better improve the importance map while using the same number of meshes, the meshing was refined around important areas of the problem. In the x and y directions, the problem was chunked up into 5 areas of meshing each. The meshing scheme can be seen in Figure 62 showing each section as: the area containing the active core (purple), the two side areas between the core's edge and the RPV (blue), and the two sides extending to the end of the model (clear). Regions of decreasing importance were given larger voxels, since the deterministic solution in those regions is less important to the overall solution. Moving away from the core, the geometry becomes less intricate so the number of meshes required to accurately represent the regions in the discretized model become less important. Table 22 provides the meshing used for different regions of the problem by each axis. In the purple portion covering the active core to the accessible area, the mesh length was reduced to roughly 8.2 cm which is a little more than 3 times the mean free path of a thermal neutron in graphite.

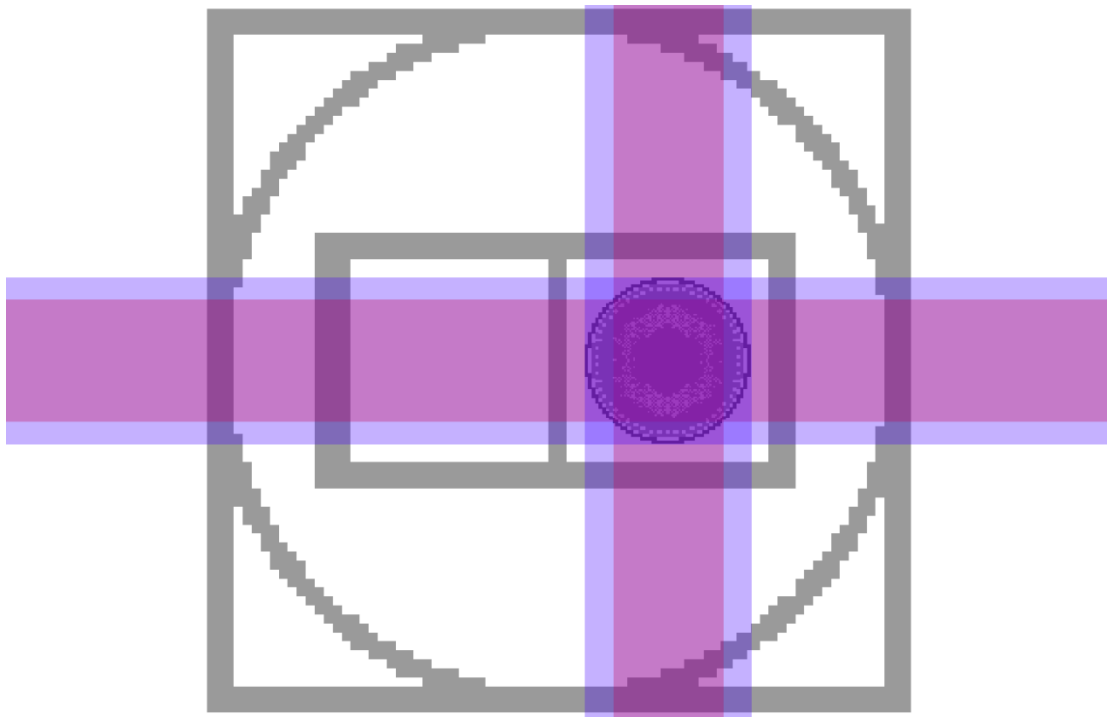


Figure 62 The mesh refinement scheme used for the Denovo.

Additionally, the P_L legendre expansions and S_N quadrature sets were also increased from 1/4 to 3/8. Increasing the quadrature set increases the amount of memory needed to solve for the forward flux using Denovo. By implementing parallel Denovo the memory requirements were distributed over multiple nodes on the cluster. Using parallel Denovo allows for finer meshing to be achieved in the solution as well, but it would be unusable by MAVRIC since the importance map is loaded onto one node. Since Denovo only solves the scalar flux, increasing the quadrature set has no effect on the size of the importance map generated by MAVRIC.

Table 22. MAVRIC performance and Denovo parameters.

<u>Denovo</u>				
<i>Global Dimensions</i>				
X (max, min, total)	(2510, -2510, 5020) cm			
Y (max, min, total)	(1610, -1610, 3220) cm			
Z (max, min, total)	(8110, 1734.8, 6375.2) cm			
Volume	103,051 m ³			
Meshing (X*Y*Z=total)	(180x140x360 = 8,012,664 voxels)			
	Meshing	Min	Max	Size
	64	-2510	120	41.09
	8	120	250	16.25
<i>X-Axis</i>	60	250	750	8.33
	8	750	880	16.25
	40	880	2510	40.75
	30	-1610	-380	41.00
	7	-380	-270	15.71
<i>Y-Axis</i>	66	-270	270	8.18
	7	270	380	15.71
	30	380	1610	41.00
	19	1734.8	2500	40.27
<i>Z-axis</i>	256	2500	4600	8.20
	85	4600	8110	41.29
Average Voxel Size	~70,000 cm ³ , ~4,300 cm ³ , ~580 cm ³			
<i>Adjoint Source Region</i>				
X (max, min, total)	(1500, -1500, 3000) cm			
Y (max, min, total)	(1350, -1350, 2700) cm			
Z (max, min, total)	(6050, 4600, 1450) cm			
Volume	11,745 m ³			

(Table 22 cont.)	
Parameters	
Quadrature sets (S_N)	8
Legendre polynomials (P_N)	3
Krylov space size	10

	1	2	3	4	5	6	7	total
Time (days)								
Forward				0.16				
Adjoint				0.13				
Total Denovo				0.28				
Denovo CPU Time				(4.48)				
Total MC	7.02	7.09	7.08	7.03	7.14	7.10	7.01	49.46
Total	7.30	7.37	7.36	7.31	7.42	7.38	7.29	49.74

MC Performance								
Batches	42	43	43	41	41	42	42	294
Particles (millions)	42	43	43	41	41	42	42	294
Time/Particle (s)	0.014	0.014	0.014	0.015	0.015	0.015	0.014	0.015

With the availability of a large cluster, there is no reason not to run large simulations in “poor man’s” parallel. The term refers to the method of manually running simulations on different processors concurrently and combining results once all have completed. In the previous study the simulation was ran for a week and the results were interpreted at one day intervals. Using “parallel,” 49 days can be simulated in 1 week by running 7 week-long runs simultaneously. A combination of a better importance map with a much longer run time should show better convergence than before. Figure 63 shows the total neutron and gamma dose rate calculated by the 7 week combined run. While the majority of the room used as the adjoint source region experiences a relatively low uncertainty (<20%), the part directly above the core has a large variance of variance. Adjacent regions above the core have relative uncertainties varying by large amounts from ~15% to ~70%.

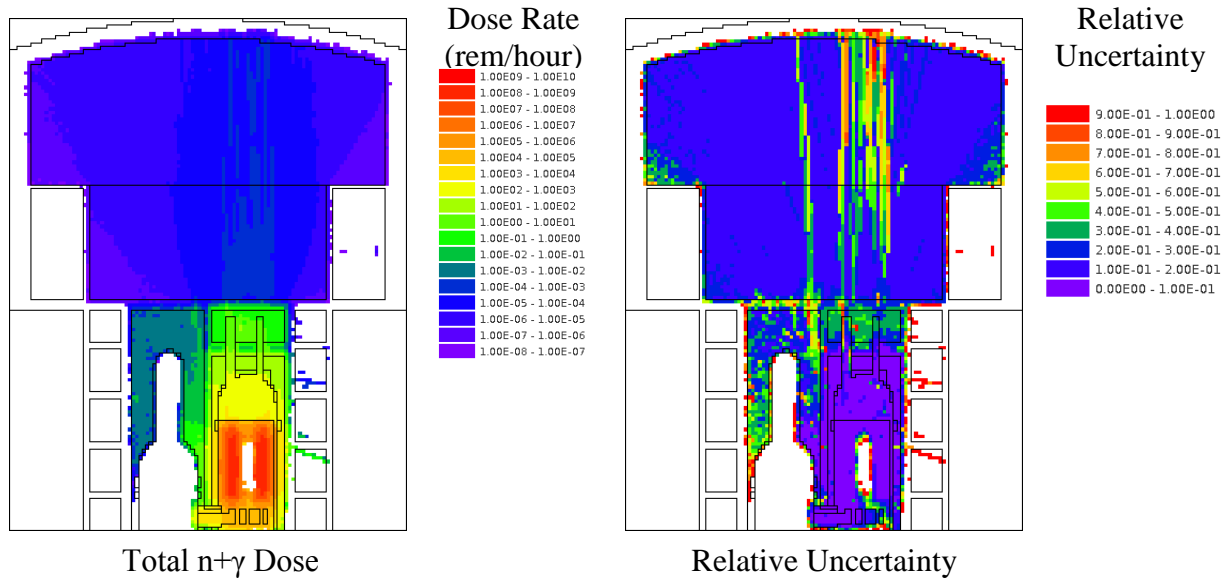


Figure 63. Total dose rate for a 7 week MC simulation (left) with the relative uncertainty (right).

According to preliminary runs, the dose rate in the dome directly above the VHTR core (ignoring shielding materials within the control rod guide tubes and borated graphite layer just inside core barrel) would be around 0.0001 rem/hr. Some areas have much larger values, such as the region directly above the core. Figure 64 shows the dose rate plotted on the x-axis for different elevations in the room. The maximum dose rate for this cross section was found to be $7.25(10^{-4}) \pm 71\%$ rem/hour, which is not an acceptable level of uncertainty but is used as it is the maximum. When uncertainty is added to the dose rate, a upper dose rate of 0.00125 rem/hour is calculated. If it is assumed that a worker was at this position for 40 hours a week for 50 weeks a year, the total dose for the year would be,

$$0.00125 \frac{rem}{hr} \cdot \frac{40hr}{1week} \cdot \frac{50 work weeks}{1yr} = 2.5 \frac{rem}{yr}. \quad (15)$$

This approximation is below the annual dose limit for the general public as defined by the 10 CFR 20 from the NRC (Standards, 2009). With shielding materials properly taken into account around the control rod assemblies, this dose rate would be reduced by absorbing particles

streaming from the core which are assumed to be causing the higher dose rates with higher variance. The majority of well converged solutions are around 10^{-4} rem/hour, which would equate to a dose of only 0.2 rem/year.

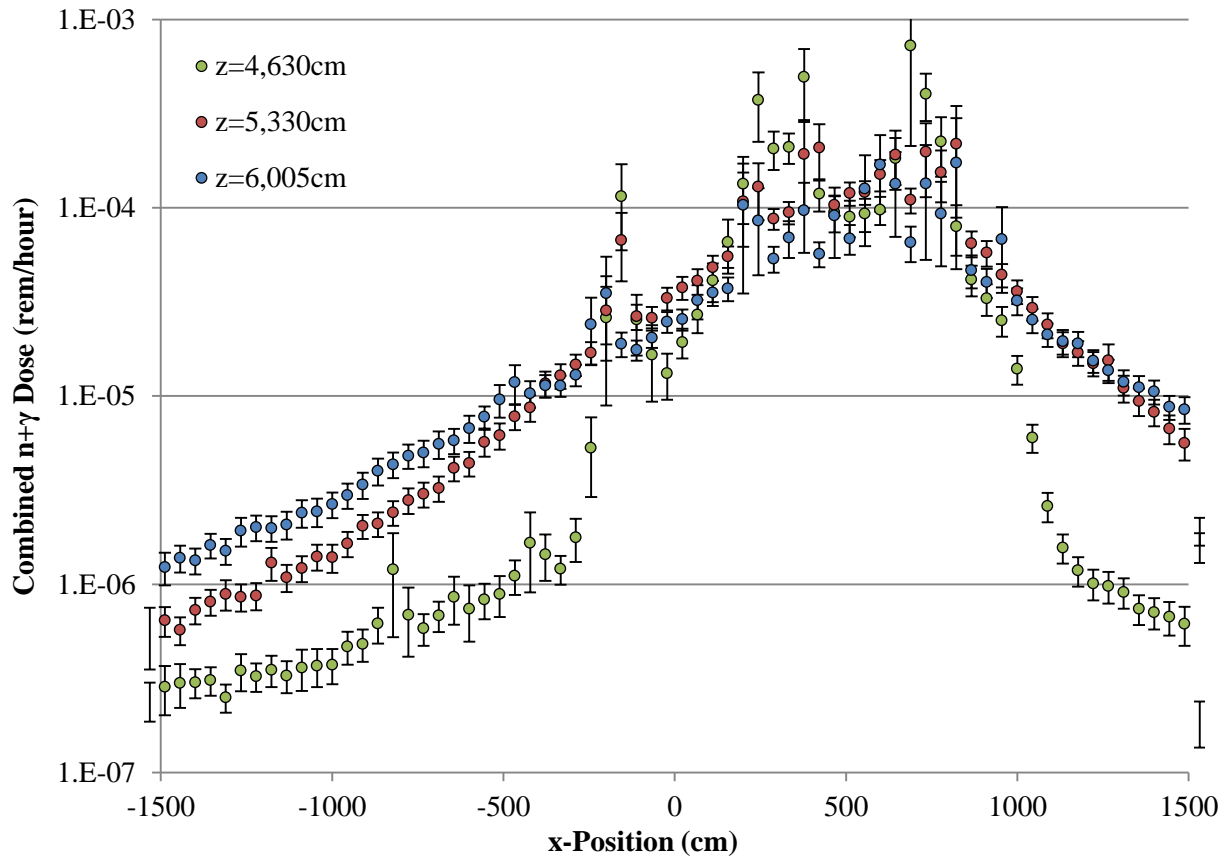


Figure 64. The total n+γ dose rate on the x-axis in the accessible room at different elevations on the centerline of the model.

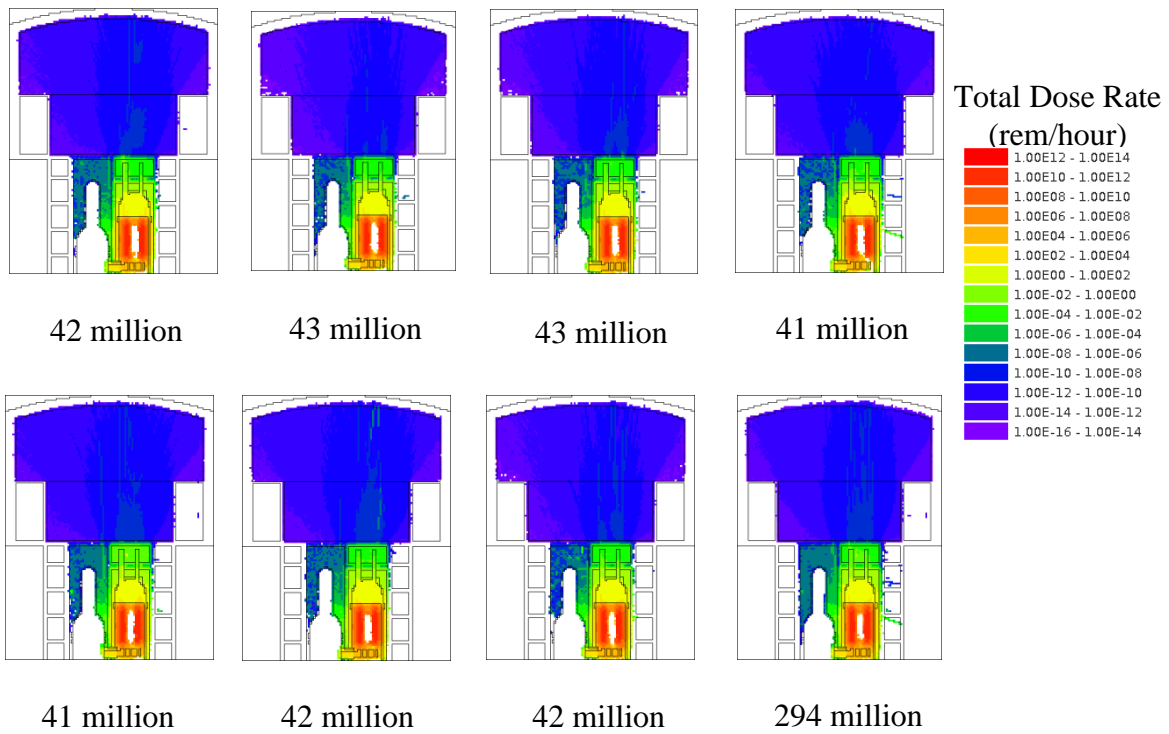


Figure 67. The total gamma and neutron dose for each week-long simulation. Note that the rightmost result on the bottom row is the combined results from each 7 day simulation.

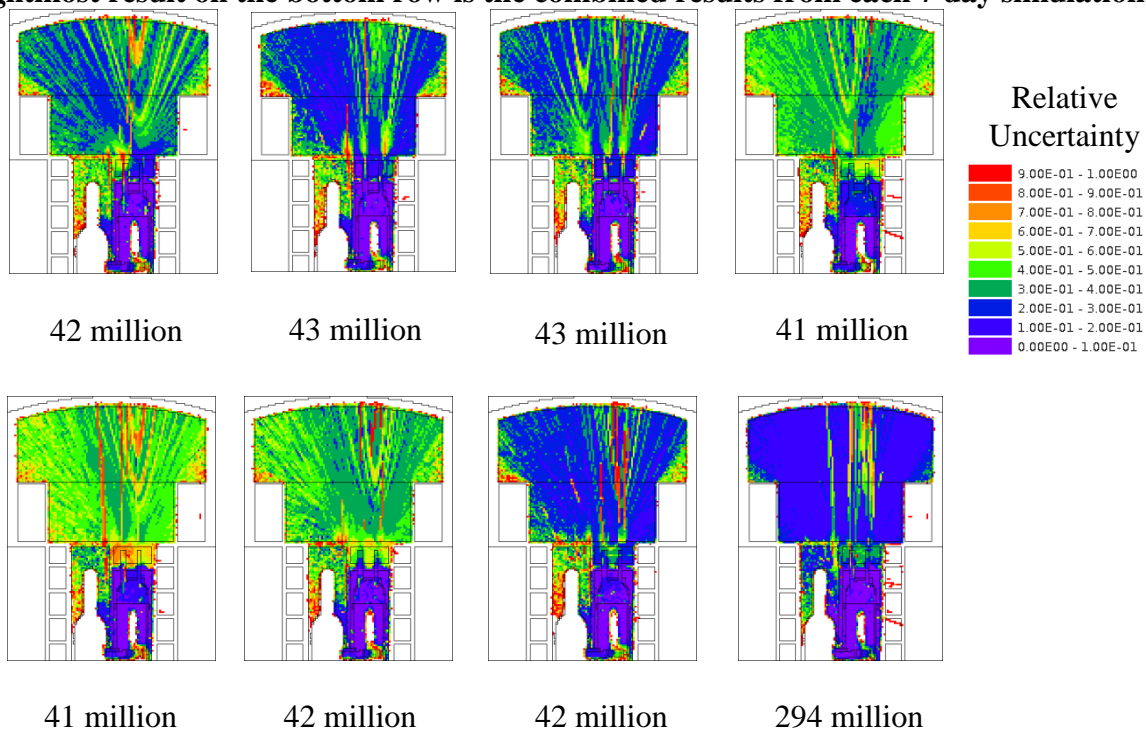


Figure 68. The total gamma and neutron dose uncertainty for each week-long simulation.

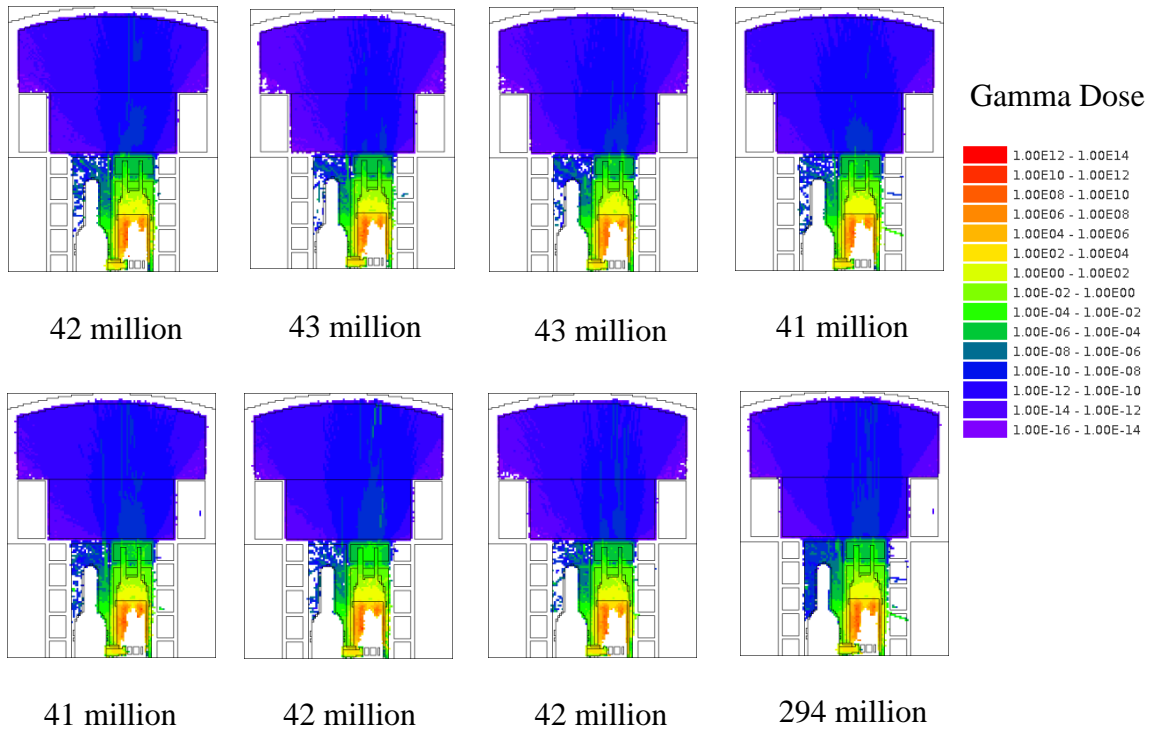


Figure 69. The total gamma dose for each week-long simulation.

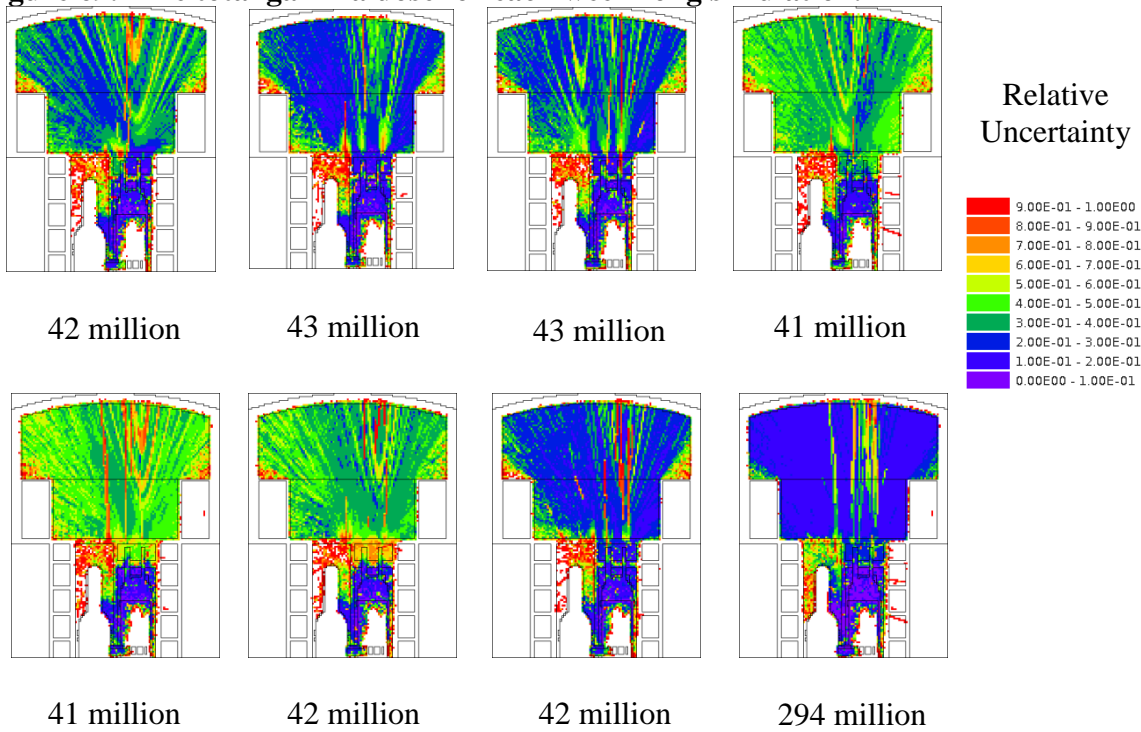


Figure 70. The total gamma dose uncertainty for each week-long simulation.

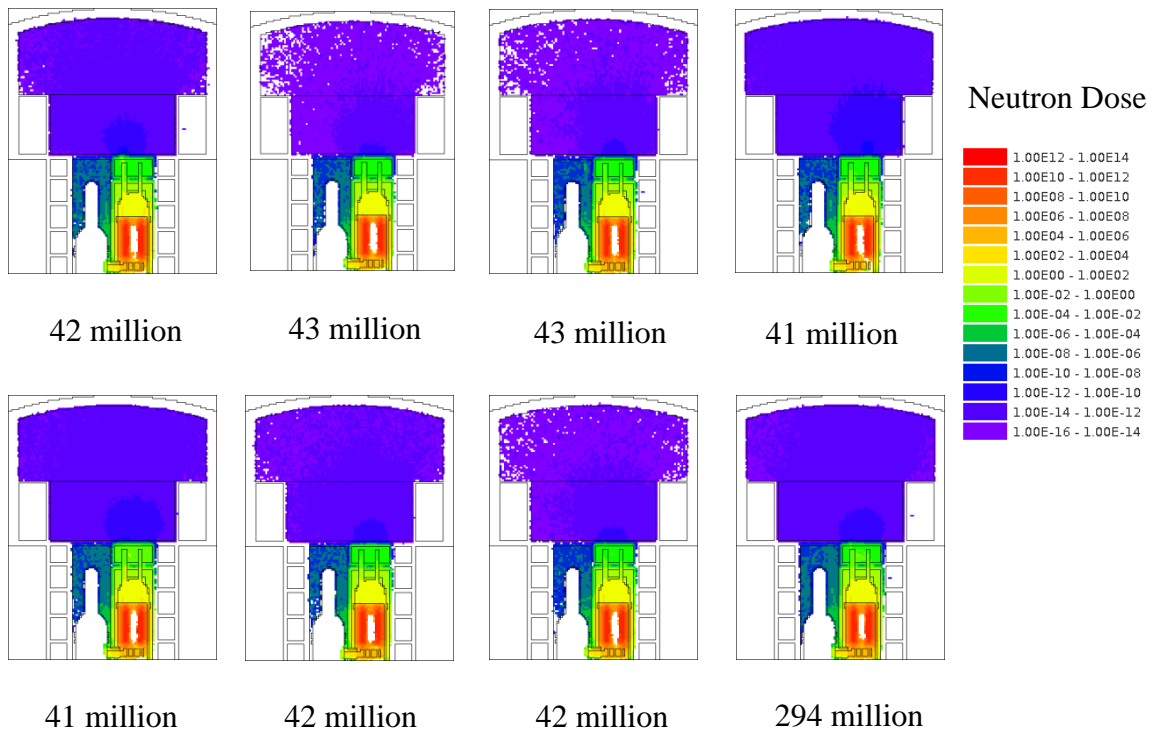


Figure 71. The total neutron dose for each week-long simulation.

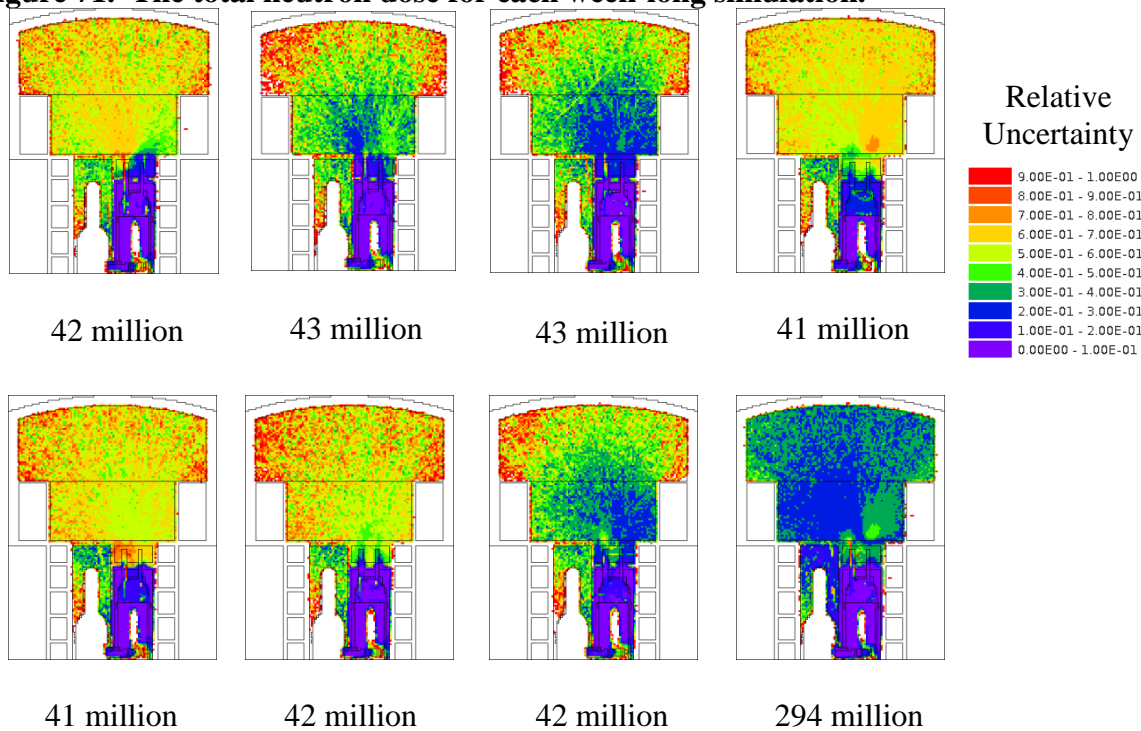


Figure 72. The total neutron dose uncertainty for each week-long simulation.

CHAPTER 8

TRITIUM PRODUCTION FROM CORE COMPONENTS

Tritium (^3H) is a radioactive isotope of the hydrogen atom with a half-life of over 12 years that decays by emitting a 18.590 keV beta particle. Being an isotope of the lightest element, tritium is difficult to contain within most atomic lattices. Therefore, it is of special concern due to its permeation through structural materials and eventual leakage into the secondary systems and out into environment (Ohashi, 2007). The VHTR design is slated to be able to supply a heat source to different industrial applications including hydrogen production. If tritium leakage to secondary systems is above EPA standards, the industrial side of the plant would then need to be licensed by the NRC. From an economics standpoint this would be very costly to the company using the process heat and would likely deter investment in the technology. Permeation models of tritium in the VHTR plant have very high levels of uncertainty. The main point of uncertainty is the source description from core components. Therefore, MAVRIC was used to demonstrate its ability to calculate accurate production rates using a full-core model.

Tritium production is dominated by ternary fission of the fuel. Other systematic pathways for tritium production come from reactions in the boron control rods, burnable absorbers and different reflector components as well as the helium coolant. Lithium and boron impurities naturally occurring in graphite add another more avoidable means of production which should be minimized as much as possible (Albenesius, 1959; Jacobs, 1968)

Ionized tritons are retained close to the site where the reaction producing them occurs. The Stopping and Range of Ions in Matter (SRIM) code uses a Monte Carlo technique to simulate ions moving through layers of differing materials in planar geometry. In ternary fission reactions, the average triton is born with an energy of 20 keV . Based on normal operating temperatures in carbon, the SRIM code calculated the range of triton atoms to be $2.07\mu\text{m}$. Based on Table 10, this is roughly two orders of magnitude less than the radius of the fuel kernel in the

TRISO particle ($175\mu\text{m}$). It can be safely assumed that tritons come to rest as tritium atoms at the production site. Thermal diffusion is enhanced by higher temperatures, but still limits the movement of tritium atoms within the primarily isotropic, carbon lattice structure. Radiation-induced fuel failure is assumed to account for the majority of tritium leakage to the coolant. The leakage rate from TRISO particles is then assumed to be dependent on the fuel failure fraction.

After being produced and diffusing within the core components, tritium may enter the coolant. Being an isotope of such a small size, tritium can easily permeate through the radiation-damaged, high-temperature core outside the nuclear island and ultimately contaminate hydrogen production or other secondary systems. Therefore, it is important to know how much is produced and how well it permeates through the system to reduce contamination. The current study does not focus on permeation, only production.

According to a report (Oh & Kim, 2011) released by INL in March of 2011 tritium generation in the core needs to be more accurately estimated in order to improve the overall contamination models for the entire industrial processes side of the theoretical plant. Another study (Ohashi, 2007) done in 2007 claims that the production rates followed by permeation would cause a level of contamination above regulatory standards. Reaction routes for tritium production and their availability within the Scale6.1 libraries are as follows:

Table 23. Important pathways of tritium production.

Process	MT #	Scale6.1
Ternary Fission	18 (x% yield)	YES
${}^6\text{Li} (n, \alpha) {}^3\text{H}$ or ${}^6\text{Li} (n, t) {}^4\text{He}$	107 105	NO YES
${}^7\text{Li} (n, n\alpha) {}^3\text{H}$ or ${}^7\text{Li} (n, nt) {}^4\text{He}$ or ${}^7\text{Li} (n, Xt)$	22 / 105 33	NO / NO NO *YES
${}^3\text{He} (n, p) {}^3\text{H}$	103	YES
${}^{10}\text{B} (n, 2\alpha) {}^3\text{H}$ or ${}^{10}\text{B} (n, t2\alpha)$	108 113	NO YES
${}^{10}\text{B} (n, \alpha) {}^7\text{Li} (n, n\alpha) {}^3\text{H}$	107 & 22	YES & NO

* Indicates taken from JENDL-4.0

Responses MT 201-207 take into account the total production of different charged particles of any amount, but are not included in the library. Having these available would eliminate the need to calculate some reactions separately. Also note that ${}^7\text{Li}(n,Xt)$ reaction rate has been used in the past to produce tritium for the weapons programs, which could be the reason that it is not included in the ENDFB-VII Library. The reaction rate was pulled from the JENDL-4.0 library.

One of the pathways for tritium production in boron is the two-step reaction ${}^{10}\text{B}(n,\alpha){}^7\text{Li}(n,\alpha)t$ shown in Table 23. The production rate is time-dependent based on the production of ${}^7\text{Li}$ via ${}^{10}\text{B}$. A set of rate equations involving the production and depletion of each isotope must be considered to derive the final time-dependent reaction rate. The flux is considered to not be dependent on time. Cross sections are processed as flux-averaged based on the total average flux in each material being calculated.

$$\sigma_a = \sigma_t - \sigma_s = \text{total absorption cross section or depletion of isotope}$$

$$\sigma_t = \text{total cross section}$$

$$\sigma_s = \sigma_{el} + \sigma_{in} = \text{total scattering cross section (elastic + inelastic)}$$

In the derivation for the tritium-producing reaction rate in ${}^7\text{Li}$ via production from ${}^{10}\text{B}$, microscopic reaction rates are assumed to be collapsed over all energy groups given by,

$$\sigma_n = \frac{\sum_g^G \phi_g \sigma_{ng}}{\phi}, \quad (22)$$

where,

$$\phi = \sum_g^G \phi_g. \quad (23)$$

Boron is a stable isotope and it is assumed that no ^{10}B is being created in fission or by any other reaction. The depletion of boron is written without production or decay as,

$$\frac{dN_{10B}(t)}{dt} = - \int_E \phi(E) \sigma_{10Ba}(E) N_{10B}(t) dE = -\phi \sigma_{10Ba} N_{10B}(t). \quad (24)$$

Using the same logic, the time-dependent concentration of the stable isotope ^7Li with production from ^{10}B would be,

$$\frac{dN_{7Li}(t)}{dt} = \phi \sigma_{10B(n,\alpha)^7Li} N_{10B}(t) - \phi \sigma_{7Li\alpha} N_{7Li}(t). \quad (25)$$

These coupled differential equations can be solved by Laplace Transformation. The Laplace integral is defined as,

$$\tilde{f}(s) = \int_0^{\infty} f(t) e^{-st} dt. \quad (26)$$

Applying the Laplace transformation to Eq. 24 and 25 gives,

$$\begin{aligned} s\tilde{N}_{10B}(s) - N_{10B}(0) &= -\phi \sigma_{10Ba} \tilde{N}_{10B}(s), \\ s\tilde{N}_{7Li}(s) - N_{7Li}(0) &= \phi \sigma_{10B(n,\alpha)^7Li} \tilde{N}_{10B}(s) - \phi \sigma_{7Li\alpha} \tilde{N}_{7Li}(s). \end{aligned} \quad (27)$$

Solving each equation for the transformed concentration term yields,

$$\begin{aligned}\tilde{N}_{10B}(s) &= \frac{N_{10B}(0)}{s + \phi\sigma_{10Ba}}, \\ \tilde{N}_{7Li}(s) &= \frac{N_{7Li}(0)}{s + \phi\sigma_{7Li a}} + \frac{\phi\sigma_{10B(n,\alpha)7Li}}{s + \phi\sigma_{7Li a}} \tilde{N}_{10B}(s).\end{aligned}\quad (28)$$

Substituting the ^{10}B term from the first equation into the second gives the transformed ^7Li concentration only dependent on initial concentrations,

$$\tilde{N}_{7Li}(s) = \frac{N_{7Li}(0)}{s + \phi\sigma_{7Li a}} + \frac{\phi\sigma_{10B(n,\alpha)7Li}}{s + \phi\sigma_{7Li a}} \frac{N_{10B}(0)}{s + \phi\sigma_{10Ba}}. \quad (29)$$

In order to take the inverse Laplace transform of the second term, it must be rewritten using partial fraction decomposition as,

$$\tilde{N}_{7Li}(s) = \frac{N_{7Li}(0)}{s + \phi\sigma_{7Li a}} + \frac{\phi\sigma_{10B(n,\alpha)7Li}N_{10B}(0)}{(\phi\sigma_{7Li a})^2 + (\phi\sigma_{10Ba})^2} \left(\frac{\phi\sigma_{10Ba} - \phi\sigma_{7Li a}}{s + \phi\sigma_{7Li a}} + \frac{\phi\sigma_{7Li a} - \phi\sigma_{10Ba}}{s + \phi\sigma_{10Ba}} \right), \quad (30)$$

or,

$$\begin{aligned}\tilde{N}_{7Li}(s) &= \frac{N_{7Li}(0)}{s + \phi\sigma_{7Li a}} \\ &+ \frac{\phi\sigma_{10B(n,\alpha)7Li}N_{10B}(0)}{(\phi\sigma_{7Li a})^2 + (\phi\sigma_{10Ba})^2} (\phi\sigma_{10Ba} - \phi\sigma_{7Li a}) \left(\frac{1}{s + \phi\sigma_{7Li a}} - \frac{1}{s + \phi\sigma_{10Ba}} \right).\end{aligned}\quad (31)$$

Finally, taking the inverse Laplacian of both sides of the equation yields the time-dependent ^7Li concentration to be,

$$N_{7Li}(t) = N_{7Li}(0)e^{-\phi\sigma_{7Li}t} + \frac{\phi\sigma_{10B(n,\alpha)7Li}N_{10B}(0)}{(\phi\sigma_{7Li})^2 + (\phi\sigma_{10Ba})^2}(\phi\sigma_{10Ba} - \phi\sigma_{7Li})(e^{-\phi\sigma_{7Li}t} - e^{-\phi\sigma_{10Ba}t}). \quad (32)$$

The tritium-producing reaction rate is simply,

$$R = \phi\sigma_{7Li(n,nt)a}N_{7Li}(t) = \phi\sigma_{7Li(n,nt)a} \left\{ N_{7Li}(0)e^{-\phi\sigma_{7Li}t} + \frac{\phi\sigma_{10B(n,\alpha)7Li}N_{10B}(0)}{(\phi\sigma_{7Li})^2 + (\phi\sigma_{10Ba})^2}(\phi\sigma_{10Ba} - \phi\sigma_{7Li})(e^{-\phi\sigma_{7Li}t} - e^{-\phi\sigma_{10Ba}t}) \right\}. \quad (33)$$

Obviously, the time-independent code being used cannot calculate this time-dependent, two-step reaction rate. But it can solve for reaction rates and flux values so that the information can be easily post-processed to yield results. Additionally, the tritium source would require an additional rate equation to be derived including the decay of tritium. Since previous studies on permeation to secondary systems generally assume that the tritium is instantaneously permeated through the core it was assumed to not be critical. Also, the focus of the study is on the MAVRIC performance within the VHTR design related to production.

Core and Source Description

Tritium production requires a more detailed core to be defined than used previously. The design report from which the original model was based did not specify materials for the burnable boron absorbers placed within fuel blocks or material impurities. The boron absorbers are assumed to be one of the main contributors to tritium production, and therefore need to be included in the model. Dan Ilas (personal communication, 2011) at ORNL provided a model used from a Triton fuel depletion calculation. The model had to be adapted since it was based on

reflective geometry as shown in Figure 73, which uses a 1/6 radial model at a height of only one fuel block. The depletion model also does not contain regions for control rod insertions which were included in the MAVRIC model. Additionally, MAVRIC does not have the ability to treat the double heterogeneity of TRISO fuel pellets within a fuel compact, as is the case in the Triton sequence. Therefore, TRISO pellets were again homogenized as well as the burnable absorbers to preserve isotopic composition uniformly across the fuel compacts. Lithium impurities were also added to the core graphite. Table 24 gives the material compositions used to replace fuel regions, burnable poisons, and core graphite components.

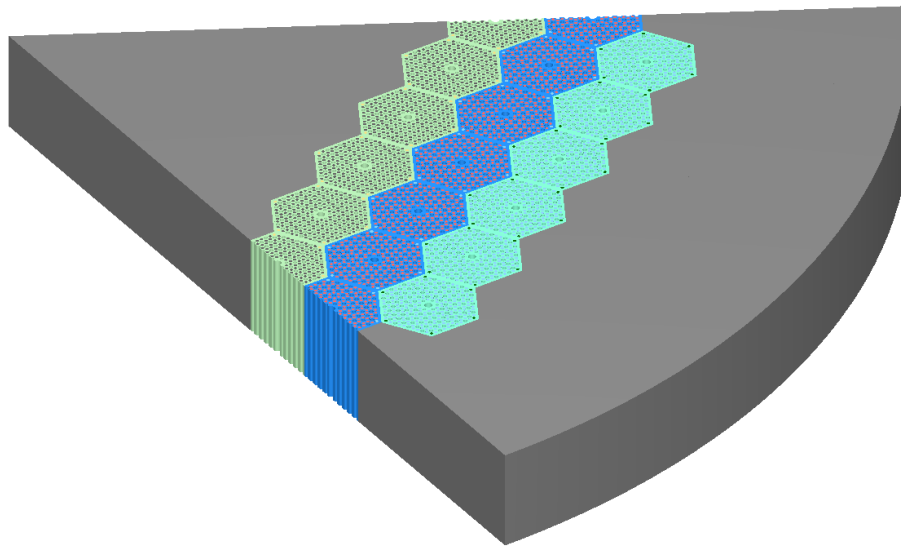


Figure 73. 1/6 core reflective core geometry from Dan Ilas.

Table 24. Material descriptions adapted from Triton depletion calculation (a/b•cm).

	Fuel Compacts	Burnable Absorbers	Core Graphite
U-234	5.15669E-07	-	-
U-235	6.71673E-05	-	-
U-238	5.73317E-04	-	-
O-16	9.61500E-04	-	-
C-graphite	6.16851E-02	6.24123E-02	8.72433E-02
B-10	4.36000E-07	1.58597E-04	4.36000E-07
B-11	-	1.60337E-05	-
Li-6	-	-	7.50000E-08
Li-7	-	-	9.25000E-07
Si	2.74368E-03	-	-

After defining new geometry and materials a new mesh-based fission source had to be generated using the KENO-VI sequence. Figure 74 shows the new fission source compared to the old using the same relative scale. The purpose of loading the core with poisons is to flatten the peaking of the flux from the inner blocks to the outer edge, which is achieved when compared to previous results. The effective neutron multiplication for the full core case was $k=1.07745 \pm 0.00021$.

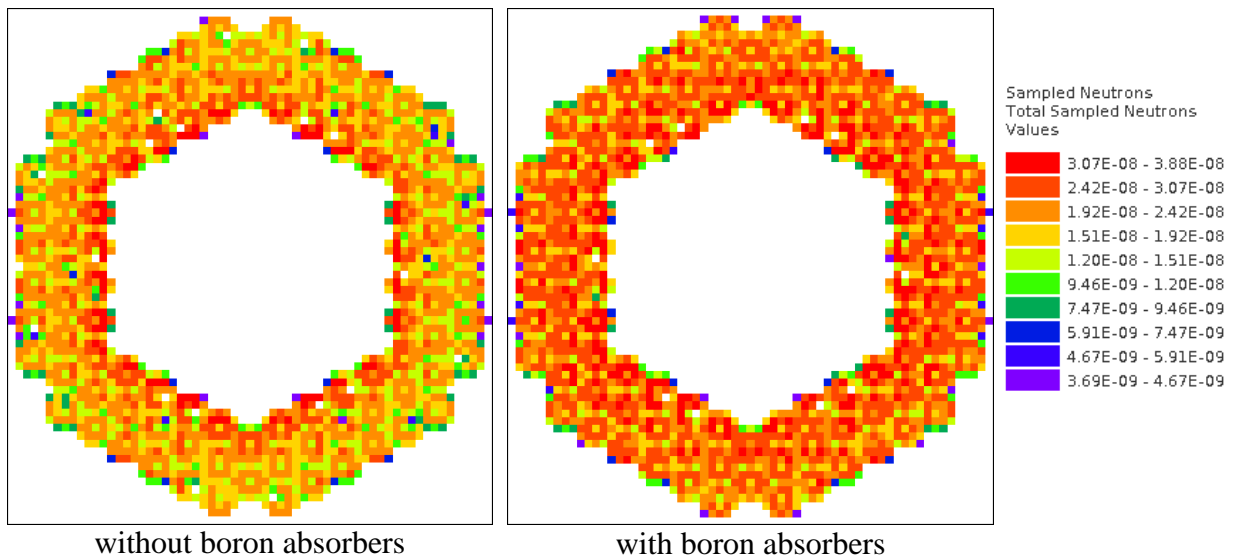


Figure 74. Neutron source comparison as simulated by KENO-VI.

Separate MAVRIC simulations were performed for each tritium pathway. Tallies were obtained in two manners for each reaction rate. The first tally is a region tally for a material over the entire model, in order to match literature. Previous studies found the production rates by using a flux-weighted cross section times the expected total scalar flux in a given material multiplied by that material's volume. These calculations are usually not accompanied with details of the assumptions used for the core configuration, the material compositions or the flux spectrum. The only information provided being simply the total scalar flux, cross section, and volume. It is expected that MAVRIC results from full-core tallies for a given material and reaction should loosely match these numbers within an order of magnitude. If past studies practiced conservative assumptions, MAVRIC region tallies should be a bit lower in magnitude

for each case. The second tally generated by MAVRIC was mesh tallies showing the distribution of each reaction rate within the geometry. The same mesh was used for each case, to provide a basis for comparison. Viewing the mesh tally is helpful for analysis, but also for ensuring that neutrons were properly sampled in the region of interest by the importance map.

Deterministic DENOVO Model

The adaptability of MAVRIC is showcased in the simulation of tritium production. For each reaction the input file only needs a few parameters to be changed in order to optimize the importance map. Since MAVRIC can be stopped after the solving of the forward flux by Denovo, it only needed to be solved once and the results could be used for each case. Therefore, time was not wasted between simulations solving for the forward flux each time. The deterministic portions were run over 16 processors further decreasing the time required by Denovo. Table 25 gives the important parameters for the Denovo portion of solving the forward flux. The results are shown in Figure 75. The top views are at elevations showing the inlet plenum, the core centerline and the outlet plenum.

Table 25. Denovo parameters.

Denovo	
<i>Global Dimensions</i>	
X (max, min, total)	(400, -400, 800) cm
Y (max, min, total)	(400, -400, 800) cm
Z (max, min, total)	(963.2, -425.2, 1388.4) cm
Volume	888,576,000 cm ³
Meshing (X*Y*Z=total)	(140x140x248 = 4,860,800 voxels)
Average Voxel Size	182.80 cm ³
<i>Parameters</i>	
Quadrature sets (S _N)	8
Legendre polynomials (P _L)	3
Krylov space size	10
Processors	16
Forward Time (hours)	1.45
Forward CPU Time (hours)	23.22

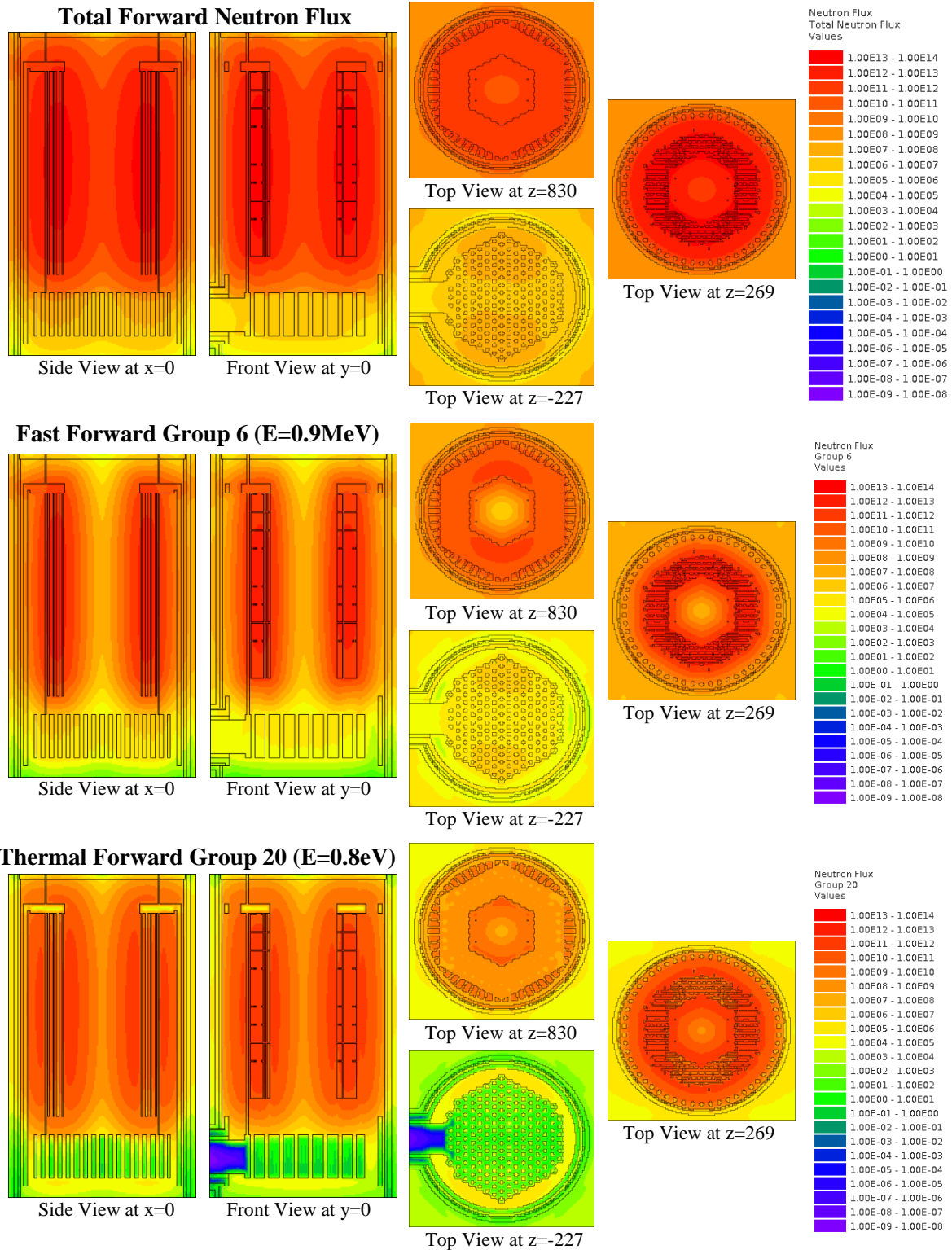


Figure 75. The total forward neutron flux with both a fast and thermal group shown.

Ternary Fission

Ternary fission releases tritium as a by-product. It is measured as the percentage yield of total fissions for a given isotope that release a triton. Different values have been suggested, but according most studies suggest the ratio of fission-to-tritium was 1×10^{-4} . Therefore, the tritium production is proportional to the fission source with the proportionality factor equal to the inverse of the above ratio, i.e., 1×10^4 tritons/fission. On a global scale the tritium production rate from ternary fission would be found from the reactor power. An HTGR with a 600 MWt power would produce tritium from ternary fission at a rate of:

$$600MWt \cdot \frac{\frac{MJ}{s}}{MW} \cdot \frac{MeV}{1.6021(10^{-19})MJ} \cdot \frac{fission}{200MeV} \cdot \frac{1.00(10^{-4})\ ^3H}{fission} = 1.827(10^{15}) \frac{n}{s} \quad (34)$$

While being redundant, MAVRIC can easily simulate this by using a multiplier coupled with the total fission reaction rate within the active fuel regions and integrating over the entire volume of the core for verification. Ternary fission should be the simplest pathway to calculate, since source particles are born in the region being calculated by the reaction of interest. The results should match the mesh-based source description from KENO-VI. Additionally, the overall integrated tritium production by ternary fission reaction rate calculated by MAVRIC should match very closely the calculation based on the source power inputted by Eq. 34. Figure 76 shows the mesh-based tritium production via ternary fission.

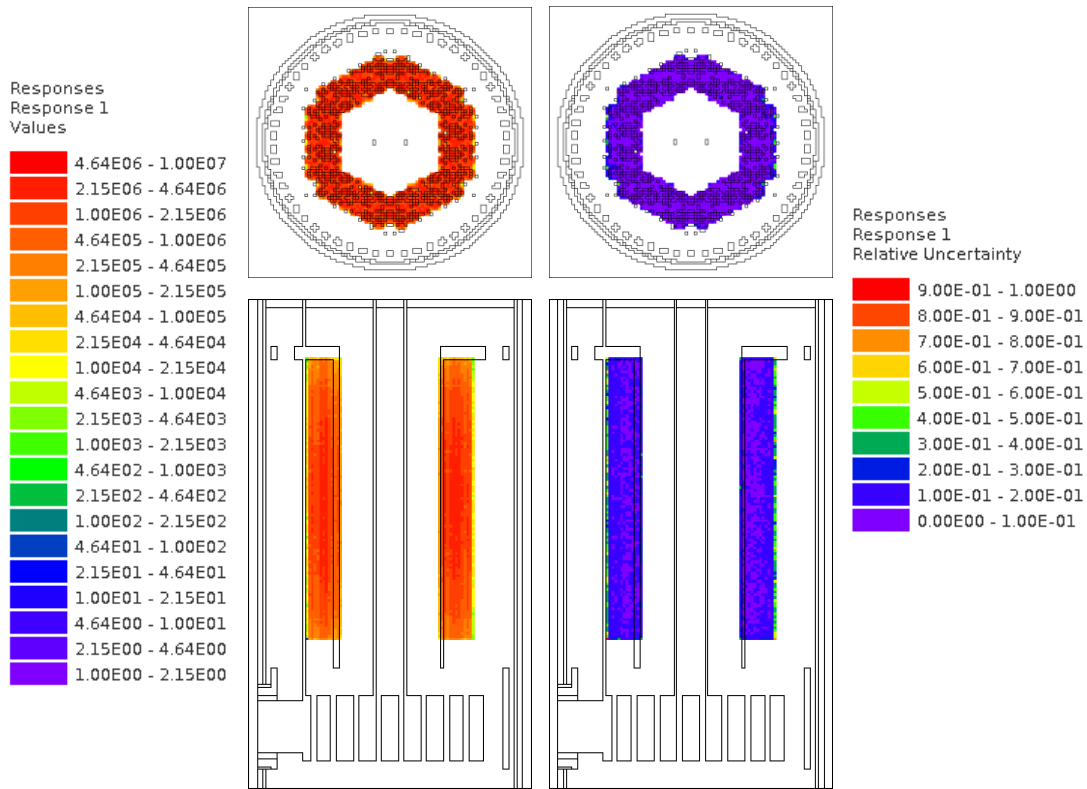


Figure 76 - (Top) Top view of the mesh-based ternary fission tritium production. (Bottom) Front view.

MAVRIC found the tritium production from ternary fission to be $1.824(10^{15}) \pm 0.00081$ t/s. Based on the fixed-source strength, the production should be $1.827(10^{15})$ t/s a difference of 0.13%. One important difference in the KENO-VI simulation generating the mesh-based fission source and the MAVRIC simulation using that source, is the cross section used for the fuel region. When processing cross sections, KENO-VI was allowed to perform a resonance self-shielding calculation to correct for the double heterogeneity of the fuel compacts. MAVRIC does not have the ability to correct for this yet and the fuel is left as a homogenized compact. As a homogenized region the uranium is dispersed evenly through the entire compact, making each uranium atom more likely to encounter a neutron. Since neutrons are not multiplied in MAVRIC, fission events are really seen as absorption events. The fast spectrum should be unchanged, but neutrons have a greater probability to be absorbed in the process of thermalizing. The overall effect of self-shielding was found to be negligible in terms of calculating the ternary

fission yield in the core. It is safe to assume that it has a minor effect on calculating other tritium production parameters within the core and shielding components.

Burnable Absorbers

Based on studies by Ohashi and Sherman, boron absorbers and control rods would be the next most-likely path for tritium production (Oh & Kim, 2009). Referring to Table 26 the two pathways of tritium production from boron are $^{10}\text{B} (n, t\alpha)$ and the two-step reaction $^{10}\text{B} (n, \alpha) ^7\text{Li} (n, X_t)$. Figure 77 shows each reaction cross section with the total cross sections for each isotope to get an idea of the magnitudes. Additionally, Figure 78 shows a CDF of each reaction rate based on these cross sections to give an idea of how important each portion of the energy spectrum is for the total reaction. The CDF is considered to be the normalized contribution of the portion of the spectrum integrated from zero to the current energy.

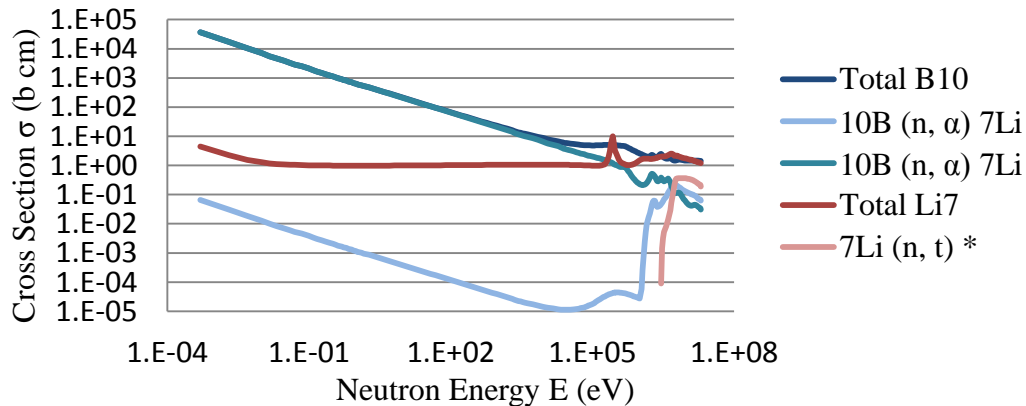


Figure 77. Important cross sections for tritium production via ^{10}B and ^7Li .

Notice that in Fig. 49 the CDF for total, absorption, and $^{10}\text{B}(n,\alpha)^7\text{Li}$ are almost exactly overlapping. These reactions are dominated by the thermal spectrum. Additionally, the ^7Li absorption cross section follows the same distribution. The reactions producing tritium of importance are $^{10}\text{B} (n, t\alpha)$ and $^7\text{Li} (n, X_t)$. These two reactions have little importance in the thermal range. The $^7\text{Li} (n, X_t)$ reaction is a fast threshold reaction with no response below 2.86

MeV. The ^{10}B (n, t 2α) reaction has about one quarter of its response in the thermal range with the remaining three-quarters being produced by the fast spectrum. The CDF comparison does not demonstrate the relative magnitude of each reaction's response compared with the others, but only demonstrates the importance of each energy portion of the neutron spectrum.

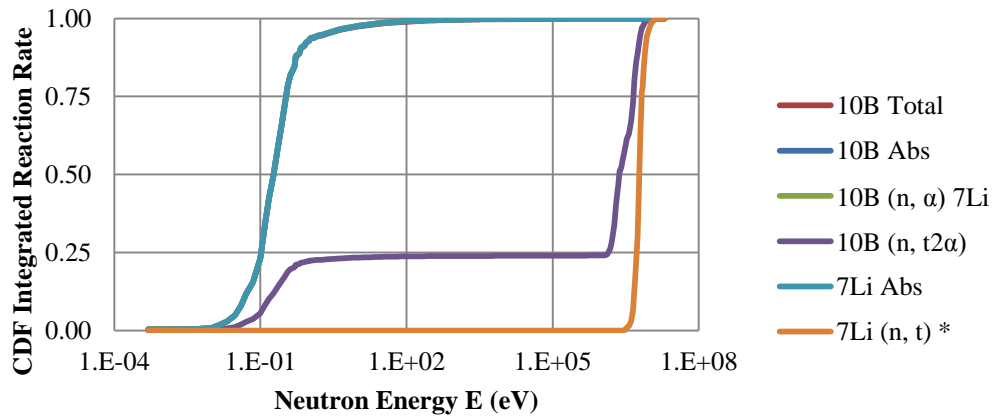


Figure 78. Cumulative Distribution Function of the reaction rates relative to tritium production from ^{10}B .

Since burnable absorbers are within the core, no importance map was used to obtain the results. The simulation is not one of deep shielding, but more similar to reactor physics quantities obtained from criticality calculations. Solving for an importance map should converge statistics faster, but would also cost extra time that was assumed to be unnecessary.

Figure 79 shows a mesh tally for the tritium production by the ^{10}B (n, t 2α) reaction alone within the burnable absorber regions. It is important to ensure that results are as desired when taking global tallies within specific regions, and mesh tallies are a very useful tool towards this goal. These tallies may also be of use in improving tritium permeation models by having an actual spatial distribution within the core, instead of assuming an essentially homogenous reactor. The top and bottom axial portion in Figure 79 show high and varying uncertainties. One issue with overlaying a mesh tally over more complicated non-Cartesian, geometries is that meshes may only contain a small fraction of a region being tallied, which can be harmful for

statics in the voxel. While the mesh-based tally is not as precise as the exact model, the distribution of burnable absorbers within the fuel elements and annular core can be distinguished.

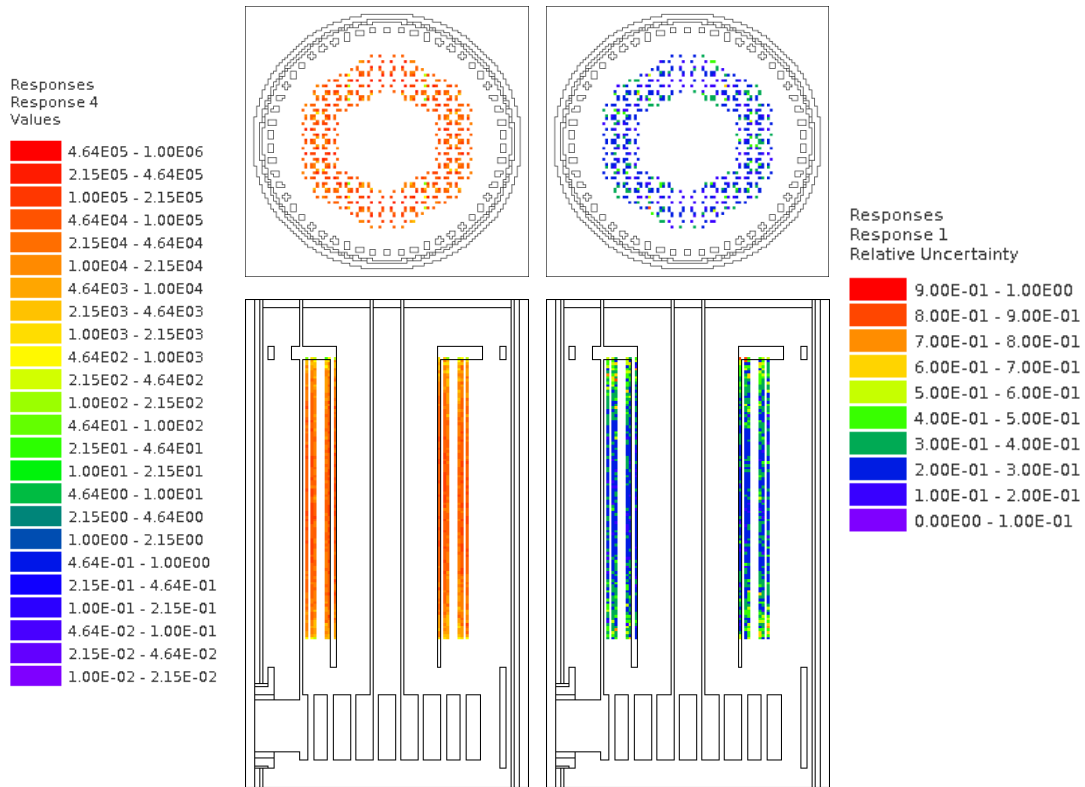


Figure 79. Views of the spatial tritium production rate in burnable absorbing rods by the $^{10}\text{B}(n,t)$ reaction as calculated by a standard MC simulation for 1 day.

Figure 80 shows a mesh tally using the same $^{10}\text{B}(n, t_2\alpha)$ reaction rate, but for the regions containing the reflector graphite within a standard MC simulation. Notice that the high levels of uncertainty that were shown in the extreme axial regions of the burnable absorbers in Figure 79 are not seen in the same voxel locations in Figure 80. As mentioned above, the main reason for the statistical variation is the amount of each region contained within each voxel. The core graphite makes up the majority of each voxel, so statistics will be better converged when looking at these regions.

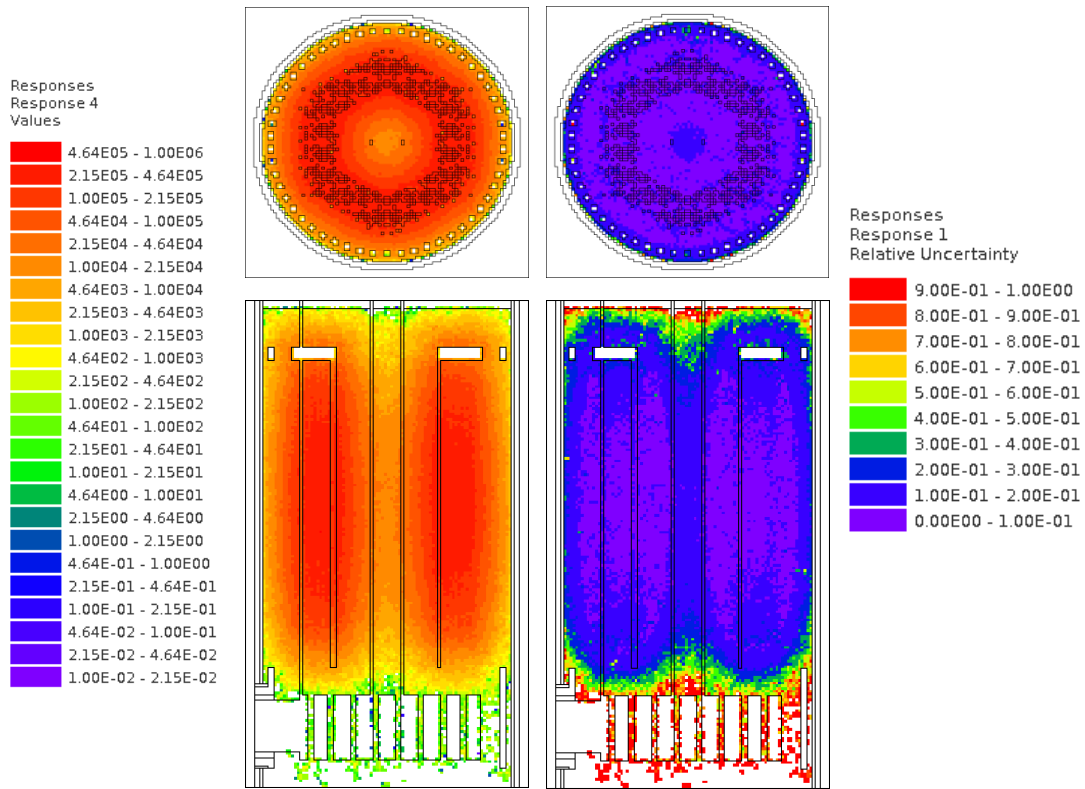


Figure 80. Views of the spatial tritium production rate in the graphite reflector by the $^{10}\text{B}(n,t)$ reaction as calculated by a standard MC simulation for 1 day.

The tritium production was calculated by summing the $^{10}\text{B}(n, t2\alpha)$ and $^7\text{Li}(n, Xt)$ reactions. The reaction rates are time-dependent and were calculated by folding the overall flux with each reaction rate for the entire region's volume. The overall, track-length estimated neutron flux energy distribution is shown in Figure 81. The total neutron flux in the absorber regions was found to be $1.16012\text{E} + 20 \pm 0.19\% \text{ n/cm}^2\text{s}$. The overall reaction cross section for the $^{10}\text{B}(n, \alpha) ^7\text{Li}$ reaction was found to be 0.00435 b. Normally, the cross section would be reported for only the important portion of the spectrum. If the flux is only folded over the thermal cross section below ($< 2.38 \text{ eV}$), the reaction cross section would be 1,356 b over a total thermal neutron flux of $4.67447\text{E} + 19 \pm 0.44\% \text{ n/cm}^2\text{s}$. The remaining reaction cross sections are compiled in Table 26.

Table 26. Important overall tritium-producing reaction cross sections averaged over the flux spectrum.

Reaction	Cross Section (b)	Energy Range (eV)	Neutron Flux (n/cm ² s)
¹⁰ B (n, α) ⁷ Li	1,356	0-2.38	4.67E+19 ± 0.44%
¹⁰ B (n, t2α)	0.0180	>0.18(10 ⁶)	1.56E+17 ± 2.95%
⁷ Li (n, Xt)	0.00732	>0.18(10 ⁶)	1.56E+17 ± 2.95%

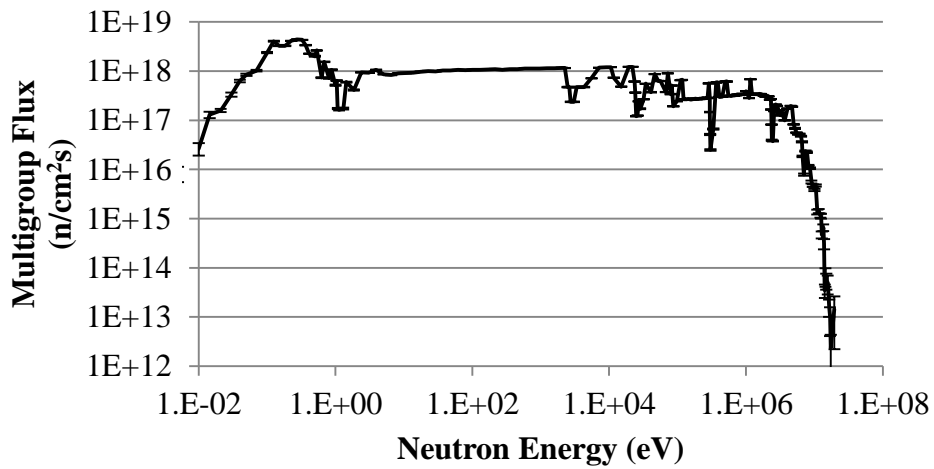


Figure 81. The neutron flux energy distribution within the burnable absorbers.

Since the ⁷Li tritium production rate is time-dependent and based on neutron capture by ¹⁰B, their combined results are presented simultaneously. Using Eq. [33], the tritium production can be found based upon time using the total cross sections given in Table 26. At t=0 the maximum combined production occurs due to ¹⁰B and is 8.02e13 ± 0.35%. For overall simulations of tritium permeation, this maximum number should be used. Figure 82 shows the time-dependence of the reaction rate in the burnable absorber elements. The total production rate by both isotopes drops by a factor of 3 from the initial value, due to the fact that the tritium producing ⁷Li reaction partly substitutes the ¹⁰B(n,t) reaction.

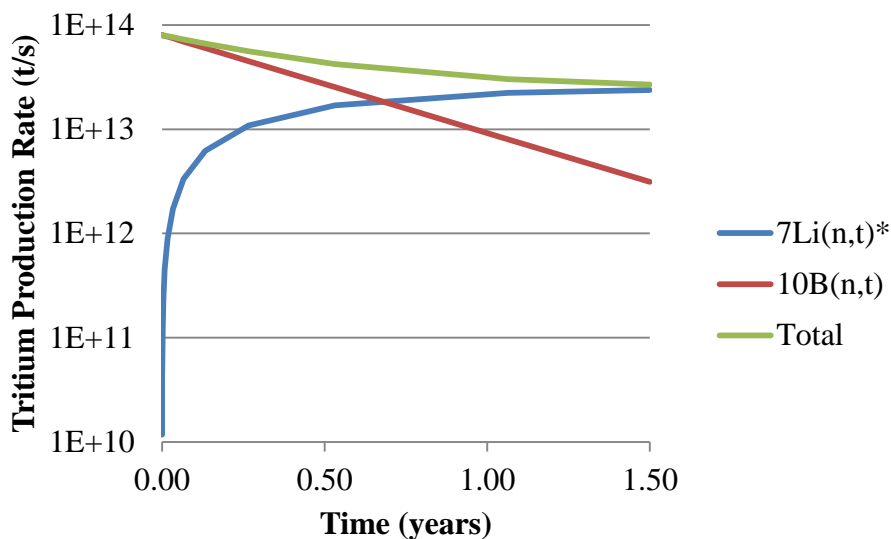


Figure 82. The time-dependent, total tritium production rate in the burnable absorbers.

Control Rods

Control rods follow a similar experience to that of the burnable absorber elements. The main difference is in the weight percent of ^{10}B starting in each material. The burnable absorber elements only contain 0.2% ^{10}B , while the control rods are 27.5% ^{10}B . Therefore, the overall absorption in control rods from boron would be over 2 orders of magnitude higher, without accounting for higher self-shielding effects within the interior radius of the rods. Neutrons will have shorter mean free paths and the thermal neutron fluence will become depressed in the center of the control rods. Again to obtain results in the control rods, standard MC was used since the locations are very close to fixed-source.

Since the effective neutron multiplication was close to 1, the control rods were not inserted in normal simulations, and the region was assumed to be filled with helium coolant. The flux was tallied in these regions. Such tallies are expected to drastically overestimate the tritium production within these regions, since the self-shielding effects are ignored. Calculating in this manner is similar to distributing all the boron from the rod at the surface so that each boron atom in the volume would see the same incoming neutron fluence. Operating rods are assumed to be

on the outer edge of the annular core as shown in Figure 21. A mesh tally is shown below demonstrating the distribution as calculated by MAVRIC.

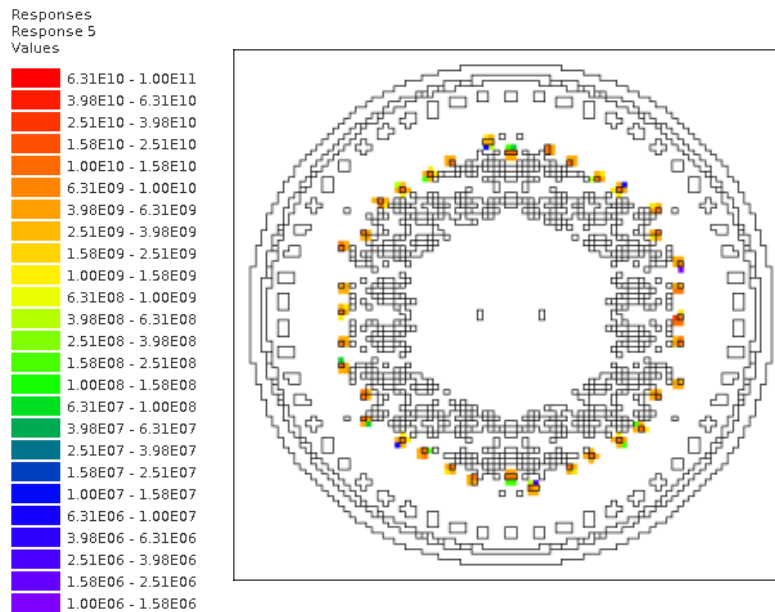


Figure 83. Top view of the spatial tritium production rate in inserted control rods as via by the $^{10}\text{B}(n,t)$ reaction as calculated by a standard MC simulation for 1 day.

Ignoring self-shielding effects, the tritium production rate from the control rods due to ^{10}B was found to be $1.6(10^{16}) \pm 0.02\%$ t/s. An insertion rate of 11% is assumed, making the tritium production rate on average to be $1.75(10^{15}) \pm 0.02\%$ t/s, which is greater than the production by ternary fission. This estimate, however, is not valid since self-shielding effects were ignored. In order to obtain a more realistic solution accounting for the flux depression, the actual control rod material needs to be included in the model. A run was performed with the adjoint source region defined as a specific control rod directly above the reactor as shown in Figure 84. The figure also shows the relative uncertainty in the calculation. The adjoint source spectrum was set as a flat spectrum in order to obtain results over the entire spectrum for multiple reactions.

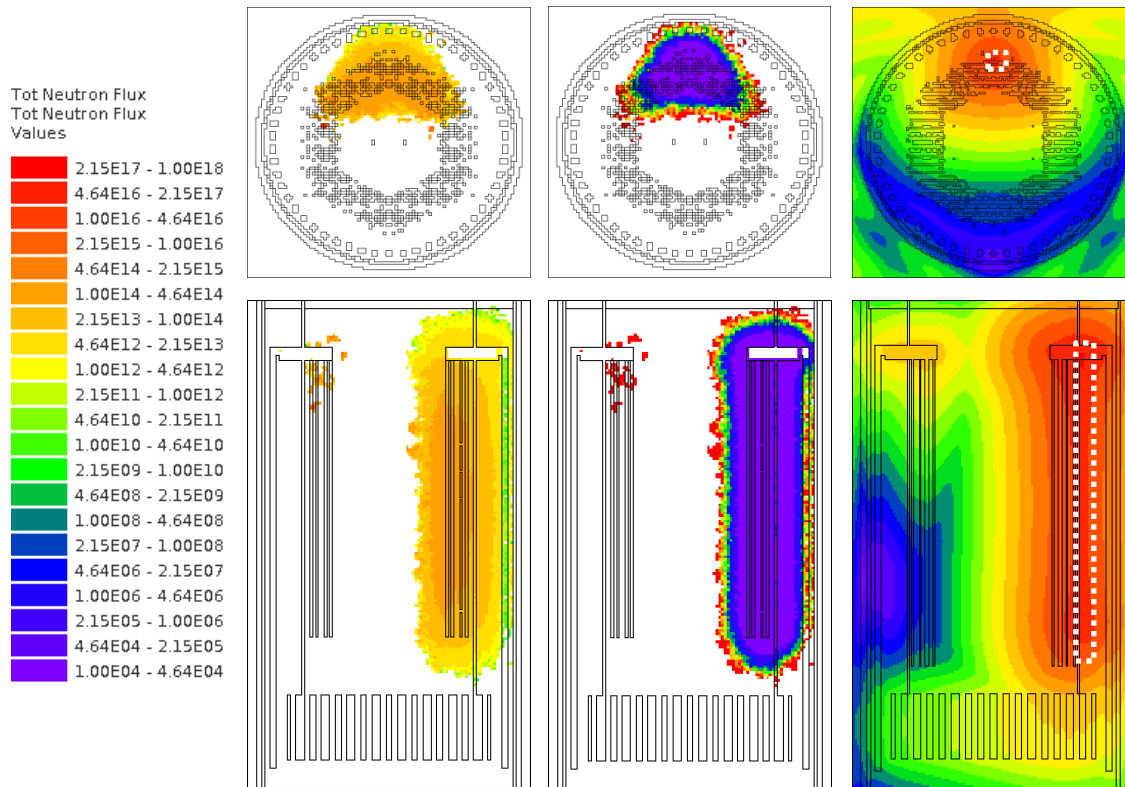


Figure 84. The FW-CADIS weighted MC flux (Left) with relative uncertainty (center). The total adjoint flux showing the source region where the specific control rod was located (right).

A distribution of the relevant reaction rates over the control rod is shown in Figure 85. Using a very fine mesh leads to a larger amount of noise between voxels, but statistics are generally well converged. Boron has a high thermal cross section, so the fast reaction rates see less of an effect by the inclusion of boron. In reality a new fixed-source distribution would need to be used, since the outer regions of the annular core would have a depressed flux due to the thermal neutron absorption. Figure 86 shows the radial attenuation of the thermal $^{10}\text{B}(n, \alpha)^7\text{Li}$ reaction rate alongside a graph demonstrating the thermal neutron fluence being depressed. The majority of thermal neutrons are absorbed within a short distance. The mean free path of a thermal neutron in the control rod material is .012 cm.

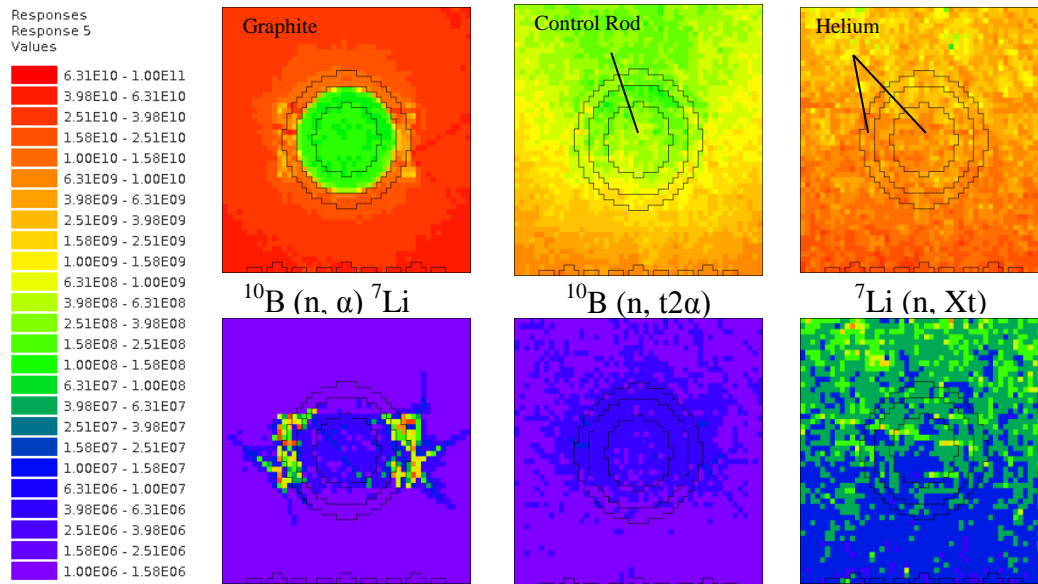


Figure 85. Reaction rate distribution around an inserted control rod.

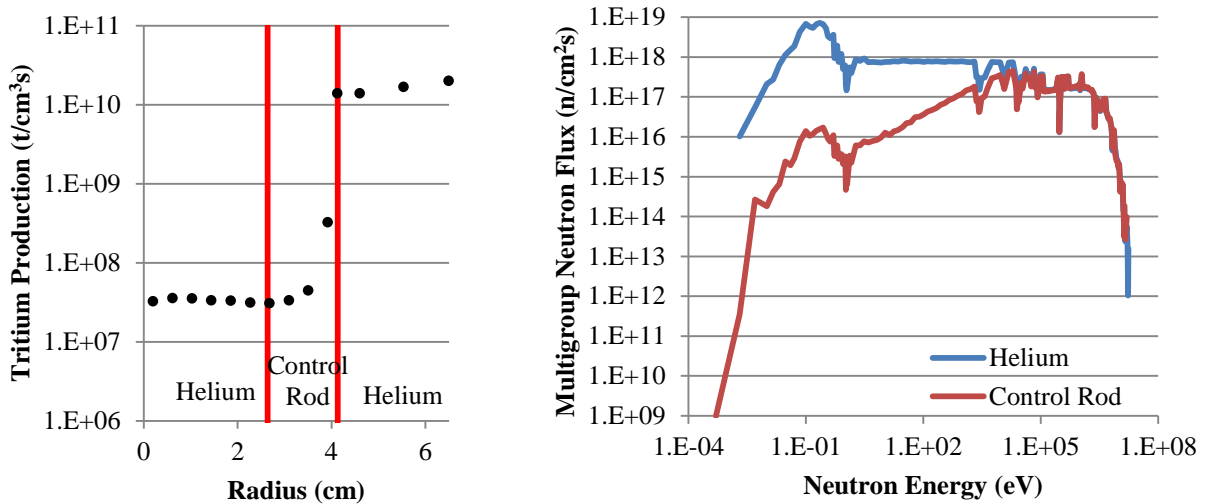


Figure 86. (Left) The $^{10}\text{B} (n, \alpha) ^7\text{Li}$ reaction rate distribution in a typical annular operating rod. (Right) The total track-length estimated neutron fluence spectrum for an operating rod, demonstrating the attenuation of the thermal neutron flux.

Using the control rod material, yields a tritium production rate in all control rod elements with an insertion percentage of 11% to be $7.74(10^{14}) \pm 0.12\% t/s$. Additionally, the reaction is time-dependent as was the case in burnable absorbers. The time-dependent reaction rate for

both reactions is given in Figure 87. Notice that unlike the production reaction in the burnable absorbers, the ^7Li reaction is never a significant contributor. Over the 1.5 year cycle assumed, the ^{10}B concentration is only depleted by 1.8%.

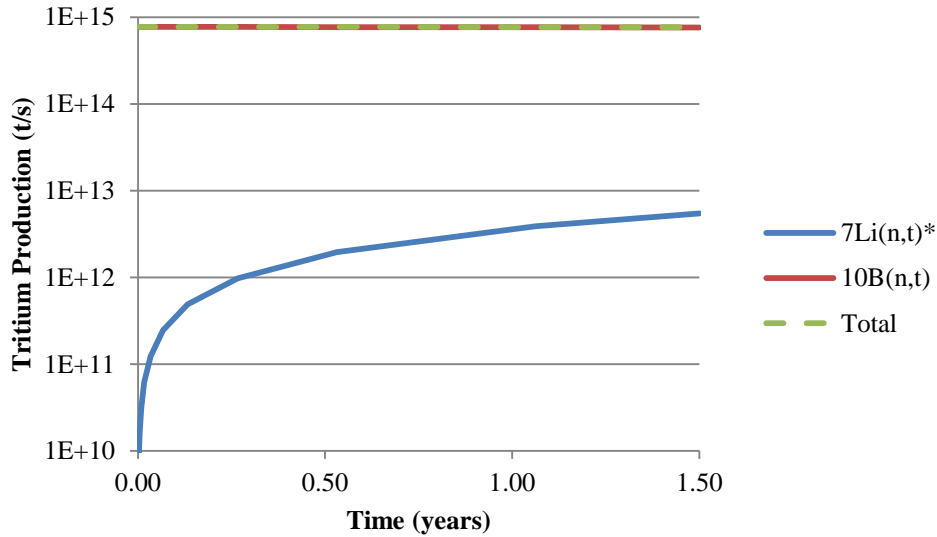


Figure 87. The time-dependent, tritium production rate in the operating control rods assuming an 11% insertion factor.

Graphite Impurities

Impurity content within core components is the only source that can be controlled without affecting the design of the core. The actual assumptions for impurity concentration scale the results and are a means of production that should be closely watched. ASTM standards only specify the boron concentration to be regulated in nuclear grade graphite, since it most significantly affects thermal neutrons. The assumed values of graphite impurities were assumed to be 1, 0.007 and 0.0863 ppm for ^{10}B , ^6Li and ^7Li .

When using MAVRIC to obtain a relative uncertainty for reaction rates occurring over the entire graphite reflector region due to impurities, the FW-CADIS methodology does not perform as well for thermal reactions in this particular model. The majority of the simulation is spent attaining results in the deepest shielding portions of the problem space, which is in the bottom reflector below the outlet plenum as can be seen in Figure 90. The biased source almost

completely neglects the center of the core both axially and radially. Additionally, the annular core is unique to this type of HTGR design and presents a new different issue, since the center of the core is a relatively deep-shielding problem.

When using FW-CADIS, the practitioner must ensure that proper care is taken when interpreting results, because an overall volume tally of the core graphite may give low uncertainty while neglecting a large part of the problem. When tallying over a large area, results may come from a large number of particles being simulated, but in actuality the portions being simulated have the lowest flux and contribute the least to the final region tally. The following section demonstrates this issue. For each reaction, a separate simulation was performed with the adjoint source set to the reaction rate within all graphite regions. The same forward neutron flux calculation was used for each case and each Denovo calculation was performed over 16 processors. Table 27 shows the MAVRIC performance for each case. The same meshing and quadrature set as in Table 25 were used for each adjoint calculation.

Table 27. The MAVRIC Performance.

		Adjoint Source Response Function			
		${}^6\text{Li}(n,t){}^4\text{He}$	${}^{10}\text{B}(n,\alpha){}^7\text{Li}$	${}^{10}\text{B}(n,t2\alpha)$	${}^7\text{Li}(n,Xt)$
Time (min)					
	Forward	87.09	87.09	87.09	87.09
	Adjoint	71.58	72.38	69.43	13.46
	Total Denovo	158.67	159.47	156.52	100.55
	Total MC	759.9	748.49	929.08	759.9
	Total	918.57	907.96	1085.60	860.45
MC Performance					
	Batches	5	14	3	100
	Particles (millions)	0.5	1.4	0.3	10
	Time/Particle (s)	0.091	0.032	0.18	0.0027

^6Li Impurities

Lithium-6 impurities produce tritium by the $^6\text{Li} (n, t) ^4\text{He}$ thermal reaction, which has a relatively high cross section. As given by Oh and Kim, the tritium production cross section in ^6Li is over 8,000 times higher than that of the $^{10}\text{B} (n, t2\alpha)$ reaction. Therefore, the production from ^6Li impurities should be the highest tritium producer amongst impurities. With the given thermal cross section, lithium impurities should be minimized as much as possible in the manufacturing process. Figure 88 compares the ^6Li cross section with other tritium-producing reactions relevant to the VHTR.

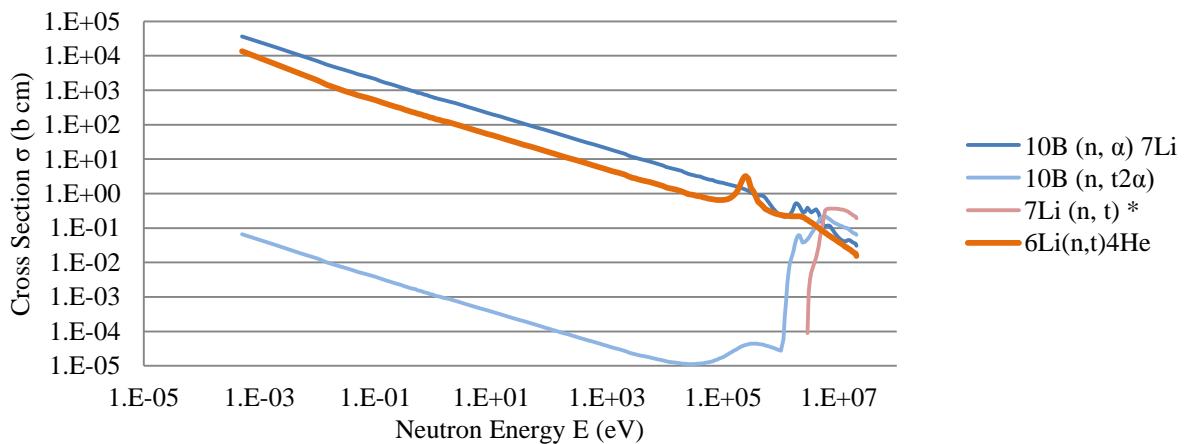


Figure 88. Important tritium-producing reaction cross sections, highlighting the $^6\text{Li} (n, t) ^4\text{He}$ reaction.

The FW-CADIS methodology implemented in this model is sensitive to thermal reactions and may perform poorly with respect to setting the adjoint source region to be the entirety of the core graphite. The total adjoint neutron flux, the fast adjoint neutron group 6 ($E=0.9\text{MeV}$) and the thermal neutron adjoint group 20 ($E=0.8\text{eV}$) can be seen in Figure 89. Weight windows are generated based on the adjoint fluxes. Additionally, the biased source is also based off of these calculations. The very bottom of the active core overlaps regions of adjoint neutron flux that are lower than the entirety of the region above. Since the biased source is based off of the inverse of the adjoint flux, these regions will be weighted over 5 orders of magnitude higher than the center of the fixed source axially.

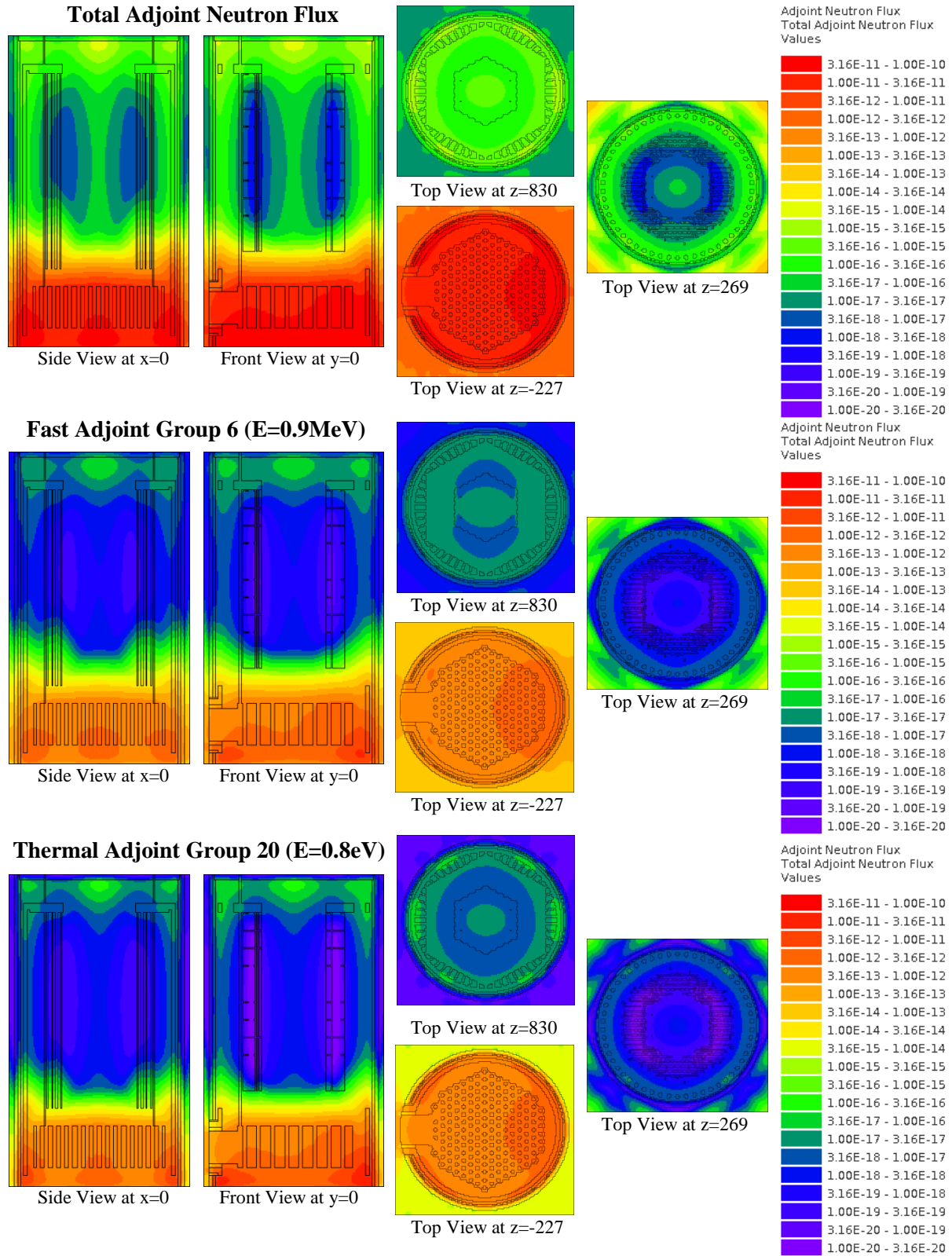


Figure 89. The total adjoint neutron flux with both a fast and thermal group displayed.

Figure 90 shows a mesh tally for the simulation using an adjoint source spectrum of the ${}^6\text{Li} (n, t) {}^4\text{He}$ reaction cross section in the graphite regions within the reactor. The biased source hardly samples any region except for the very bottom of the active core, leading to a neutron fluence only being simulated in the region of lowest fluence. The resulting tritium production rate in the ${}^6\text{Li}$ impurity within core graphite from this calculation was $3.41(10^{15}) \pm 9\%$ (t/s), which is larger than the production rate from ternary fission. Although the value is assumed to be not accurate, it presents a large tritium source. Based on these results, the graphite used in the reactor would need to be further purified to remove traces of ${}^6\text{Li}$ as it is a controllable means of tritium production.

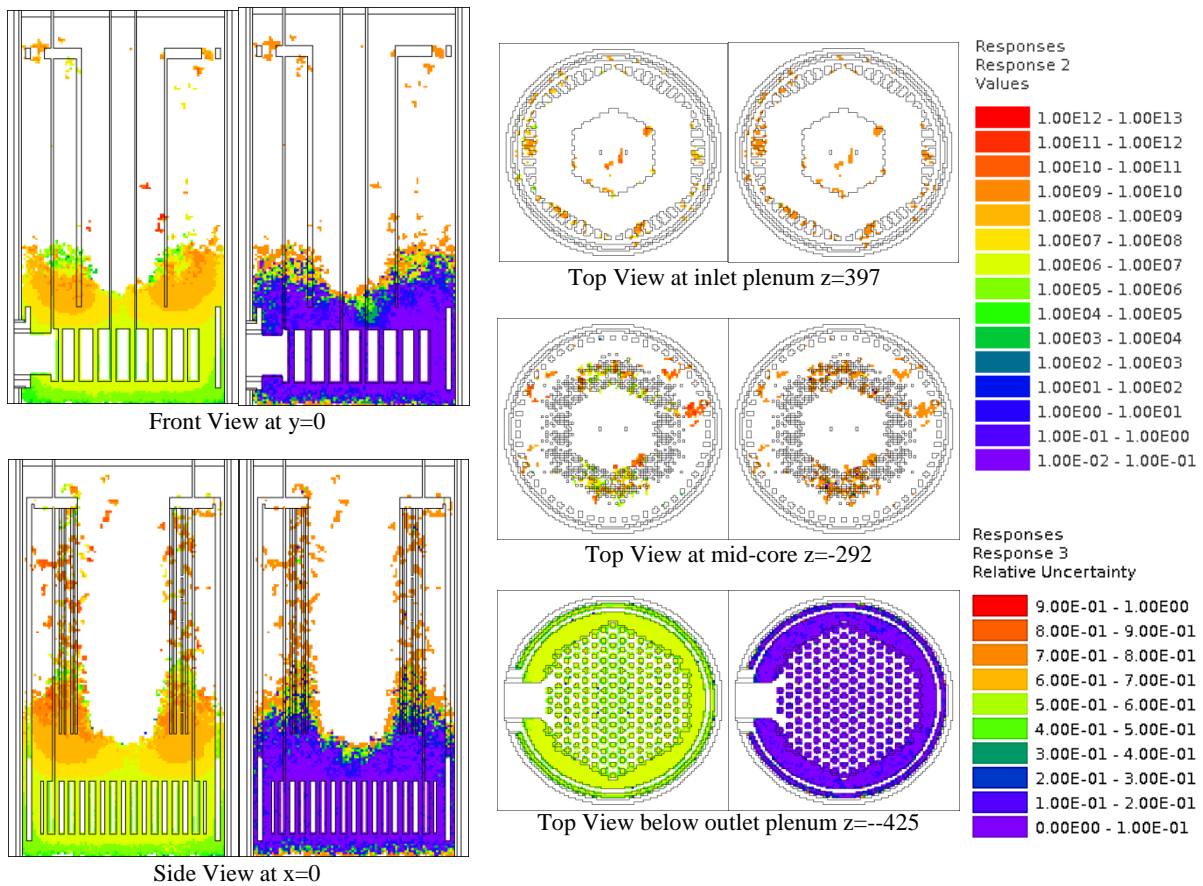
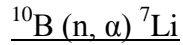


Figure 90. The ${}^6\text{Li} (n, t) {}^4\text{He}$ reaction rate spatial distribution in graphite. For each location the response is given on the left while the relative uncertainty is on the right.



The next thermal reaction of interest is the ^{10}B reaction that produces ^7Li , which may ultimately produce tritium. The reaction has a higher thermal cross section than that of ^6Li , but since it produces tritium in a two-step reaction it is expected to have less of an impact on the overall production rate. As can be seen in The cross section for this reaction is almost identical in shape to that of $^6\text{Li}(n, t) ^4\text{He}$. Therefore, the performance of MAVRIC should follow the same experience as discussed for that reaction. The overall lithium production rate from this simulation was found to be $9.0(10^{17}) \pm 10\%$ ($^7\text{Li}/s$).

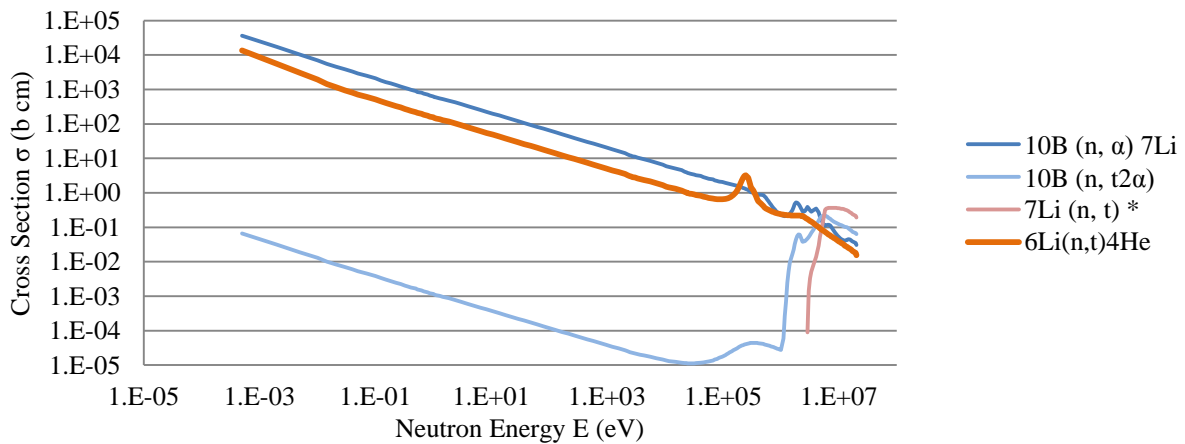


Figure 88

Figure 91. A comparison of microscopic cross sections in ^{10}B and the lithium isotopes.

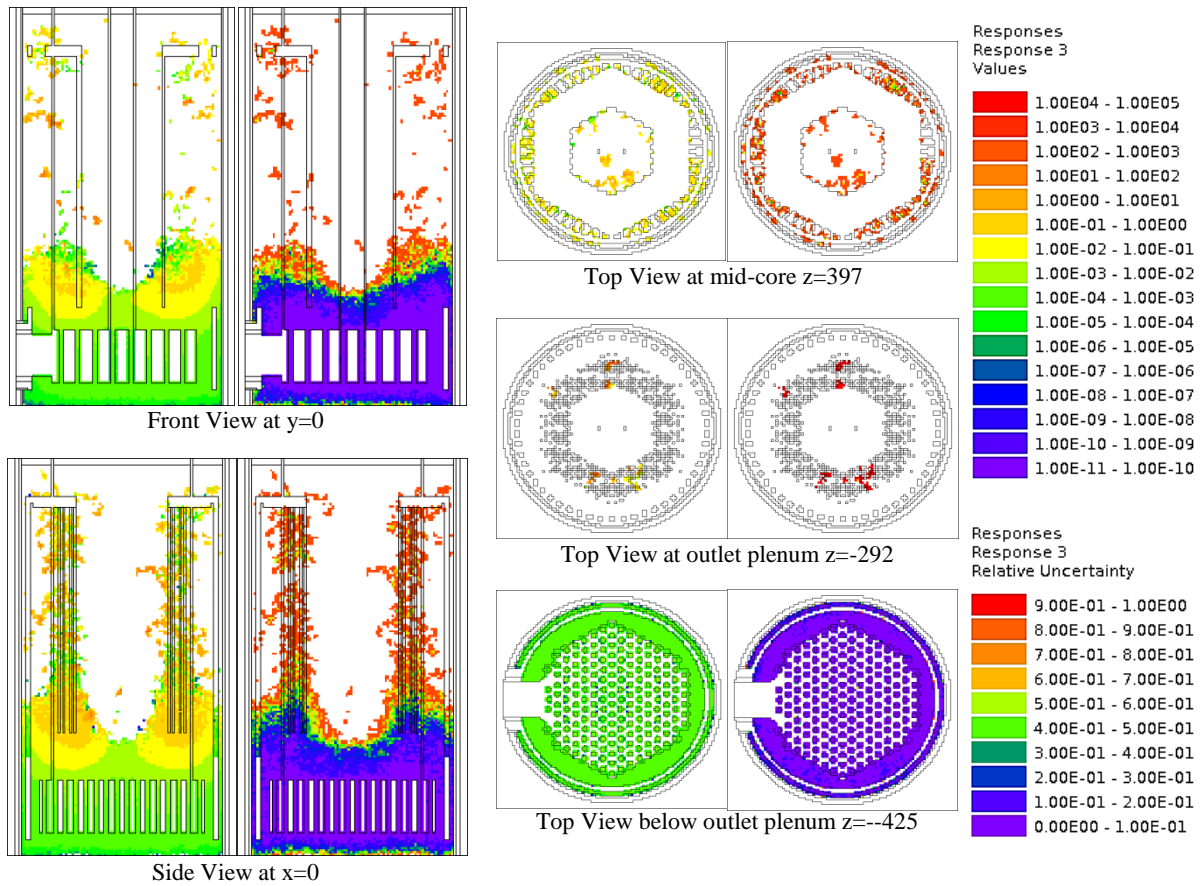
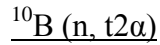


Figure 92. The $^{10}\text{B}(n,\alpha)^7\text{Li}$ reaction rate distribution as calculated by MAVRIC.



The only reaction rate in boron that directly produces tritium is the $^{10}\text{B}(n, t2\alpha)$ reaction. Referring back to the CDF of reaction rates in Figure 78, this reaction is actually mainly a fast reaction, with roughly one quarter occurring in the thermal spectrum. As will be shown later, the main issue has been using the FW-CADIS method to bias particles toward a thermal reaction. Despite the fact that this reaction is primarily fast, the results follow the same pattern as the preceding thermal reaction rate calculations. The spread away from the bottom is minimally increased, and may be due to the importance of the fast spectrum in the reaction rate. The partial results found the tritium production from ^{10}B via this reaction alone to be $3.333(10^{12}) \pm 2.8\%$ (t/s).

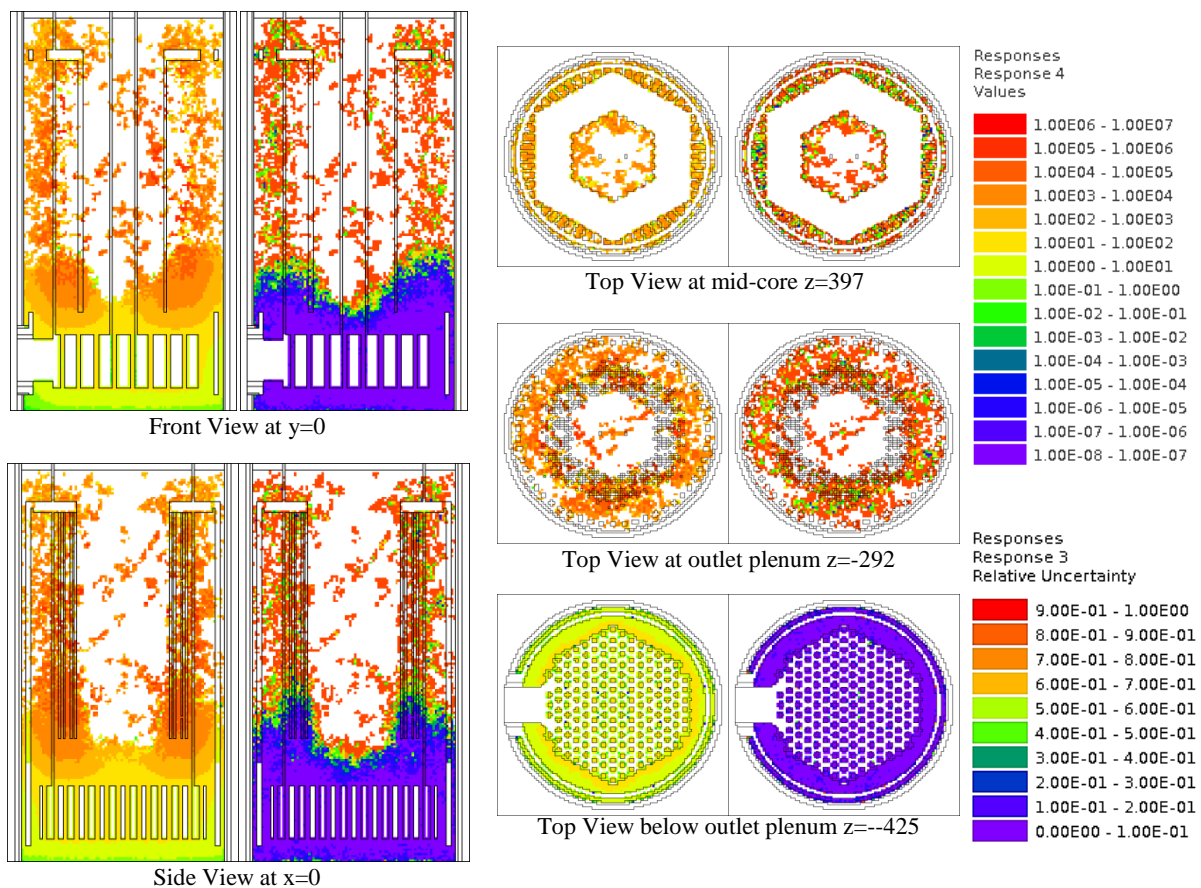


Figure 93. The $^{10}\text{B}(n, t2\alpha)$ reaction rate distribution as calculated by MAVRIC.

⁷Li Impurities

Lithium-7 presents a new case of interest when compared to other impurities producing tritium due to the two-step reaction discussed above and the fact that it is a fast, threshold reaction. It is an impurity that is assumed to be present in all carbon-based components in the core, which is almost everything except for the kernel of the TRISO particles and the helium coolant. Additionally, ¹⁰B impurities in carbon components have a high thermal cross section dominated by the production of ⁷Li. Every neutron absorbed in ¹⁰B is either producing a triton or more ⁷Li. In order to calculate the time-dependence, the total absorption for ⁷Li should also be calculated.

A run was performed, biasing particles towards the ⁷Li (n, Xt) reaction shown in Figure 77. The MC results from the simulation can be seen in Figure 94. Compared to the previous thermal reactions, the FW-CADIS methodology performs significantly better. The overall statistics within the core barrel seem to be uniformly converging, with a couple of primary issues. The most glaring problem would be in the region directly below the outlet plenum, which has drastically varying uncertainties. In terms of the overall tritium production reaction rate via ⁷Li, these areas are many orders of magnitude lower than others and are a relatively small region. Simulating for a longer period of time would converge statistics in these areas. From the simulation, the overall calculated ⁷Li tritium production from impurities in the graphite came out to be $1.158(10^{12}) \pm 0.136\% t/s$.

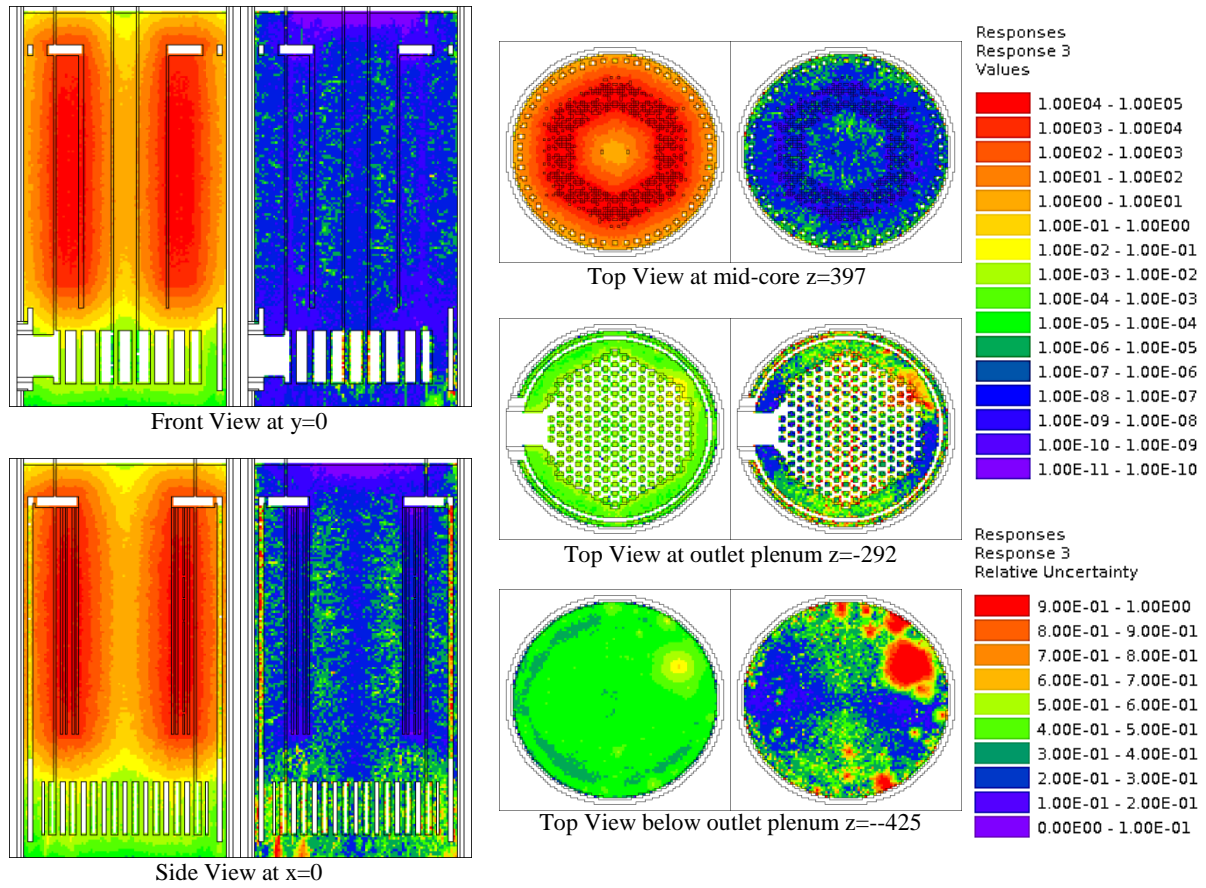


Figure 94. The distribution of tritium production strictly from ^7Li impurities in the core graphite.

Helium Coolant

The largest volume of helium in the model is contained in the areas above and below the reactor in the inlet and outlet plenums. Compared to the core helium, these experience a lower neutron flux. MAVRIC will spend a lot of time biasing particles towards these large regions which may contribute an insignificant amount to the overall production rate.

The first attempt to calculate tritium production from helium was to bias globally towards the helium mixture, as defined in the Denovo model. Since Denovo discretizes space, materials are found by using the mesh-centered material for each voxel. For transport the less helium used in Denovo the better, since regions are generally smaller than the voxel and cross sections are closer to void than graphite or fuel regions. If Denovo only biases toward the top and bottom of the reactor, the core will have no particles sampled in the axial-centered region. MAVRIC attempts to have universal variance reduction in helium, but is not accounting for certain regions of helium in the importance map to bias toward true global variance reduction. The simulation calculated the tritium production from ^4He to be $4.36(10^{11}) \pm 8.1\%$ t/s.

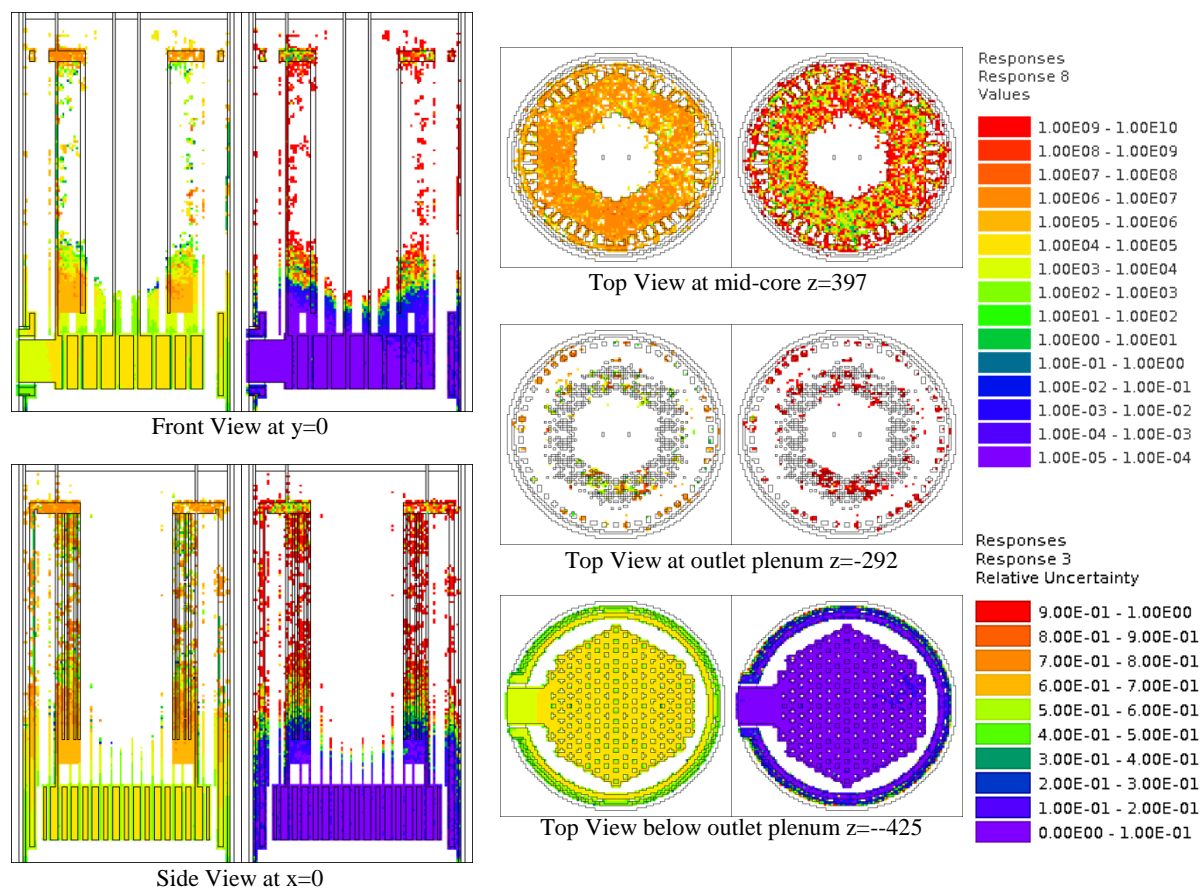


Figure 95. The ${}^3\text{He}$ (n, p) ${}^3\text{H}$ reaction distribution when using FW-CADIS with an adjoint source set to the helium in the entire model and the ${}^3\text{He}$ (n, p) ${}^3\text{H}$ reaction.

The second method defines the whole model as the adjoint source region with the ${}^3\text{He}$ (n, p) ${}^3\text{H}$ reaction defined as the adjoint source spectrum. In terms of the biasing game, this would theoretically waste time by trying to obtain global variance reduction in unimportant regions. Despite the wasted MC time, the global tally for tritium production in helium should be accurate. Figure 96 shows the results from the simulation. The method did perform better since it has more converged statistics above and not just below the core. However, the central region of the model is still not being sampled by MAVRIC. The final tally for tritium production from the second simulation was $2.11(10^{14}) \pm 11\%$. Therefore, this method calculated a flux close to three orders of magnitude higher than the previous result $(4.36(10^{11}) \pm 8.1\% \text{ t/s})$, but had a larger relative uncertainty. The upper plenum region receives a higher flux since it is directly

above the core, which most likely was the cause of the much larger reaction rate. Since the a larger portion of the particles were directed towards the bottom outlet plenum, the statistics are worse for the overall tally which is primarily from the upper plenum. The model still is not simulating a large part of the problem space, meaning that the results are still unacceptable.

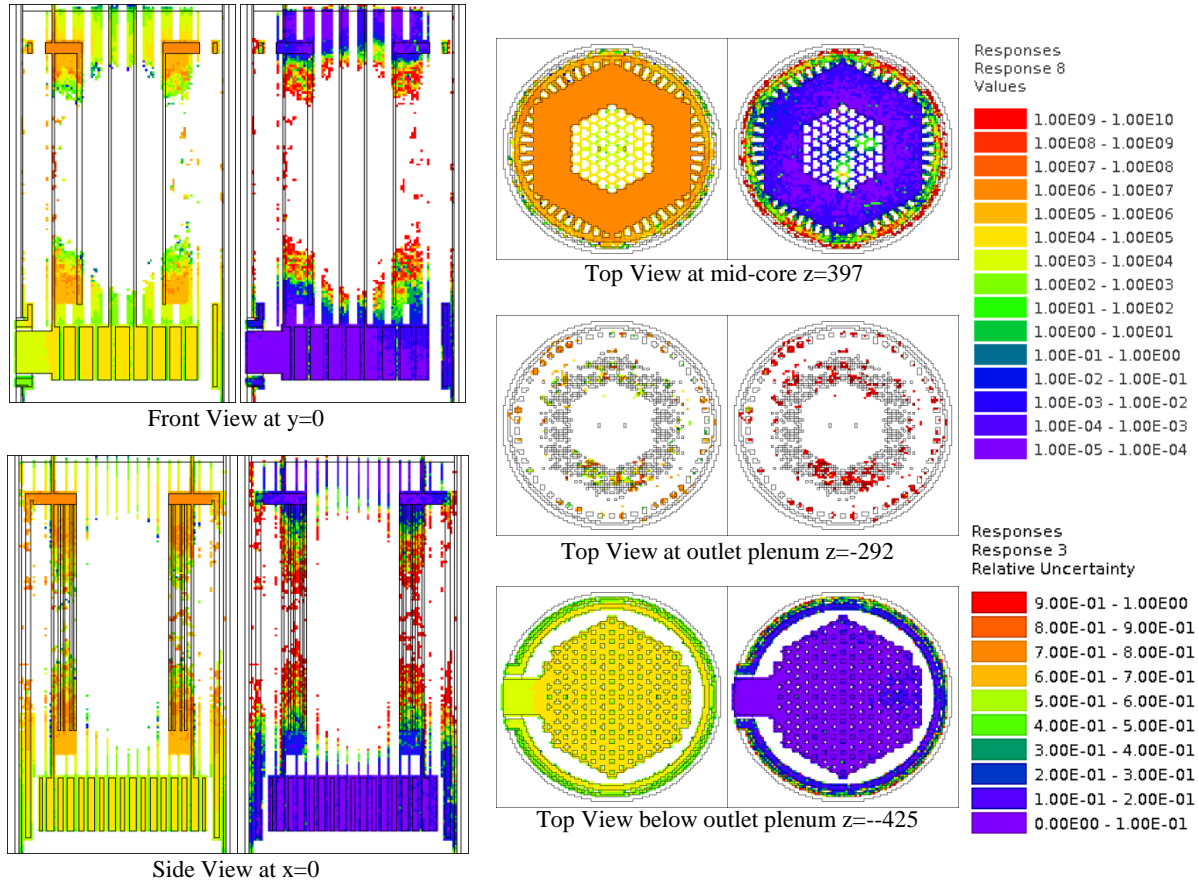


Figure 96. The $^3\text{He} (n, p) ^3\text{H}$ reaction distribution when using FW-CADIS with an adjoint source set to the entire model and the $^3\text{He} (n, p) ^3\text{H}$ reaction.

Sectional Method

Up to this point, the performance of FW-CADIS for thermal reactions has been an issue. When calculating a volume integrated reaction rate within the core barrel in a specific material, tallies have proven to be both deceptive and illusive. As noted above, large-volume region tallies may have a very low apparent uncertainty, but be inaccurate. The volume is large and has a many simulated track lengths in certain areas, which leads to a misleadingly low variance. Regions seeing the highest neutron fluence within the core barrel may have been left out by the methodology. Applying FW-CADIS to the entire model produces a biased source that samples very few particles in the center of the core. The lack of simulated particles in the central region leads to a very large percent of the volume of the graphite reflector with the highest neutron fluence receiving zero particle tracks. One important aspect of this issue is the annular core. The central reflector region is actually as deep of a shielding problem as the radially outer-most graphite reflector. It is a large volume with a high flux that will produce a significant amount of tritium. However, the FW-CADIS method sees the bottom graphite regions as having a much higher importance, leading to the radial reflector region being neglected.

In order to obtain variance reduction for the entire model, a “sectional method” was implemented. The method divides the problem into three simulations as shown in Figure 97. The first simulation biases particles towards the lower regions by using the FW-CADIS methodology with the adjoint source set as the entire neutron spectrum in the bottom portion of the model directly below the active core. The second simulation uses an adjoint source set to the axial level surrounding the active core region. The third and final simulation calculates the fluence above the core.

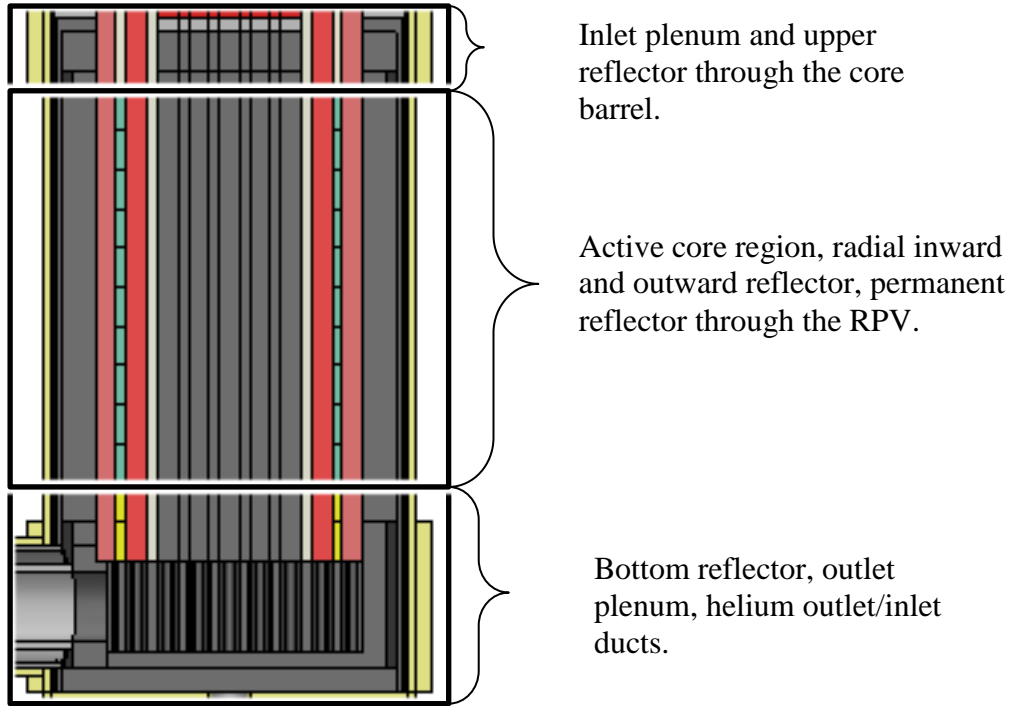


Figure 97. The three sections used for biasing particles in separate simulations.

For tallying, the model is divided into the same three regions with each having a mesh tally containing only one voxel. A mesh tally of one voxel set to a specific material acts as a volume-integrated region tally over only the problem space contained within that voxel.

Dividing the problem space in this way allows for a final tally that includes only the regions that the simulation was intended to bias towards. Overlapping areas that have particle tracks in the same region as other simulations will not be double counted. The total track-length estimated fluxes and reaction rates are given by the voxel tally times the volume contained in that voxel. Additionally, the poor statistics in a certain region of one simulation will not affect the overall tally since other simulations provide that good statistics for that region. The total of the three equals that of a region tally over the entire model for a specific mixture. Simulations covering each region may be used to obtain both an accurate and precise solution for tritium production for each pathway. By biasing the simulations towards the entire flux spectrum, it is expected that each relevant reaction rate can be tallied at once between the three separate runs. Figure 98

demonstrates the idea of combining results from different simulations, showing the advantage of breaking the tallies into sections.

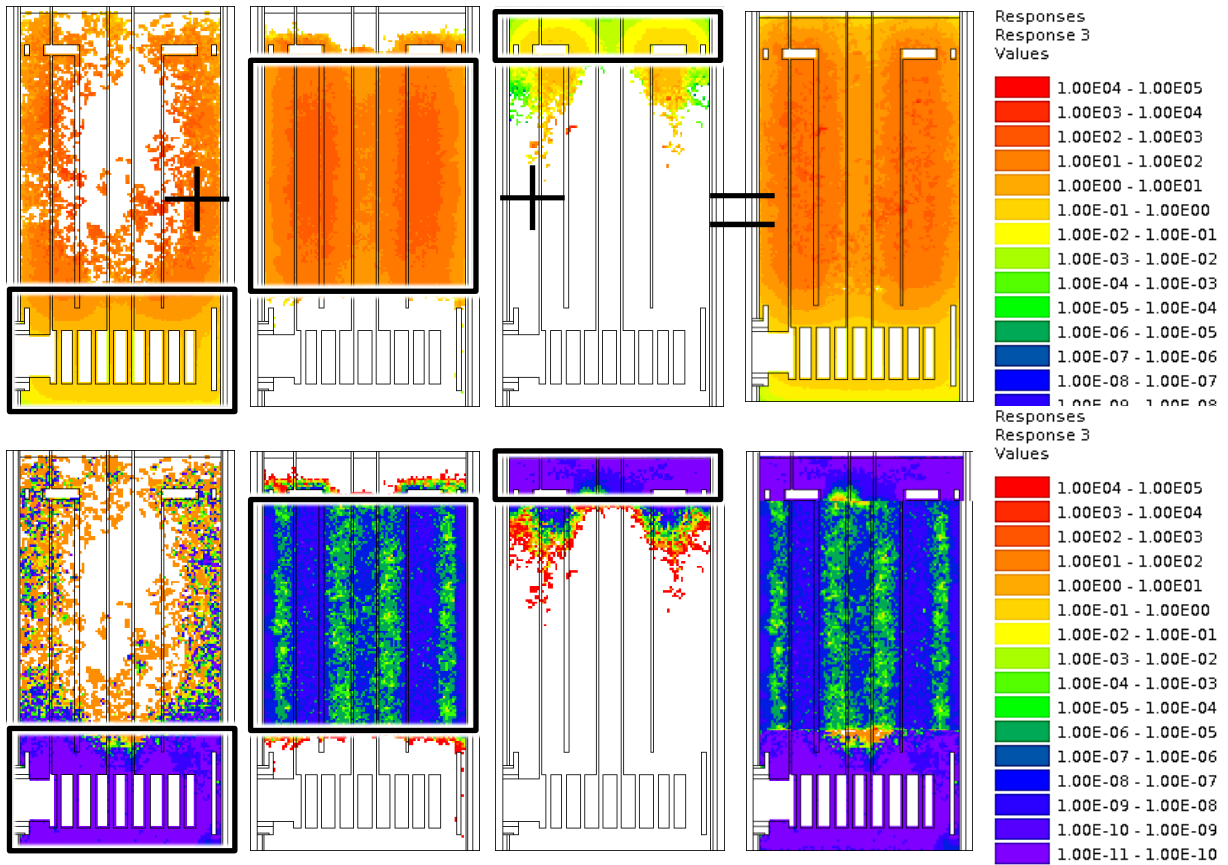


Figure 98. Combined results demonstrated by the ${}^7\text{Li}(n,t)^*$ reaction.

The pathway shown in Figure 98 was the ${}^7\text{Li}(n,Xt)$ reaction. As a fast, threshold reaction, the FW-CADIS was demonstrated previously to be effective in calculating this reaction rate. The tritium source via ${}^7\text{Li}$ was found to produce $1.158(10^{12}) \pm 0.136\%$ t/s . The sectional tallies should match that previous results and were combined to obtain a reaction rate of $1.161(10^{12}) \pm 0.150\%$ t/s . The difference between the two tallies came to be only 0.26%, which is 2σ of the combined uncertainty of the separate calculations.

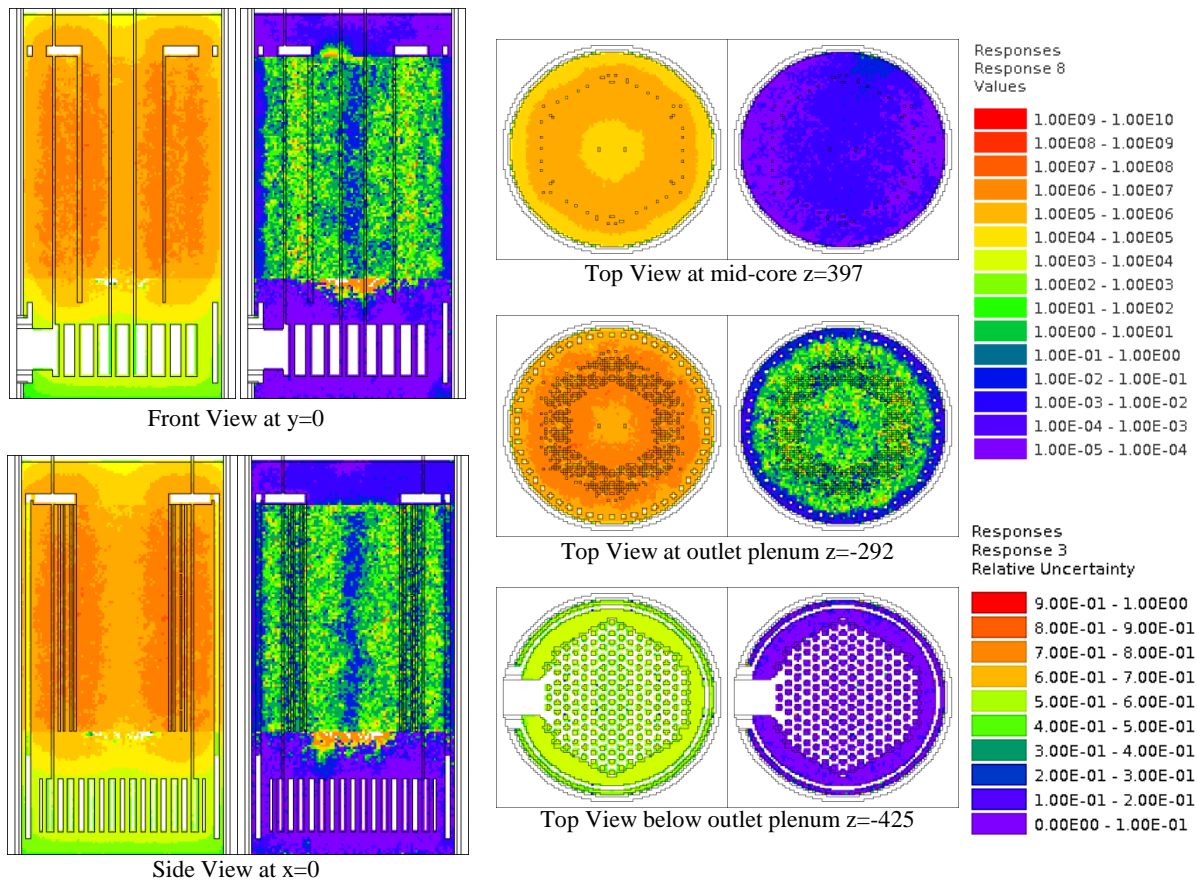


Figure 99. The ${}^6\text{Li}(n,t)$ reaction.

As noted before, the ${}^6\text{Li}(n,t){}^4\text{He}$ and ${}^{10}\text{B}(n,\alpha){}^7\text{Li}$ reactions have almost the same shape of cross sections, with the ${}^{10}\text{B}$ reaction being slightly more absorbent. The tallies had almost identical track length paths and distributions as should be expected when taken from the same simulation. For this reason only the mesh tally for the ${}^6\text{Li}$ reaction is given in Figure 99. On the down side, the central reflecting region still has a large amount of uncertainty in the majority of voxels. Previously, the production rates for the ${}^6\text{Li}(n,t){}^4\text{He}$ and ${}^{10}\text{B}(n,\alpha){}^7\text{Li}$ reactions were found to be $3.4(10^{15}) \pm 9\%$ (t/s) and $9.0(10^{17}) \pm 10\%$ (${}^7\text{Li}/s$), respectively. The newer method found the rates to be $3.15(10^{17}) \pm 0.9\%$ (t/s) and $9.17(10^{18}) \pm 1\%$ (${}^6\text{Li}/s$). For both cases, the previous, less-converged answers under predicted reaction rates by at least an order of magnitude.

Figure 100 shows the $^{10}\text{B}(n,t\alpha)$ reaction rate distribution provided by the “sectional method.” Since the reaction cross section is more dependent on the energy of fission spectrum, it has a smaller relative uncertainty in the active core region. Outside of fixed source the tallies’ uncertainties are almost identical to that from the other thermal reaction rates, which is still less than desirable. The new method found the reaction rate to be $3.45(10^{13}) \pm .5\%$ (t/s) compared with $3.333(10^{12}) \pm 2.8\%$ (t/s) from the previous study, which is an increase of more than an order of magnitude.

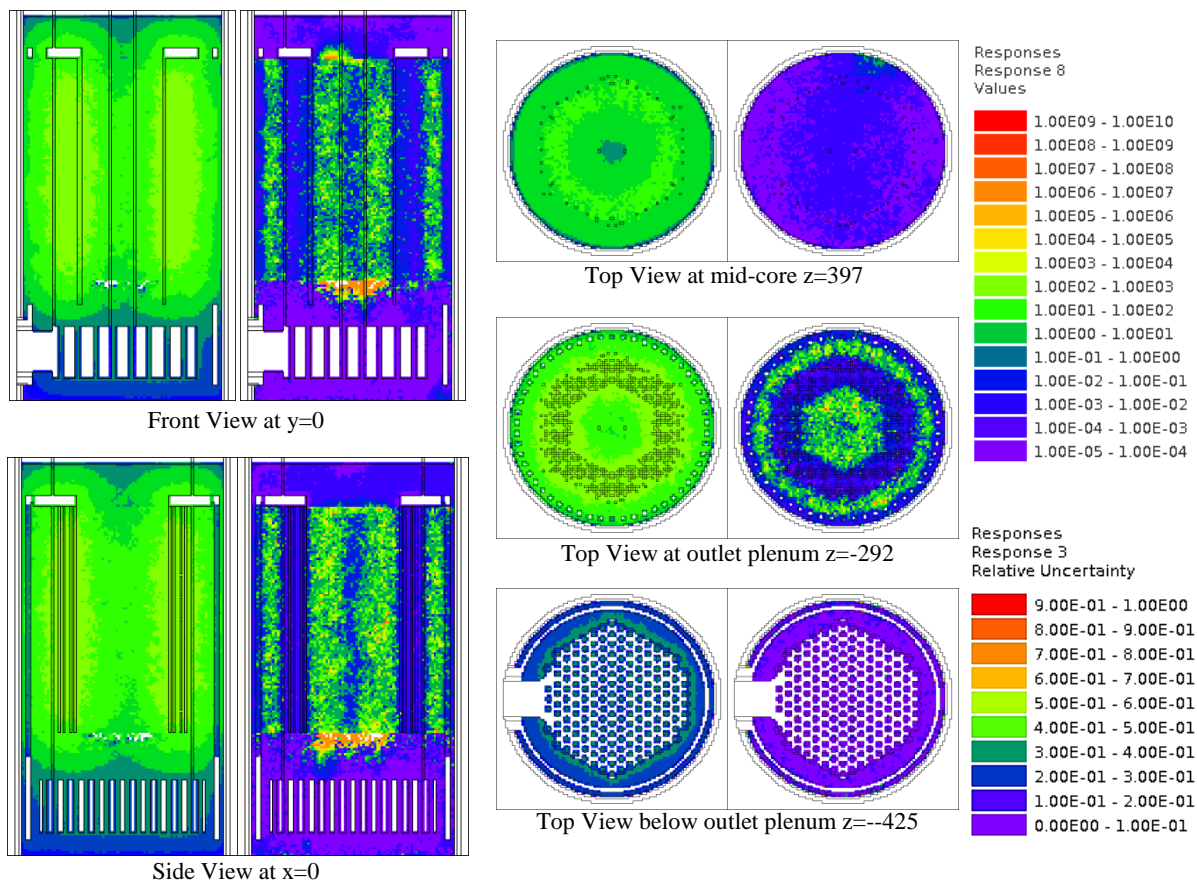


Figure 100. The reaction rate distribution for the $^{10}\text{B}(n,t\alpha)$ reaction is shown.

The $^3\text{He}(n,p)t$ reaction rate experiences similar improvements as those seen within the graphite impurity reactions. Figure 101 shows the improved results. The helium in the middle portion of the reactor and the inlet plenum directly above the active core react orders of more

than the portion below the core in terms of reaction rate density. While the largest volume of helium may be below the bottom reflector, it is receiving a much smaller fluence. The previous study biasing particles towards the reaction in the entire problem space found the tritium production rate to be $2.11(10^{14}) \pm 11\%$. With the full core simulated properly, the production rate increases by almost 4 orders of magnitude to $2.53(10^{15}) \pm 1.0\%$ t/s.

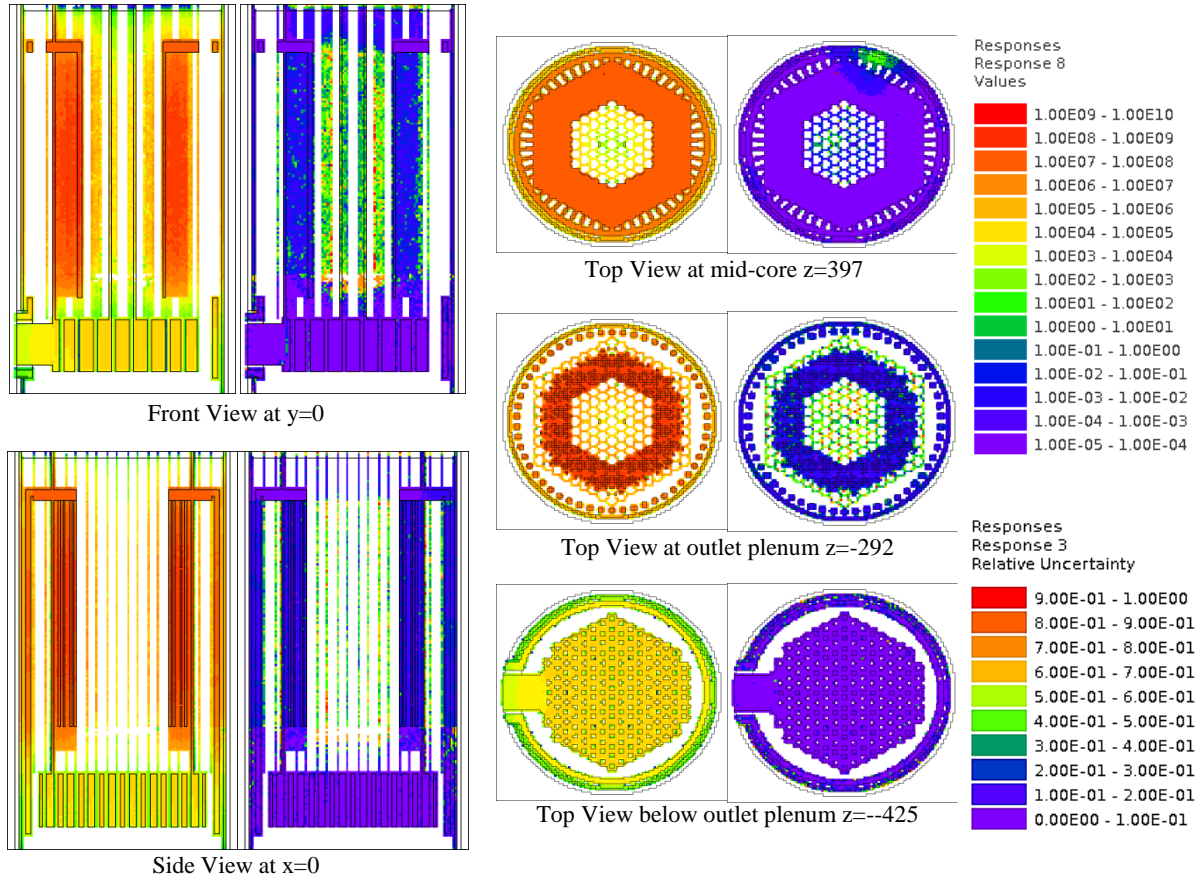


Figure 101. The reaction rate distribution for the ${}^3\text{He}(n,p)\text{t}$ reaction is shown.

Standard MC

For the thermal reaction rates, the FW-CADIS methodology has not been effective in obtaining global variance reduction in the core region and its radial surrounding. The majority of tritium production occurs close to the active core region where thermal and fast neutron fluences are the highest. The tallies in these regions could have been done simultaneously with the criticality calculation that provided the fixed-source distribution. However, a full picture of the overall production rate within the entire core barrel region would not have been calculated properly. Ignoring the outermost regions causes a slight underestimation of total tritium production, which is corrected by implementing MAVRIC in various ways. A standard MC simulation was performed for 1 day. Figure 102 shows the spatial distribution of uncertainties for each important impurity reaction in the graphite reflector.

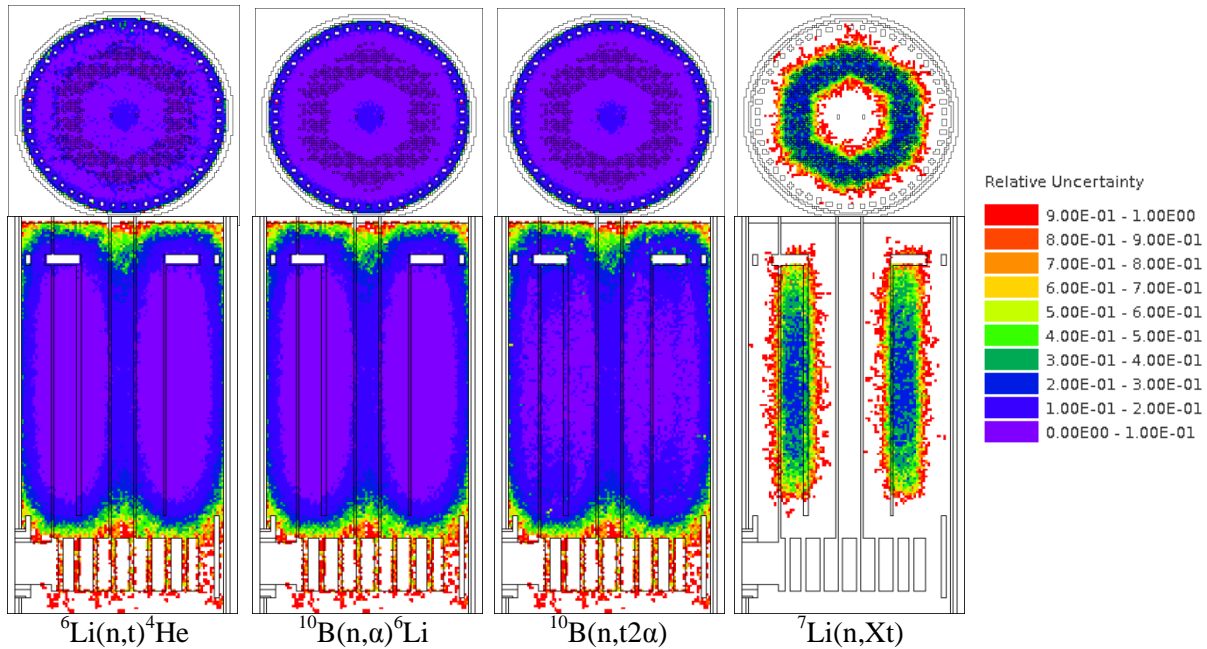


Figure 102. The relative uncertainty distribution in each impurity, tritium-producing reactions in graphite.

Compared with the results from previous simulations, the standard MC performs better for thermal reaction rates within the reflector element surrounding the inner and outer annulus of the core radially. However, using standard MC, fast neutrons are hardly simulated outside of the

active core region, as can be seen in the ${}^7\text{Li}(n,Xt)$ reaction. Final tallies using the “sectional method” for thermal reaction rates were redone using standard MC for the middle section surrounding the active fuel region. The combined “sectional” results with uncertainties for the thermal reaction rates are given in Figure 103 through Figure 106.

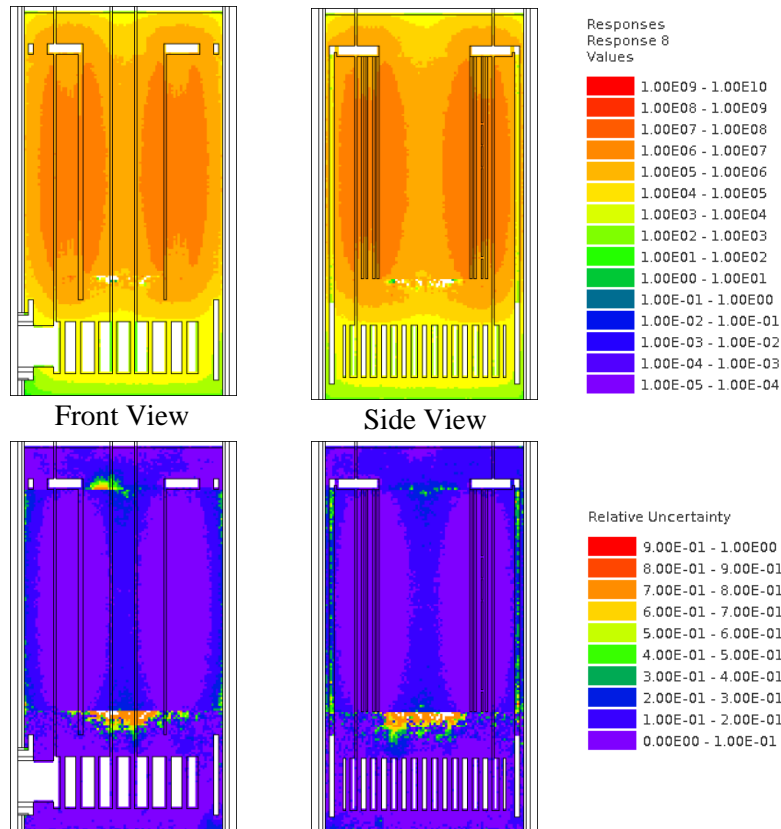


Figure 103. "Sectional Method" results for the ${}^6\text{Li}$ tritium-production rate in graphite.

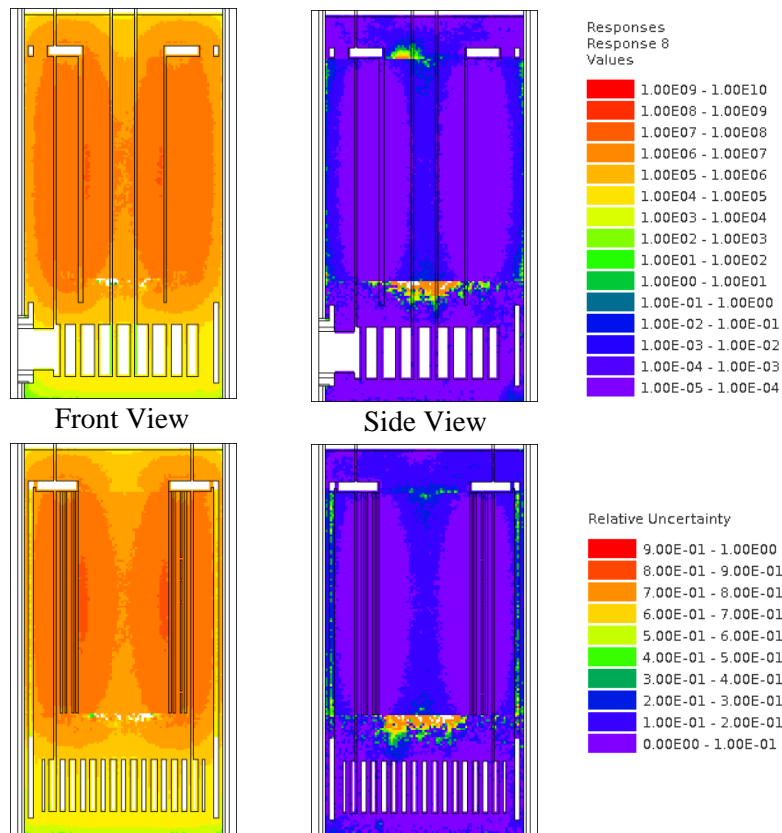


Figure 104. "Sectional Method" results for the ^{10}B lithium-production rate in graphite.

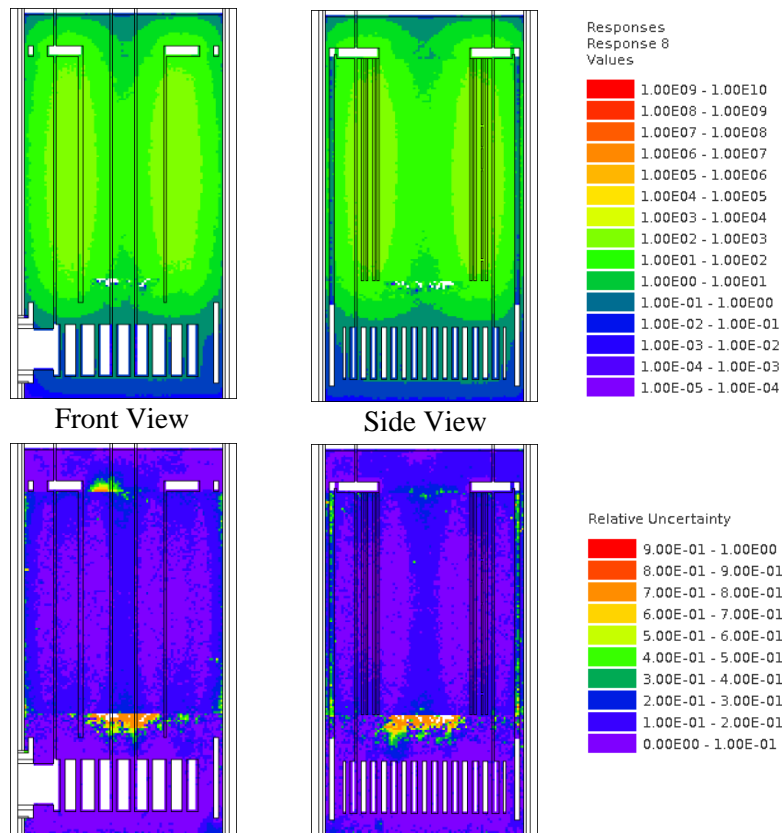


Figure 105. "Sectional Method" results for the ^{10}B tritium-production rate in graphite.

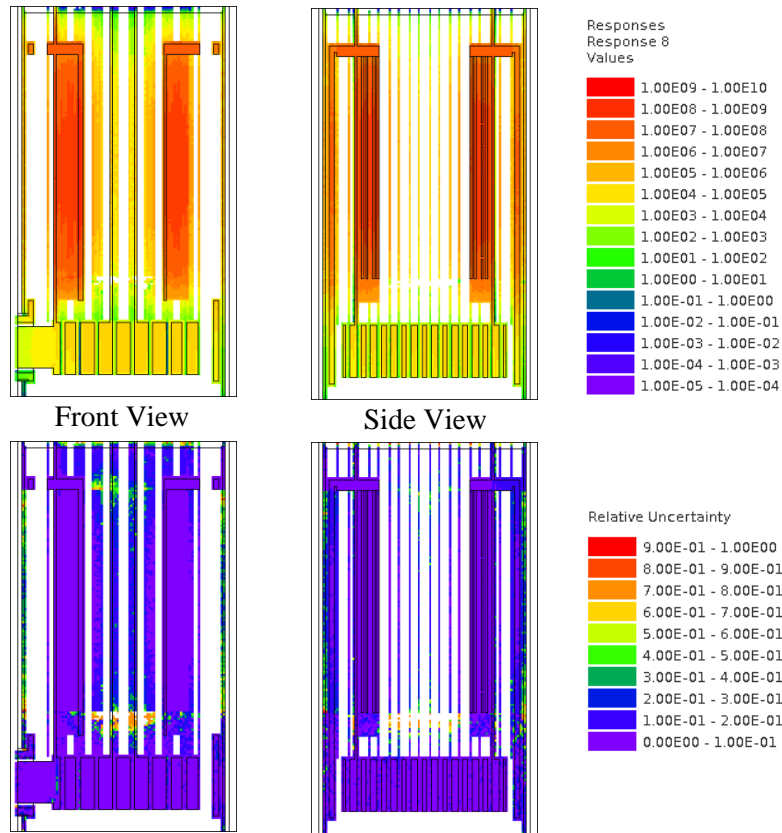


Figure 106. "Sectional Method" results for the ^3He tritium-production rate in graphite.

Total Tritium Source

Oh and Kim have performed complete analysis on tritium production permeating from core components to an ultimate hydrogen product (Oh & Kim, 2011). The basic assumption is a homogenized reactor core with a one group neutron flux for each reaction. The reaction rates are calculated as the integrated macroscopic cross section times the volume times the average flux. The actual tritium production rates are only given as percentage of the total amount, and were extrapolated from there. Table 28 gives assumed tritium production rates from Oh and Kim.

Table 28. Sources of tritium production in VHTRS (Oh & Kim, 2011).

Tritium Source	% total	Release Potential
Ternary Fission	62	Time at temperature
From ^3He	18	Produced in Helium coolant
From ^6Li	~12	Partly retained in graphite; Released during H ₂ O ingress
Core Graphite	2	
Core Matrix	10	
Reflector (replaceable)	<1	
Reflector (permanent)	<1	
From ^{10}B	~8	Apparently retained at source
Control Rod	7	
Burnable Poisson	1	
Reflector	<1	

The ternary fission is based on the reactor power and can be assumed from Eq. 32 to be $1.498(10^{15})$ t/s. Using the known tritium production from ternary fission, the other production rates from each pathway can be extrapolated. These results are compared to those obtained using MAVRIC in Table 29. The rates are provided in both t/s and bq/yr, which matches regulatory guidelines. Based on geometric and material assumptions the total tritium production calculated by MAVRIC was found to be 2.28 times the calculated amount given by Oh and Kim.

Table 29. A comparison of the tritium sources.

Pathway	Assumed values from Table 28		Calculated values using MAVRIC		Ratio (C/A)
	Activity (Bq/y)	Production (t/s)	Activity (Bq/y)	Production (t/s)	
Ternary Fission	1.03E+14 (62.0%)	1.83E+15	1.03E+14 (29.8%)	1.83E+15	1.00
From ³ He	2.98E+13 (18.0%)	5.30E+14	1.43E+13 (4.1%)	2.53E+14	0.48
From ⁶ Li	2.32E+13 (14.0%)	4.12E+14	1.78E+14 (51.6%)	3.16E+15	7.67
Core Graphite	3.31E+12 (2.0%)	5.89E+13	} 5.45E+13 (15.8%)	9.68E+14	2.74
Core Matrix	1.66E+13 (10.0%)	2.94E+14			
Reflector	3.32E+12 (2.0%)	5.88E+13			
From ¹⁰ B	1.49E+13 (9.0%)	2.65E+14	5.00E+13 (14.5%)	8.89E+14	3.36
Control Rod	1.16E+13 (7.0%)	2.06E+14	4.35E+13 (12.6%)	7.74E+14	3.75
Absorber	1.66E+12 (1.0%)	2.94E+13	4.51E+12 (1.3%)	8.02E+13	2.72
Reflector	1.66E+12 (1.0%)	2.94E+13	2.00E+12 (.6%)	3.56E+13	1.21
Total	1.71E+14	3.03E+15	3.45E+14 (100.0%)	6.13E+15	2.02
Total (Bq/y/MWt)	2.84E+11		7.88E+11		2.77

A large percent of the higher calculated tritium production by MAVRIC comes from impurities within the graphite reflector and the helium coolant. Boron produces a significant amount of tritium, but mainly coming from the control rods and burnable absorbers (13.9%). Only 0.6% of tritium production comes from ¹⁰B impurities, which were assumed to be 5ppm. Lithium-6 impurities were assumed to be 0.007 ppm of the carbon-based, graphite matrix but contribute 51.6% to the total tally. The ⁶Li impurities were on the low side of estimations and could be as high as 0.21 ppm, which is 30 times higher.

Impurities in the helium coolant make up 30.1% of the total production, but the atomic concentration of the helium impurity is subject to a number of degrees of freedom. The density of helium was taken as $4.81(10^{-4})$ a/bcm, which assumes a temperature of 675°C and a pressure of 6.3MPa. The core inlet temperature is expected to be 325°C with an outlet temperature of 750°C. The core pressure is slated to be 6MPa instead of 6.3MPa. Using different coolant temperatures or pressures can cause the coolant density (and subsequently the reaction rate) to

increase up to 33% or decrease by 13%. Also different impurity concentration of ^3He can be assumed. From previous HTGRs, the number ranged from 0.137 to 0.3 ppm. The former was assumed. Changing the impurity concentration could increase the reaction rate by 120%.

Depending on the assumptions made, the tritium production through helium impurities could vary between 300% and 90% of the calculated value. Table 30 and Table 31 give the worst- and best-case scenarios for tritium production based on varying the ^6Li and ^3He impurities. The best-case scenario was done assuming ^6Li contents could be reduced to around 1ppb. The best-case scenario tritium production, $3.18\text{E}+11$ Bq/y/MWt, fits within results obtained from past HTGRs, ranging from $2.14\text{E}+11$ to $4.29\text{E}+11$. Certain materials producing tritium are part of the VHTR design, such as, the fuel, burnable absorbers, and control rods. Neglecting the impurity reaction rates, the overall tritium production from materials included by design would be $2.51\text{E}+11$ Bq/y/MWt. That number would be the minimum tritium production rate, since it none of the reactions can be removed without changing the layout and neutronics of the core design being used.

Table 30. The tritium sources assuming worst-case scenario for impurities.

Pathway	Assumed values from Table 28		Calculated values using MAVRIC		Ratio (C/A)
	Activity (Bq/y)	Production (t/s)	Activity (Bq/y)	Production (t/s)	
Ternary Fission	1.03E+14 (62.0%)	1.83E+15	1.03E+14 (1.9%)	1.83E+15	1.00
From ^3He	2.98E+13 (18.0%)	5.30E+14	4.28E+13 (.8%)	7.60E+14	1.43
From ^6Li	2.32E+13 (14.0%)	4.12E+14	5.33E+15 (96.5%)	9.48E+16	230.07
Core Graphite	3.31E+12 (2.0%)	5.89E+13	} 1.63E+15 (29.5%)	2.90E+16	82.20
Core Matrix	1.66E+13 (10.0%)	2.94E+14			
Reflector	3.32E+12 (2.0%)	5.88E+13			
From ^{10}B	1.49E+13 (9.0%)	2.65E+14	5.00E+13 (.9%)	8.89E+14	3.36
Control Rod	1.16E+13 (7.0%)	2.06E+14	4.35E+13 (.8%)	7.74E+14	3.75
Absorber	1.66E+12 (1.0%)	2.94E+13	4.51E+12 (.1%)	8.02E+13	2.72
Reflector	1.66E+12 (1.0%)	2.94E+13	2.00E+12 (.0%)	3.56E+13	1.21
Total	1.71E+14	3.03E+15	5.53E+15 (100.0%)	9.83E+16	32.42
Total (Bq/y/MWt)	2.84E+11		9.22E+12		32.42

Table 31. The tritium sources assuming best-case scenario for impurities.

Pathway	Assumed values from Table 28		Calculated values using MAVRIC		Ratio (C/A)
	Activity (Bq/y)	Production (t/s)	Activity (Bq/y)	Production (t/s)	
Ternary Fission	1.03E+14 (62.0%)	1.83E+15	1.03E+14 (53.8%)	1.83E+15	1.00
From ³ He	2.98E+13 (18.0%)	5.30E+14	1.28E+13 (6.7%)	2.28E+14	0.43
From ⁶ Li	2.32E+13 (14.0%)	4.12E+14	2.54E+13 (13.3%)	4.51E+14	1.10
Core Graphite	3.31E+12 (2.0%)	5.89E+13	} 7.78E+12 (4.1%)	1.38E+14	0.39
Core Matrix	1.66E+13 (10.0%)	2.94E+14			
Reflector	3.32E+12 (2.0%)	5.88E+13			
From ¹⁰ B	1.49E+13 (9.0%)	2.65E+14	5.00E+13 (26.2%)	8.89E+14	3.36
Control Rod	1.16E+13 (7.0%)	2.06E+14	4.35E+13 (22.8%)	7.74E+14	3.75
Absorber	1.66E+12 (1.0%)	2.94E+13	4.51E+12 (2.4%)	8.02E+13	2.72
Reflector	1.66E+12 (1.0%)	2.94E+13	2.00E+12 (1.0%)	3.56E+13	1.21
Total	1.71E+14	3.03E+15	1.91E+14 (100.0%)	3.39E+15	1.12
Total (Bq/y/MWt)	2.84E+11		3.18E+11		1.12

Permeation to Hydrogen Product

The helium coolant carries tritium from core components to the secondary system, allowing it to contaminate hydrogen product. Tritium produced in the solid core regions will mostly be contained where produced. Reaction rates in helium may be more important to overall contamination than other pathways despite being lower. There is no diffusion barrier to reach the coolant since tritons are produced within the coolant. Helium is expected to contain about $1.37(10^{-06}) \text{ At\% } ^3\text{He}$. Figure 107 shows the tritium distribution in the VHTR system. Sensitivity analysis done by Oh and Kim (2011) shows the greatest source of uncertainty for tritium permeation to the hydrogen product to be the production rates within the core.

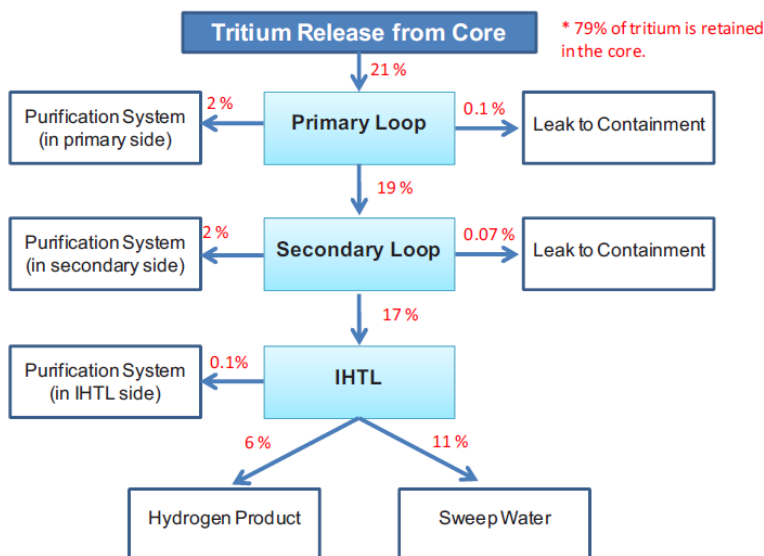


Figure 107. The tritium distribution from core to hydrogen product. (Oh & Kim, 2011)

Therefore, best-case scenario would leave $1.14(10^{13}) \text{ Bq/yr}$ entering the hydrogen product. The reference does not directly connect the tritium production numbers with the final release to hydrogen, but did say that only 1% of the samples in the study were within effluent limits. Since the MAVRIC calculation simulated a higher tritium production, it is assumed that the limits are exceeded by the current design. More work should be done to improve helium purification systems and reduce impurities.

CHAPTER 9

CONCLUSIONS AND FUTURE WORK

The MAVRIC sequence of the Scale6.1 code package successfully demonstrated its capability in simulating a range of radiation indicators in the VHTR power plant. The primary objective was verifying the FW-CADIS methodology when applied to different shielding quantities with respect to the VHTR. After validating methodology and the model within the code package, three studies were performed each biasing particles through different amounts of shielding. The first focused on RPV dosimetry using a mockup surveillance capsule monitoring program to calculate reactions rates, fast fluences and DPA. The second investigated calculating deep-shielding dose-rate calculations in an accessible area in the nuclear island. The final study explored different mechanisms of tritium production, calculating steady state rates within the core barrel.

The first study analyzed RPV dosimetry within the VHTR model. Mimicking a typical surveillance capsule monitoring program, activation reaction rates were calculated in different positions inside and outside of the RPV. At the same time the DPA and fast (>1 MeV) and semi-fast (>0.1 MeV) neutron fluences were found for the expected 60-year lifetime of the plant. Within the helium riser channels, the majority of reaction rates had uncertainties below 5%. The reaction rates outside of the RPV had high uncertainties between 10% and 25%, indicating that the importance map needed further improvement. Note that between the two regions there was generally an attenuation of between 2 and 3 orders of magnitude. Future improvements to the model would use mesh subsampling to define the material in the deterministic Denovo forward and adjoint calculations to include a better representation of the geometry of the barrel and RPV.

Using the MAVRIC sequence, dose rates were calculated in the room directly above the reactor within the nuclear island which is a very deep shielding problem over a large problem space. Dose rates are reduced by close to 15 orders of magnitude between the reactor core and

the area of interest. Therefore, MAVRIC needs to be exceptionally efficient with biasing in order to obtain decent results. In order to improve the importance map, a mesh-refinement scheme was used in combination with parallel Denovo to increase the quadrature set (P_3/S_8). By implementing an optimized importance map (~8 million voxels) and increasing the MC run time (wall clock 7 days, CPU time 7 weeks), the majority of relative uncertainties for dose rates in the mesh covering the room were converged to less than 20% with a high variance of variance. Neighboring cells could jump between 70% and 20%. Streaming paths through control rod assemblies are a large contributor to these varying uncertainties, and future work would seek to mitigate these issues while further refining the importance map. Subsequently, the maximum dose rate calculated within the room was below the allowed public dose over a given year-long work schedule.

The tritium-producing reaction rates within the core barrel were calculated demonstrating the advantage of MAVRIC in being able to produce many different simulations with minimal input by the user. The majority of production occurs in the active core region and was easily calculated using standard MC with no biasing. This holds true especially for thermal reactions. For the majority of reaction rates, more than 98% of the total value calculated using the “sectional method” was reported using standard MC. The main outlier was tritium production in helium since the majority of the helium is contained in the outlet plenum below the bottom reflector. However, standard MC still calculated 90% of the final value found for tritium production in helium. Fast reactions were not as successful using standard MC and should use FW-CADIS or CADIS.

In general, the FW-CADIS methodology is used to obtain global variance reduction. It biases particles towards the adjoint source spectrum in regions that contribute the least to a global tally for that desired adjoint source distribution. This is a feature of the methodology, not an issue. If the goal is to obtain an overall reaction-rate distribution than FW-CADIS should be

used, but it proved to be problematic when applied to thermal reactions within the VHTR model. The large problem space below the bottom reflector containing the outlet plenum led to a biased source distribution that very heavily sampled particles in the bottom portion of the fixed-source. The adjoint flux in the bottom of the core as solved by Denovo was orders of magnitude higher than that in the center. The biased source is sampled proportionally to the adjoint flux, leading to the middle and upper portions of the problem having very few particles sampled in those regions.

A “sectional method” was used to find distributions of tritium-producing reaction rates over the core barrel. Using FW-CADIS for the top and bottom portions separately, the method could be combined with standard MC results in the center of the core to obtain the most converged overall tally and distribution for each thermal reaction rate.

With the combined results, the total tritium production calculated using MAVRIC was found to match previous studies using a homogenized reactor within an order of magnitude. Therefore, the MAVRIC sequence was found to be effective in calculating tritium production. For finding rates in the core standard MC should be used. For finding fast reaction rate everywhere within the core barrel, FW-CADIS was the most effective. For finding thermal reaction rates everywhere, a “sectional method” combining results from FW-CADIS and standard MC proved the most effective. Finally if seeking only the total reaction rate, the CADIS methodology should give the best results and future work would verify this assumption.

APPENDIX A: RESULTS FROM THE VENUS-3 SIMULATION

⁵⁸Ni (n,p)

Position (x, y, z)	Experimental	Calculated (KENO)	C/E	Calculated (Benchmark)	C/E
Inner Baffle					
(-4.41, -0.63, 114.50)	1.23E+09	1.19E+09 ± 0.09%	0.97	1.31E+09 ± 0.13%	1.06
(-4.41, -0.63, 131.45)	1.74E+09	2.05E+09 ± 0.08%	1.17	1.76E+09 ± 0.14%	1.01
(-4.41, -0.63, 131.55)	1.76E+09	2.24E+09 ± 0.08%	1.27	1.64E+09 ± 0.14%	0.93
(-4.41, -0.63, 145.50)	1.25E+09	1.48E+09 ± 0.09%	1.19	1.26E+09 ± 0.11%	1.01
(-4.41, -4.41, 114.50)	1.47E+09	1.60E+09 ± 0.09%	1.08	1.67E+09 ± 0.10%	1.14
(-4.41, -4.41, 131.45)	2.09E+09	2.70E+09 ± 0.08%	1.29	2.58E+09 ± 0.10%	1.24
(-4.41, -4.41, 131.55)	2.10E+09	2.30E+09 ± 0.07%	1.10	2.18E+09 ± 0.10%	1.04
(-4.41, -4.41, 145.50)	1.52E+09	1.88E+09 ± 0.08%	1.23	1.60E+09 ± 0.11%	1.05
Region Average C/E Ratio		(1.16 ± 0.08) ± 0.11		(1.06 ± 0.12) ± 0.09	
Outer Baffle					
(-39.69, -0.69, 106.50)	9.80E+07	9.72E+07 ± 0.09%	0.99	1.06E+08 ± 0.13%	1.08
(-39.69, -0.69, 110.50)	1.36E+08	1.56E+08 ± 0.09%	1.15	1.71E+08 ± 0.11%	1.26
(-39.69, -0.69, 114.50)	1.75E+08	1.70E+08 ± 0.08%	0.97	1.97E+08 ± 0.11%	1.13
(-39.69, -0.69, 118.50)	2.11E+08	2.60E+08 ± 0.07%	1.23	1.97E+08 ± 0.11%	0.93
(-39.69, -0.69, 122.50)	2.58E+08	2.84E+08 ± 0.07%	1.10	2.60E+08 ± 0.09%	1.01
(-39.69, -0.69, 125.50)	3.09E+08	3.60E+08 ± 0.07%	1.17	3.38E+08 ± 0.10%	1.09
(-39.69, -0.69, 128.50)	3.88E+08	4.85E+08 ± 0.06%	1.25	4.49E+08 ± 0.09%	1.16
(-39.69, -0.69, 131.50)	5.00E+08	5.95E+08 ± 0.06%	1.19	5.00E+08 ± 0.08%	1.00
(-39.69, -0.69, 134.50)	5.57E+08	6.83E+08 ± 0.06%	1.23	5.78E+08 ± 0.08%	1.04
(-39.69, -0.69, 137.50)	5.73E+08	5.94E+08 ± 0.05%	1.04	5.61E+08 ± 0.08%	0.98
(-39.69, -0.69, 141.50)	5.54E+08	6.61E+08 ± 0.06%	1.19	5.59E+08 ± 0.08%	1.01
(-39.69, -0.69, 145.50)	4.95E+08	4.97E+08 ± 0.06%	1.01	4.75E+08 ± 0.08%	0.96
(-39.69, -0.69, 149.50)	4.05E+08	3.87E+08 ± 0.06%	0.96	4.43E+08 ± 0.08%	1.09
(-39.69, -0.69, 153.50)	2.91E+08	2.38E+08 ± 0.08%	0.82	3.35E+08 ± 0.10%	1.15
(-39.69, -5.67, 114.50)	1.64E+08	1.81E+08 ± 0.07%	1.10	1.57E+08 ± 0.10%	0.96
(-39.69, -5.67, 131.50)	4.64E+08	5.24E+08 ± 0.06%	1.13	5.05E+08 ± 0.07%	1.09
(-39.69, -5.67, 145.50)	4.64E+08	4.70E+08 ± 0.06%	1.01	4.94E+08 ± 0.07%	1.06
(-39.69, -11.97, 114.50)	1.36E+08	1.34E+08 ± 0.07%	0.98	1.33E+08 ± 0.10%	0.98
(-39.69, -11.97, 131.50)	3.80E+08	4.28E+08 ± 0.05%	1.13	3.91E+08 ± 0.07%	1.03
(-39.69, -11.97, 145.50)	3.78E+08	4.16E+08 ± 0.05%	1.10	3.64E+08 ± 0.07%	0.96
(-39.69, -18.27, 114.50)	9.00E+07	1.03E+08 ± 0.08%	1.14	8.94E+07 ± 0.11%	0.99
(-39.69, -18.27, 131.50)	2.21E+08	2.79E+08 ± 0.05%	1.26	2.08E+08 ± 0.07%	0.94
(-39.69, -18.27, 145.50)	2.17E+08	2.39E+08 ± 0.05%	1.10	1.90E+08 ± 0.08%	0.88
(-37.17, -20.79, 114.50)	1.06E+08	1.08E+08 ± 0.07%	1.02	1.09E+08 ± 0.09%	1.03
(-37.17, -20.79, 131.50)	2.40E+08	2.12E+08 ± 0.06%	0.89	2.55E+08 ± 0.07%	1.06

(-37.17, -20.79, 145.50)	2.22E+08	2.39E+08 ± 0.06%	1.08	1.96E+08 ± 0.07%	0.88
(-30.87, -20.79, 114.50)	3.08E+08	3.24E+08 ± 0.05%	1.05	3.68E+08 ± 0.07%	1.19
(-30.87, -20.79, 131.50)	5.19E+08	6.78E+08 ± 0.05%	1.30	5.29E+08 ± 0.07%	1.02
(-30.87, -20.79, 145.50)	4.34E+08	4.95E+08 ± 0.05%	1.14	4.62E+08 ± 0.07%	1.06
(-24.57, -20.79, 114.50)	6.24E+08	6.79E+08 ± 0.05%	1.09	7.05E+08 ± 0.07%	1.13
(-24.57, -20.79, 131.50)	9.24E+08	1.19E+09 ± 0.05%	1.28	9.25E+08 ± 0.06%	1.00
(-24.57, -20.79, 145.50)	7.11E+08	7.84E+08 ± 0.05%	1.10	7.01E+08 ± 0.07%	0.99
Region Average C/E Ratio		(1.10 ± 0.06) ± 0.11		(1.04 ± 0.09) ± 0.09	
Core Barrel					
(-49.77, -0.63, 106.50)	1.69E+07	1.97E+07 ± 0.12%	1.16	1.83E+07 ± 0.15%	1.08
(-49.77, -0.63, 110.50)	2.22E+07	2.33E+07 ± 0.12%	1.05	2.25E+07 ± 0.14%	1.01
(-49.77, -0.63, 114.50)	2.82E+07	3.56E+07 ± 0.11%	1.26	3.70E+07 ± 0.13%	1.31
(-49.77, -0.63, 118.50)	3.60E+07	4.40E+07 ± 0.10%	1.22	3.78E+07 ± 0.13%	1.05
(-49.77, -0.63, 122.50)	4.39E+07	4.01E+07 ± 0.10%	0.91	4.94E+07 ± 0.13%	1.13
(-49.77, -0.63, 125.50)	4.94E+07	5.59E+07 ± 0.11%	1.13	5.01E+07 ± 0.13%	1.01
(-49.77, -0.63, 128.50)	5.54E+07	6.36E+07 ± 0.10%	1.15	5.00E+07 ± 0.12%	0.90
(-49.77, -0.63, 131.50)	6.09E+07	8.39E+07 ± 0.09%	1.38	7.35E+07 ± 0.13%	1.21
(-49.77, -0.63, 134.50)	6.45E+07	7.07E+07 ± 0.10%	1.09	7.36E+07 ± 0.13%	1.14
(-49.77, -0.63, 137.50)	6.68E+07	7.70E+07 ± 0.10%	1.15	5.49E+07 ± 0.12%	0.82
(-49.77, -0.63, 141.50)	6.44E+07	7.71E+07 ± 0.11%	1.20	6.96E+07 ± 0.13%	1.08
(-49.77, -0.63, 145.50)	5.87E+07	6.08E+07 ± 0.10%	1.03	6.08E+07 ± 0.15%	1.04
(-49.77, -0.63, 149.50)	4.93E+07	5.01E+07 ± 0.12%	1.02	4.55E+07 ± 0.13%	0.92
(-49.77, -0.63, 153.50)	3.76E+07	4.21E+07 ± 0.11%	1.12	3.56E+07 ± 0.13%	0.95
(-49.77, -0.63, 114.50)	2.49E+07	3.56E+07 ± 0.11%	1.43	3.70E+07 ± 0.13%	1.49
(-49.77, -0.63, 131.50)	5.21E+07	8.39E+07 ± 0.09%	1.61	7.35E+07 ± 0.13%	1.41
(-49.77, -0.63, 145.50)	5.04E+07	6.08E+07 ± 0.10%	1.21	6.08E+07 ± 0.15%	1.21
(-47.25, -18.27, 106.50)	1.42E+07	1.52E+07 ± 0.10%	1.08	1.34E+07 ± 0.15%	0.95
(-47.25, -18.27, 110.50)	1.92E+07	2.24E+07 ± 0.09%	1.16	2.11E+07 ± 0.12%	1.10
(-47.25, -18.27, 114.50)	2.38E+07	2.81E+07 ± 0.09%	1.18	2.59E+07 ± 0.14%	1.09
(-47.25, -18.27, 118.50)	2.96E+07	3.73E+07 ± 0.08%	1.26	3.02E+07 ± 0.12%	1.02
(-47.25, -18.27, 122.50)	3.56E+07	4.46E+07 ± 0.09%	1.25	3.67E+07 ± 0.12%	1.03
(-47.25, -18.27, 125.50)	4.04E+07	4.76E+07 ± 0.07%	1.18	4.22E+07 ± 0.11%	1.04
(-47.25, -18.27, 128.50)	4.54E+07	5.56E+07 ± 0.08%	1.22	4.89E+07 ± 0.10%	1.08
(-47.25, -18.27, 131.50)	5.03E+07	5.76E+07 ± 0.07%	1.14	5.22E+07 ± 0.12%	1.04
(-47.25, -18.27, 134.50)	5.41E+07	6.42E+07 ± 0.07%	1.19	5.03E+07 ± 0.11%	0.93
(-47.25, -18.27, 137.50)	5.52E+07	6.10E+07 ± 0.07%	1.10	5.50E+07 ± 0.11%	1.00
(-47.25, -18.27, 141.50)	5.35E+07	5.08E+07 ± 0.08%	0.95	5.88E+07 ± 0.10%	1.10
(-47.25, -18.27, 145.50)	4.78E+07	4.83E+07 ± 0.08%	1.01	4.87E+07 ± 0.10%	1.02
(-47.25, -18.27, 149.50)	4.04E+07	4.60E+07 ± 0.08%	1.14	4.34E+07 ± 0.11%	1.07
(-47.25, -18.27, 153.50)	3.07E+07	3.11E+07 ± 0.09%	1.01	3.38E+07 ± 0.12%	1.10
(-45.99, -22.05, 114.50)	2.19E+07	2.37E+07 ± 0.09%	1.08	2.48E+07 ± 0.12%	1.14
(-45.99, -22.05, 131.50)	4.35E+07	5.16E+07 ± 0.07%	1.19	5.33E+07 ± 0.10%	1.23

(-45.99, -22.05, 145.50)	4.09E+07	4.54E+07 ± 0.07%	1.11	3.71E+07 ± 0.11%	0.91
(-44.73, -24.57, 114.50)	2.11E+07	2.44E+07 ± 0.08%	1.16	2.34E+07 ± 0.12%	1.11
(-44.73, -24.57, 131.50)	3.94E+07	4.55E+07 ± 0.08%	1.15	4.38E+07 ± 0.10%	1.11
(-44.73, -24.57, 145.50)	3.67E+07	3.89E+07 ± 0.08%	1.06	3.31E+07 ± 0.10%	0.90
(-42.21, -28.35, 114.50)	2.88E+07	2.75E+07 ± 0.09%	0.96	2.38E+07 ± 0.12%	0.83
(-42.21, -28.35, 131.50)	4.48E+07	4.41E+07 ± 0.07%	0.98	4.36E+07 ± 0.10%	0.97
(-42.21, -28.35, 145.50)	3.93E+07	3.75E+07 ± 0.08%	0.96	3.89E+07 ± 0.10%	0.99
(-38.43, -33.39, 114.50)	2.53E+07	2.80E+07 ± 0.09%	1.10	2.50E+07 ± 0.11%	0.98
(-38.43, -33.39, 131.50)	3.76E+07	4.08E+07 ± 0.07%	1.08	3.99E+07 ± 0.11%	1.06
(-38.43, -33.39, 145.50)	3.06E+07	3.41E+07 ± 0.08%	1.12	3.65E+07 ± 0.11%	1.19
(-35.91, -35.91, 106.50)	1.75E+07	1.47E+07 ± 0.09%	0.84	1.67E+07 ± 0.13%	0.96
(-35.91, -35.91, 110.50)	2.25E+07	2.64E+07 ± 0.09%	1.17	2.41E+07 ± 0.11%	1.07
(-35.91, -35.91, 114.50)	2.74E+07	3.01E+07 ± 0.08%	1.10	3.00E+07 ± 0.12%	1.09
(-35.91, -35.91, 118.50)	3.16E+07	3.30E+07 ± 0.09%	1.04	3.70E+07 ± 0.10%	1.17
(-35.91, -35.91, 122.50)	3.53E+07	4.11E+07 ± 0.07%	1.16	4.14E+07 ± 0.09%	1.17
(-35.91, -35.91, 125.50)	3.74E+07	4.87E+07 ± 0.08%	1.30	4.27E+07 ± 0.11%	1.14
(-35.91, -35.91, 128.50)	3.85E+07	5.30E+07 ± 0.08%	1.38	4.65E+07 ± 0.10%	1.21
(-35.91, -35.91, 131.50)	3.86E+07	4.08E+07 ± 0.08%	1.06	4.54E+07 ± 0.10%	1.17
(-35.91, -35.91, 134.50)	3.84E+07	4.30E+07 ± 0.07%	1.12	3.97E+07 ± 0.12%	1.03
(-35.91, -35.91, 137.50)	3.81E+07	3.36E+07 ± 0.08%	0.88	4.16E+07 ± 0.11%	1.09
(-35.91, -35.91, 141.50)	3.51E+07	4.19E+07 ± 0.08%	1.20	3.69E+07 ± 0.10%	1.05
(-35.91, -35.91, 145.50)	3.09E+07	3.25E+07 ± 0.09%	1.05	3.56E+07 ± 0.10%	1.15
(-35.91, -35.91, 149.50)	2.55E+07	2.55E+07 ± 0.09%	1.00	3.13E+07 ± 0.12%	1.23
(-35.91, -35.91, 153.50)	1.97E+07	2.17E+07 ± 0.09%	1.10	1.97E+07 ± 0.13%	1.00
(-18.27, -47.25, 106.50)	3.42E+07	3.74E+07 ± 0.09%	1.09	3.54E+07 ± 0.12%	1.04
(-18.27, -47.25, 110.50)	4.65E+07	4.77E+07 ± 0.08%	1.03	4.37E+07 ± 0.11%	0.94
(-18.27, -47.25, 114.50)	5.72E+07	5.99E+07 ± 0.08%	1.05	5.53E+07 ± 0.10%	0.97
(-18.27, -47.25, 118.50)	6.50E+07	7.46E+07 ± 0.08%	1.15	6.36E+07 ± 0.10%	0.98
(-18.27, -47.25, 122.50)	7.10E+07	8.58E+07 ± 0.08%	1.21	8.28E+07 ± 0.09%	1.17
(-18.27, -47.25, 125.50)	7.48E+07	6.20E+07 ± 0.07%	0.83	6.98E+07 ± 0.10%	0.93
(-18.27, -47.25, 128.50)	7.52E+07	9.91E+07 ± 0.07%	1.32	8.30E+07 ± 0.09%	1.10
(-18.27, -47.25, 131.50)	7.68E+07	9.98E+07 ± 0.07%	1.30	8.66E+07 ± 0.09%	1.13
(-18.27, -47.25, 134.50)	7.49E+07	7.99E+07 ± 0.07%	1.07	8.18E+07 ± 0.10%	1.09
(-18.27, -47.25, 137.50)	7.24E+07	8.58E+07 ± 0.07%	1.19	6.46E+07 ± 0.10%	0.89
(-18.27, -47.25, 141.50)	6.64E+07	7.46E+07 ± 0.07%	1.12	7.34E+07 ± 0.10%	1.11
(-18.27, -47.25, 145.50)	5.72E+07	6.48E+07 ± 0.08%	1.13	5.97E+07 ± 0.11%	1.04
(-18.27, -47.25, 149.50)	4.67E+07	4.79E+07 ± 0.08%	1.03	4.52E+07 ± 0.10%	0.97
(-18.27, -47.25, 153.50)	3.45E+07	3.78E+07 ± 0.10%	1.10	3.36E+07 ± 0.13%	0.98
(-0.63, -49.77, 106.50)	4.32E+07	5.00E+07 ± 0.12%	1.16	4.01E+07 ± 0.16%	0.93
(-0.63, -49.77, 110.50)	5.81E+07	6.03E+07 ± 0.09%	1.04	7.02E+07 ± 0.13%	1.21
(-0.63, -49.77, 114.50)	7.08E+07	8.30E+07 ± 0.11%	1.17	6.71E+07 ± 0.13%	0.95
(-0.63, -49.77, 118.50)	8.20E+07	7.40E+07 ± 0.09%	0.90	8.63E+07 ± 0.15%	1.05

(-0.63, -49.77, 122.50)	8.94E+07	1.12E+08 ± 0.10%	1.25	1.03E+08 ± 0.14%	1.15
(-0.63, -49.77, 125.50)	9.40E+07	1.02E+08 ± 0.10%	1.09	1.07E+08 ± 0.13%	1.14
(-0.63, -49.77, 128.50)	9.54E+07	1.32E+08 ± 0.10%	1.39	8.37E+07 ± 0.13%	0.88
(-0.63, -49.77, 131.50)	9.62E+07	1.24E+08 ± 0.10%	1.29	1.17E+08 ± 0.12%	1.22
(-0.63, -49.77, 134.50)	9.43E+07	1.15E+08 ± 0.10%	1.22	9.80E+07 ± 0.12%	1.04
(-0.63, -49.77, 137.50)	9.06E+07	1.12E+08 ± 0.09%	1.23	1.09E+08 ± 0.12%	1.20
(-0.63, -49.77, 141.50)	8.21E+07	8.68E+07 ± 0.09%	1.06	8.70E+07 ± 0.15%	1.06
(-0.63, -49.77, 145.50)	7.17E+07	6.52E+07 ± 0.11%	0.91	9.02E+07 ± 0.14%	1.26
(-0.63, -49.77, 149.50)	5.81E+07	5.63E+07 ± 0.12%	0.97	6.94E+07 ± 0.15%	1.20
(-0.63, -49.77, 153.50)	4.32E+07	4.33E+07 ± 0.11%	1.00	4.37E+07 ± 0.14%	1.01
Region Average C/E Ratio		(1.13 ± 0.09) ± 0.13		(1.07 ± 0.12) ± 0.12	
Water Gap					
(-44.73, -0.63, 106.50)	3.74E+07	3.74E+07 ± 0.11%	1.00	4.14E+07 ± 0.15%	1.11
(-44.73, -0.63, 110.50)	5.03E+07	4.89E+07 ± 0.11%	0.97	6.41E+07 ± 0.15%	1.28
(-44.73, -0.63, 114.50)	6.37E+07	6.81E+07 ± 0.10%	1.07	6.26E+07 ± 0.15%	0.98
(-44.73, -0.63, 118.50)	7.68E+07	8.21E+07 ± 0.11%	1.07	7.94E+07 ± 0.13%	1.03
(-44.73, -0.63, 122.50)	9.57E+07	1.13E+08 ± 0.09%	1.19	8.90E+07 ± 0.13%	0.93
(-44.73, -0.63, 125.50)	1.12E+08	1.14E+08 ± 0.09%	1.02	1.15E+08 ± 0.13%	1.02
(-44.73, -0.63, 128.50)	1.33E+08	1.44E+08 ± 0.08%	1.08	1.48E+08 ± 0.12%	1.11
(-44.73, -0.63, 131.50)	1.51E+08	1.95E+08 ± 0.09%	1.29	1.43E+08 ± 0.12%	0.95
(-44.73, -0.63, 134.50)	1.65E+08	1.84E+08 ± 0.08%	1.12	1.84E+08 ± 0.11%	1.12
(-44.73, -0.63, 137.50)	1.68E+08	1.76E+08 ± 0.09%	1.05	1.60E+08 ± 0.13%	0.95
(-44.73, -0.63, 141.50)	1.64E+08	2.10E+08 ± 0.08%	1.28	1.62E+08 ± 0.13%	0.99
(-44.73, -0.63, 145.50)	1.45E+08	1.43E+08 ± 0.09%	0.99	1.67E+08 ± 0.12%	1.15
(-44.73, -0.63, 149.50)	1.21E+08	1.29E+08 ± 0.10%	1.07	1.19E+08 ± 0.13%	0.99
(-44.73, -0.63, 153.50)	8.65E+07	9.08E+07 ± 0.11%	1.05	1.06E+08 ± 0.14%	1.23
Region Average C/E Ratio		(1.12 ± 0.09) ± 0.11		(1.06 ± 0.13) ± 0.11	
PLSA					
(-37.17, 0.63, 106.50)	1.65E+08	1.59E+08 ± 0.13%	0.96	1.71E+08 ± 0.19%	1.04
(-37.17, 0.63, 110.50)	2.30E+08	2.25E+08 ± 0.13%	0.98	2.45E+08 ± 0.17%	1.07
(-37.17, 0.63, 114.50)	2.95E+08	3.20E+08 ± 0.12%	1.09	2.44E+08 ± 0.15%	0.83
(-37.17, 0.63, 118.50)	3.55E+08	3.69E+08 ± 0.11%	1.04	3.45E+08 ± 0.15%	0.97
(-37.17, 0.63, 122.50)	4.28E+08	4.24E+08 ± 0.10%	0.99	4.47E+08 ± 0.14%	1.05
(-37.17, 0.63, 125.50)	5.06E+08	5.98E+08 ± 0.10%	1.18	4.49E+08 ± 0.14%	0.89
(-37.17, 0.63, 128.50)	6.75E+08	8.29E+08 ± 0.09%	1.23	7.87E+08 ± 0.13%	1.17
(-37.17, -0.63, 131.05)	1.08E+09	1.17E+09 ± 0.07%	1.08	1.09E+09 ± 0.10%	1.01
(-37.17, -0.63, 134.15)	1.23E+09	1.37E+09 ± 0.07%	1.11	1.29E+09 ± 0.10%	1.05
(-37.17, -0.63, 137.25)	1.28E+09	1.36E+09 ± 0.06%	1.06	1.38E+09 ± 0.09%	1.08
(-37.17, -0.63, 141.35)	1.23E+09	1.22E+09 ± 0.07%	1.00	1.15E+09 ± 0.10%	0.93
(-37.17, -0.63, 145.45)	1.11E+09	1.19E+09 ± 0.07%	1.07	1.10E+09 ± 0.10%	0.99
(-37.17, -0.63, 149.55)	9.13E+08	9.14E+08 ± 0.08%	1.00	9.21E+08 ± 0.10%	1.01
(-37.17, -0.63, 153.65)	7.03E+08	4.79E+08 ± 0.10%	0.68	6.48E+08 ± 0.11%	0.92

(-34.65, 0.63, 106.50)	2.71E+08	2.63E+08 ± 0.14%	0.97	2.66E+08 ± 0.14%	0.98
(-34.65, 0.63, 110.50)	3.84E+08	3.80E+08 ± 0.11%	0.99	4.37E+08 ± 0.17%	1.14
(-34.65, 0.63, 114.50)	4.90E+08	5.67E+08 ± 0.11%	1.16	5.11E+08 ± 0.14%	1.04
(-34.65, 0.63, 118.50)	5.90E+08	6.28E+08 ± 0.10%	1.06	7.03E+08 ± 0.17%	1.19
(-34.65, 0.63, 122.50)	6.95E+08	7.77E+08 ± 0.10%	1.12	6.55E+08 ± 0.13%	0.94
(-34.65, 0.63, 125.50)	7.98E+08	9.12E+08 ± 0.09%	1.14	1.02E+09 ± 0.12%	1.28
(-34.65, 0.63, 128.50)	1.03E+09	1.03E+09 ± 0.09%	1.00	9.87E+08 ± 0.11%	0.96
(-34.65, 0.63, 131.05)	1.62E+09	1.79E+09 ± 0.06%	1.10	1.61E+09 ± 0.10%	1.00
(-34.65, 0.63, 134.15)	1.85E+09	2.08E+09 ± 0.06%	1.13	2.05E+09 ± 0.08%	1.11
(-34.65, 0.63, 137.25)	1.90E+09	2.05E+09 ± 0.06%	1.08	1.87E+09 ± 0.09%	0.99
(-34.65, 0.63, 141.35)	1.85E+09	2.05E+09 ± 0.06%	1.11	1.98E+09 ± 0.08%	1.07
(-34.65, 0.63, 145.45)	1.63E+09	1.49E+09 ± 0.06%	0.91	1.47E+09 ± 0.09%	0.90
(-34.65, 0.63, 149.55)	1.35E+09	1.19E+09 ± 0.08%	0.88	1.33E+09 ± 0.09%	0.98
(-34.65, 0.63, 153.65)	1.03E+09	7.52E+08 ± 0.09%	0.73	1.05E+09 ± 0.09%	1.02
(-32.13, -0.63, 131.05)	2.28E+09	2.30E+09 ± 0.06%	1.01	2.38E+09 ± 0.08%	1.04
(-32.13, -0.63, 134.15)	2.43E+09	2.73E+09 ± 0.06%	1.13	2.41E+09 ± 0.08%	0.99
(-32.13, -0.63, 137.25)	2.44E+09	2.46E+09 ± 0.06%	1.01	2.34E+09 ± 0.09%	0.96
(-32.13, -0.63, 141.35)	2.31E+09	2.41E+09 ± 0.06%	1.04	2.53E+09 ± 0.08%	1.09
(-32.13, -0.63, 145.45)	2.03E+09	2.10E+09 ± 0.06%	1.03	2.11E+09 ± 0.08%	1.04
(-32.13, -0.63, 149.55)	1.66E+09	1.68E+09 ± 0.07%	1.02	1.34E+09 ± 0.09%	0.81
(-32.13, -0.63, 153.65)	1.25E+09	8.03E+08 ± 0.09%	0.64	1.16E+09 ± 0.10%	0.93
(-32.13, 0.63, 106.50)	5.12E+08	4.80E+08 ± 0.12%	0.94	4.84E+08 ± 0.15%	0.95
(-32.13, 0.63, 110.50)	7.16E+08	7.30E+08 ± 0.09%	1.02	7.33E+08 ± 0.13%	1.02
(-32.13, 0.63, 114.50)	9.11E+08	9.84E+08 ± 0.08%	1.08	8.49E+08 ± 0.13%	0.93
(-32.13, 0.63, 118.50)	1.09E+09	1.32E+09 ± 0.08%	1.21	1.36E+09 ± 0.11%	1.25
(-32.13, 0.63, 122.50)	1.26E+09	1.53E+09 ± 0.07%	1.21	1.25E+09 ± 0.11%	0.99
(-32.13, 0.63, 125.50)	1.40E+09	1.45E+09 ± 0.08%	1.03	1.36E+09 ± 0.10%	0.97
(-32.13, 0.63, 128.50)	1.62E+09	1.49E+09 ± 0.07%	0.92	1.65E+09 ± 0.09%	1.01
(-37.17, -14.49, 106.50)	1.14E+08	1.14E+08 ± 0.12%	1.00	1.15E+08 ± 0.15%	1.01
(-37.17, -14.49, 110.50)	1.48E+08	1.48E+08 ± 0.12%	1.00	1.73E+08 ± 0.15%	1.17
(-37.17, -14.49, 114.50)	1.79E+08	1.90E+08 ± 0.10%	1.06	2.54E+08 ± 0.13%	1.42
(-37.17, -14.49, 118.50)	2.21E+08	2.44E+08 ± 0.10%	1.10	2.52E+08 ± 0.13%	1.14
(-37.17, -14.49, 122.50)	2.65E+08	3.62E+08 ± 0.09%	1.37	2.91E+08 ± 0.13%	1.10
(-37.17, -14.49, 125.50)	3.20E+08	2.42E+08 ± 0.09%	0.76	3.16E+08 ± 0.12%	0.98
(-37.17, -14.49, 128.50)	4.48E+08	5.22E+08 ± 0.08%	1.16	5.12E+08 ± 0.11%	1.14
Region Average C/E Ratio		(1.03 ± 0.09) ± 0.13		(1.03 ± 0.12) ± 0.11	
3.3% Fuel Positions					
(-29.61, -0.63, 106.05)	9.32E+08	6.41E+08 ± 0.10%	0.69	9.70E+08 ± 0.10%	1.04
(-29.61, -0.63, 110.15)	1.28E+09	1.21E+09 ± 0.07%	0.95	1.34E+09 ± 0.09%	1.05
(-29.61, -0.63, 114.25)	1.64E+09	1.68E+09 ± 0.07%	1.02	1.67E+09 ± 0.10%	1.02
(-29.61, -0.63, 118.35)	1.99E+09	2.25E+09 ± 0.06%	1.13	2.00E+09 ± 0.09%	1.01
(-29.61, -0.63, 122.45)	2.28E+09	2.66E+09 ± 0.06%	1.17	2.49E+09 ± 0.09%	1.09

(-29.61, -0.63, 125.55)	2.49E+09	2.50E+09 ± 0.07%	1.00	2.57E+09 ± 0.09%	1.03
(-29.61, -0.63, 128.65)	2.68E+09	3.06E+09 ± 0.06%	1.14	2.76E+09 ± 0.09%	1.03
(-29.61, -0.63, 131.75)	2.86E+09	2.65E+09 ± 0.06%	0.93	2.52E+09 ± 0.09%	0.88
(-29.61, -0.63, 134.85)	2.93E+09	3.38E+09 ± 0.06%	1.15	2.85E+09 ± 0.09%	0.97
(-29.61, -0.63, 137.95)	2.86E+09	3.28E+09 ± 0.06%	1.15	2.82E+09 ± 0.08%	0.99
(-29.61, -0.63, 141.05)	2.74E+09	2.71E+09 ± 0.06%	0.99	2.81E+09 ± 0.08%	1.03
(-29.61, -0.63, 145.15)	2.41E+09	2.42E+09 ± 0.06%	1.00	2.17E+09 ± 0.08%	0.90
(-29.61, -0.63, 149.25)	1.97E+09	1.98E+09 ± 0.07%	1.00	1.94E+09 ± 0.09%	0.99
(-29.61, -0.63, 153.35)	1.47E+09	1.01E+09 ± 0.10%	0.69	1.48E+09 ± 0.10%	1.01
(-27.09, 0.63, 106.05)	1.14E+09	7.59E+08 ± 0.10%	0.66	1.11E+09 ± 0.11%	0.97
(-27.09, 0.63, 110.15)	1.59E+09	1.54E+09 ± 0.08%	0.97	1.61E+09 ± 0.10%	1.01
(-27.09, 0.63, 114.25)	2.01E+09	1.81E+09 ± 0.07%	0.90	2.12E+09 ± 0.09%	1.05
(-27.09, 0.63, 118.35)	2.42E+09	2.48E+09 ± 0.07%	1.02	2.35E+09 ± 0.08%	0.97
(-27.09, 0.63, 122.45)	2.77E+09	3.01E+09 ± 0.07%	1.08	2.60E+09 ± 0.10%	0.94
(-27.09, 0.63, 125.55)	2.99E+09	3.50E+09 ± 0.06%	1.17	2.87E+09 ± 0.09%	0.96
(-27.09, 0.63, 128.65)	3.16E+09	3.27E+09 ± 0.07%	1.04	3.29E+09 ± 0.08%	1.04
(-27.09, 0.63, 131.75)	3.27E+09	3.63E+09 ± 0.07%	1.11	3.31E+09 ± 0.09%	1.01
(-27.09, 0.63, 134.85)	3.30E+09	3.28E+09 ± 0.06%	0.99	3.09E+09 ± 0.08%	0.94
(-27.09, 0.63, 137.95)	3.22E+09	3.24E+09 ± 0.07%	1.01	3.37E+09 ± 0.08%	1.05
(-27.09, 0.63, 141.05)	3.05E+09	3.28E+09 ± 0.07%	1.08	3.37E+09 ± 0.09%	1.11
(-27.09, 0.63, 145.15)	2.68E+09	2.75E+09 ± 0.07%	1.03	2.63E+09 ± 0.09%	0.98
(-27.09, 0.63, 149.25)	2.20E+09	2.27E+09 ± 0.07%	1.03	2.21E+09 ± 0.10%	1.01
(-27.09, 0.63, 153.35)	1.65E+09	1.48E+09 ± 0.09%	0.90	1.58E+09 ± 0.10%	0.96
(-30.87, -3.15, 106.05)	7.66E+08	5.70E+08 ± 0.10%	0.74	6.49E+08 ± 0.12%	0.85
(-30.87, -3.15, 110.15)	1.06E+09	9.20E+08 ± 0.08%	0.87	1.13E+09 ± 0.10%	1.07
(-30.87, -3.15, 114.25)	1.35E+09	1.32E+09 ± 0.07%	0.98	1.17E+09 ± 0.10%	0.87
(-30.87, -3.15, 118.35)	1.62E+09	1.53E+09 ± 0.07%	0.94	1.59E+09 ± 0.09%	0.98
(-30.87, -3.15, 122.45)	1.88E+09	2.20E+09 ± 0.07%	1.17	1.71E+09 ± 0.09%	0.91
(-30.87, -3.15, 125.55)	2.07E+09	2.19E+09 ± 0.06%	1.06	2.03E+09 ± 0.08%	0.98
(-30.87, -3.15, 128.65)	2.28E+09	2.38E+09 ± 0.06%	1.04	2.25E+09 ± 0.08%	0.99
(-30.87, -3.15, 131.75)	2.53E+09	2.96E+09 ± 0.06%	1.17	2.85E+09 ± 0.10%	1.13
(-30.87, -3.15, 134.85)	2.63E+09	2.86E+09 ± 0.06%	1.09	2.79E+09 ± 0.07%	1.06
(-30.87, -3.15, 137.95)	2.62E+09	2.67E+09 ± 0.06%	1.02	2.55E+09 ± 0.08%	0.97
(-30.87, -3.15, 141.05)	2.50E+09	2.39E+09 ± 0.06%	0.96	2.71E+09 ± 0.07%	1.09
(-30.87, -3.15, 145.15)	2.21E+09	2.32E+09 ± 0.06%	1.05	2.30E+09 ± 0.09%	1.04
(-30.87, -3.15, 149.25)	1.83E+09	1.74E+09 ± 0.06%	0.95	1.68E+09 ± 0.08%	0.92
(-30.87, -3.15, 153.35)	1.38E+09	9.25E+08 ± 0.09%	0.67	1.35E+09 ± 0.09%	0.98
(-0.63, -32.13, 106.05)	1.29E+09	8.85E+08 ± 0.09%	0.69	1.31E+09 ± 0.10%	1.02
(-0.63, -32.13, 110.15)	1.77E+09	1.76E+09 ± 0.07%	0.99	1.66E+09 ± 0.09%	0.94
(-0.63, -32.13, 114.25)	2.21E+09	2.47E+09 ± 0.06%	1.12	1.89E+09 ± 0.08%	0.86
(-0.63, -32.13, 118.35)	2.61E+09	2.65E+09 ± 0.06%	1.02	2.84E+09 ± 0.08%	1.09
(-0.63, -32.13, 122.45)	2.90E+09	3.49E+09 ± 0.06%	1.21	2.84E+09 ± 0.08%	0.98

(-0.63, -32.13, 125.55)	3.05E+09	2.80E+09 ± 0.06%	0.92	3.31E+09 ± 0.09%	1.09
(-0.63, -32.13, 128.65)	3.12E+09	3.63E+09 ± 0.06%	1.16	3.57E+09 ± 0.09%	1.14
(-0.63, -32.13, 131.75)	3.12E+09	3.36E+09 ± 0.06%	1.08	3.01E+09 ± 0.09%	0.96
(-0.63, -32.13, 134.85)	3.05E+09	3.34E+09 ± 0.07%	1.10	3.11E+09 ± 0.08%	1.02
(-0.63, -32.13, 137.95)	2.89E+09	3.21E+09 ± 0.06%	1.11	3.09E+09 ± 0.08%	1.07
(-0.63, -32.13, 141.05)	2.71E+09	2.66E+09 ± 0.06%	0.98	2.75E+09 ± 0.09%	1.02
(-0.63, -32.13, 145.15)	2.33E+09	2.37E+09 ± 0.06%	1.02	2.43E+09 ± 0.09%	1.04
(-0.63, -32.13, 149.25)	1.89E+09	1.65E+09 ± 0.08%	0.87	2.14E+09 ± 0.10%	1.13
(-0.63, -32.13, 153.35)	1.40E+09	9.66E+08 ± 0.09%	0.69	1.35E+09 ± 0.10%	0.97
Region Average C/E Ratio		(0.99 ± 0.07) ± 0.14		(1.00 ± 0.09) ± 0.07	
Reaction Average C/E Ratio		(1.07 ± 0.08) ± 0.14		(1.04 ± 0.11) ± 0.10	

¹¹⁵In (n,n')

Position (x, y, z)	Experimental	Calculated (KENO)	C/E	Calculated (Benchmark)	C/E
Inner Baffle					
(-4.41, -0.63, 131.50)	2.25E+09	2.02E+09 ± 0.08%	0.90	2.12E+09 ± 0.14%	0.94
(-4.41, -4.41, 131.50)	2.71E+09	2.95E+09 ± 0.08%	1.09	3.23E+09 ± 0.10%	1.19
		(0.99 ± 0.08) ± 0.13		(1.07 ± 0.12) ± 0.17	
Outer Baffle					
(-39.69, -0.69, 106.50)	1.19E+08	1.17E+08 ± 0.11%	0.99	1.05E+08 ± 0.13%	0.88
(-39.69, -0.69, 110.50)	1.70E+08	1.90E+08 ± 0.09%	1.12	1.75E+08 ± 0.12%	1.03
(-39.69, -0.69, 114.50)	2.18E+08	2.06E+08 ± 0.08%	0.94	2.04E+08 ± 0.11%	0.94
(-39.69, -0.69, 118.50)	2.66E+08	3.08E+08 ± 0.08%	1.16	2.61E+08 ± 0.12%	0.98
(-39.69, -0.69, 122.50)	3.26E+08	2.57E+08 ± 0.10%	0.79	2.97E+08 ± 0.10%	0.91
(-39.69, -0.69, 125.50)	3.87E+08	3.88E+08 ± 0.08%	1.00	3.50E+08 ± 0.10%	0.91
(-39.69, -0.69, 128.50)	4.86E+08	4.77E+08 ± 0.07%	0.98	5.09E+08 ± 0.09%	1.05
(-39.69, -0.69, 131.50)	6.11E+08	5.86E+08 ± 0.07%	0.96	5.80E+08 ± 0.08%	0.95
(-39.69, -0.69, 134.50)	6.92E+08	7.01E+08 ± 0.06%	1.01	6.37E+08 ± 0.08%	0.92
(-39.69, -0.69, 137.50)	7.20E+08	7.73E+08 ± 0.06%	1.07	7.75E+08 ± 0.08%	1.08
(-39.69, -0.69, 141.50)	6.89E+08	7.73E+08 ± 0.07%	1.12	6.95E+08 ± 0.08%	1.01
(-39.69, -0.69, 145.50)	6.18E+08	5.98E+08 ± 0.06%	0.97	5.67E+08 ± 0.09%	0.92
(-39.69, -0.69, 149.50)	5.06E+08	4.53E+08 ± 0.07%	0.90	5.11E+08 ± 0.09%	1.01
(-39.69, -0.69, 153.50)	3.61E+08	2.64E+08 ± 0.08%	0.73	3.92E+08 ± 0.10%	1.08
Region Average C/E Ratio		(0.98 ± 0.08) ± 0.12		(0.98 ± 0.10) ± 0.07	
Water Gap					
(-44.73, -0.63, 106.50)	3.77E+07	3.15E+07 ± 0.12%	0.84	4.45E+07 ± 0.15%	1.18
(-44.73, -0.63, 110.50)	5.19E+07	5.86E+07 ± 0.10%	1.13	6.24E+07 ± 0.14%	1.20
(-44.73, -0.63, 114.50)	6.61E+07	6.67E+07 ± 0.11%	1.01	5.87E+07 ± 0.13%	0.89
(-44.73, -0.63, 118.50)	8.27E+07	8.65E+07 ± 0.12%	1.05	9.17E+07 ± 0.13%	1.11
(-44.73, -0.63, 122.50)	9.99E+07	1.08E+08 ± 0.12%	1.08	1.05E+08 ± 0.13%	1.05
(-44.73, -0.63, 125.50)	1.19E+08	9.46E+07 ± 0.10%	0.80	1.12E+08 ± 0.15%	0.94

(-44.73, -0.63, 128.50)	1.41E+08	1.49E+08 ± 0.09%	1.06	1.53E+08 ± 0.11%	1.09
(-44.73, -0.63, 131.50)	1.55E+08	1.88E+08 ± 0.09%	1.21	1.52E+08 ± 0.12%	0.98
(-44.73, -0.63, 134.50)	1.73E+08	2.19E+08 ± 0.08%	1.27	1.76E+08 ± 0.11%	1.02
(-44.73, -0.63, 137.50)	1.84E+08	1.86E+08 ± 0.08%	1.01	1.56E+08 ± 0.12%	0.85
(-44.73, -0.63, 141.50)	1.79E+08	2.21E+08 ± 0.08%	1.24	1.70E+08 ± 0.12%	0.95
(-44.73, -0.63, 145.50)	1.60E+08	1.79E+08 ± 0.09%	1.12	1.58E+08 ± 0.12%	0.99
(-44.73, -0.63, 149.50)	1.34E+08	1.24E+08 ± 0.10%	0.92	1.39E+08 ± 0.13%	1.04
(-44.73, -0.63, 153.50)	1.00E+08	8.10E+07 ± 0.10%	0.81	1.04E+08 ± 0.15%	1.03
Region Average C/E Ratio		(1.04 ± 0.10) ± 0.15		(1.02 ± 0.13) ± 0.10	
Core Barrel					
(-49.77, -0.63, 106.50)	1.90E+07	1.92E+07 ± 0.11%	1.01	1.67E+07 ± 0.17%	0.88
(-49.77, -0.63, 110.50)	2.63E+07	2.60E+07 ± 0.10%	0.99	2.47E+07 ± 0.14%	0.94
(-49.77, -0.63, 114.50)	3.36E+07	3.29E+07 ± 0.09%	0.98	2.88E+07 ± 0.11%	0.86
(-49.77, -0.63, 118.50)	4.17E+07	4.25E+07 ± 0.10%	1.02	4.81E+07 ± 0.13%	1.15
(-49.77, -0.63, 122.50)	5.08E+07	6.12E+07 ± 0.09%	1.21	5.41E+07 ± 0.13%	1.06
(-49.77, -0.63, 125.50)	5.86E+07	5.70E+07 ± 0.09%	0.97	6.13E+07 ± 0.14%	1.05
(-49.77, -0.63, 128.50)	6.61E+07	6.81E+07 ± 0.10%	1.03	6.41E+07 ± 0.13%	0.97
(-49.77, -0.63, 131.50)	7.53E+07	8.40E+07 ± 0.08%	1.12	8.39E+07 ± 0.12%	1.11
(-49.77, -0.63, 134.50)	7.86E+07	9.45E+07 ± 0.10%	1.20	8.81E+07 ± 0.12%	1.12
(-49.77, -0.63, 137.50)	8.18E+07	8.62E+07 ± 0.09%	1.05	9.81E+07 ± 0.11%	1.20
(-49.77, -0.63, 141.50)	7.95E+07	7.57E+07 ± 0.10%	0.95	8.37E+07 ± 0.11%	1.05
(-49.77, -0.63, 145.50)	7.19E+07	7.56E+07 ± 0.09%	1.05	6.71E+07 ± 0.14%	0.93
(-49.77, -0.63, 149.50)	6.07E+07	4.98E+07 ± 0.09%	0.82	5.29E+07 ± 0.12%	0.87
(-49.77, -0.63, 153.50)	4.54E+07	4.70E+07 ± 0.09%	1.04	4.85E+07 ± 0.14%	1.07
(-49.77, -9.45, 114.50)	3.11E+07	3.29E+07 ± 0.08%	1.06	3.40E+07 ± 0.13%	1.09
(-49.77, -9.45, 131.50)	6.65E+07	6.77E+07 ± 0.07%	1.02	6.96E+07 ± 0.11%	1.05
(-49.77, -9.45, 145.50)	6.49E+07	6.37E+07 ± 0.08%	0.98	7.17E+07 ± 0.10%	1.10
(-47.25, -18.27, 114.50)	3.15E+07	3.49E+07 ± 0.08%	1.11	3.22E+07 ± 0.14%	1.02
(-47.25, -18.27, 131.50)	6.53E+07	7.35E+07 ± 0.07%	1.13	6.13E+07 ± 0.09%	0.94
(-47.25, -18.27, 145.50)	6.32E+07	6.04E+07 ± 0.08%	0.96	6.07E+07 ± 0.09%	0.96
(-45.99, -22.05, 114.50)	2.92E+07	3.02E+07 ± 0.09%	1.03	3.34E+07 ± 0.12%	1.15
(-45.99, -22.05, 131.50)	5.78E+07	6.28E+07 ± 0.10%	1.09	5.91E+07 ± 0.09%	1.02
(-45.99, -22.05, 145.50)	5.41E+07	6.57E+07 ± 0.07%	1.21	5.35E+07 ± 0.10%	0.99
(-45.99, -22.05, 106.50)	1.62E+07	1.42E+07 ± 0.09%	0.88	1.66E+07 ± 0.11%	1.03
(-45.99, -22.05, 110.50)	2.25E+07	2.49E+07 ± 0.08%	1.11	2.21E+07 ± 0.11%	0.98
(-44.73, -24.57, 114.50)	2.84E+07	2.59E+07 ± 0.09%	0.91	3.31E+07 ± 0.11%	1.17
(-44.73, -24.57, 118.50)	3.42E+07	3.62E+07 ± 0.07%	1.06	3.53E+07 ± 0.10%	1.03
(-44.73, -24.57, 122.50)	4.04E+07	4.31E+07 ± 0.08%	1.07	4.39E+07 ± 0.10%	1.09
(-44.73, -24.57, 125.50)	4.45E+07	4.61E+07 ± 0.09%	1.03	5.07E+07 ± 0.11%	1.14
(-44.73, -24.57, 128.50)	4.94E+07	4.80E+07 ± 0.07%	0.97	5.02E+07 ± 0.10%	1.02
(-44.73, -24.57, 131.50)	5.33E+07	6.02E+07 ± 0.07%	1.13	5.56E+07 ± 0.10%	1.04
(-44.73, -24.57, 134.50)	5.58E+07	6.40E+07 ± 0.06%	1.15	5.57E+07 ± 0.09%	1.00

(-44.73, -24.57, 137.50)	5.71E+07	6.63E+07 ± 0.07%	1.16	5.58E+07 ± 0.11%	0.98
(-44.73, -24.57, 141.50)	5.48E+07	6.01E+07 ± 0.07%	1.10	5.94E+07 ± 0.09%	1.08
(-44.73, -24.57, 145.50)	4.89E+07	5.34E+07 ± 0.07%	1.09	4.72E+07 ± 0.09%	0.97
(-44.73, -24.57, 149.50)	4.33E+07	3.68E+07 ± 0.08%	0.85	4.21E+07 ± 0.12%	0.97
(-44.73, -24.57, 153.50)	3.04E+07	2.44E+07 ± 0.12%	0.80	2.72E+07 ± 0.12%	0.90
(-42.21, -28.35, 106.50)	1.70E+07	1.69E+07 ± 0.09%	1.00	1.70E+07 ± 0.13%	1.00
(-42.21, -28.35, 110.50)	2.32E+07	2.38E+07 ± 0.09%	1.02	2.41E+07 ± 0.13%	1.04
(-42.21, -28.35, 114.50)	2.88E+07	3.45E+07 ± 0.07%	1.20	2.66E+07 ± 0.11%	0.92
(-42.21, -28.35, 118.50)	3.45E+07	3.66E+07 ± 0.07%	1.06	3.85E+07 ± 0.09%	1.12
(-42.21, -28.35, 122.50)	3.96E+07	4.37E+07 ± 0.07%	1.10	3.89E+07 ± 0.10%	0.98
(-42.21, -28.35, 125.50)	4.34E+07	4.85E+07 ± 0.10%	1.12	5.08E+07 ± 0.10%	1.17
(-42.21, -28.35, 128.50)	4.67E+07	5.31E+07 ± 0.06%	1.14	4.72E+07 ± 0.10%	1.01
(-42.21, -28.35, 131.50)	4.95E+07	5.19E+07 ± 0.06%	1.05	4.99E+07 ± 0.09%	1.01
(-42.21, -28.35, 134.50)	5.08E+07	5.32E+07 ± 0.07%	1.05	4.86E+07 ± 0.09%	0.96
(-42.21, -28.35, 137.50)	5.12E+07	5.05E+07 ± 0.07%	0.99	5.70E+07 ± 0.09%	1.11
(-42.21, -28.35, 141.50)	4.86E+07	4.86E+07 ± 0.06%	1.00	5.25E+07 ± 0.09%	1.08
(-42.21, -28.35, 145.50)	4.39E+07	4.27E+07 ± 0.07%	0.97	4.61E+07 ± 0.10%	1.05
(-42.21, -28.35, 149.50)	3.85E+07	3.65E+07 ± 0.07%	0.95	3.67E+07 ± 0.11%	0.95
(-42.21, -28.35, 153.50)	2.70E+07	2.64E+07 ± 0.10%	0.98	2.23E+07 ± 0.13%	0.82
(-38.43, -33.39, 114.50)	2.93E+07	3.21E+07 ± 0.08%	1.10	2.97E+07 ± 0.10%	1.02
(-38.43, -33.39, 131.50)	4.46E+07	4.63E+07 ± 0.06%	1.04	4.78E+07 ± 0.09%	1.07
(-38.43, -33.39, 145.50)	3.61E+07	3.57E+07 ± 0.07%	0.99	3.49E+07 ± 0.11%	0.97
(-35.91, -35.91, 114.50)	3.19E+07	2.97E+07 ± 0.07%	0.93	2.94E+07 ± 0.11%	0.92
(-35.91, -35.91, 131.50)	4.60E+07	4.67E+07 ± 0.06%	1.01	4.29E+07 ± 0.09%	0.93
(-35.91, -35.91, 145.50)	3.65E+07	4.57E+07 ± 0.07%	1.25	4.56E+07 ± 0.09%	1.25
(-18.27, -47.25, 114.50)	7.29E+07	7.84E+07 ± 0.10%	1.07	7.02E+07 ± 0.10%	0.96
(-18.27, -47.25, 131.50)	1.00E+08	1.07E+08 ± 0.07%	1.07	1.05E+08 ± 0.09%	1.05
(-18.27, -47.25, 145.50)	7.48E+07	7.56E+07 ± 0.08%	1.01	7.85E+07 ± 0.12%	1.05
(-0.63, -49.77, 106.50)	5.58E+07	5.30E+07 ± 0.09%	0.95	6.02E+07 ± 0.13%	1.08
(-0.63, -49.77, 110.50)	7.18E+07	7.43E+07 ± 0.09%	1.03	8.28E+07 ± 0.11%	1.15
(-0.63, -49.77, 114.50)	8.63E+07	8.68E+07 ± 0.08%	1.01	1.01E+08 ± 0.11%	1.17
(-0.63, -49.77, 118.50)	9.99E+07	1.18E+08 ± 0.08%	1.19	1.04E+08 ± 0.13%	1.04
(-0.63, -49.77, 122.50)	1.10E+08	1.32E+08 ± 0.09%	1.20	1.11E+08 ± 0.12%	1.01
(-0.63, -49.77, 125.50)	1.14E+08	1.01E+08 ± 0.09%	0.88	1.11E+08 ± 0.11%	0.97
(-0.63, -49.77, 128.50)	1.17E+08	1.28E+08 ± 0.09%	1.10	1.14E+08 ± 0.12%	0.98
(-0.63, -49.77, 131.50)	1.16E+08	1.37E+08 ± 0.09%	1.18	9.43E+07 ± 0.13%	0.81
(-0.63, -49.77, 134.50)	1.15E+08	1.14E+08 ± 0.08%	0.99	1.14E+08 ± 0.10%	0.99
(-0.63, -49.77, 137.50)	1.11E+08	1.12E+08 ± 0.09%	1.01	1.23E+08 ± 0.11%	1.11
(-0.63, -49.77, 141.50)	1.01E+08	1.08E+08 ± 0.09%	1.08	1.03E+08 ± 0.13%	1.02
(-0.63, -49.77, 145.50)	8.69E+07	7.37E+07 ± 0.09%	0.85	1.18E+08 ± 0.11%	1.36
(-0.63, -49.77, 149.50)	7.62E+07	7.39E+07 ± 0.11%	0.97	7.72E+07 ± 0.14%	1.01
(-0.63, -49.77, 153.50)	5.05E+07	4.39E+07 ± 0.10%	0.87	6.01E+07 ± 0.17%	1.19

Region Average C/E Ratio	$(1.04 \pm 0.08) \pm 0.10$	$(1.03 \pm 0.11) \pm 0.10$
Reaction Average C/E Ratio	$(1.03 \pm 0.09) \pm 0.11$	$(1.02 \pm 0.11) \pm 0.10$

²⁷Al(n,α)

Position (x, y, z)	Experimental	Calculated (KENO)	C/E	Calculated (Benchmark)	C/E
Inner Baffle					
(-4.41, -4.41, 131.50)	1.93E+09	2.24E+09 ± 0.10%	1.16	1.95E+09 ± 0.15%	1.01
(-4.41, -0.63, 131.50)	1.56E+09	1.80E+09 ± 0.10%	1.15	1.76E+09 ± 0.14%	1.13
Region Average C/E Ratio		$(1.05 \pm 0.09) \pm 0.12$		$(1.07 \pm 0.15) \pm 0.08$	
Outer Baffle					
(-39.69, -0.69, 114.50)	1.85E+08	2.28E+08 ± 0.12%	1.23	1.97E+08 ± 0.15%	1.07
(-39.69, -0.69, 131.50)	4.79E+08	5.88E+08 ± 0.08%	1.23	5.10E+08 ± 0.11%	1.07
(-39.69, -0.69, 145.50)	4.77E+08	4.43E+08 ± 0.08%	0.93	5.29E+08 ± 0.11%	1.11
Region Average C/E Ratio		$(1.13 \pm 0.10) \pm 0.17$		$(1.08 \pm 0.14) \pm 0.04$	
Water Gap					
(-44.73, -0.63, 114.50)	8.38E+07	9.48E+07 ± 0.17%	1.13	7.64E+07 ± 0.19%	0.91
(-44.73, -0.63, 131.50)	1.87E+08	2.15E+08 ± 0.13%	1.15	1.95E+08 ± 0.17%	1.04
(-44.73, -0.63, 145.50)	1.78E+08	2.07E+08 ± 0.12%	1.16	1.78E+08 ± 0.16%	1.00
Region Average C/E Ratio		$(1.15 \pm 0.14) \pm 0.01$		$(0.98 \pm 0.18) \pm 0.07$	
Core Barrel					
(-49.77, -0.63, 114.50)	4.11E+07	4.35E+07 ± 0.17%	1.06	3.96E+07 ± 0.21%	0.96
(-49.77, -0.63, 131.50)	7.67E+07	8.32E+07 ± 0.16%	1.09	6.52E+07 ± 0.19%	0.85
(-49.77, -0.63, 145.50)	7.27E+07	8.25E+07 ± 0.15%	1.14	8.20E+07 ± 0.17%	1.13
(-49.77, -9.45, 114.50)	3.20E+07	3.06E+07 ± 0.16%	0.96	3.24E+07 ± 0.23%	1.01
(-49.77, -9.45, 131.50)	6.32E+07	7.74E+07 ± 0.14%	1.23	5.53E+07 ± 0.17%	0.88
(-49.77, -9.45, 145.50)	6.03E+07	5.93E+07 ± 0.16%	0.98	6.64E+07 ± 0.21%	1.10
(-47.25, -18.27, 114.50)	3.16E+07	2.66E+07 ± 0.16%	0.84	2.43E+07 ± 0.20%	0.77
(-47.25, -18.27, 131.50)	6.02E+07	7.90E+07 ± 0.12%	1.31	6.60E+07 ± 0.19%	1.10
(-47.25, -18.27, 145.50)	5.71E+07	5.69E+07 ± 0.13%	1.00	5.77E+07 ± 0.18%	1.01
(-45.99, -22.05, 114.50)	3.05E+07	2.26E+07 ± 0.15%	0.74	3.01E+07 ± 0.22%	0.99
(-45.99, -22.05, 131.50)	5.33E+07	5.62E+07 ± 0.13%	1.05	5.18E+07 ± 0.18%	0.97
(-45.99, -22.05, 145.50)	4.80E+07	4.73E+07 ± 0.12%	0.99	4.77E+07 ± 0.18%	0.99
(-44.73, -24.57, 114.50)	2.75E+07	2.57E+07 ± 0.16%	0.93	3.51E+07 ± 0.20%	1.27
(-44.73, -24.57, 131.50)	4.98E+07	4.81E+07 ± 0.13%	0.97	4.73E+07 ± 0.19%	0.95
(-44.73, -24.57, 145.50)	4.33E+07	3.89E+07 ± 0.13%	0.90	4.44E+07 ± 0.16%	1.03
(-42.21, -28.35, 114.50)	3.17E+07	4.00E+07 ± 0.13%	1.26	2.89E+07 ± 0.19%	0.91
(-42.21, -28.35, 131.50)	5.15E+07	5.94E+07 ± 0.14%	1.15	5.04E+07 ± 0.17%	0.98
(-42.21, -28.35, 145.50)	4.35E+07	4.17E+07 ± 0.12%	0.96	3.63E+07 ± 0.17%	0.83
(-18.27, -47.25, 114.50)	6.81E+07	7.59E+07 ± 0.13%	1.11	6.29E+07 ± 0.18%	0.92
(-18.27, -47.25, 131.50)	8.92E+07	1.24E+08 ± 0.13%	1.39	1.07E+08 ± 0.15%	1.20

(-18.27, -47.25, 145.50)	6.55E+07	6.16E+07 ± 0.14%	0.94	5.68E+07 ± 0.16%	0.87
(-0.63, -49.77, 114.50)	9.55E+07	9.64E+07 ± 0.16%	1.01	6.58E+07 ± 0.17%	0.69
(-0.63, -49.77, 131.50)	1.20E+08	1.72E+08 ± 0.12%	1.43	1.40E+08 ± 0.15%	1.17
(-0.63, -49.77, 145.50)	8.85E+07	9.19E+07 ± 0.13%	1.04	9.31E+07 ± 0.17%	1.05
Region Average C/E Ratio		(1.13 ± 0.13) ± 0.19		(0.98 ± 0.18) ± 0.14	
Reaction Average C/E Ratio		(1.08 ± 0.14) ± 0.16		(1.00 ± 0.18) ± 0.12	

REFERENCES

1. Albenesius, E. L. (1959, September 15). Tritium as a Product of Fission. *Physics Review Letter*. Vol. 3. pp. 274–275.
2. ANSI/ANS-6.1.2.1999, American National Standard Neutron and Gamma-Ray Cross Sections for Nuclear Radiation Protection Calculations for Nuclear Power Plants, American Nuclear Society, La Grange Park, Illinois.
3. ASTM Standard E482, 2011, *Standard Guide for Application of Neutron Transport Methods for Reactor Vessel Surveillance*, ASTM International, West Conshohocken, PA, 2003, DOI: 10.1520/E0482-11, www.astm.org.
4. ASTM Standard E693. 2001 (2007). *Standard Practice for Characterizing Neutron Exposures in Iron and Low Alloy Steels in Terms of Displacements Per Atom*. ASTM International. West Conshohocken, PA. 2003. DOI: 10.1520/E0693-01R07. www.astm.org.
5. ASTM Standard E1035. 2001 (2008). *Standard Practice for Determining Neutron Exposures for Nuclear Reactor Vessel Support Structures*. ASTM International. West Conshohocken, PA. 2003. DOI: 10.1520/E1035-08. www.astm.org.
6. Baccaglini, G., Ball, S., Burchell, T., Corwin, B., Fewell, T., LaBar, M., ... Vollman, R. (2003). *Survey of Materials Research and Development Needs to Support Early Deployment*. INEEL/EXT-03-00141.
7. Chadwick, M. B., Herman, M., Oblozinsky P., Dunn, M. E., Dannon, Y., Kahler, A. C., ... Young, P. G. (2001). *ENDF/B-VII.1 Nuclear Data for Science and Technology: Cross Sections, Covariances, Fission Product Yields and Decay Data*. Nucl. Data Sheets. 112. 2887-2996.
8. Copinger, D. A. & Moses, D. L. (2004, January). *Fort Saint Vrain Gas Cooled Reactor Operational Experience*. NUREG/CR-6839 prepared for the U.S. Nuclear Regulatory Commission by Oak Ridge National Laboratory. ORNL/TM-2003/223.
9. *Design Features and Technology Uncertainties for the Next Generation Nuclear Plant*. (2004, June 30). Independent Technology Review Group. INEEL/EXT-04-01816. Idaho National Laboratory.
10. *Energy Policy Act of 2005*. (2005). Public Law 109-58. U. S. statutes at Large.
11. Everett, J. L. & E. J. Kohler. (1978). Peach Bottom Unit No. 1: A High Performance Helium Cooled Nuclear Power Plant. *Annals of Nuclear Energy*. Vol. 5. pp. 321-335.
12. *GT-MHR Conceptual Design Description Report*. (1996). General Atomics. GA/NRC-337-02.

13. Hartmangruber, D. (2010, December). *Using MAVRIC Sequence in SCALE6 to Determine the Dose Rate in Accessible Areas of the IRIS Nuclear Power Plant*. M.S. Dissertation. Georgia Institute of Technology. Atlanta, Georgia.
14. Hunter, H.T., Ingersoll, D. T., Roussin, R. W., Slater, C. O., Sartori, E., & Kodeli, I. (1994, April 24). SINBAD- A shielding Integral Benchmark Archive and Database for PC's, *Proceedings of the 8th International Conference on Radiation Shielding*. Arlington, Texas. p 795.
15. D. Ilas (personal communication 2011)
16. International Reactor Dosimetry File 2002. (2006). International Atomic Energy Agency.
17. Jacobs, D. G. (1968, December). *Sources of Tritium and its Behavior upon Release to the Environment*. ORNL/NSIC-37.
18. Kupitx, J. & Dee, J. B. (2011). International status of HTGRs. *IAEA Bulletin*, 26(4).
19. Maerker, R. E. (1989). *Analysis of the VENUS-3 Experiments*, NUREG/CR-5338 (ORNL/TM- 11106). prepared for the U. S. Nuclear Regulatory Commission by Oak Ridge National Laboratory.
20. McElroy, W.N. (1981, July). *LWR Pressure Vessel Surveillance: Dosimetry Improvement Program: PCA Experiments and Blind Test*. NUREG/CR-186. prepared for the U.S. Nuclear Regulatory Commission by Hanford Engineering Development Laboratory.
21. *NGNP Point Design – Results of the Initial Neutronics and Thermal-Hydraulic Assessments*. (2003). INEEL/EXT-03-00870. Revision 1.
22. Oh, C. H. & Kim, E. S. (2009, September). *Development and Verification of Tritium Analyses Code for Very High Temperature Reactor*. INL/EXT-09-16743.
23. Oh, C. H. & Kim, E. S. (2011, March). *Scoping Analyses on Tritium Permeation to VHTR Integrated Industrial Application Systems*. INL/EXT-10-19607.
24. Ohashi, H. & Sherman, S. (2007, June). *Tritium Movement and Accumulation in the NGNP System Interface and Hydrogen Plant*. INL/EXT-07-12746.
25. Partain, K., Saurwein, J., & Shenoy, A. (2007, July 10). *Preconceptual Engineering Services For the Next Generation Nuclear Plant (NGNP) with Hydrogen Production*. Document 911107. Rev. 0. General Atomics.
26. Peplow, D. E. (2009, January). *MAVRIC: MONACO with Automated Variance Reduction using Importance Calculations*. ORNL/TM-2005/39. UT-Battelle, LLC. Oak Ridge National Laboratory
27. Peplow, D. E. (2009, January). *Monaco: A Fixed-Source, Multi-Group Monte Carlo Transport Code for Shielding Applications*. ORNL/TM-2005/39. UT-Battelle, LLC. Oak Ridge National Laboratory.

28. Petti, D. (2010, August). *NGNP Research and Development Status*. INL/EXT-10-19259
29. Price, M.S.T. (2012). The Dragon Project origins, achievements and legacies. *Nuclear Engineering and Design*, article in press. (2012).
30. Remec, I. & Kam, F. B. K. (1997, July). *Pool Critical Assembly Pressure Vessel Facility Benchmark*. NUREG/CR-6454 (ORNL/TM-13205). prepared for the U.S. Nuclear Regulatory Commission by Oak Ridge National Laboratory.
31. Risner, J. M., Wiarda, D., Miller, T. M., Peplow, D. E., Patton, B. W., Dunn, M. E., & Parks, B. T. (2011). *Production and Testing of the VITAMIN-B7 Fine-Group and BUGLE-B7 Broad-Group Coupled Neutron/Gamma Cross-Section Libraries Derived from ENDF/B-VII.0 Nuclear Data*. Oak Ridge National Laboratory. Oak Ridge, TN. NUREG/CR-7045; ORNL/TM-2011/12.
32. Saito, S., Tanaka, T., Sudo, Y., Baba, O., Shiozawa, S., & Okubo, M. (1991). Design and safety consideration in the High-Temperature engineering Test Reactor (HTTR), *Energy*, 16(1–2). pp. 449-458.
33. *SCALE: A Modular Code System for Performing Standardized Computer Analyses for Licensing Evaluation*. (2009, January). ORNL/TM-2005/39. Version 6. Vols. I–III. Oak Ridge National Laboratory. Oak Ridge, Tenn..
34. Shenoy, A. (1996, July 16). *GT-MHR Conceptual Design Description Report*, Document 910720. Rev. 1. General Atomics.
35. Shenoy, A. (1997, July 10). *NGNP and Hydrogen Production Preconceptual Design Studies Report*. Document 911107. Rev. 0. General Atomics.
36. Shibata, K., Iwamoto, O., Nakagawa, T., Iwamoto, N., Ichihara, A., Kunieda, S. ... Katakura, J. (2011). JENDL-4.0: A New Library for Nuclear Science and Engineering, *Journal of Nuclear Science Technology*. 48(1).
37. Sloth, N., Horrocks, D. L., Boyce, E. J., & Studier, M. H. (1962, April). Tritium in the Thermal Neutron Fission of Uranium—235. *Journal of Inorganic and Nuclear Chemistry*. 24(4). pp. 337-341.
38. *Standards for Protection Against Radiation*. (2009). 10 CFR 20. United States.
39. Strizak, J. P., Burchell, T. D., & Windes W. (2006, September). *Status of Initial Assessment of Physical and Mechanical Properties of Graphite Grades for NNGP Applications*. ORNL/TM-2006/553.
40. Wagner, J.C., Blakeman, E.D., & Peplow, D.E. (2007) Forward-Weighted CADIS Method for Global Variance Reduction. *Transactions of the American Nuclear Society*. Vol. 97. pp. 630-633.

41. Wagner, J.C. & Haghghat, A. (1998) Automated Variance Reduction of Monte Carlo Shielding Calculations Using the Discrete Ordinates Adjoint Function. *Nuclear Science and Engineering*. Vol. 128. pp. 186-208.